Novel Instrumentation to Reach the 0.1% Polarization Accuracy for the Chromospheric Lyman-Alpha Spectro-Polarimeter

Giono Gabriel

Doctor of Philosophy

Department of Astronomical Science
School of Physical Sciences
SOKENDAI (The Graduate University for Advanced Studies)

Novel Instrumentation to Reach the 0.1% Polarization Accuracy for the Chromospheric Lyman-Alpha Spectro-Polarimeter

by

Giono Gabriel

Dissertation

submitted to the Department of Astronomical Science
in partial fulfilment of the requirements for the degree of

Doctor of Philosophy

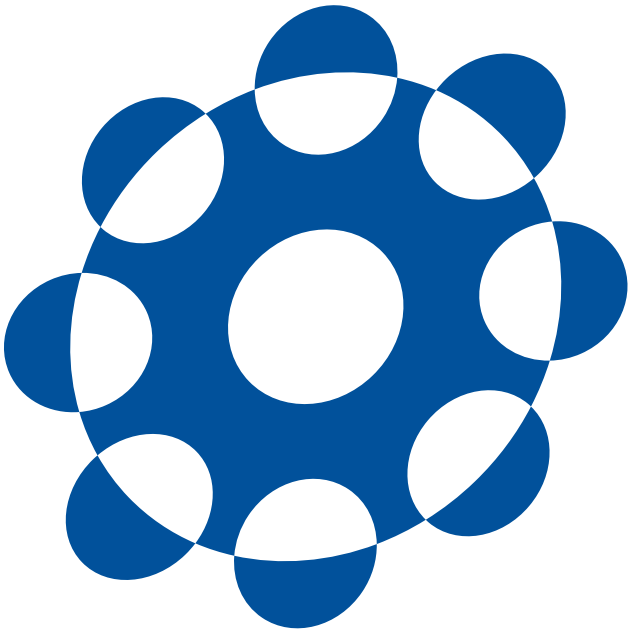

SOKENDAI (The Graduate University for Advanced Studies)
March 2016

Abstract

Observations revealed temperature higher than a million degrees kelvin in the solar corona. This is unexpected, as the photospheric temperatures are only around 6,000K. The heating mechanism of the upper-atmosphere is not understood yet, although the key element is most likely related with the conversion of the magnetic energy into thermal and kinetic energies at the chromospheric and transition region height. These two layers are located in between the photosphere and the corona, where the temperature rapidly rises.

Filamentary structures seen in these two regions implies that the dynamic is dominated by the magnetic field: low plasma β (gas/magnetic pressure ratio) holds there, and indicates that the magnetic field might be a key component of the heating mechanism in the upper solar atmosphere. However, direct measurements of the weak chromospheric and transition region magnetic fields are extremely difficult, as the Zeeman effect is usually unobservable due to the Doppler width of the line being larger than the Zeeman splitting. Yet, the less-explored Hanle effect can be used, as it changes the polarization emitted from scattering processes in the presence of magnetic field regardless of the line Doppler width. Recent progress in the theoretical field and numerical simulations enable to diagnose the weak magnetic field in the upper atmosphere via the analysis of the polarization from the Hanle effect, which pushed the need for new instrumentation to measure the magnetic field in the upper solar atmosphere.

With this background, the Chromospheric Lyman-Alpha SpectroPolarimeter (CLASP) was proposed as a sounding rocket experiment designed to measure the linear polarization of the hydrogen Lyman-alpha line (121.6nm). The line is emitted in the upper-chromosphere and transition region, and the Hanle effect is expected to operate in the core of this spectral line for magnetic field between 10 to 250 Gauss. Detecting its polarization signature requires an instrumentation with an unprecedentedly high polarization sensitivity of 0.1% in the vacuum ultraviolet (VUV) range. A dedicated design of the instrument and its experimental verification was crucial to ensure the scientific success of the project. However, developing a space instrument for VUV also comes with a lot of technical difficulties: tests and calibrations under vacuum condition, molecular contamination requiring careful baking of the instrumental parts to avoid outgasing under vacuum, robust optics able to survive launch vibration, etc. For these reasons, the development of CLASP was unique and very challenging.

The novel experimental solutions developed to ensure the required optical and polarimetric performances of the instrument are presented in this work:

- Telescope optical alignment: The telescope is a classical two-mirror Cassegrain design, and adjusting not only the tilt but also the despace and the decenter of the secondary mirror with respect to the primary is crucial to ensure the image quality. To avoid experiment under vacuum, the telescope was aligned by measuring its wavefront error using a visible-light laser interferometer in a double-pass configuration, even with the primary mirror's cold mirror coating of narrow passband Ly-α filter reflecting less than 0.1% of visible-light. The secondary mirror was adjusted by shimming to remove coma and defocus aberration at the center of the field of view. The alignment was successfully performed, reaching better than required spatial resolution.

- Spectro-polarimeter optical alignment: The spectro-polarimeter is a inverse-Wadsworth mounting design, where a reflecting grating separates the light from the slit into two channels, for

each of which a camera mirror re-image the slit onto a CCD detector. Adjusting the grating and camera mirrors' tilts is required to meet the spatial and spectral resolution requirement. A unique alignment procedure was developed for spectro-polarimeter optical alignment to minimize the experiment under vacuum. The camera mirrors were aligned in visible-light (He-Ne 632.8nm) by using a custom-made grating of same diffraction angle as the flight Lyman-α grating by tuning its ruling density for the He-Ne wavelength. The camera mirrors were successfully aligned by diagnosing the observed spot shape on the CCD with optical simulation performed prior to the alignment experiment. The visible-light grating was then replaced by the Lyman-α grating, and only its tilts, as well as the CCD focus positions were adjusted under vacuum by injecting VUV lights from a Deuterium lamp. Optical simulations were used to provide quantitative comparison for the alignment under vacuum, and the spectro-polarimeter was successfully aligned within the required spatial and spectral resolution.

- Telescope focus position adjustment: The telescope focus position was adjusted to the spectro-polarimeter slit plane using a configuration in which white-light source was placed in the back of the slit to introduce the light into the slit and in which a flat mirror located in front of the telescope aperture, reflecting the light back into the telescope and slit-jaw optics. By inducing a small tilt on the flat mirror, the image of the reflected slit was observed by the slit-jaw optics and the width of the slit image provided indication on the focus position of the telescope. Several measurements for different shim thickness inserted between the telescope and the spectro-polarimeter parts successfully determined the best focus position of the telescope onto the slit.

- Optical checks though the tests: Two measurement methods were designed to confirm the telescope focus position and the spectro-polarimeter optical performances during the integration of the instrument. Measurements were performed before and after the various vibration tests performed prior to launch and also after shipments from the different locations from Japan to USA. Results from every measurements performed showed that changes of the optical performances were within the requirement, ensuring the healthiness of the instrument until launch.

- Polarization calibration: An unprecedentedly precise polarization calibration of the spectro-polarimeter was performed at Lyman-α to estimate the artificial polarization created by cross-talks between the different Stokes parameters and to achieve the required 0.1% polarization accuracy in VUV for the first time ever. A Lyman-α light-source with linear polarizers able to provide a known polarized input under vacuum was designed. Long exposures (i.e. 15 minutes) on each of the polarization states were required to achieve the needed accuracy due to the weak intensity of the Lyman-α light-source. Two different methods were used to change the polarization input to the spectro-polarimeter: the direct method in which the entire light-source was rotated, and the waveplate method in which a half-waveplate with rotating motor was installed after the light-source. The interpretation of the polarization measured was complex, as the multiple effects of CLASP rotating half-waveplate (e.g. drift of polarization angle over time due to non-uniformity of rotation speed), the Lyman-α light-source (i.e. illumination angle creating a polarization gradient along the slit and off-axis illumination creating a shift of polarization input) and half-waveplate used for the calibration (i.e. retardance changing the input to the spectro-polarimeter) were quantified and taken

into account. By combining both methods and removing the previously cited artefacts, the response matrix of the spectro-polarimeter, composed of the spurious polarization, the scale factor and the azimuth error terms, was successfully determined within the required tolerances.

The integration and tests resulted in CLASP instrument satisfying all of its scientific requirements, and the payload was successfully launched on September 3^{rd}, 2015. The preliminary results from the limb observation confirmed the scattering polarization in the Lyman-α line for the first time and the disc center observation were analysed to confirm the pre-flight polarization calibration. Polarization signals created by the local anisotropy of the solar atmosphere were detected even at disc center. Therefore, a statistical approach was adopted to cancel out the solar fluctuations by summing pixel spatially along the slit. This method revealed a spurious polarization level smaller than the measurement from the pre-flight calibration, determined with a 3-σ. Further investigations were conducted to understand the origin of the discrepancy on the spurious polarization estimated pre-flight and in-flight. As a result, it turned out that the influence of the cross-talks from the incoming linear polarization to the measured intensity was underestimated during the pre-flight calibration. These terms of the response matrix were thought to only imply an additional error on the other matrix elements, but actually produced a similar effect as of the spurious polarization terms in case of a highly polarized incoming light such as the pre-flight calibration. Hence, a new method was developed to estimate these two additional terms, alongside with the spurious polarization, scale factor and azimuth error terms of the response matrix, from the measurements recorded during the pre-flight polarization calibration. The results indicated a much smaller spurious polarization level compared to the previous estimation, which was consistent with the in-flight calibration. However, this new method could not reach the required accuracy on the spurious polarization terms, due to the limitation of the pre-flight calibration measurements. The combined results of the pre-flight polarization calibration response matrix and the spurious polarization derived during the in-flight polarization calibration provided a complete response matrix of the instrument, which ensured the required 0.1% polarization accuracy. In addition, the flight observations were used to confirm the achieved spatial and spectral resolutions, which is consistent with the expected resolutions from the optical alignment.

Acknowledgements

These last three years in Japan were an incredible experience, on both the personal and the professional aspects of life, and were concluded with the completion of this PhD thesis. Many persons are related to this invaluable experience, and I would like to acknowledge them as best as I can hereafter.

First of all, I would like to express my thanks to my parents and family, who sharpened my curiosity about the world as a child and allowed me to study toward an academic degree with their moral and financial supports. I would also like to thank Laura, for all the moral support and inspiration during the three-years period of the thesis, as she greatly changed my vision of the world and influenced the person I became and wish to become.

My thesis-related thanks are numerous, and probably the most important one goes to Prof. Saku Tsuneta without whom this work would not have been possible. I want to thank him for proposing me to work on the CLASP project which allowed me to pursue my studies in Japan, for his help with the administrative procedures and for his positive feedback on my achievements throughout the thesis. I would also like to thank my thesis advisors: Dr. Yoshinori Suematsu, Dr. Hirohisa Hara and Dr. Yukio Katsukawa, for their guidance and teaching. Special thanks go to Dr. Katsukawa, for his patience and careful revision of my reports, publications and thesis. Similarly, I would like to thank the CLASP team from NAOJ, for their patient teaching, explanations and revisions of my work: Dr. Ryouhei Kano, Dr. Ryoko Ishikawa, Dr. Noriyuki Narukage, Dr. Masahito Kubo, Dr. Shin-nosuke Ishikawa and Takamasa Bando. From the international collaborators to the CLASP project, I want to particularly thank Dr Javier Trujillo Bueno for helping me grasp the underlying physics of the atomic polarization and the Hanle effect, which are at the core of the instrument's scientific purpose. Finally, thanks to the SOKENDAI university for supporting the graduate program of my thesis and the JSPS KAKENHI Grant Numbers 23340052, 24740134, 24340040, and 25220703 which funded the CLASP project and the related activities conducted on the instrument during this thesis

On a more personal level, I would like to especially thank Patrick Antolin, for his friendship and for our invaluable discussions on broad topics which refined my vision of the world. Additionally, I want to thank my friends from the Kyokushin karate Tokyo Josai branch, who helped me balancing my stress level during the difficult times of the thesis by joyfully beating me down. You are among the nicest people I have met, and thank you for making me feel integrated even with my struggling Japanese!

The last part of my acknowledgements goes to my supervisors from earlier internships: Dr. Andrzej Krasiński from the Centrum Astronomiczne im. M. Kopernika (Warsaw, Poland) and Joe Zender from the European Space Agency (ESTEC, Noordwijk, The Netherlands), who allowed me carry out my first experiences in the scientific world and indirectly paved my way toward this PhD thesis. Equivalently, I would also like to thank the Université Claude Bernard Lyon 1 and its professors, because this is where it all begun.

Contents

Chapter 1

Introduction

1.1 The solar chromosphere

The Sun's "surface" is called the photosphere and is the observational limit of the Sun's interior. Below this layer, as the density increases, the optical depth becomes too large for the photons to directly escape into space. However, the photosphere is not a layer fixed at a given height: the various emission lines from the atomic elements are forming at different optical depth and with different optical thickness and the temperature and the density change locally in both space and height. In this region, temperature ranges from 6,500K at the deepest observable depth to a minimum around 4000K ([1],[2]). The solar atmosphere starts from the photosphere, and extends in outer space with the solar corona. Spectroscopic observations of the corona performed during solar eclipses revealed emission lines produced by temperatures higher than 1MK ([3], [4]). Utraviolet (UV) observations from space instruments (e.g. Skylab [5]) also confirmed this temperature increase in the solar atmosphere, and theoretical models of the solar atmosphere (e.g. VAL models, [6], [7]) were developed to picture the stratification of the atmosphere above the photosphere, with the chromosphere, the transition region and the corona (shown in Figure 1.1). The density rapidly decrease above the photosphere, dropping by six orders of magnitude in the chromosphere and the temperature decreases from the photospheric temperature to the temperature minimum, before rising again to around 10,000K. A rapid rise in temperature occurs in the transition region, from the chromospheric temperature to more than one million degrees in the corona. This increase in temperature is counter-intuitive, as the temperature should be expected to decrease radially from the center of the Sun. This is one of the major unexplained phenomenon in solar physics, called coronal heating problem.

The region from the chromosphere to the corona is also dominated by the magnetic energy: as the density decrease with height, the ratio between gas pressure and magnetic pressure or plasma β becomes smaller than unity (see Figure 1.1). In this regime, the plasma motion is driven by the magnetic forces. This results in a very dynamic layer, and in structures such as coronal loop where the plasma motion follows the magnetic field lines.

Magnetic reconnections can occur when magnetic field lines "collide" ([10]), reconfiguring rapidly the magnetic field organization and transferring the magnetic energy into thermal and kinetic energy of the plasma. This mechanism is thought to be a major magnetic energy release mechanism of solar flares of solar flares ([11]), which are the most energetic events of the solar atmosphere in which the plasma is heated to more than ten millions of kelvins. Small scale re-

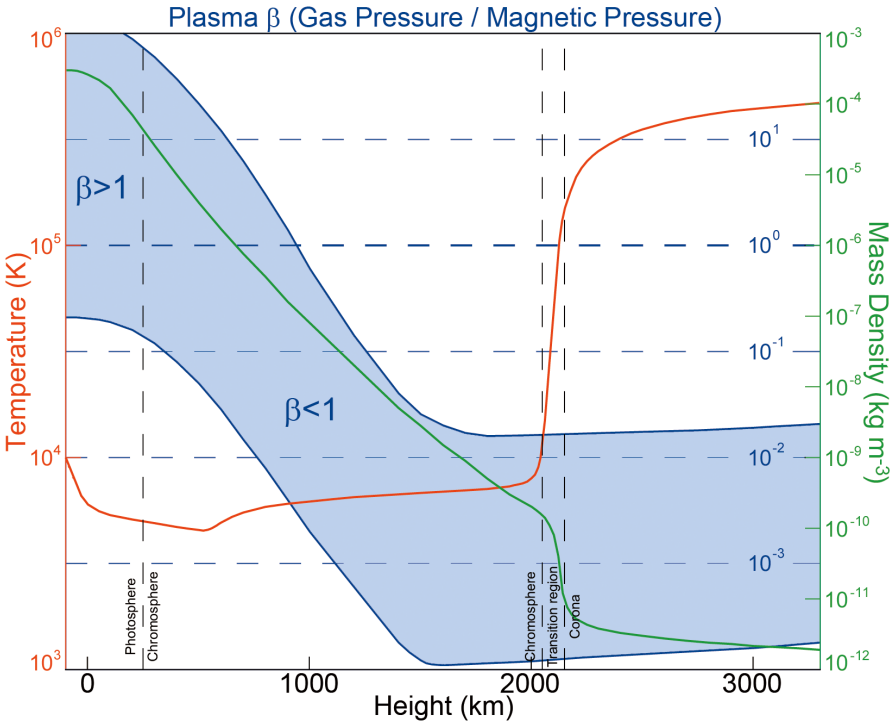

Figure 1.1: Evolution of the temperature (red), density (green) and plasma β (blue) as a function of height in the solar atmosphere. Figure adapted from [8] and [9]

connection processes in the solar upper-chromosphere and transition region are a candidate of the heating problem ([12],[13]). Another possible theory is the heating by magneto-hydrodynamic (MHD) waves propagating upward from the photosphere. Such propagating waves were observed in the structure of the solar atmosphere, as in spicules ([14]), and could carry energy from the photosphere to the corona. The magnetic field in the solar upper-atmosphere is one of the important physical quantities to fully understand these MHD waves.

Both theories are related to the chromospheric and transition region magnetic fields, making it a crucial quantity to probe in order to confront observation and theory.

1.2 Magnetic field measurement through polarimetric measurements

The polarization is the two-dimensional oscillations of the light-wave electric field in the plan perpendicular to its direction of propagation, and can be describe using the Stokes formalism. Stokes parameters are convenient quantities for describing the polarization of the light and are shown in Figure 1.2. In simple words, the Stokes parameter I describes the total intensity of the optical beam; the second parameter Q describes the preponderance of LHP (horizontally linearly polarized) light over LVP (vertically linearly polarized) light; the third parameter U the preponderance of L+45P (+45° linearly polarized) light over L−45P (−45° linearly polarized) light and, finally, V the preponderance of RCP (right-handed circularly polarized) light over LCP (left-

handed circularly polarized) light. These four parameters can completely define any polarization states of a light-wave.

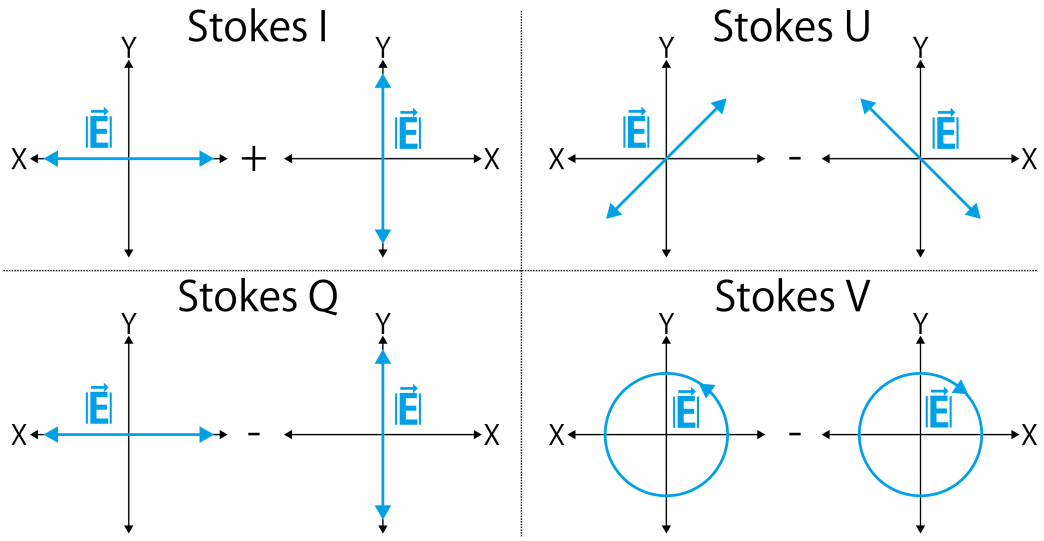

Figure 1.2: Definition of the Stokes parameter I, Q, U and V. The blue arrows symbolize the amplitude (i.e. modulus) of the electric field vector along the given arrow. For Stokes V, it symbolize the left-handed and right-handed amplitude of the electric field.

In the framework of quantum mechanic, the quantum states of an electron inside an atom are restrained to particular transition depending on the different energy levels of the atom. The quantum state of the electron is determined by the four quantum numbers: n (principal quantum number), l (azimuthal quantum number), m (magnetic quantum number) and s (spin quantum number). The quantum number l and s are coupled to form the total angular momentum number J (i.e. spin-orbit interaction), with a degenerated magnetic quantum number M with values ranging from $-J$ to J. In the presence of a magnetic field, the magnetic sublevels of quantum numbers M split, with a separation equal to $\mu_B B M g_J$ where μ_B is the Bohr magneton and g_J is the Lande factor. In a case where $J = 1$, the magnetic sublevel with M equal ± 1 happen to emit and absorb only circularly polarized light along the quantization axis of the atom (i.e. taken here as the direction of the magnetic field). This is known as the longitudinal Zeeman effect, and is used for magnetic field diagnostic in the strong magnetic field of the photosphere along the line-of-sight by measuring the Zeeman splitting of the circular polarization components. If the atoms is observed from a direction perpendicular to the quantization axis, the polarization emitted by the $M = \pm 1$ components is seen as linear polarization, at 90° from the linear polarization emitted by the $M = 0$ component. This configuration is referred as the transverse Zeeman effect. Figure 1.3 summarizes the two possible configurations of the Zeeman effect.

However, the Zeeman effect is only easily observable if the magnetic field is strong enough to split the polarized components with a larger separation than the line Doppler width (i.e. broadening of the line due to the temperature). It is otherwise complicated to measure the weak polarization amplitude (i.e. weak field regime). This limitation makes the Zeeman effect of little interest to investigate the weak magnetic field in the hot upper-chromosphere and transition region. Nevertheless, the less-explored Hanle effect ([15]) can be used, as it changes the polarization emitted

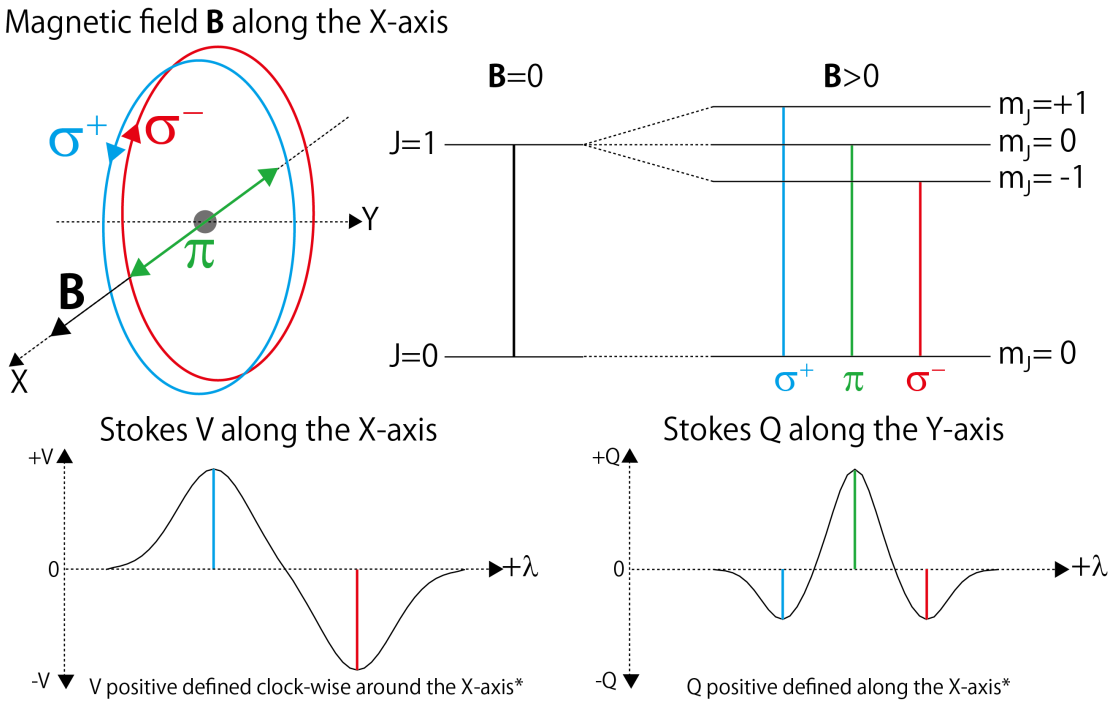

Figure 1.3: Explanation of the Zeeman effect. Top-left shows the three possible orbitals (π, σ^+ and σ^-) of an electron in a $J = 1$ level due to magnetic sublevel splitting by the action of the magnetic field (top-right). Bottom-left shows the resulting polarization as seen along the magnetic field axis (longitudinal Zeeman effect) and bottom-right shows the polarization at 90° from the magnetic field axis (transverse Zeeman effect).

from scattering processes in the presence of magnetic field regardless of the line Doppler width. In a presence of a magnetic field, the Hanle effect affects the quantum coherences between the magnetic sublevels pertaining to each J-levels. For a given J-level, the population of each magnetic sublevels is given by the density matrix $\langle J, M'|\rho|J, M\rangle = \rho_J(M, M')$. For example, if considering a two-level atom with a lower-level $J_l = 0$ and an upper-level $J_u = 1$, M for the upper-level can only take three discrete values: $+1$, 0 and -1. Hence, the density matrix for this upper-level is a 3x3 matrix as shown in Equation (1.1). The diagonal terms of this matrix represent the population of each magnetic sublevels, and the non-diagonal terms are the quantum coherences between the magnetic sublevels.

$$\rho_{J_u=1}(M, M') = \begin{pmatrix} \rho(+1,+1) & \rho(0,+1) & \rho(-1,+1) \\ \rho(+1,0) & \rho(0,0) & \rho(-1,0) \\ \rho(+1,-1) & \rho(0,-1) & \rho(-1,-1) \end{pmatrix} \tag{1.1}$$

Two concepts are important to understand the origin of atomic polarization and the Hanle effect: selective absorption/emission and quantum coherence.

- Selective absorption/emission: As mention previously, the $M = \pm 1$ magnetic sublevels of a $J_u = 1$ level can only absorb and emit perfectly circular polarization along the quantization axis of the atom (i.e. Stokes V equal to ± 1). On the other hand, the magnetic sublevel $M = 0$

absorbs and emits linearly polarized light along the quantization axis. These selection rules for absorption and emission can creates selective absorption and selective emission which lead to atomic population imbalance. In a presence of a perfectly isotropic illumination (i.e. equal in all directions), the density matrix is simply unity: the atomic populations are equal in all three levels. However, in a presence of an anisotropic illumination, these selection rules are important. Two extreme cases are presented as an example: an unidirection radiation field along the quantization axis of the atoms and an omnidirectional radiation field contained in the plane perpendicular to the quantization axis of the atoms, as shown in Figure 1.4. The incident radiation field is assumed to be unpolarized and with axial symmetry along the quantization axis of the atoms. In the first case, the unpolarized light can be considered as a sum of perfectly circular polarization to the left and to the right. Only the magnetic sublevels $M = \pm 1$ can absorb light from the radiation field, which depopulate the $M = 0$ magnetic sublevel. In the second case, the radiation field can be considered as a sum of perfectly polarized light along and perpendicular to the quantization axis. In this case, the $m = 0$ magnetic sublevel can absorb half of the radiation (i.e. along the quantization axis) whereas the $M = \pm 1$ magnetic sublevels can only absorb a quarter of the radiation each, creating a depopulation of the $M \pm 1$ magnetic sublevels. This process of atomic levels population and depopulation by the radiation field is referred as repopulation pumping and creates atomic population imbalance, resulting in a net emission or absorption of the polarization signal. The anisotropy of the radiation field depends on various parameters: the cosine of the heliocentric angle μ at which the observation are made but also the wavelength (i.e. depending the amount of limb darkening or brightening) and the local topology of the solar atmosphere (i.e. temperature and density).

- Quantum coherence : Non-zero quantum coherences exist when the wave function presents a well defined phase relationship between the pure quantum states $|J, M\rangle$ and $|J, M'\rangle$. In the absence of magnetic fields, all coherences are zero if the quantization axis of total angular momentum is chosen along the symmetry axis of the pumping radiation beam. Non-zero quantum coherences appear in the presence of an inclined magnetic field with respect to the symmetry axis of the radiation field.

The Hanle effect is the action of the magnetic field onto the quantum coherence of the magnetic sublevels. To discuss the Hanle effect, the density matrix has to be expressed in the magnetic field reference frame : two rotations of the density matrix are required in the classical $|J, M\rangle$ representation. Alternatively, the multipole components (ρ^K_Q) can be used, which has the advantage of only required one rotation. Equation (1.2) shows the conversion from the classical representation to the multipole components representation, where the matrix is the Wigner 3-j symbols.

$$\rho^K_Q(J) = \sum_{MM'} (-1)^{J-M} \sqrt{2K+1} \begin{pmatrix} J & J & K \\ M & M' & -Q \end{pmatrix} \rho_J(M, M') \tag{1.2}$$

The K and Q of the multipole components representation are indices which depends on the initial J and M indices. The ρ^K_Q with $Q = 0$ are real numbers composed of linear combination of the population of the various magnetic sublevels M, whereas the ρ^K_Q with $Q \neq 0$ are complex numbers given by linear combination of the quantum coherences between those sublevels. In this representation, the Hanle effect can be simply expressed as shown in Equation (1.3), where $\Gamma_u = 8.79 \times 10^6 B g_{J_u}/A_{ul}$ with the magnetic field B, the Lande factor of the level g_{J_u} and the Einstein

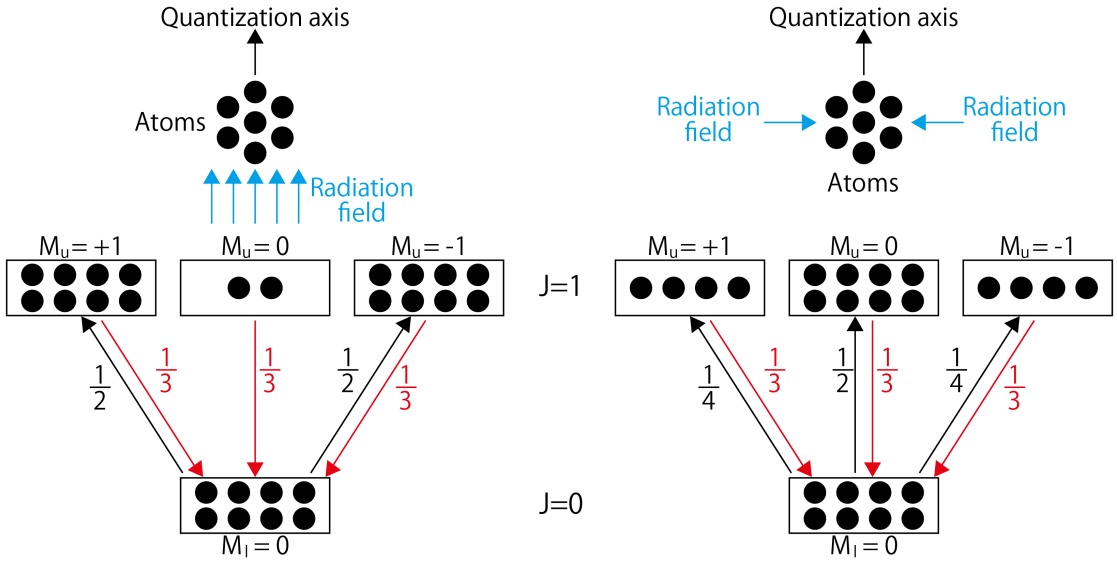

Figure 1.4: Explanation of the atomic population imbalance by selective absorption due to radiative pumping. Left shows the case for an unidirection radiation field along the quantization axis of the atoms. Note that, given enough time, the upper level with M_u will be completely depopulated. Right shows the case for an omnidirectional radiation field contained in the plane perpendicular to the quantization axis of the atoms. The incident radiation field is assumed to be unpolarized and with axial symmetry along the quantization axis of the atoms.

coefficient of the transition upper-lower level A_{ul}. The $[\rho^K_Q]_{B=0}$ are the ρ^K_Q elements for a non-magnetic case defined in a reference frame where the quantization axis is aligned with the magnetic field vector. Equation (1.3) summarizes the action of the Hanle effect, clearly showing that the population imbalances (i.e. ρ^K_Q with $Q = 0$) are unaffected, whereas the quantum coherences (i.e. ρ^K_Q with $Q \neq 0$) are reduced and dephased compared to the non-magnetic case.

$$\rho^K_Q(J_u) = \frac{1}{1 + iQ\Gamma_u}[\rho^K_Q]_{B=0} \tag{1.3}$$

The previously given explanations on the atomic polarization and the Hanle effect were presented for the purpose of the introduction. More rigorous explanations can be found in ([16]) and ([17]). Recent progress in numerical simulations enabled possible diagnostics of the solar polarization via the Hanle effect ([18], [19]). Hanle effect diagnostics has been applied to prominences and coronal fields in the visible and the near infrared via the polarimetric observations. For example, the Helium multiplet at 1083nm was successfully used to derive the magnetic fields in prominences and spicules ([20], [21]). Yet, no instrument was capable of performing polarimetric observation of the upper-chromosphere and transition region in the Quiet Sun region of the solar disk, therefore pushing the need for new instrumentation.

1.3 Motivation for new instrumentation

1.3.1 The Lyman-α line

The Lyman-α line (121.56nm) is emitted by the transition from the first excited level to the ground-level of the hydrogen atom. Due to the abundance of hydrogen in the solar atmosphere (92% of the Sun composition) and its transition from the first excited level to the ground level, the Lyman-α line is the strongest emission line of the solar spectra. The core of the line is emitted from the lower transition region, whereas the wings are formed more deeply in the chromosphere due to radiative transfer processes, as shown in Figure 1.5. Therefore, this line is suitable for investigating the lower transition region and the upper-chromosphere.

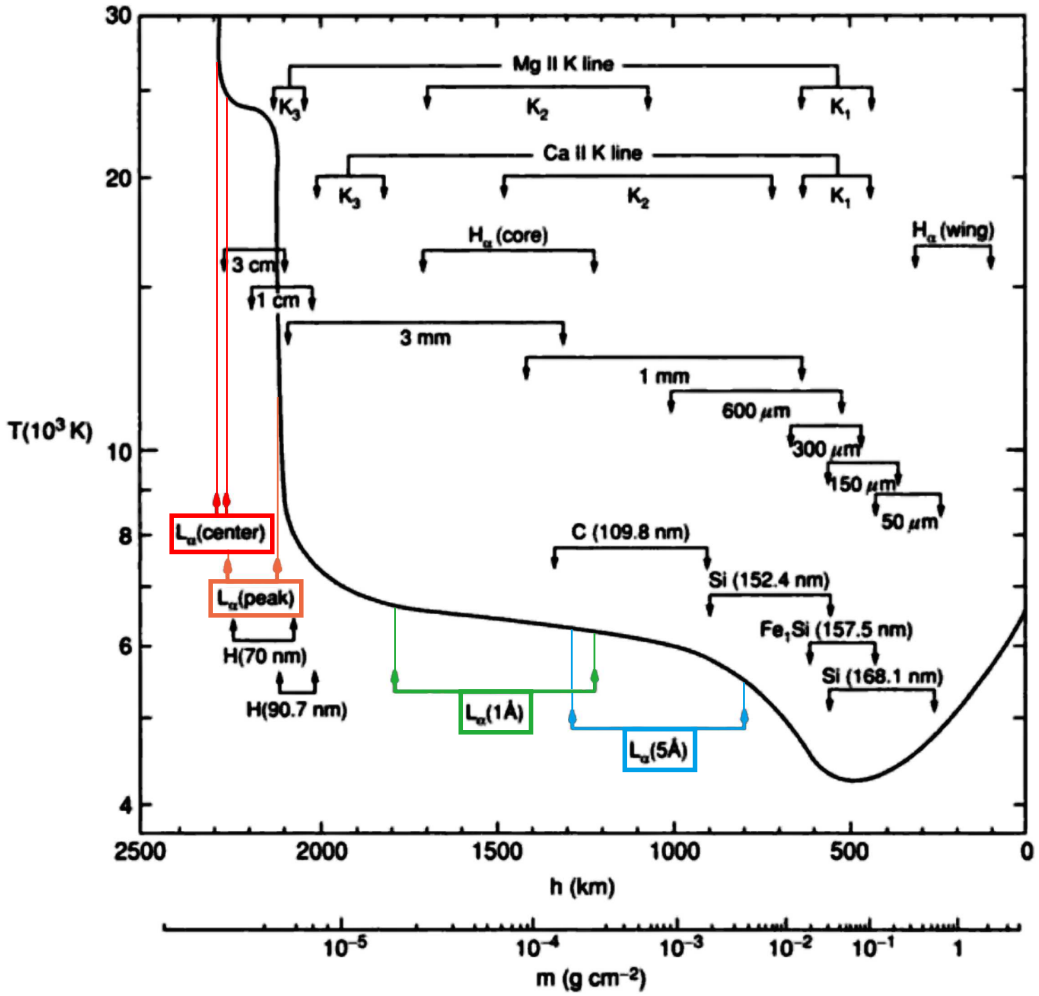

Figure 1.5: Temperature versus height in the chromosphere and transition region, showing the formation heigh of the Lyman-α line core and wings. Figure from [7].

The Lyman-α wavelength is located in the vacuum ultraviolet (VUV) region of the spectrum and is absorbed by the Earth's atmosphere. As the VUV's wavelengths are absorbed by Earth's

atomsphere, observation of the Sun in this wavelength range is extremely hard. Only few previous missions successfully observed the intensity profile of the Lyman-α line: for example the Solar Ultraviolet Measurements of Emitted Radiation spectrograph (SUMER, onboard the SOHO spacecraft, [22]) or the Orbiting Solar Observatory 8 LPSP instrument (OSO8 spacecraft, [23]). An example of the Lyman-α intensity is presented in Figure 1.6, showing the self-reversed profile of the line. The Very high Angular resolution Ultraviolet Telescope sounding rocket (VAULT, [24]) also provided intensity images of the lower transition region and upper-chromosphere around 121.6nm and with a subarsecond spatial resolution (0.5") during its several flights from 1999 to 2014. This instrument revealed an inhomogeneous layer composed of dark regions and mossy bright patches with filamentary thread-like structures (~1"width, ~10"length) in the Quiet Sun, as shown in Figure 1.7. These thread-like structures were supposed to be supported by the local magnetic field, but no instrument was capable to provide the magnetic field informations.

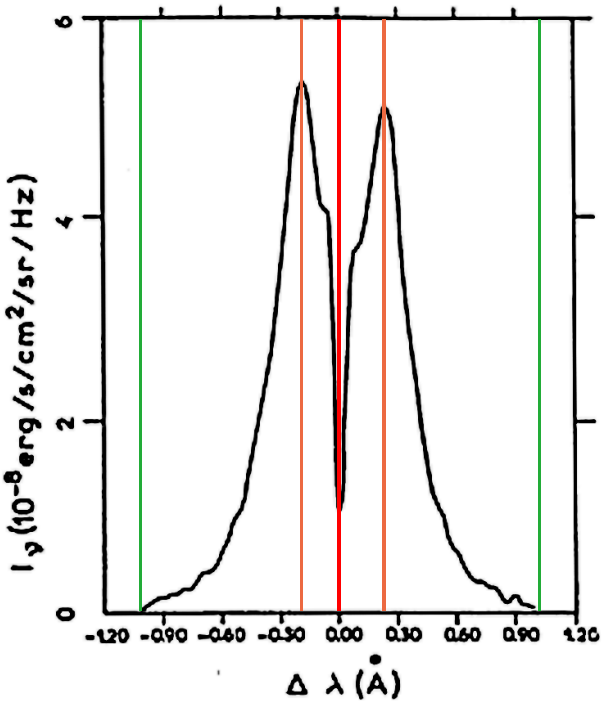

Figure 1.6: Intensity profile of the Lyman-α line observed by the OSO8 spacecraft. The intensity decrease in the line-center is due to geocoronal absorption. Vertical line shows the position of the center, peak and wings as in Figure 1.5. Profile from [23].

Recent theoretical investigations ([19], [25], [26], [27]) revealed that one of the upper level of the Lyman-α transition ($2p_{3/2}$, see Figure 1.8) can produce scattering polarization in the line core due to population imbalances and quantum coherences between its magnetic sublevels. The investigations also revealed a critical Hanle field B_H =~$50G$ for this Lyman-α transition, providing sensitivity to the magnetic field strength and orientation between 10G and 250G, as shown in Figure 1.9. Such range of magnetic field strength is expected in the Quiet Sun regions, meaning the linear polarization of the Lyman-α line can be used to determine the magnetic field strength and orientation in the lower transition region and upper-chromosphere.

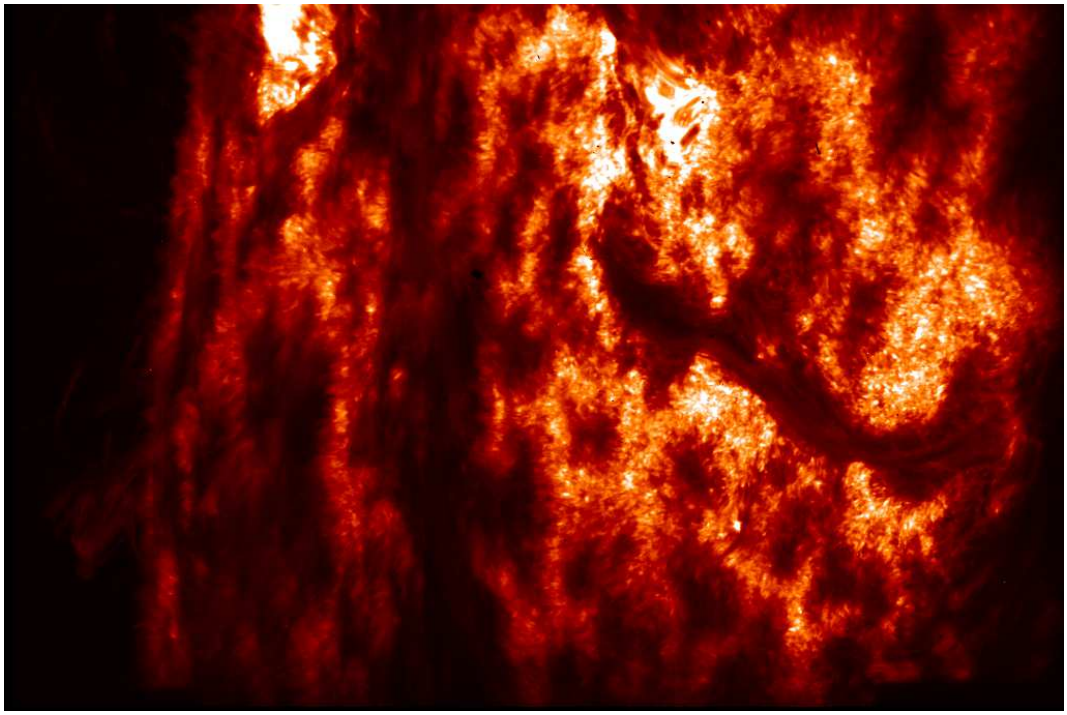

Figure 1.7: Lyman-α observation from the VAULT sounding rocket.

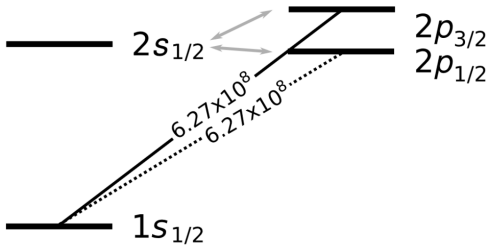

Figure 1.8: Grotrian diagram of the hydrogen model atom. The components of Lyman-α are indicated along with their Einstein A_u coefficient (in s^{-1}). The grey arrows connecting the fine-structure levels of $n = 2$ indicate the weakly inelastic depolarizing transitions due to proton and electron collisions. Figure taken from [27]

However, polarimetric observations in VUV are even harder to achieve than photometry. Measuring polarization requires additional optical elements such as linear retarder (i.e. waveplate) and a high-throughput is also required to ensure the polarization accuracy of the measurement. Only few materials can provide acceptable transmittance (e.g. MgF_2) and reflectivity (e.g. multilayer coatings). For these reasons, only few missions attempted polarimetry in the VUV. Two examples are the UltraViolet SpectroPolarimeter (UVSP, onboard the SMM spacecraft,[28]) and the Solar Ultraviolet Magnetograph Investigation sounding rocket experiment (SUMI, [29]). The UVSP instrument measured between 175nm to 360nm in the holographic grating's first order and between 115nm to 180nm in the grating's second order, but only reached a polarization accuracy just below

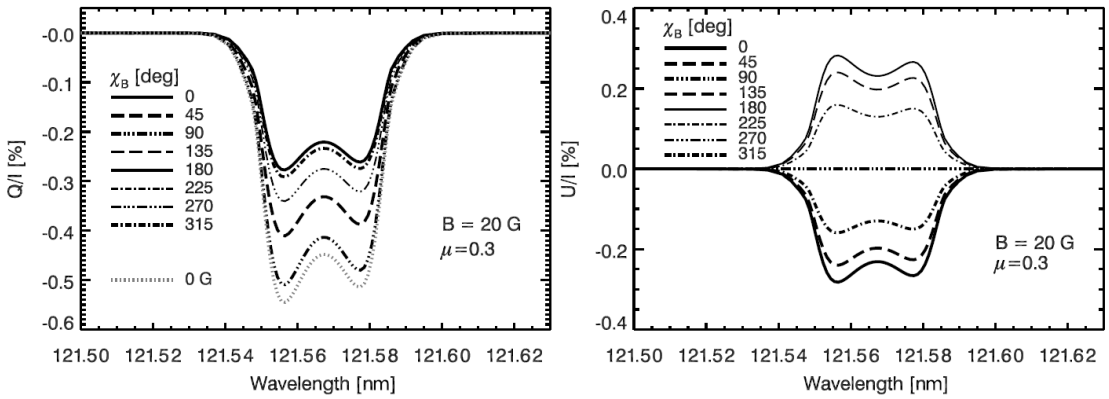

Figure 1.9: Theoretical estimation of the Q/I and U/I line-core signals in Ly-α (for a line-of-sight with $\mu = 0.3$) produced by scattering processes in the solar transition region, taking into account the Hanle effect of a 20G horizontal magnetic field. The various profiles correspond to the indicated values of the magnetic field azimuth (χ_B), measured with respect to the X-axis of the reference system (where the X-axis is the projection of the line-of-sight onto the solar surface plane and the Z-axis is the local vertical). The positive reference for Stokes Q is parallel to the nearest limb (i.e. parallel to the Y-axis). Figure taken from [19].

1% in the C_{IV} line at 155nm, giving estimation of magnetic field in sunspot and no conclusive results in the Quiet Sun ([30], [31]). The SUMI sounding rocket experiment was designed to simultaneously measure the polarization emitted by the C_{IV} and Mg_{II} lines at 155nm and 280nm, respectively. The instrument flew twice, in 2010 and 2012, but only provided mitigated results due to technical failures: mirrors holding screws broke due to higher than expected G-force and a malfunction of the waveplate's rotating mechanism occurred during the first flight ([32]). A drift of the pointing due to a thermal deformation of the secondary mirror's holder degraded the quality of the data recorded during the second flight, which are still being analysed. Concerning the Lyman-α line, only one instrument attempted slitless polarimetric observation onboard a Soviet satellite Intercosmos, but was unsuccessful as molecular contamination drastically reduced its throughput ([33]).

Hence, an international collaboration lead by the National Astronomical Observatory of Japan (Mitaka, Japan) and NASA Marshall Space Flight Center (Huntsville, USA) proposed the Chromospheric Lyman-Alpha SpectroPolarimeter (CLASP, [34], [35]) as a new instrument to investigate the linear polarization of the Lyman-α line created by scattering processes in the upper-chromosphere and lower transition region with a 0.1% polarization sensitivity, as a tool to unveil the magnetic field vector via the Hanle effect.

1.3.2 Design

Based on the simulations of polarization profiles shown in Figure 1.9 and previous observations of the Lyman-α intensity from Figure 1.7, the scientific requirements for the instrument were defined as shown in Table 1.1

The instrument was designed to fulfil the scientific requirements from Table 1.1, also taking into account the limitation of the rocket payload (e.g. size, weight). The optical layout is presented

Table 1.1: Scientific requirements, from [36]

Observable	Requirement
Polarization sensitivity	0.1% (line core), 0.5% (line wings)
Spectral resolution	0.01nm
Spectral window	$>\pm$0.05nm
Spatial resolution	<10”

in Figure 1.10 and is composed of a classical two-mirrors Cassegrain telescope with $\phi = 270$mm aperture that focuses the light onto a 400” long and 1.45” wide slit. The light transmitted by the slit propagates inside an inverse Wadsworth mounting spectrograph: the diffraction grating selects the Lyman-α wavelength, which is reflected toward two channels (diffraction order ± 1). Off-axis parabolic mirrors on each channel re-image the slit onto the two CCD cameras. The untransmitted light by the slit is reflected to a slit-jaw optics system with Lyman-α filter, to obtain context images. Polarimetry is ensured by a continuously-rotating half-waveplate located prior to the slit, and by a polarization analyzer just before the cameras on each channel. These two polarization analyzers are rotated by 90° from each other, allowing simultaneous measurements of the two orthogonal states of polarization, perpendicular to the slit for channel 1 and parallel to it for channel 2. The optics and instrument’s structures were designed and assembled by the National Astronomical Observatory of Japan, whereas the NASA Marshall Space Flight Center provided the CCDs cameras, the cooling system and the rocket. The spectro-polarimeter’s grating was provided by the Institut d’Astrophysique Spatiale in Paris. The specifications of the instrument are summarized in Table 1.2.

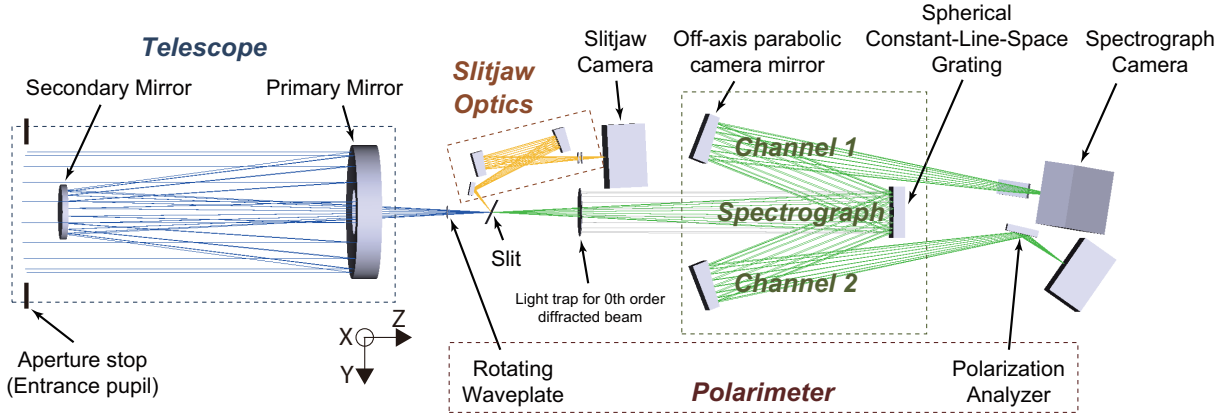

Figure 1.10: CLASP optical design from [36]

Many aspects of the design were improved compared to the predeceasing instruments, based on the technical issues they experienced. A “cold mirror" coating (i.e. narrow band filtering coating) was applied on the primary mirror to reduce the heat-load on the other optical elements. The structure of the instrument was also realized in an ultra-low-expansion super-invar material to avoid the thermal deformation seen in SUMI. Additionally, the polarization modulation was

Table 1.2: Summary of the instrument specifications

Telescope	
Entrance pupil	ϕ270 mm
Effective focal length	2614 mm
F number	9.68
Plate scale at slit	1.03 arcsec/13.0 µm
Primary mirror	
Conic constant	Paraboloid (K=−1)
Clear aperture	ϕ282 mm
Curvature radius	2054.5 mm
Surface figure (RMS)	24 nm (Fabrication)
Coating	Narrow band filter (“cold mirror")
Secondary mirror	
Conic constant	Hyperboloid (K=−5.27)
Clear aperture	ϕ111 mm
Curvature radius	1243.0 mm
Surface figure (RMS)	24 nm (Fabrication)
Magnification	2.54
Coating	Al+MgF_2
Slit-jaw	
Magnification	1
Filter	Narrow band Lyman-α
Plate scale at slit	1.03 arcsec/13.0 µm
Spectro-polarimeter	
Magnification	0.93
Slit	
Width	18.4 µm (= 1.45 arcsec)
Length	5.1 mm (= 400 arcsec)
Distance to grating	905.7 mm
Grating	
Groove density	3000 grooves/mm
Line spacing	Constant
Conic surface	Spherical (K=0)
Curvature radius	1749.3 mm
Off-axis Parabolic Camera Mirror	
Conic surface	Paraboloid (K=−1)
Off-axis value	180.0 mm
Curvature radius	1655.0 mm
Distance to CCD	827.5 mm
Polarization analyzer	
Coating	Multilayer SiO_2+MgF_2
CCD cameras	
CCD Pixel size	13.0 µm
Spatial plate scale	1.11 arcsec/13.0 µm
Spectral plate scale	0.0048 nm/13.0 µm

ensured by a continuous-rotation mechanism to avoid the dead time between exposures which can occur with a fixed-step mechanism when changing the waveplate angular orientation, as used by SUMI. High-reflectivity Lyman-α coatings were developed ([37]) to ensure the highest throughput possible at the observing wavelength. The contamination by outgasing of the instrument when under vacuum condition was monitored at all stages of the development, and a careful baking of every equipment was performed to avoid possible degradation of the instrument's throughput, as experienced by [33]. An axisymmetric telescope design was selected to minimize the instrumental polarization. Similarly, the spectro-polarimeter was designed with a minimum number of optical surfaces, and the two channels allowed for simultaneous observation of the two orthogonal polarization states to minimize possible instrumental cross-talks. Finally, the electronics were greatly improved compared to previous missions: low read-out noise CCD detectors were specially developed by NASA Marshall Space Flight Center, and cooled down to -20°C. These cameras allowed the modulation of the polarization to be accomplished in a short time (i.e. 1.2s) with fast and low-noise exposure (i.e. 300ms) which reduced the polarization errors due to intensity variation of the Sun and jitter/drift of the telescope pointing, therefore improving the overall polarization sensitivity of the instrument.

The requirements for the alignment of the instrument in term of RMS (i.e. root mean square) spot radius at the edge of the slit were set based on the design and are shown in Table 1.3. Considering the plate scale at the spectro-polarimeter's cameras, the spatial and spectral resolution at the edge of the slit can be derived as twice the RMS spot radius, and is shown in Table 1.4. Note that only the spectro-polarimeter's RMS spot radius affects the spectral resolution. The achievable polarization sensitivity was also determined by considering the possible contribution from photon noise, read-out noise of the CCD, fluctuation of the exposure time and jitter of the rocket pointing, as shown by [38].

Table 1.3: RMS spot radius requirement at the edge of the field of view and the edge of the slit for the telescope, spectro-polarimeter and slit-jaw imager.

	RMS spot radius	Note
Telescope	13.0 µm	Edge of the SJ FOV (±264",±264")
Spectro-polarimeter	13.5 µm	Edge of the slit (±200",0")
Slit-jaw	18.7 µm	Edge of the SJ FOV (±264",±264")
Telescope + Spectro-polarimeter	18.1 µm	$\sqrt{(13.0 \times 0.93)^2 + (13.5)^2}$
Telescope + Slit-jaw	22.8 µm	$\sqrt{(13.0)^2 + (18.7)^2}$

1.3.3 Polarimetry

Polarimetric capabilities at Lyman-α are the uniqueness of the instrument and therefore the polarimetry performed by CLASP is presented in more details hereafter. The Stokes formalism is used to describe the polarization state of the light and is defined with respect to the coordinate system of the instrument, as shown in Figure 1.11. The $+Q$ direction is defined along the slit (X-axis), and the $+U$ clock-wise as seen from the entrance aperture.

Table 1.4: Instrumental requirement at the edge of the slit, derived from the design.

Observable	Design
Polarization sensitivity	<0.039% (spurious polarization)
Spectral resolution	0.010 nm
Spatial resolution	3.1" (spectro-polarimeter) and 3.6" (slit-jaw)

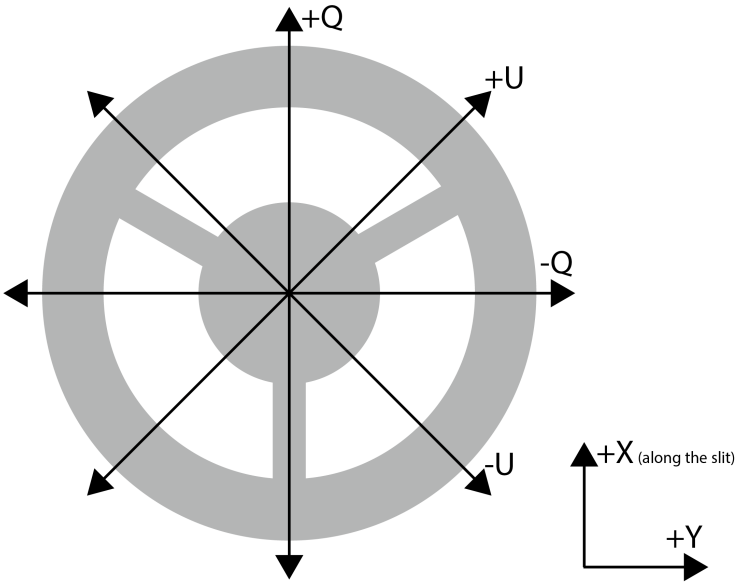

Figure 1.11: Coordinate system used for to describe the polarization states, as seen from the entrance aperture of the instrument.

The incoming polarization signal is modulated using a rotating half-waveplate and two linear polarization analyzers, one on each channel (see Figure 1.10). The half-waveplate is located inside the Polarization Modulation Unit (PMU, [39]), which ensures a continuous and homogeneous rotation of the waveplate. The PMU sends the first trigger for exposure to the spectro-polarimeter cameras when the principal-axis of the PMU half-waveplate crosses the $+Q$ direction, and then sends the following triggers every 300ms. The cameras take the exposure between two triggers. During each exposure, the PMU half-waveplate angle rotates by 22.5°. The exposure taken between the first and the second trigger is called D_1, the exposure taken between the second and the third trigger is called D_2, etc. The cycle is repeated after one full PMU rotation (4.8s, 16 exposures per PMU rotation). The linear polarization analyzers are flat mirrors with high-reflection coating optimized for Lyman-α (SiO_2+MgF_2 multilayer coating based on the design by [40], see [37]) set at Brewster's angle. The combination of the rotating half-waveplate and the polarization analyzers results in a modulation of the incoming Q and U signals, as shown in Figure 1.12 for channel 2 (opposite sign for channel 1).

The incoming polarization signal can be retrieved by combining several consecutive exposures containing the modulated intensity, using the demodulation scheme shown in Equation (1.4) for

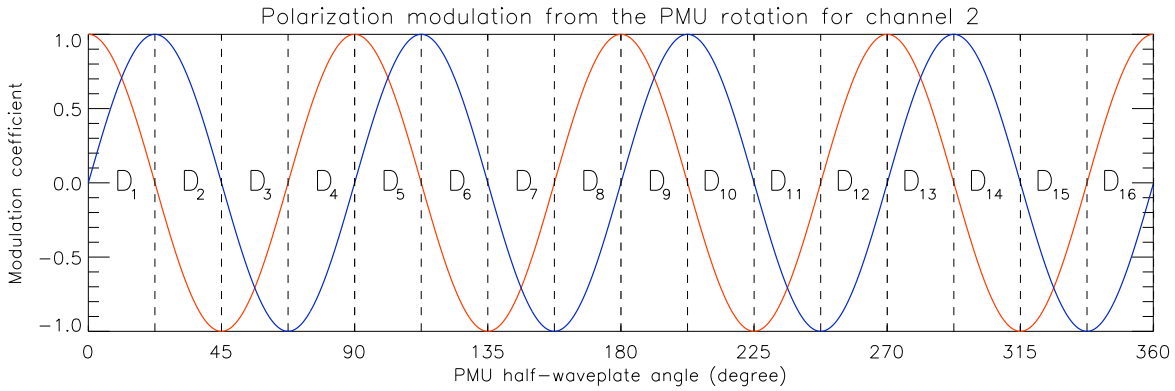

Figure 1.12: Modulation coefficient for Stokes Q (red) and Stokes U (blue) as a function of the PMU half-waveplate angle for channel 2.

channel 2, where D_i is the measured intensity taken in the i^{th} exposure for a given PMU rotation. This equation is derived from the expression of the Mueller matrix (see Appendix A) considering an ideal linear retarder and a prefect polarizer. For channel 1, a minus sign has to be applied due to the different orientation of the polarization analyzer. In these equations, I', Q' and U' refer to the demodulated Stokes parameters I, Q and U, the apostrophe indicating the output parameters.

$$\begin{aligned} \frac{Q'}{I'} &= \frac{\pi}{2}\left(\frac{D_1 - D_2 - D_3 + D_4}{D_1 + D_2 + D_3 + D_4}\right) \\ \frac{U'}{I'} &= \frac{\pi}{2}\left(\frac{D_1 + D_2 - D_3 - D_4}{D_1 + D_2 + D_3 + D_4}\right) \end{aligned} \tag{1.4}$$

The demodulation scheme from Equation (1.4) is derived for a perfect polarization modulation where the retardance δ of the PMU half-waveplate equals 180°. Investigation were conducted to develop a high-quality MgF_2 half-waveplate for the instrument ([41]), and its retardance was carefully measured at a synchrotron facilities for the Lyman-α wavelength : $\delta = 178.8° \pm 1.3°$. In addition, it is important to notice that the demodulation scheme presented for U'/I' does not minimize the spurious polarization cause by the $\mathrm{d}I/\mathrm{dt}$ if the intensity of the observed source fluctuates during the modulation. This might occur during the flight observation (solar origin, e.g. dynamic event, but also instrumental origin, e.g. pointing jitter and drift) and therefore the baseline for the flight demodulation of U'/I' is to use a similar scheme as for Q'/I' but with shifted exposures instead, as $D_2 - D_3 - D_4 + D_5$ for channel 2. However, in this case, Q'/I' and U'/I' are no longer derived from the same exposures. The demodulation scheme used to retrieve the polarization signal in the following work is discussed in more details in Chapter 6 and in Chapter 8.

1.4 Contribution of the thesis to the CLASP project

The personal contribution of the author to the overall CLASP project (from the Japanese side only, not including participation from the other international collaborators) is shown in Figure 1.13. This includes the work presented in this thesis, which mainly focuses on the novel instrumentation methods developed for the optical alignment of the telescope and spectro-polarimeter, as well as the unprecedented polarization calibration performed under vacuum at Lyman-α. The thesis is structured in six chapters, each of which are covering a particular aspect of the instrument development realized during the three years period of the PhD course and highlighted in Figure 1.13. The last chapters of the thesis covers the analysis of the flight data recorded at disc center, to provide a confirmation of the achieved spatial and spectral resolutions, as well as an in-flight polarization calibration of the instrument. This was compared to the pre-flight polarization calibration to provide a complete picture of the instrument's polarimetric capabilities. In addition, some contribution to co-author publications ([37] and [39]) were not included in the thesis.

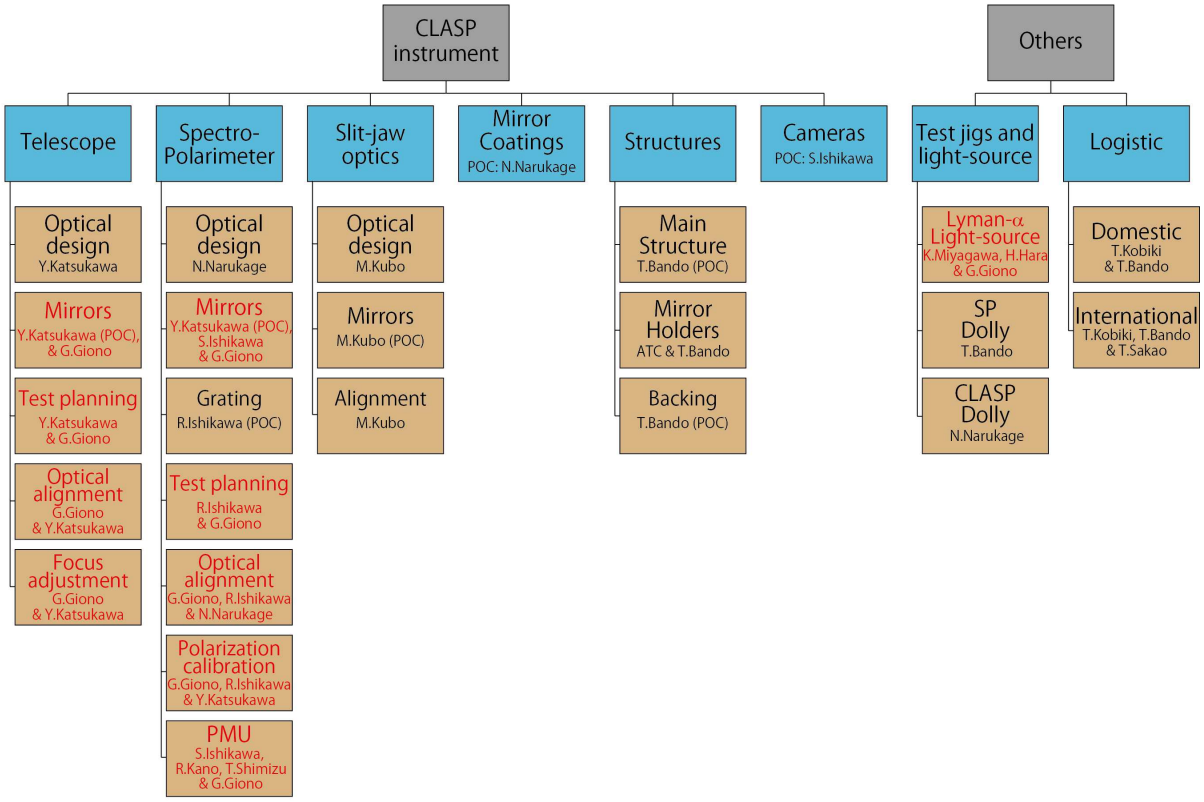

Figure 1.13: Summary of CLASP project action-items for the Japanese-side, as defined by the Japanese Principal Investigator (R.Kano). Red indicates the involvement of the author.

Chapter 2

Optical alignment of the telescope assembly

2.1 Introduction

Aligning the optical surfaces of the telescope is crucial to ensure the spatial resolution of the spectro-polarimeter and slit-jaw imager. Misalignments of the secondary mirror with respect to the primary mirror, namely tilt, decenter or despace, induce optical aberrations in the telescope's wavefront error (WFE), degrading the image quality. For a classical Cassegrain telescope, tilts of the secondary mirror mainly create coma aberrations, and the despace of the secondary mirror induces defocus. The purpose of the telescope alignment was to remove the coma and defocus aberrations at the center of the field of view (FOV), by adjusting the secondary mirror's tilt and despace.

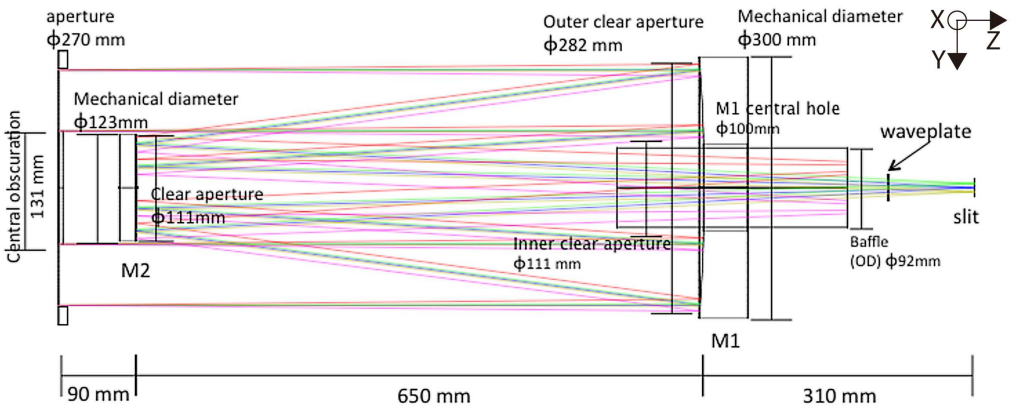

Figure 2.1: Conceptual drawing of the telescope assembly, with the distances between the optical elements and the coordinate system used for the alignment.

Figure 2.1 shows the coordinate system used in the alignment experiment and the distances between the various optical elements. In such configuration, tilt of the secondary mirror refers to a tilt around the X-axis or around the Y-axis, decenter corresponds to a positional shift of the

secondary mirror along the X-axis or the Y-axis, and finally despace refers to a positional shift of the secondary mirror along the Z-axis.

Note that the telescope alignment only aimed to adjust the secondary mirror tilts and despace with respect to the primary mirror. The holding mechanism of the primary mirror was not designed for tilt and/or position adjustment. On the other hand, the holder for the secondary mirror was attached to the telescope structure by three screws, allowing tilt and/or despace adjustment by shimming at the basis of the screws. Decenter adjustment was not considered for the secondary mirror: its position was ensured with an alignment pin inserted through the central hole of the holder. Because the secondary mirror decenter was not adjusted, a perfect compensation for the possible tilt of the primary mirror could not be achieved. Removing coma and defocus aberrations at the center of the field of view by only adjusting the secondary mirror tilts and despace was possible, but the trade-off to pay was a tilt of both the entrance-axis and the exit-axis. These axes are defined with respect to the mechanical-axis of the instrument, as shown in Figure 2.2. Both the entrance-axis and the exit-axis coincide with the mechanical-axis in a ideally aligned telescope. Adjusting the tilt of the secondary mirror induces a shift of the exit pupil, therefore tilting the entrance-axis and the exit-axis with respect to the mechanical-axis. A large tilt of the exit-axis can be problematic, as it can shift the illumination of the telescope onto the spectro-polarimeter's grating outside of its clear aperture.

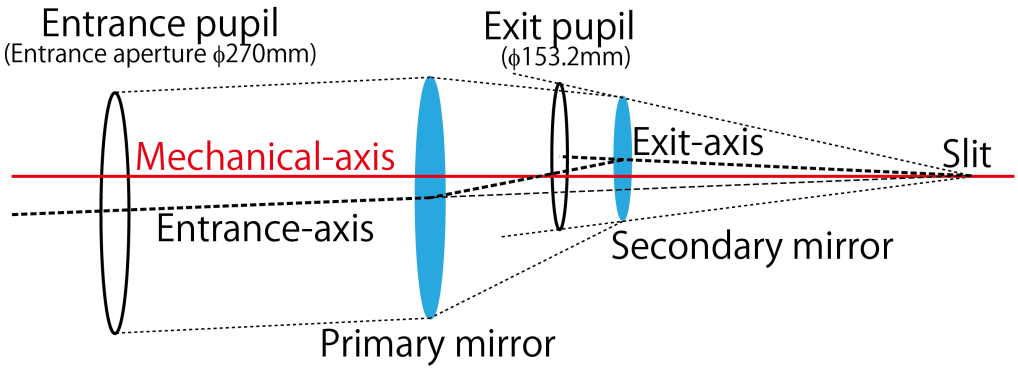

Figure 2.2: Drawing showing the entrance and the exit pupil of the telescope assembly. The entrance-axis is the axis passing by the center of the entrance pupil and the center of the field of view (slit). The exit-axis is the axis passing by the center of the exit pupil and the center of the slit. Both axis are defined with respect to the mechanical-axis.

2.2 Tolerance

Tolerance for the telescope alignment were determined during the design of the assembly, to ensure the 13 µm RMS spot radius required from the scientific requirement (i.e. corresponding to 1.03" in radius at the slit), at the edge of the field of view. The tolerance brake down into the three main contributions : defocus, low-order aberrations and high-order aberrations (i.e. astigmatism, surface figure error...), as shown in Table 2.1. For the high-order aberrations, the RMS spot radius requirement of 5.9 µm was converted to the telescope WFE using the Marechal criterion. This RMS spot radius only for the high-order aberrations correspond to 0.47" resolution. For this resolution

Table 2.1: Tolerance break-down for the telescope RMS spot radius at the edge of the FOV.

	RMS spot radius	Note
Telescope	13.0 µm	$13.0 = \sqrt{9.2^2 + 7.1^2 + 5.9^2}$
−Defocus	9.2 µm	Defocus aberrations
−Low-order aberrations	7.1 µm	Residual alignment error (Coma)
−High-order aberrations	5.9 µm	Surface figure deformation/roughness

of 0.47", the diffraction limit formula gives $1.22\lambda_d/\mathrm{D}$=0.47"×2. The Marechal criterion provides an estimation of the wavefront error for the diffraction limit as $\lambda_d/14$, as same unit as λ_d, resulting in a 72nm RMS WFE for the high-order aberrations.

The quality of the mirrors was controlled by measuring their surface figures, which are shown in Figure 2.3 for their respective clear aperture. The RMS error of the surface figure for the primary mirror was 16.3 nm, and 9.2 nm for the secondary mirror. These values for the mirror's surface figure quality are within the requirements, shown in Table 1.2 from Section 1.3.2.

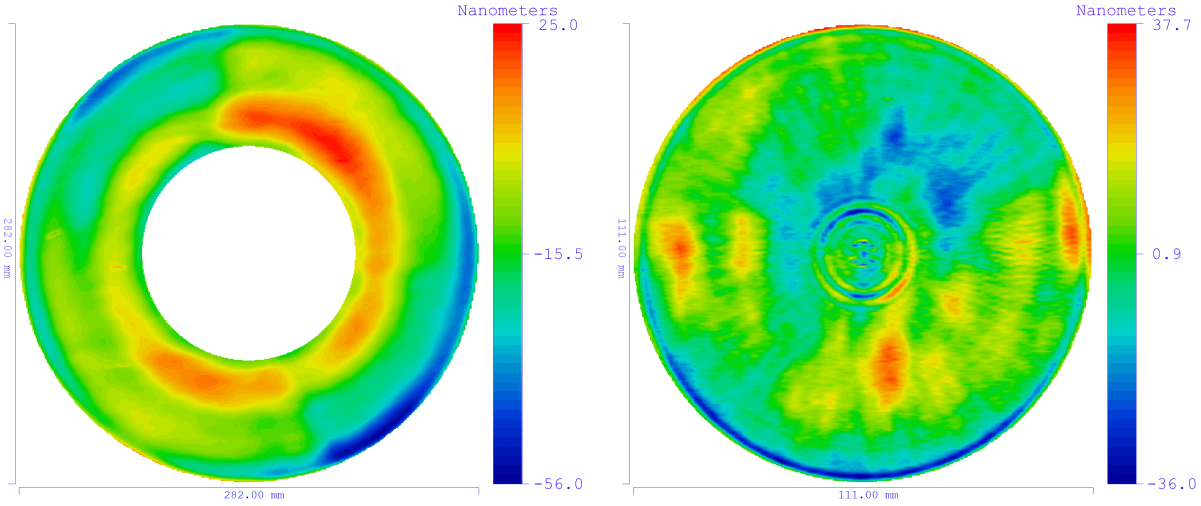

Figure 2.3: Surface figures of the primary mirror (left) and secondary mirror (right).

These measurements were included in the optical simulations, to estimate the WFE of the telescope and its Point Spread Function (PSF) at the center of the field of view, as shown in Figure 2.4. One can see that the diffraction is dominant against the surface figure deformation at the He-Ne wavelength, and oppositely at Lyman-α. RMS spot radius for the PSF at Lyman-α was estimated at 6.2 µm. Although the actual orientation of the secondary mirror with respect to the primary mirror was unknown (rotation around the Z-axis), the estimated WFE gave an approximation of the WFE measured after the alignment of the secondary mirror, assuming the surface figure errors are the main contributors for the high-order aberrations. The optical simulations were also used to derive the relationship between the secondary mirror misalignments and the WFE. The aberrations were estimated using the Zernike polynomials (see Appendix B), by

Table 2.2: Tolerance of the secondary mirror in term of WFE aberrations and achievable mechanical accuracy.

	Design tolerance	Mechanical pitch	Aberration coefficient pitch
Tilt X (coma Y)	$\pm 1.4'$	$1.5'$	0.05 λ
Tilt Y (coma X)	$\pm 1.4'$	$0.6'$	0.02 λ
Despace (defocus)	± 0.1 mm	10 µm	0.08 λ

fitting the 37^{th} first polynomials onto the WFE and extracting the coefficients (i.e. amplitudes) of each aberration. In the following, the aberration coefficients are described in unit of λ, with λ being the He-Ne wavelength: 632.8nm. The three following equations were obtained from the optical simulation:

$$\begin{aligned} \text{Coma X}(\lambda) &= -0.032 \times \text{M2 Y-tilt (arcmin)} \\ \text{Coma Y}(\lambda) &= -0.032 \times \text{M2 X-tilt (arcmin)} \\ \text{Defocus }(\lambda) &= 7.86 \times \text{M2 despace (mm)} \end{aligned} \tag{2.1}$$

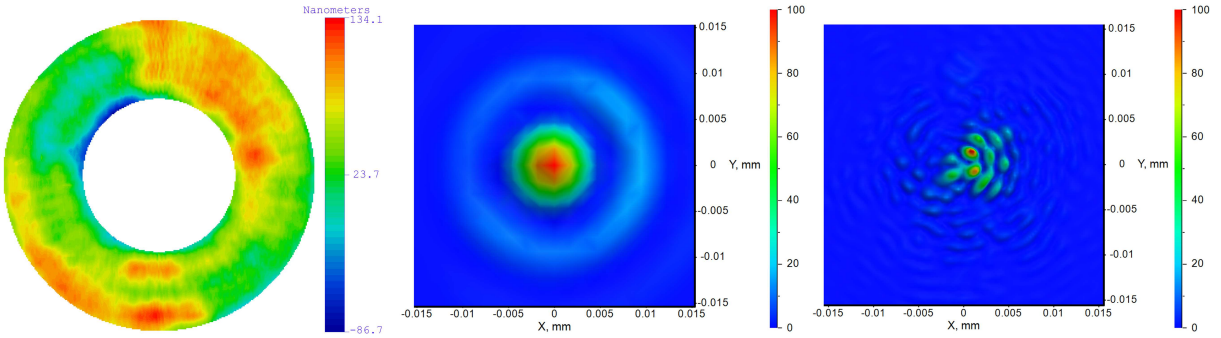

Figure 2.4: Left: estimated WFE from the simulation for a given orientation of the primary and secondary mirrors, including the surface figure errors. Middle: corresponding estimated PSF of the telescope at the center of the field of view at the He-Ne wavelength (632.8nm). Right: corresponding estimated PSF of the telescope at the center of the field of view at the Lyman-α wavelength (121.6nm). RMS spot radius for the PSF at Lyman-α was estimated at 6.2 µm.

The requirements were translated to the mechanical tolerance and the pitch of the secondary mirror tilt and despace was determined considering the minimum shim thickness available (10 µm), the design of the secondary mirror holder and using the previously introduced relationships linking the misalignments to the optical aberrations. These items are summarized in Table 2.2.

The tolerance on the tilt of the exit-axis were determined considering the exit pupil position and the corresponding illumination footprint onto the spectro-polarimeter's grating, as shown in Figure 2.5. Based on the configuration, the clearance for the illumination footprint on the grating is ±4.1mm.

From this, ±1.1mm were allocated for the decenter of the exit pupil position and the slit, which correspond to ±1.72mm at the exit pupil (i.e. 1.42mm for the decenter of the exit pupil position,

0.3mm for the decenter of the slit). Hence, a ±1.72mm tolerance on the exit-pupil position is required to ensure the illumination footprint of the telescope to be within the clear aperture of the grating. This requirement is equivalent to a $\pm 4'$ tolerance on the exit-axis.

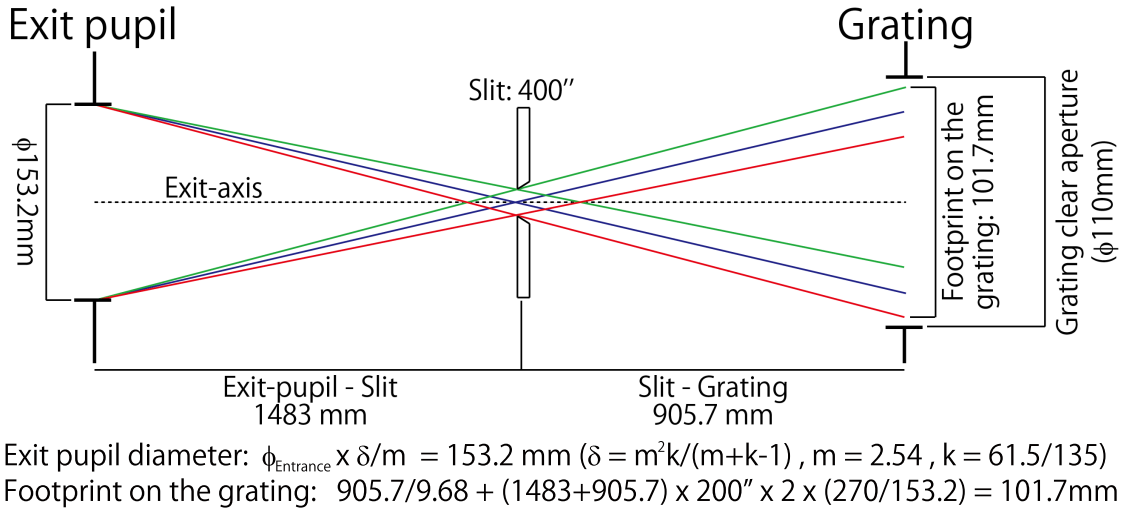

Figure 2.5: Relation between the telescope exit pupil and the illumination footprint on the spectro-polarimeter's grating.

2.3 Wavefront error measurement

Measuring the telescope WFE was required to estimate the defocus and coma aberrations. For this purpose, the telescope was installed in a double-pass configuration, as shown in the left part of Figure 2.7. A laser interferometer (He-Ne, 632.8nm) was set up to illuminate the telescope focus position with a F/7.2 lens, slightly larger angle than the telescope F/9.68. A large flat mirror (ϕ=600mm, 15 nm rms WFE) was positioned in front of the telescope entrance aperture, reflecting the laser beam inside the telescope and to the interferometer. Interference fringes were observed even though the narrow band filter coating applied on the primary mirror only reflected ∼3.5% of visible-light on each reflection (see Figure 2.6).

To estimate the WFE at the center of the slit, the laser interferometer was aligned to this exact location using a mirror-target (i.e. mirror with coated and un-coated concentric rings, shown in the right part of Figure 2.7). This mirror-target was attached on the back-surface of the telescope assembly, with a jig composed of a 3-leg spider and a cylinder. This jig purpose was to position the mirror-target at the position of the slit (310 mm from the back-surface of the primary mirror, see Figure 2.1).

The mirror-target surface had to be adjusted parallel to the back surface of the primary mirror. The tilt of the back-surface was measured using a theodolite: the mirror-target was attached to the spider jig without the cylinder jigs, and its tilt was measured for three different orientations, rotating the spider jig by 120° each. The average of these three measurements provided the tilt of the back-surface, as shown in Table 2.3 (in the reference frame of the theodolite). Then, the mirror-target was installed on top of the cylinder jig, positioning it at the slit position, and the base

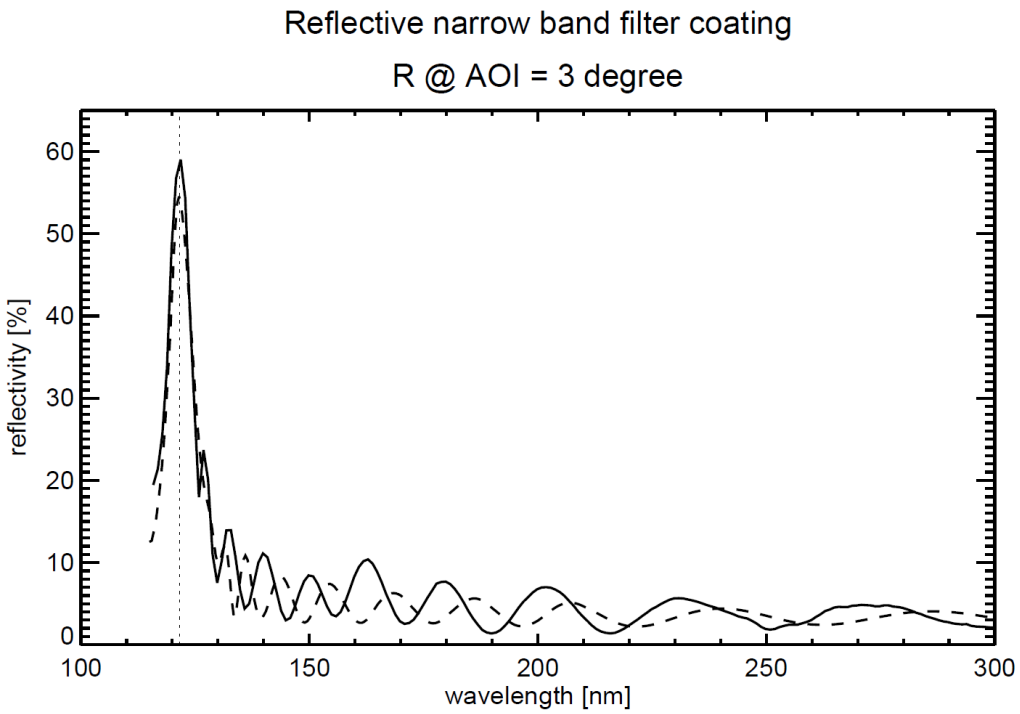

Figure 2.6: Reflectivity of the narrow band filter coating applied on the primary mirror, measured as a function of wavelength at a 3° angle of incidence. Dashed line shows the simulated reflectivity. Figure from [37].

Table 2.3: Alignment of the mirror target with respect to the telescope back-surface.

Measurement	Angle around X	Angle around Y
Spider only at 0°	+0°0′00”	90°04′17”
Spider only at 120°	+0°0′00”	90°04′13”
Spider only at 240°	−0°0′05”	90°04′21”
Telescope back-surface tilt (average)	−0°0′01”	90°04′17”
Cylinder+spider at 0°	−0°0′11”	90°07′01”
Cylinder+spider+shim at 0°	−0°0′10”	90°04′49”
Difference with average	−0°0′09”	00°00′32”

of the spider jig was shimmed to minimize the difference between the mirror-target tilt and the telescope back-surface tilt. As a result, the mirror-target was aligned to the telescope back-surface with a 30” accuracy.

Using the coated area at the center of the mirror target, null-fringes (i.e. a single large interference fringe covering the entire detector, which indicate an alignment without tilt and defocus) were obtained by adjusting the position of the laser interferometer with the 6-axis table. This

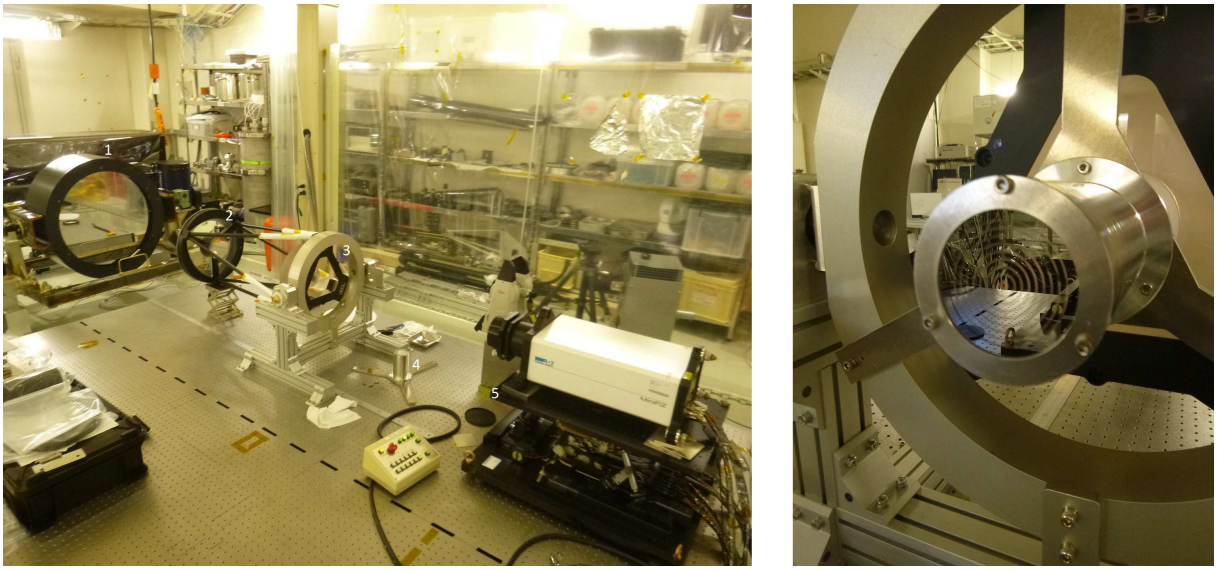

Figure 2.7: Left: The double-pass configuration, with the large flat mirror (1), the secondary mirror (2), the primary mirror (3), the mirror-target attached to its jig (4) and the laser interferometer on the 6-axis table (5). Right: Close-up to the mirror target, attached to the back-surface of the telescope assembly.

ensured the alignment of the interferometer beam to the center of the slit. Then, the mirror-target was removed and the tilt of the large flat mirror was adjusted to reflect the laser beam exactly to the interferometer and obtain null-fringes, therefore aligning the entire double-pass configuration.

The phase carried method ([42]) was used to retrieve the wavefront error directly from the fringes pattern. A known tilt was introduced in the interference fringes by tilting the interferometer's reference sphere in the diagonal directions (i.e. $(+X,+Y)$ and $(-X,-Y)$ tilts). Left panel of Figure 2.8 shows an example of measured interference fringes with induced-tilt. The purpose of this induced-tilt was to carry the WFE frequencies away from the aperture frequencies from the telescope. The frequencies contained in the fringes were obtained using a Fast Fourier Transform (FFT) algorithm, and the result is shown in the middle panel of Figure 2.8. The star-like shape in the frequency domain are the frequencies from the telescope aperture and spider, and the WFE frequencies were carried away by the frequency of the induced-tilt, shown inside the white box. Note that these frequencies are also present in the negative part of the frequency domain, by symmetry. The phase could be then retrieved by applying an inverse-FFT on the extracted WFE frequencies only, and is shown in the right panel of Figure 2.8. The phase was affected by a 2π-uncertainty, creating discontinuities, and was corrected using a custom-made software. The raw WFE was obtained after correcting the phase, and divided by two to account for the double-pass configuration.

Zernike polynomials were fitted (up to the 37^{th}) onto the raw WFE to extract the optical aberrations. Figure B.1 shown in Appendix B shows the first eight Zernike polynomials, which are the most important for the telescope alignment. Piston, tilt X and tilt Y are the lowest order aberrations coming from the residual misalignment between the interferometer and the telescope. These were always removed from the raw WFE. Defocus is the aberration related to the secondary

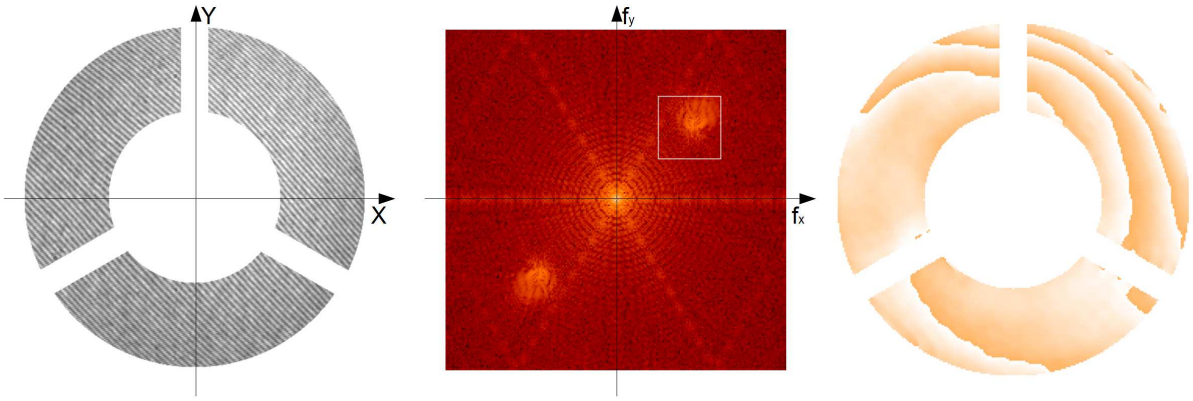

Figure 2.8: Process to retrieve the WFE from the fringes: left panel shows the interference fringes with high-tilt. Middle panel shows the image in frequencies domain after FFT: the white box is centred around the maximum of frequency (frequency of the high-tilt). Right panel shows the phase, retrieve with a inverse-FFT on the white box frequencies, uncorrected for the 2π uncertainty.

mirror despace, as explained previously. Coma X and Y are defined as the low-order aberrations in the previously described tolerance, and are linked to the secondary mirror tilt. Finally, the astigmatism 0° and astigmatism 45° are the first aberrations of the high-order aberrations tolerance, and were not adjusted. All aberrations with superior Zernike order representing possible spherical aberration or higher order comas and astigmatisms were also included in the high-order aberrations tolerance.

2.4 Telescope optical axis alignment to the center of the slit

Each WFE measurement was recorded with the same procedure: ten images of the interference fringes were recorded for a positive-tilt, and ten images for a negative-tilt of the reference sphere (i.e. $(+X,+Y)$ and $(-X,-Y)$ tilts of the interferometer's lens, respectively). Taking images with both positive and negative tilts was important to cancel out possible optical aberrations from the reference sphere and interferometer optics, by averaging the measurements recorded on both the tilts. Each fringe image was carefully checked to confirm its quality, as the recording software sometimes produced glitches in the images. The previously described method was applied on all twenty images to retrieve the raw WFEs. The final raw WFE for the measurement was then computed as the average of all twenty raw WFEs.

Numerous WFE measurements were performed during the alignment experiment and are summarized in Table 2.4. The first WFE measurement revealed a large coma aberrations (0.7λ) in the X-direction, which was the direction of gravity in this configuration. Two other measurements were performed after rotating the telescope assembly by 120° and 240° (due to the 3-points attachment of the telescope structure) to estimate if the coma aberrations were due to gravity, but it appeared to be independent of the telescope orientation.

The observed coma aberrations was larger than the expected stroke for the secondary mirror possible tilt, and was traced back to an error in the secondary mirror position. The secondary mirror position was fixed mechanically using a mechanical pin coming through a socket placed on the telescope structure. The position of this socket was adjusted to compensate a 1.4 mm shift

Table 2.4: Summary of the measurements performed during the telescope optical alignment.

Telescope orientation	M2 orientation	M2 shims (tilt X/Y)	Socket orientation	Note
120°	120°	Nominal	Initial position	First measurement
240°	120°	Nominal	Initial position	Check gravity
0°	120°	Nominal	Initial position	Check gravity
0°	120°	Nominal	180°	Check socket orientation
0°	240°	Nominal	Initial position	Check M2 orientation
0°	0°	Nominal	Initial position	Check M2 orientation
0°	0°	Nominal	180°	M2 and socket orientation
0°	0°	$-3.4'/+3.4'$	180°	First shimming
0°	0°	$+3.4'/-3.4'$	180°	Corrected shimming
0°	0°	$+3.4'/-3.4'$	180°	Check gravity
120°	0°	$+3.4'/-3.4'$	180°	Check gravity
240°	0°	$+3.4'/-3.4'$	180°	Check gravity
0°	0°	$+4.7'/-5.3'$	180°	Adjusted shimming
0°	0°	$+4.7'/-5.3'$	180°	Flight screws
120°	0°	$+4.7'/-5.3'$	180°	Check gravity with flight screws
240°	0°	$+4.7'/-5.3'$	180°	Check gravity with flight screws
0°	0°	$+4.7'/-5.3'$	180°	X:0mm / Y:0mm
0°	0°	$+4.7'/-5.3'$	180°	X:+2.5mm Y:0mm
0°	0°	$+4.7'/-5.3'$	180°	X:−2.5mm Y:0mm
0°	0°	$+4.7'/-5.3'$	180°	X:0mm Y:+2.5mm
0°	0°	$+4.7'/-5.3'$	180°	X:0mm Y:−2.5mm
0°	0°	$+4.7'/-5.3'$	180°	X:0mm Y:−2.5mm (2^{nd} measurement)
0°	0°	$+4.7'/-5.3'$	180°	X:0mm Y:0mm (2^{nd} measurement)
0°	0°	$+4.7'/-5.3'$	180°	X:+2.5mm Y:0mm (2^{nd} measurement)

of the secondary mirror position with respect to the primary mirror, given by a 3D measurement of the telescope structure. This socket was installed with the wrong orientation, which shifted the position of the secondary mirror by 2.8 mm instead of correcting it, and was the cause of the large coma aberrations observed in the WFE. After correcting the socket orientation and readjusting the secondary mirror position with the pin, measurements with different the orientation of the secondary mirror around the Z-axis were conducted. The secondary mirror's holder allowed for three different orientations (0°, 120° and 240°), and these measurements were performed to determine which orientation of the mirror minimizes the WFE deformations (i.e. orientation of the secondary mirror surface figure to best cancel out the primary mirror surface figure deformations.). The socket and secondary mirror orientation were fixed, and the measured WFE only presented a $\sim 0.11\lambda$ aberration for both coma X and coma Y. The coma and defocus aberrations were then reduced by two consecutive shimmings, and the flight screws were installed and torqued. The telescope was rotated three times to observe the effect of gravity onto the final WFE. Figure 2.9 shows the measured final WFE for the three orientations of the telescope, and Table 2.5 reports the aberration coefficients extracted from the Zernike polynomials fitting. The Peak-to-Valley (i.e. difference between maximum and minimum surface figure deformation) can easily be calculated from the WFE scaling, showing similar values between the WFE measured and the expected WFE from Figure 2.4. The zero-G WFE was also included, calculated as the average of the WFEs measured at the three orientations of the telescope. The coma aberrations were successfully reduced to around 0.01λ by adjusting the secondary mirror tilt. The residual coma aberrations were smaller than the tolerance. The defocus aberration still remained around 0.18λ even after adjustment, as precise measurement of the effect of the shimming was difficult due to the larger uncertainty. However, as the final focus adjustment were performed when the telescope part was attached to the spectro-polarimeter part, with a stroke of ± 0.5mm between both parts. This stokes correspond to a defocus aberration of $\pm 0.50\lambda$. The remaining defocus aberration measured in the WFE was below this stroke, and was therefore finally removed when the telescope was attached to the spectro-polarimeter. The effect of gravity on the WFE was measured to be smaller than the precision achievable for the coma aberrations, and of the same order for the astigmatism aberrations. Hence, given this approximation, measurements performed for any telescope orientation were used. The error on the aberration coefficients was derived as the standard deviation from the aberration coefficients extracted on the twenty WFEs extracted (i.e. the ten with positive-tilt and the ten with negative-tilt) from each measurements, and is also presented in Table 2.5. A larger uncertainty on the defocus aberration was measured, and can be understood as the air fluctuation could easily affect the optical path length of the laser between two measurements, affecting the observed defocus aberration.

Table 2.5: Aberrations from the Zernike fitting on the final WFE measurements.

	Defocus	Astigma--tism 0°	Astigma--tism 45°	Coma X	Coma Y	RMS WFE w/o defocus
0°	0.15λ	-0.03λ	-0.13λ	0.01λ	-0.01λ	46.9nm
120°	0.21λ	-0.07λ	-0.02λ	0.01λ	0.00λ	42.2nm
240°	0.13λ	-0.09λ	-0.09λ	0.02λ	-0.01λ	45.3nm
Zero-G	0.18λ	-0.07λ	-0.08λ	0.02λ	-0.01λ	41.4nm
Error (1σ)	0.10λ	0.04λ	0.04λ	0.03λ	0.03λ	-

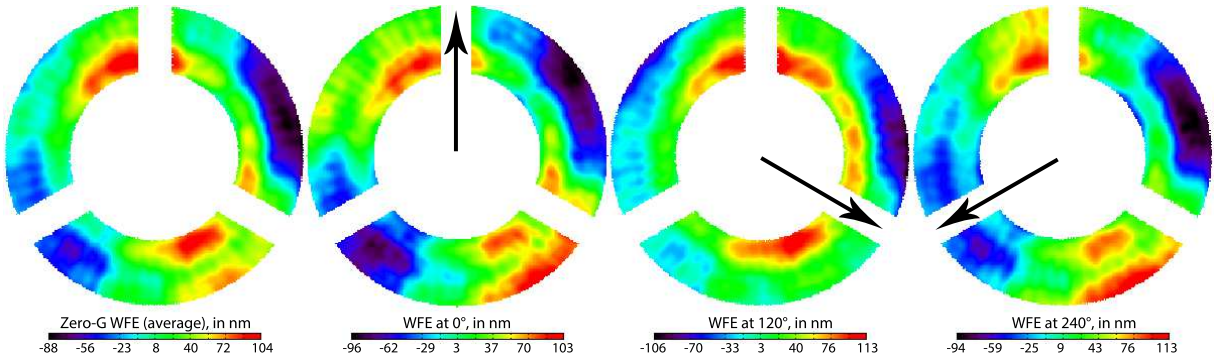

Figure 2.9: WFE measured after final alignment on the secondary mirror, displaying from left to right the zero-G WFE (computed as the average of the three positions), WFE taken with telescope at 0°, WFE taken with telescope at 120° and WFE taken with telescope at 240°. The black arrows shows the direction of the gravity on each measurements.

The spot shape at the center of the slit could be estimated from the measured zero-G WFE. The derivative in X and Y directions of the WFE provided the X and Y angles across the WFE surface, which would deflect a collimated ray coming through the telescope (i.e. one ray per WFE pixel). The spot shown in Figure 2.10 was obtained by multiplying the X and Y derivatives with the telescope focal length (2614 mm). The resulting RMS spot radius at the center of the slit was estimated at 6.6 µm using Equation (2.2). In this equation, x_i and y_i are the (x, y) coordinate of the i^{th} ray, and n is the total number of rays. This RMS spot radius was smaller than the 9.2 µm RMS spot radius of the combined low-order and high-order aberrations from the tolerance (i.e. $\sqrt{7.1^2 + 5.9^2}$ in Table 2.1).

$$R_{rms} = \sqrt{\frac{1}{n}\sum_{i=0}^{n} r_i^2}, \text{ where } r_i = \sqrt{(x_i^2 + y_i^2)} \tag{2.2}$$

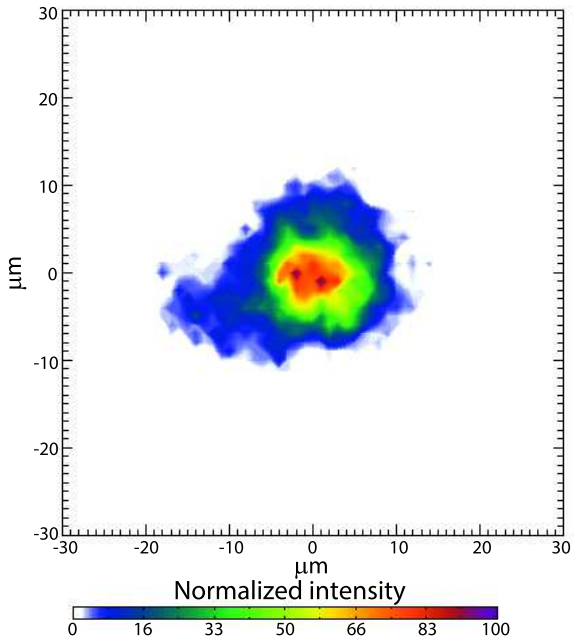

Figure 2.10: Spot shape at the center of the FOV, estimated using the derivative of the zero-G WFE from Figure 2.9.

The experimental alignment of the telescope successfully reduced the coma aberrations at the center of the slit to values comparable to the achievable accuracy. The resulting RMS WFE and RMS spot radius recorded at the center of the FOV were both smaller than the tolerance.

2.5 Confirmation of optical performance across the FOV

Using the 6-axis table, the position of the interferometer was adjusted to measure the WFE at various locations of the FOV. The alignment to the laser perpendicularly to the slit surface was controlled using the mirror target, and measurements were performed at five positions: (0",0") i.e. center of the slit, (+200",0") i.e. top of the slit, (−200",0") i.e. bottom of the slit, (0",+200") and (0",−200"). From simulations, the coma aberrations are expected to be affected by a $\pm 0.05\lambda$ shift at the edge of the field of view (±200"), which is comparable to the achievable accuracy. Note that coma X is affected when moving in the Y-direction and coma Y in the X-direction. The extracted aberration coefficients for these five measurements are presented in Table 2.6, as well as the corresponding RMS spot radius derived from the WFE without defocus with the previously described method.

Table 2.6: Aberration coefficients from the Zernike fitting, RMS WFE without defocus and corresponding RMS spot radius for the five measurements at across the FOV.

X	Y	Defocus	Astigma--tism 0°	Astigma--tism 45°	Coma X	Coma Y	RMS WFE without defocus	RMS spot radius
0”	0”	0.16λ	-0.04λ	-0.13λ	0.01λ	-0.01λ	40.0nm	6.8µm
+200	0”	0.21λ	0.00λ	-0.13λ	0.04λ	0.03λ	39.7nm	7.0µm
−200”	0”	0.11λ	-0.05λ	-0.06λ	-0.03λ	-0.07λ	36.7nm	7.4µm
0”	+200”	0.20λ	-0.02λ	-0.12λ	-0.02λ	-0.03λ	45.6nm	8.0µm
0”	−200”	0.14λ	0.00λ	-0.10λ	0.08λ	-0.03λ	30.3nm	7.0µm

Table 2.6 clearly shows a smaller RMS WFE even with comas at the edge of the FOV when compared to the RMS WFE tolerance for high-order aberrations and high-order plus low-order aberrations combined from Table 2.2, respectively. The RMS spot radius for the perfectly aligned telescope (i.e. defocus aberration removed) was also two third smaller than the tolerance. As previously mentioned, the remaining defocus aberration in the telescope WFE was corrected later in the development of the instrument, when the telescope was aligned with the spectro-polarimeter (see Chapter 4).

2.6 Tilt of the entrance-axis and shift of the exit pupil

The telescope's entrance-axis was measured after the optical alignment, using theodolites. The double-pass configuration was perfectly aligned by adjusting the large flat mirror to obtain null-fringes with the interferometer, aligned to the center of the slit. Theodolites were used to measure the tilt angle of the large flat mirror (representing the entrance-axis of the telescope) with respect to the tilt angle of the mirror-target (i.e. mechanical-axis of the instrument). Three measurements were performed, which are reported in Table 2.7. Although no tolerance was required on the tilt of the entrance-axis since the Sun sensor was finally aligned to the entrance-axis, a $\pm 4'$ indicative tolerance (i.e. same as for the exit-axis) can be given for comparison.

Table 2.7: Tilt of the entrance-axis with respect to the mechanical axis, after adjustment of the secondary mirror.

Entrance-axis	Measurement #1	Measurement #2	Measurement #3	Average
X-tilt	$-1'43$”	$-1'05$”	$-1'06$”	$-1'18$”
Y-tilt	$+1'03$”	$+1'08$”	$+0'55$”	$+1'02$”

The position of the exit pupil is directly linked to the exit-axis tilt, and was also measured experimentally. A theodolite was aligned to the center of the mirror-target (i.e. aligned with the mechanical-axis) and used to measure the edges of the aperture's central obscuration through the telescope double reflection. The entrance aperture was illuminated using white-light, to help the

Table 2.8: Measured shift of the telescope exit pupil with respect to the mechanical axis, after adjustment of the secondary mirror.

Exit pupil	Measurement #1	Measurement #2	Average	Tolerance
X-position	+498 µm	+551 µm	+525 µm	±1720 µm
Y-position	−771 µm	−849 µm	−810 µm	±1720 µm

observation due to the attenuation after refection by the primary mirror. The observed aperture was the exit pupil. Using the distance between the theodolite to the mirror target, and the distance between the telescope's focus position to the exit pupil, the shift of the exit pupil was determined. Two measurements were performed and are shown in Table 2.8. Both the measurements are below the ±1.72 mm tolerance.

2.7 Conclusion on the telescope optical alignment

The coma aberrations were successfully removed from the telescope WFE at the center of the FOV by adjusting the tilt of the secondary mirror, ensuring the telescope assembly optical alignment. The resulting WFE and image quality were almost twice better than the allocated tolerance, which should fulfil the scientific requirement on the spatial resolution for both the slit-jaw and the spectro-polarimeters. In addition, the shift of the exit pupil position introduced by the adjustment on the secondary mirror were confirmed to be within the tolerance.

Chapter 3

Optical alignment of the spectro-polarimeter

3.1 Introduction and alignment procedure

The spectro-polarimeter includes the optical elements located after the slit, which are the diffraction grating and the two channels, each of which is composed of an off-axis parabolic mirror, a polarization analyzer and a CCD camera ([34],[43], [35]). Figure 3.1 presents the spectro-polarimeter design with its coordinate system.

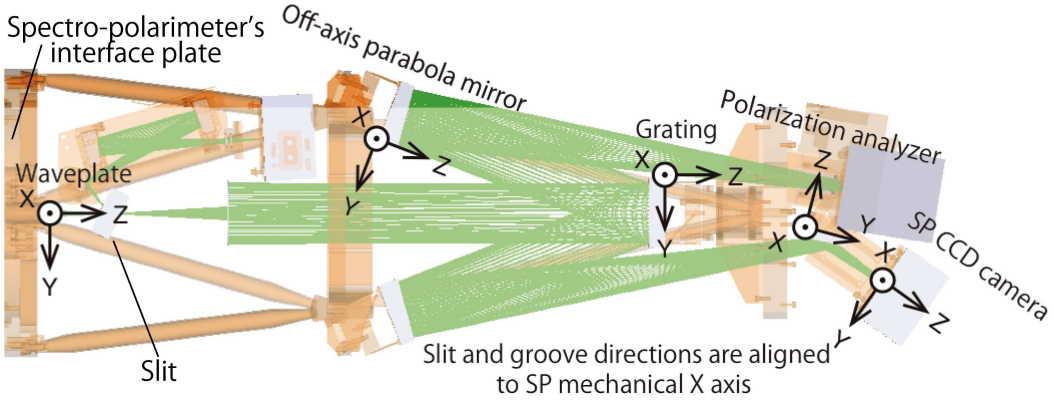

Figure 3.1: Drawing of the spectro-polarimeter, with the optical elements and the coordinate system defined. The mechanical-axis is defined by the axis perpendicular to the spectro-polarimeter interface plate and passing by the center of the slit.

The optics create an image of the slit onto the two cameras: misalignment of any of the optical elements would induce optical aberrations, blurring the formed image and therefore degrading the spectro-polarimeter performances. Hence, an optical alignment of each element was required to ensure the spectropolarimeter spatial and spectral resolutions. The spectro-polarimeter presents six degrees of freedom which affect the image quality: tilts of the grating around the X-axis, Y-axis and Z-axis, tilts of the off-axis parabolic mirrors (also referred as M3s) around the X-axis and the Y-axis, and position of the cameras along the Z-axis to adjust the image focus. Note that the X-position and the Y-position of the cameras was not directly adjusted: a custom shim plate was

prepared after the alignment to position the cameras in their optimal X/Y/Z position (i.e. image of the center of the slit close the the X/Y center of the CCD detector, and best focus position along the Z-axis). A rotary stage was used to adjust the grating Z-tilt and a translation stage for the camera position. On the other hand, the tilts around the X-axis and the Y-axis for both the grating and the M3s are adjusted by inserting shims at the base of their respective holders.

A custom alignment procedure for the optical alignment of the spectro-polarimeter was developed, as shown in Figure 3.2. At first, the alignment of the grating X-tilt and Y-tilt could be fairly simply performed with a theodolite, using the zeroth-order light reflected by the grating. The theodolite had to be aligned with respect to the spectro-polarimeter mechanical axis, represented using a mirror-target (i.e. similar as for the optical alignment of the telescope, see Chapter 2) attached on the spectro-polarimeter's interface plate. A theodolite was used to check the alignment between the mirror-target and the grating holder before installing the grating. After aligning the theodolite to the mirror-target, the grating X-tilt and Y-tilt were measured and the center of curvature of the grating was adjusted with respect to the mechanical axis. However, aligning the other degrees of freedom required to input light into the optical system and to measure the resulting image quality on the cameras. The alignment of the flight grating (i.e. Lyman-α grating) had to be conducted at Lyman-α, which implies aligning the spectro-polarimeter's optics by shimming under vacuum condition. The solution to minimize the activities under vacuum was to align the M3s in visible-light (VL) at first, using a custom-designed alignment grating with similar specifications (curvature radius, clear aperture, size) as the flight Lyman-α grating but with ruling density tuned for the wavelength of the He-Ne laser (632.8nm). Therefore, the alignment grating provided the same diffraction angle as for the flight grating at Lyman-α, but at in visible-light. This alignment grating replaced the flight grating, with its tilts around the X-axis and the Y-axis aligned in a similar fashion using a theodolite. The alignment grating Z-tilt and M3s X-tilt and Y-tilt were then aligned by checking the image quality using a He-Ne laser. After fixing the tilts of the M3s mirrors, this alignment grating was replaced by the Lyman-α grating, and only the Z-tilt of the Lyman-α grating, as well as the Z-position for the cameras were adjusted under vacuum condition using motorized rotary and translation stages, respectively.

A point-like object was required to estimate the image quality of the spectro-polarimeter during the alignment of the grating Z-tilt, M3s X-tilt, M3s Y-tilt and camera Z-position. For this purpose, the slit (5 mm by 18.4 µm rectangle) was not adequate and a pinhole array (PHA) was used instead, i.e. five 10 µm diameter pinholes located along a line 1.25 mm apart from each other. Each pinhole provided a "point-like" object for the spectro-polarimeter, imaged onto the cameras. The tolerance on each degree of freedom was determined from design to meet the required image quality of 13.5 µm RMS spot radius at the edge of the slit, and is summarized in Table 3.1.

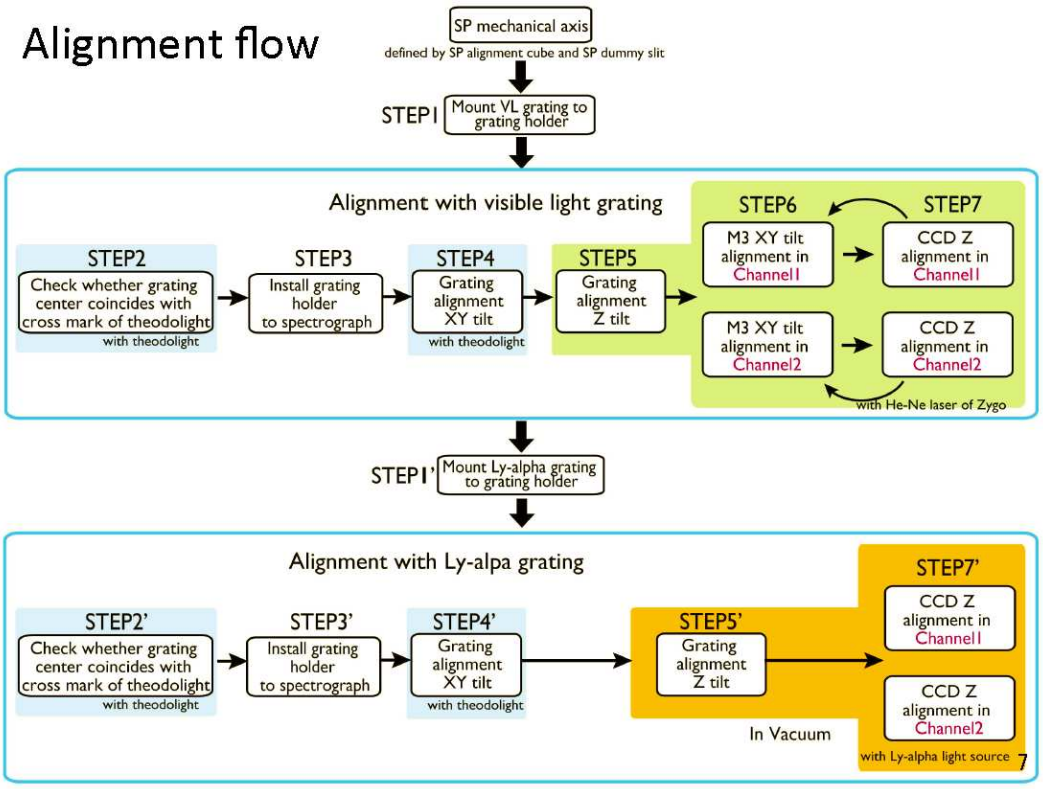

Figure 3.2: Alignment flow for the alignment of the spectro-polarimeter.

Table 3.1: Tolerance and pitch of each optical element to be aligned in the spectro-polarimeter.

	Tolerance	Pitch	Adjustment method
Grating X-tilt	$\pm 1.5'$	$\pm 0.6'$	Shims
Grating Y-tilt	$\pm 2.9'$	$\pm 1.2'$	Shims
Grating Z-tilt	$\pm 7.5'$	$\pm 3.0'$	Rotary stage
M3 X-tilt	$\pm 2.7'$	$\pm 1.0'$	Shims
M3 Y-tilt	$\pm 7.8'$	$\pm 1.0'$	Shims
CCD Z-position	$\pm 220\,\mu m$	$\pm 90\,\mu m$	Translation stage

3.2 Alignment in visible-light

3.2.1 Initial preparation for the visible-light alignment

3.2.1.1 Setup configuration and jigs

The spectro-polarimeter's interface-plate was attached to a custom-made dolly for the purpose of the alignment in visible-light, as shown in Figure 3.3.

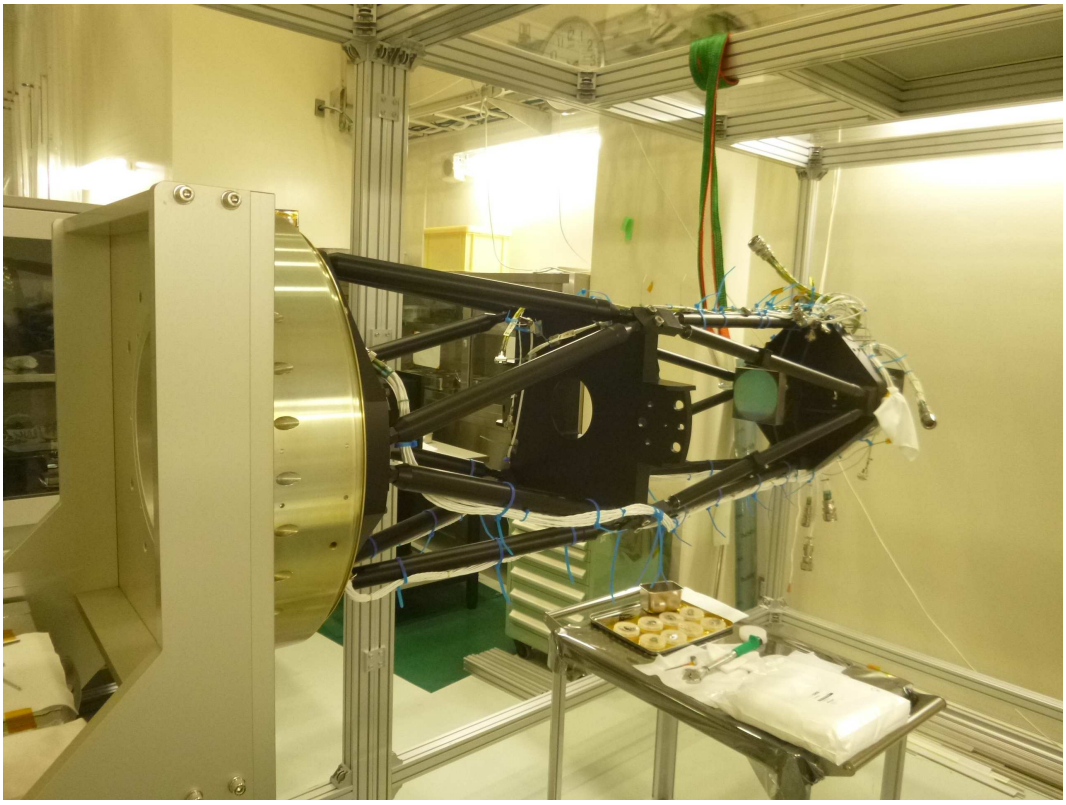

Figure 3.3: Experimental configuration for the alignment in visible-light, with the spectro-polarimeter attached to the dolly (left) by its interface plate. In this picture, the alignment grating was attached to the structure but not the M3s yet.

The alignment grating and M3s were attached to the spectro-polarimeter structure with their nominal shims. The nominal shims positioned the optical elements to their expected position from the optical design (i.e. reference tilt (X,Y)=(0",0")). Commercial CCD cameras with 4.4 µm pixels were used instead of the flight camera (13 µm pixel) during the visible-light alignment to improve the accuracy of the spot measurement. Non-flight holders were designed to connect these cameras to the translation stages. In addition, a non-flight holder was also prepared to house the pinhole-array and attached it at the slit location. Figure 3.4 shows a picture of these two holders used for the visible-light alignment.

The distance between the central position of the CCD detectors and the central pinhole arrays to their respective holder's alignment pins was precisely measured using a laser-microscope and adjust to be within a ±100 µm tolerance from their design value. The alignment pins were used to

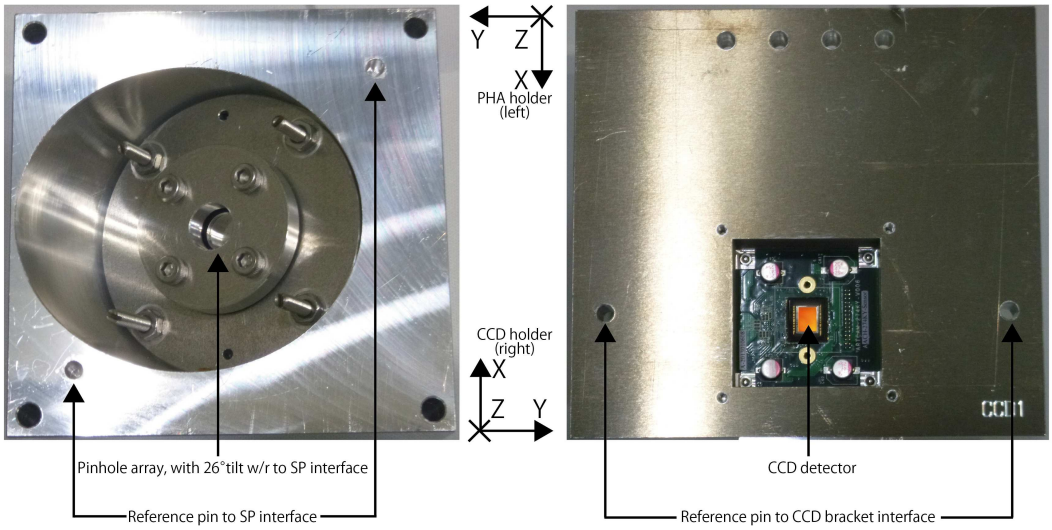

Figure 3.4: Pinhole array holder (left) with reference pin to the spectro-polarimeter interface (slit location) and visible-light camera holder for channel 1 (right) with reference pin to the spectro-polarimeter interface (camera position). Camera holder for channel 2 was similar.

Table 3.2: Measured position of the central pinhole and the center of the CCD detector to reference pins on their respective holders, compared to the nominal value from design and required tolerance.

Item	Measured value	Design value	Difference	Tolerance
PHA X-position to pin (−X,−Y)	27.985 mm	28.000 mm	−15 µm	±100 µm
PHA X-position to pin (+X,+Y)	28.044 mm	28.000 mm	+44 µm	±100 µm
PHA Y-position to pin (−X,−Y)	27.996 mm	28.000 mm	−4 µm	±100 µm
PHA Y-position to pin (+X,+Y)	27.975 mm	28.000 mm	−25 µm	±100 µm
PHA Z-position to slit interface	15.039 mm	15.000 mm	+39 µm	±100 µm
PHA tilt around Z-axis	1.6′	0′	+1.6′	±6′
Channel 1 CCD center to pin (−Y)	59.988 mm	60.000 mm	−12 µm	±100 µm
Channel 1 CCD center to pin (+Y)	60.001 mm	60.000 mm	+1 µm	±100 µm
Channel 2 CCD center to pin (−Y)	59.989 mm	60.000 mm	−11 µm	±100 µm
Channel 2 CCD center to pin (+Y)	60.014 mm	60.000 mm	+14 µm	±100 µm

align the holders to the spectro-polarimeter's structure and therefore ensure the alignment of the pinhole array and of the cameras to the spectro-polarimeter's mechanical axis. This was crucial for the pinhole array since it had to coincide with the flight slit (i.e. both the position and the orientation). Table 3.2 summarizes the laser-microscope measurements and compares with the nominal values.

3.2.1.2 Improved alignment procedure

Although the method to align the grating X-tilt and Y-tilt is clearly defined by the previously presented procedure, the alignment of the grating Z-tilt, M3 X-tilt, M3 Y-tilt and camera Z-position only relies on the observed image quality. Adjusting each degree of freedom with the RMS spot radius of the pinhole array image as the only measure to estimate the quality of the spectro-polarimeter alignment can be inefficient and time-consuming. Knowledge about how each degree of freedom affects the image quality was required to diagnosis which optical elements had to be adjusted. Hence, a more detailed alignment plan was created for adjusting these four degrees of freedom.

The first improvement on the initial procedure was for the grating Z-tilt alignment in visible-light. The grating Z-tilt was the only degree of freedom affecting the dispersion direction (i.e. wavelength direction), as it rotates the grating's ruling direction. Noting that the dispersion direction had to be perpendicular to the slit direction, an improved procedure was designed. This experiment aimed to measure experimentally both the dispersion direction and the slit direction with respect to the camera (i.e. pixel grid) in order to adjust the grating Z-tilt until obtaining a 90° angle between both the directions. On one hand, measuring the slit direction can be performed by illuminating the slit with a monochromatic He-Ne laser, resulting in an image of the slit formed onto the cameras. On the other hand, the dispersion direction can be determined by illuminating the pinhole array with white-light. The image formed onto the cameras were composed of five lines, one for each of the five pinholes, with white-light being diffracted along the dispersion direction. The Z-position of the cameras are adjusted on both the measurements to obtain the finest dispersion lines and slit width. The grating Z-tilt can be then aligned from these two measurements, even with the M3s unaligned yet. Figure 3.5 provides a visual explanation for the grating Z-tilt alignment procedure.

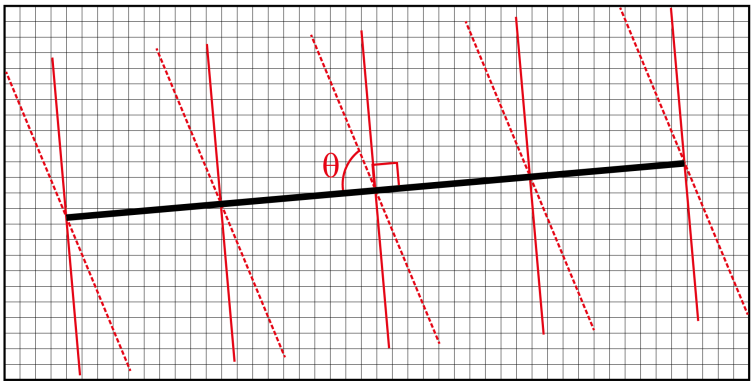

Figure 3.5: Explanation on the grating Z-tilt alignment. The grid shows the CCD pixels. The black line is the image of the slit as observed with the He-Ne laser. The dashed red lines show the diffraction direction as measured with the pinhole arrays illuminated with white-light. For an arbitrary grating Z-tilt angle, the diffraction direction forms an angle θ with the slit direction. Red solid line shows the diffraction direction for an aligned grating Z-tilt, with angle $\theta = 90°$

The second improvement was to provide quantitative knowledge on the M3 X-tilt and Y-tilt alignment based on the shape of the observed spot. The misalignments of the M3s induce optical aberrations that deform the spot shape in a characteristic manner. These aberrations

can be observed by defocusing the cameras, using the Z-position adjustment mechanism. By taking several images at different focus position, the sign of the aberrations can be determined and therefore provides an indication on which M3 tilts has to be adjusted. Optical simulations were used to model the spectro-polarimeter configuration and confirmed this procedure.

On one hand, the M3 Y-tilt can be determined by observing the symmetry around the central pinhole. In a perfectly aligned configuration, pinhole spots at the top of the slit are symmetric with the spots at the bottom of the slit. Figure 3.6 shows the defocused spots (−0.6mm) for various M3 Y-tilt, clearly showing the symmetry imbalance along X-axis. This can be also observed with the RMS spot radius calculated on each spots. It was also also observed that grating Z-tilt has a similar effect as the M3 Y-tilt.

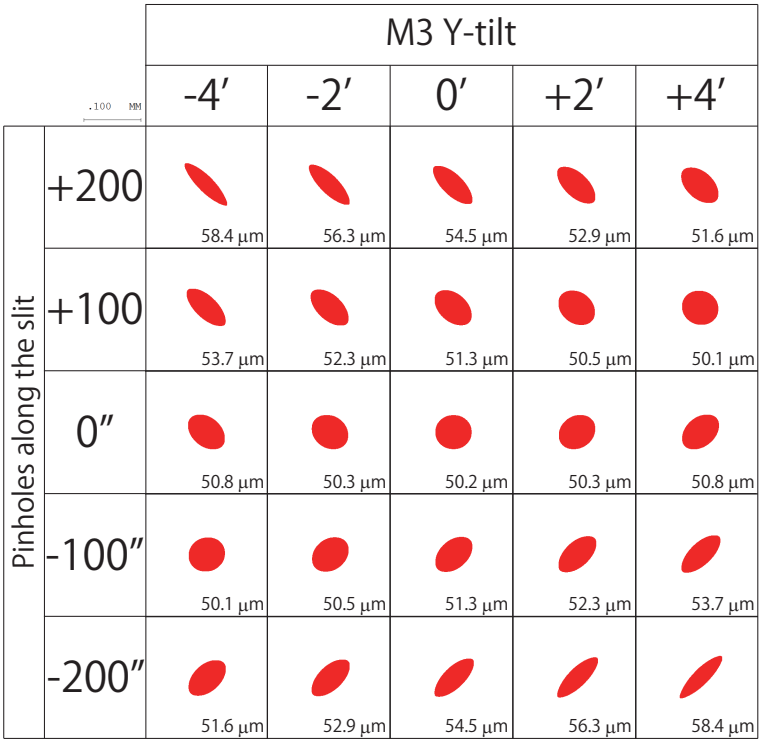

Figure 3.6: Simulated pinhole array spots for various M3 Y-tilt for a fixed defocus of −0.6mm. The RMS spot radius calculated from the simulation for each spots is included. Diffraction limit effects were not included.

On the other hand, the M3 X-tilt introduces astigmatism in the image. This is particularly seen in the central pinhole: the image shape changed from a shape elongated along the Y-axis to a shape elongated along the X-axis across the focus position, as shown by Figure 3.7 for various M3 X-tilt. Note that both X-tilt and Y-tilt of the M3 are also shifting the image position on the camera detector: a large tilt can move the image of some pinholes outside of the CCD detector. This was not an issue for the purpose of the alignment if only one pinhole was located outside the camera. After the alignment, the final position of the flight cameras was adjusted in the X-direction and the Y-direction by fabricating a custom shim plate.

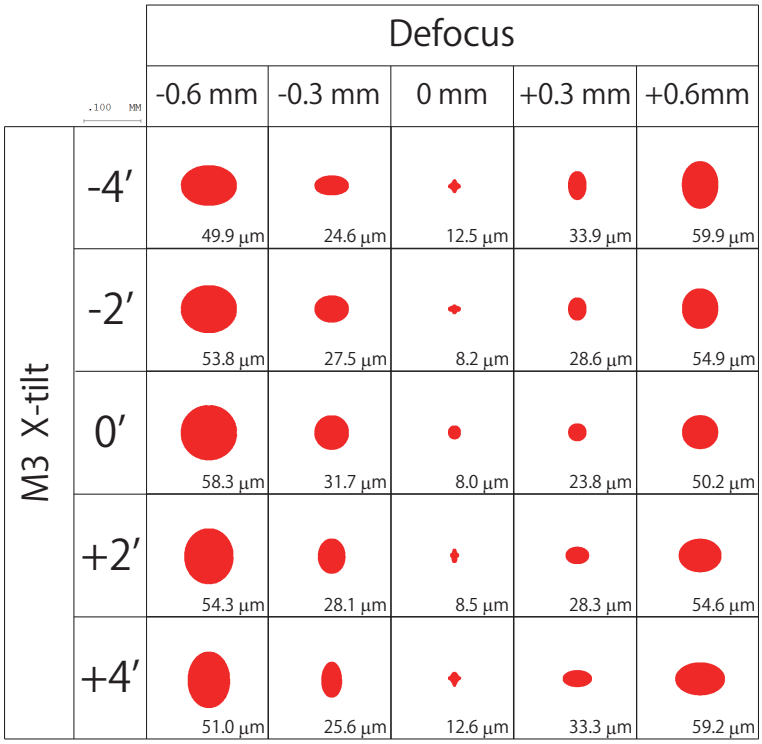

Figure 3.7: Simulated central pinhole spots for various M3 X-tilt and various defocus values around the best focus position. The RMS spot radius calculated from the simulation for each spots is included. Diffraction limit effects were not included.

In conclusion, simulation provided a robust guideline for the M3s alignment: at first the Y-tilt should be adjusted in order to obtain symmetric of the spot shape around the central pinhole. Then, X-tilt should be adjusted to minimize the astigmatism at the central pinhole.

3.2.2 Alignment of the alignment grating X-tilt and Y-tilt.

After installing the alignment grating, the theodolite was aligned to be perpendicular to the mirror-target surface, attached on the spectro-polarimeter interface plate and representing the mechanical axis of the system, passing by the center of the slit. The mirror-target was removed and the tilts of the grating around the X-axis and Y-axis were measured. Considering the design of the grating holder and the thickness of the shims available, the grating holder was shimmed to be aligned with the theodolite direction (i.e. spectro-polarimeter mechanical axis). Table 3.3 reports the measured tilts. Note that with this method, the theodolite actually measured the position of the center of curvature of the grating because the theodolite is focusing at the center of curvature of the grating in order to get the zeroth-order reflection from the grating's spherical surface. During this measurement, the distance between the theodolite and the grating was measured (~3250 mm), and the distance theodolite to grating's center of curvature was estimated to be around 1500 mm, after subtracting the grating curvature radius (1743 mm). Considering these distances, the actual tilts of the grating could be estimated from the theodolite measurements.

Table 3.3: Alignment of the alignment grating X-tilt and Y-tilt with respect to the mechanical axis (mirror-target). The angles marked with the (T) symbol are measured in the coordinate system of the theodolite. The shift is given along the corresponding axis.

Measurement	X-axis	Y-axis
Mirror-target (mechanical axis)	+00°00′00” (T)	+00°03′12” (T)
Grating tilt (nominal)	+00°01′02” (T)	+00°05′14” (T)
Grating tilt (after shimming)	−00°00′20” (T)	+00°02′54” (T)
Difference (after shimming)	−00°00′20” (T)	−00°00′18” (T)
Center of curvature shift	−131 µm	+146 µm
Final grating tilt	+00°00′09”	−00°00′08”

As a result, the alignment grating X-tilt and Y-tilt were aligned to the mechanical axis well below the required tolerance.

3.2.3 Alignment of the visble-light grating Z-tilt

The grating Z-tilt was aligned to obtain the dispersion direction perpendicular to the slit direction. The slit direction was measured on the CCD detectors using a He-Ne laser: the monochromatic light made a sharp image of the slit with no dispersion in the wavelength direction. The dispersion direction, which is directly related to the grating Z-tilt, was measured after replacing the slit by the pinhole array and the He-Ne laser by a white-light lamp. The image formed onto the cameras revealed the dispersion direction for the five pinholes. Figure 3.8 shows an example of the slit and dispersion direction images.

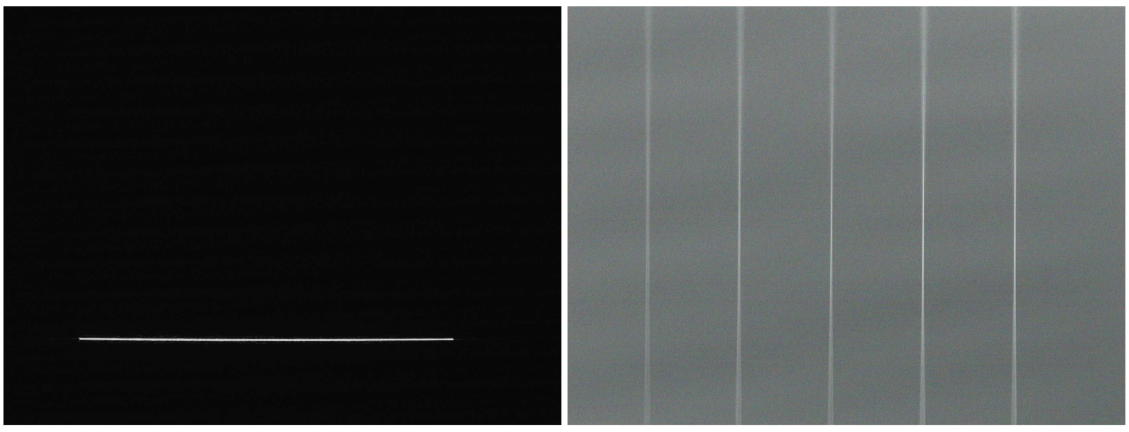

Figure 3.8: Example of the grating Z-tilt alignment. Left shows the slit imaged on channel 1 camera with the He-Ne laser. Right shows the five images of the pinhole array on channel 1 camera with white-light illumination. The vertical line shows the dispersion direction. Same images were recorded for channel 2.

The grating Z-tilt was adjusted using a rotating micrometer, with graduation in degree. The micrometer rotation was transferred to the grating rotation around the Z-axis with a mechanical jigs. Hence, both rotations were not directly proportional. The dispersion direction was estimated for the central pinhole using multiple Gaussian fitting along each dispersion line to get the position, and Figure 3.9 shows the resulting angle difference between the slit and the dispersion direction for different positions of the micrometer. The best position of the micrometer was estimated where the angle difference to 90° (i.e. angle difference minus 90°) was closest to zero for both the channels. After setting the micrometer to this position (i.e. micrometer at 203°), final measurement were taken which provided an angle difference to 90° of $-6.7'$ for channel 1 and $+3.9'$ for channel 2. The final alignment were worse than the value measured during the micrometer scan, which might be due to the accuracy of the micrometer (i.e. repeatability of the measurements). Nevertheless this value was still within the tolerance for the grating Z-tilt alignment, and therefore acceptable.

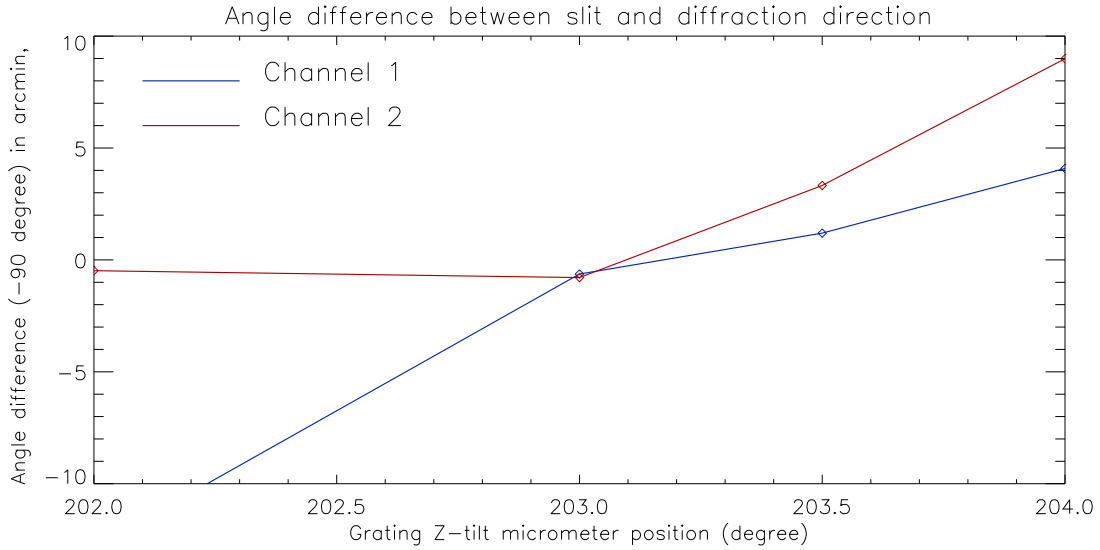

Figure 3.9: Results of the angle difference between the slit and the dispersion direction as a function of the micrometer position. 90° were removed from the angle difference, given in arcmin. Blue line is for channel 1 and red line is for channel 2.

.

3.2.4 Alignment of the M3 X-tilt and Y-tilt

With the alignment grating fully aligned (X, Y and Z tilts), the next step was to align both the M3s, which was performed using the pinhole array and a He-Ne laser. The laser was installed with a focusing lens to increase the intensity of the light on the pinholes and images of the pinholes were observed onto the cameras. However, although the transmitted light was dominated by diffraction due to the diameter of the pinholes ($\phi = 10\,\mu m$), the alignment of the laser to the mechanical axis and the F number of the lens used was important for the alignment of the spectro-polarimeter. The position of the laser illumination onto the pinhole array was adjusted using the 6-axis table, and its alignment quality was controlled by observing the uniformity of the spectro-polarimeter's pupil illumination by highly defocusing the cameras. The alignment of the spectro-polarimeter

was conducted after obtaining a uniform illumination of the pupil for the central pinhole. At first, the Y-tilt on channel 1 was adjusted. the defocus was set at approximatively $-0.6mm$ from the possible best focus position (roughly estimated visually with a focus scan) and defocused images were recorded for the nominal shims (referred as $0'$ tilt). Then, the M3 mirror was shimmed to change the Y-tilt to a $+1'$, $-1'$ and $-2'$ tilts. Images were taken for a fixed defocus of the cameras, controlled by the adjustable jig's micrometer. The measured spots were displayed as shown in the left part of Figure 3.10 for channel 1 and compared to the prediction from the simulations. From these images, the spots for a Y-tilt of $-1'$ appeared to be the most symmetric around the central pinhole, as the others show a strong inclination of the central pinhole spot. Note that the pixel grid direction can be approximated to the X-axis due to the careful alignment of the camera's jig (see Section 3.2.1.1). The same method was applied for channel 2, where the spots were measured for a $0'$, $-1'$ and $-2'$ tilts. Spot images for channel 2 are shown in the right part of Figure 3.10, and also indicated the best alignment of the M3 Y-tilt for a $-1'$ tilt.

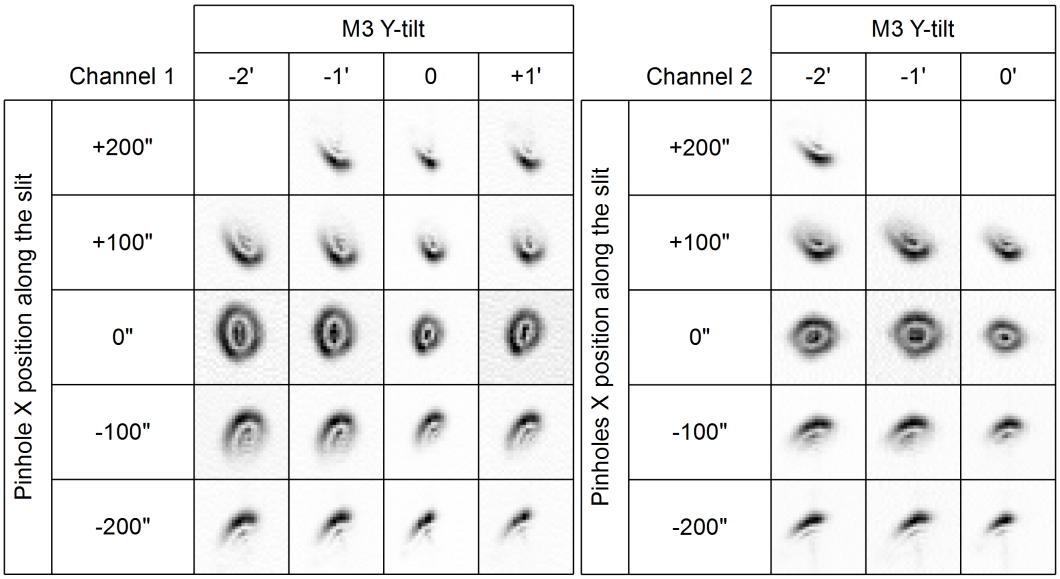

Figure 3.10: Spot images for the Y-tilt alignment of the M3s, showing channel 1 (left) and channel 2 (right). Horizontal shows the various Y-tilt values, and vertical shows the different pinholes. Note that the image of the pinhole at the edge was outside of the CCD for some M3 tilt values.

Then, the X-tilt for both the channels' M3s was adjusted. The aim was to remove astigmatism at the center of the field of view. Images were recorded for five different defocus positions, around the possible best focus and at -0.6mm, -0.3mm, $+0.3$mm and $+0.6$mm, by adjusting the camera's Z-position. This measurement method was applied to various X-tilt of the channel 1's M3: $0'$, $-1.2'$, $-2.4'$, $-3.0'$ and $-3.6'$. The spot diagram showing the shape of the central pinhole through the focus is shown in the left part of Figure 3.11. The astigmatism is minimum for a X-tilt between $-2.4'$ and $-3.0'$, revealing a symmetric spot shape in the X-direction and in the Y-direction through the focus. The last value was selected as the best alignment. For channel 2, the M3 X-tilt was adjusted five times, at $0'$, $-1.2'$, $-1.8'$, $-2.4'$ and $-3.6'$ as shown in the right part of Figure 3.11, and the best X-tilt alignment was selected at $-1.8'$.

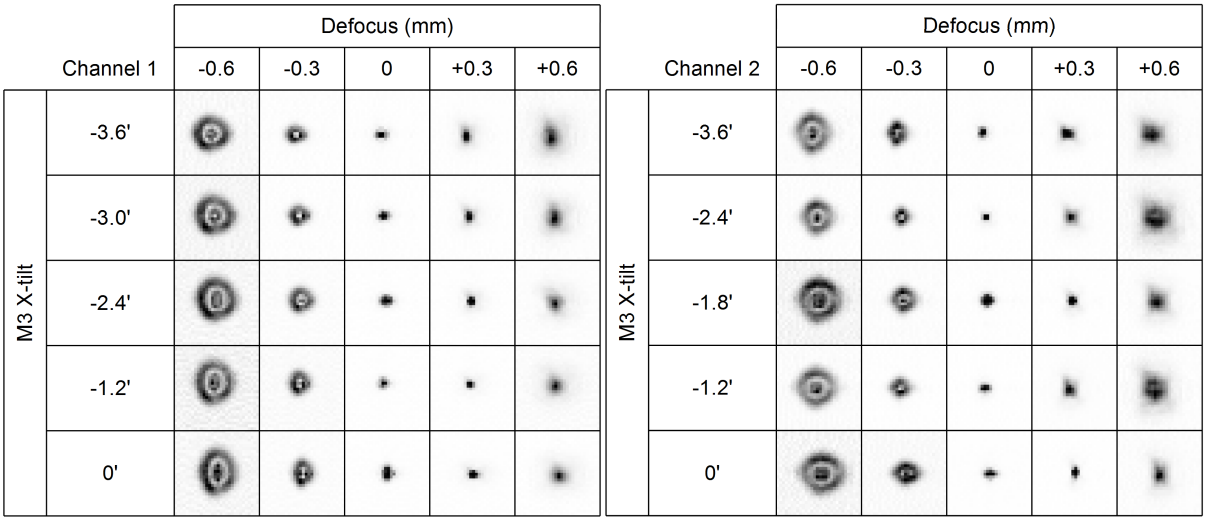

Figure 3.11: Spot diagram for the X-tilt alignment of the M3s, showing the central pinhole spot of channel 1 (left) and channel 2 (right). Horizontal shows the defocus distance from the possible best focus position (0mm) and vertical shows the various X-tilt values.

3.2.5 Alignment of the cameras Z-position

The final step to complete the alignment of the spectro-polarimeter in visible-light was to find the best focus position for the cameras. The alignment was performed by scanning the focus position using the micrometer on the camera's adjustable mechanism. Images of the spots were recorded for each micrometer position, resulting in eleven images per cameras. Figure 3.12 shows an example of focus scan for the three central pinholes. On each spot of the central pinhole, a 2D Gaussian function was fitted. The form of this function is given by:

$$z = A\exp\left(-\left(\frac{(x-x_0)^2}{2\sigma_x^2} + \frac{(y-y_0)^2}{2\sigma_y^2}\right)\right) \tag{3.1}$$

The σ_x and σ_y gives a measure of the spot elongation in the X-direction and Y-direction, respectively. A Gaussian "radius" was computed as the root sum square of the two sigmas. Although this "radius" is an approximation, it provided an estimation of the global size of the spot. The best focus position for each camera was then determined by finding the micrometer position which minimized the Gaussian "radius" of the central pinhole spot, as shown in Figure 3.13.

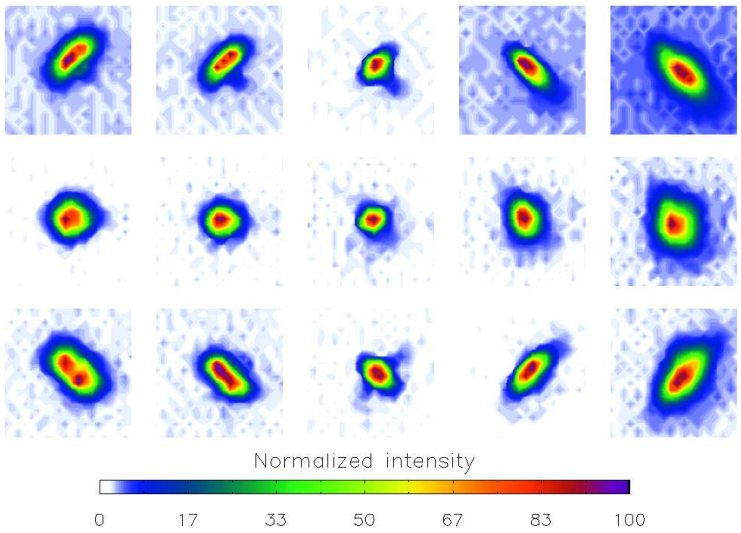

Figure 3.12: Focus scan example for channel 2, with five positions along the focus. Middle row shows the central pinhole whereas top and bottom rows show the pinholes at the edge of the slit. Each box is 21x21 pixels (i.e. 92x92 microns)

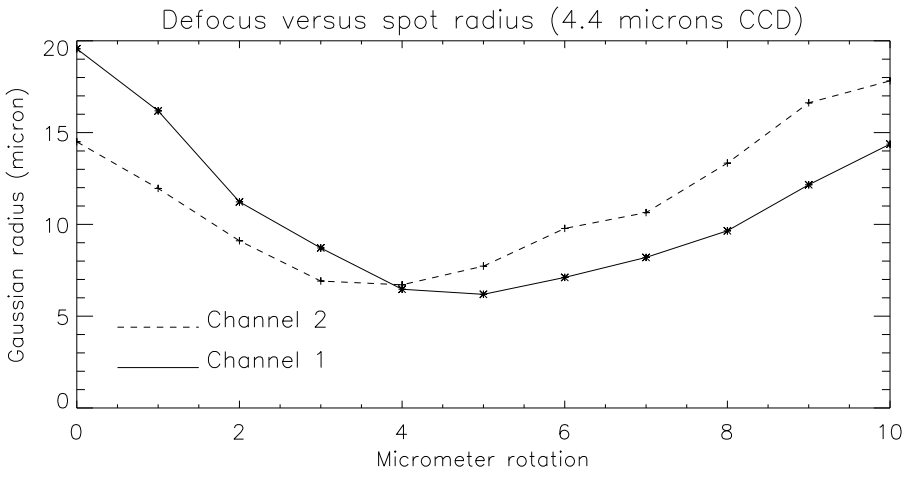

Figure 3.13: Defocus versus spot radius for a focus scan in channel 1 (solid) and in channel 2 (dashed). Spot radius is estimated as the Gaussian "radius" of the central pinhole. Defocus is measure as micrometer rotation of the camera adjustment mechanism. Crosses show the measured values, for each rotation.

3.2.6 Final spots with visible-light cameras

The final spots obtained at the best focus position after alignment of the optics are shown in Figure 3.14. The RMS spot radius for each of these spots was computed using the formula introduced for the telescope alignment (Section 2.4). The noise level on each spot was estimated from the surrounding and subtracted. Results are reported in Table 3.4. Note that some pinhole images were located outside of the CCD detectors, but this was not relevant since the final position of the camera was adjusted for the flight cameras. The final spots demonstrated that the alignment in visible-light was successful, as the resulting RMS spot radius at the edge of the slit was smaller than the required tolerance of 13.5 µm.

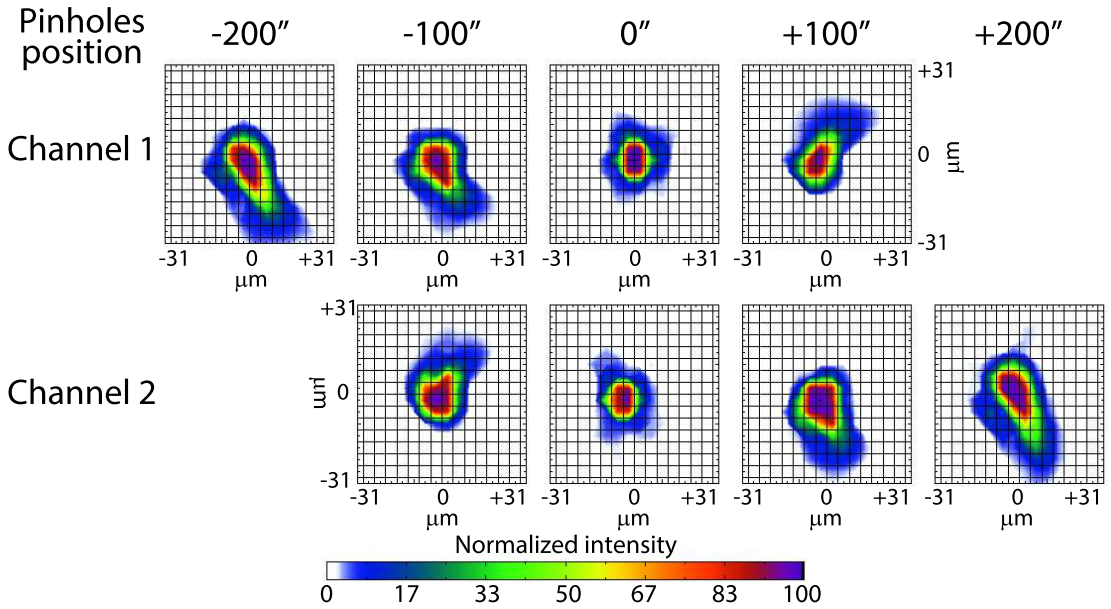

Figure 3.14: Spots recorded at the best focus position with the VL cameras. Pixel grid is shown (4.4 µm).

Table 3.4: RMS spot radius for the final spots of the five pinholes. N/A indicates a pinhole image outside of the CCD detector.

	−200”	−100”	0”	+100”	+200”
Channel 1 RMS spot radius (µm)	11.7	10.5	8.1	10.2	N/A
Channel 2 RMS spot radius (µm)	N/A	9.7	7.7	9.9	11.3

3.2.7 Final spots in visible-light with flight cameras

The visible-light cameras with 4.4 µm pixels were replaced by the flight cameras with 13.0 µm pixels, and the focus of these cameras was also adjusted using the scanning method described previously. Figure 3.15 shows the resulting focus scan for both the channels. The accuracy achieved was limited by the larger pixel size: the restricted sampling compared to the visible-light cameras case affected the accuracy of the 2D Gaussian fitting.

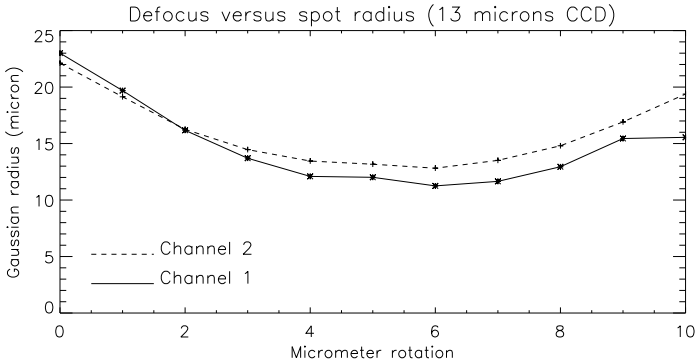

Figure 3.15: Defocus versus spot radius for the focus scan with the flight cameras, for channel 1 (solid) and channel 2 (dashed).

Nevertheless, the best focus position could be estimated. Spots at this location are shown in Figure 3.16. In this case, due to the larger size of the detector format, the five pinholes could be observed in the channel 2. However, the bottom pinhole remained marginally outside the channel 1 detector. The RMS spot radius was computed for these spots as well, and results are reported in Table 3.5. The RMS spot radius appeared larger in this configuration, which was also due to the limited sampling size of the pixel affecting the calculation accuracy. The 4.4 µm/pixel camera should be used for judging the alignment quality in visible-light.

Table 3.5: RMS spot radius for the final spots of the five pinholes.

	−200”	−100”	0”	+100”	+200”
Channel 1 RMS spot radius (µm)	16.0	19.6	13.0	13.3	N/A
Channel 2 RMS spot radius (µm)	16.8	16.1	14.1	12.5	13.2

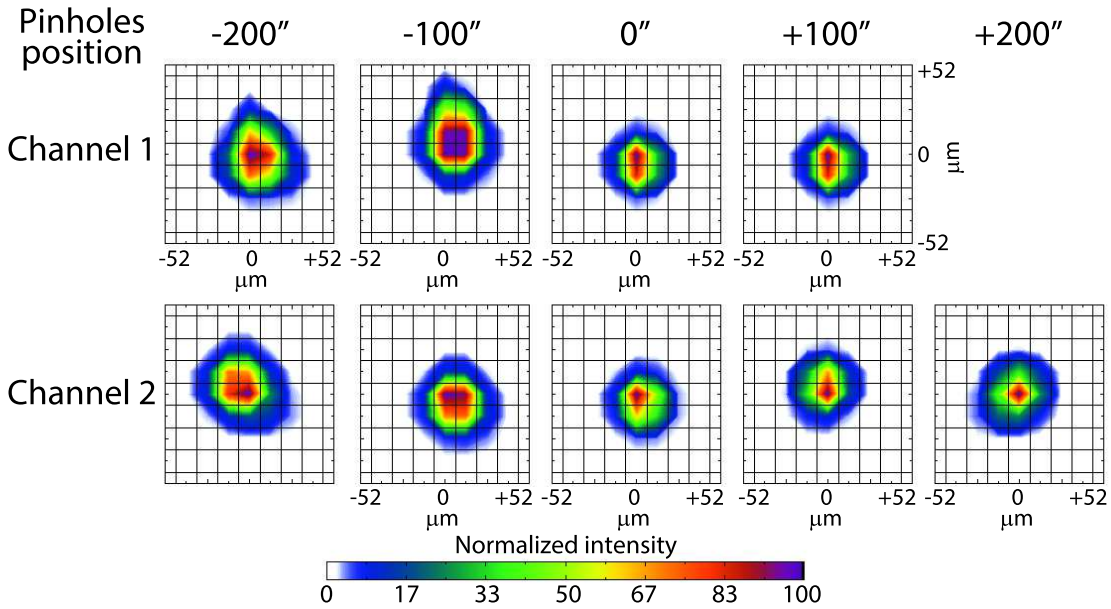

Figure 3.16: Spots recorded at the best focus position with the flight cameras. Pixel grid is shown (13 µm).

3.3 Alignment in vacuum

3.3.1 Alignment of the flight grating X-tilt and Y-tilt

Similarly as for the alignment grating, the Lyman-α grating X-tilt and Y-tilt were adjusted using a theodolite, aligned with the center of the mirror-target. Table 3.6 reports the measured tilt. The actual tilts of the grating were calculated considering the distance from the theodolite to the grating, measured ∼3800mm for this configuration. The Lyman-α grating X-tilt and Y-tilt were aligned to the mechanical axis below the required tolerance.

Table 3.6: Alignment of the Lyman-α grating X-tilt and Y-tilt with respect to the mechanical axis (mirror-target). The angles marked with the (T) symbol are measured in the coordinate system of the theodolite. The shift is given along the corresponding axis.

Measurement	X-axis	Y-axis
Mirror-target (mechanical axis)	+00°00′00” (T)	+00°29′52” (T)
Grating tilt (nominal)	+00°00′41” (T)	+00°29′09” (T)
Grating tilt (after shimming)	+00°00′14” (T)	+00°29′24” (T)
Difference (after shimming)	+00°00′14” (T)	−00°00′28” (T)
Center of curvature shift	+278 µm	+139 µm
Final grating tilt	−00°00′08”	−00°00′16”

3.3.2 Alignment of the grating Z-tilt

Due to an issue on the surface figure of the off-axis parabolic mirrors, the mirrors were replaced by new ones. More details are given in Appendix C. However, because of time-constraints on the instrument schedule, the new-M3s could not be properly aligned in visible-light. Instead, they were installed with the same tilt adjustment as measured for the old-M3s. Indeed, the bonding process to the M3's holder was performed with a similar technique for both the old-M3s and the new-M3s. Therefore, the tilt measured for the old-M3s adjustment was assumed to be caused by the instrument's structure, and applied equally to the new-M3s.

The grating Z-tilt alignment for the Lyman-α grating was conducted under vacuum condition, with a deuterium lamp illuminating the pinhole array. This deuterium lamp provided its strongest emission at the deuterium Lyman-α wavelength (121.534nm) but emission at the hydrogen Lyman-α (121.567nm) was also visible. A focusing MgF_2 lens was used mimic the telescope F/9.68 and focus the light onto the pinhole array. Therefore, the spot created by the light-source at the pinhole array could not properly illuminate all five pinholes: when aligned to the central pinhole, only the three central pinholes received enough light. In addition, multiple other weak emission lines could be seen, probably due to additional residual elements inside the deuterium lamp.

The grating Z-tilt was adjusted using a motorized rotating mechanism operated remotely from the outside of the vacuum chamber, and the best position was selected by checking the shape of the defocused spots at the 0" and $\pm$100". Figure 3.17 and Figure 3.18 present the measurements recorded for a camera defocus $\sim$1mm from the best focus position, for different grating Z-tilt and for channel 1 and channel 2, respectively. The grating Z-tilt is expressed in steps, which corresponds to the rotating motor incrementation. By considering the rotating mechanism used, 40 steps corresponds to $\sim 3'$.

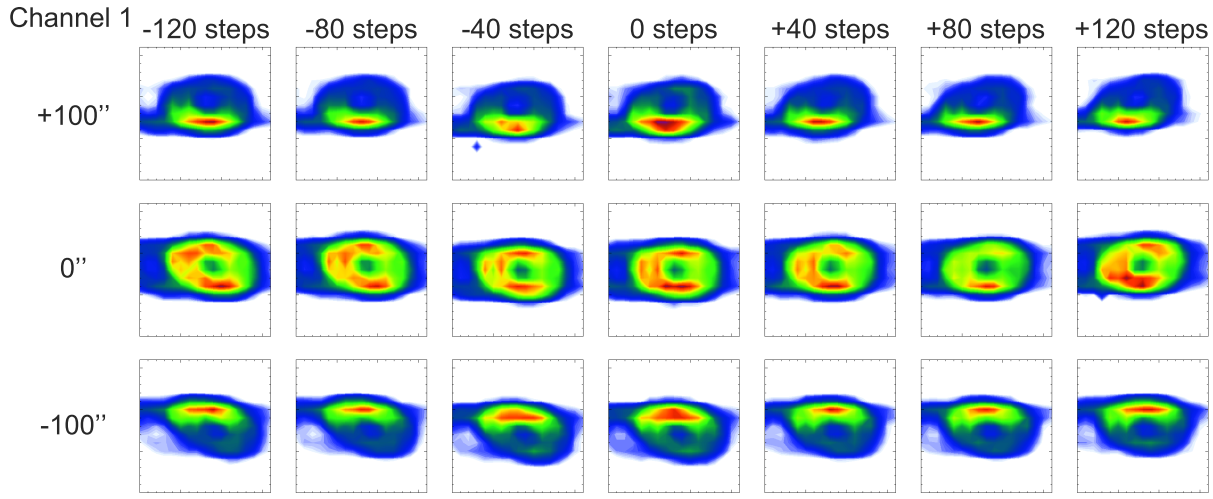

Figure 3.17: Lyman-α grating Z-tilt adjustment with new-M3s for channel 1. +X-axis is toward the top and $+\lambda$ toward the left. Spots are displayed in a 17x17 pixels box (221x221µm).

In channel 1, the spot at 0" was aligned with the X-axis for +40 steps, whereas it is closer to -120 steps for channel 2. The larger difference was due to the residual misalignment of the new-M3s: one single solution of the grating Z-tilt could not be found. Nevertheless, the average

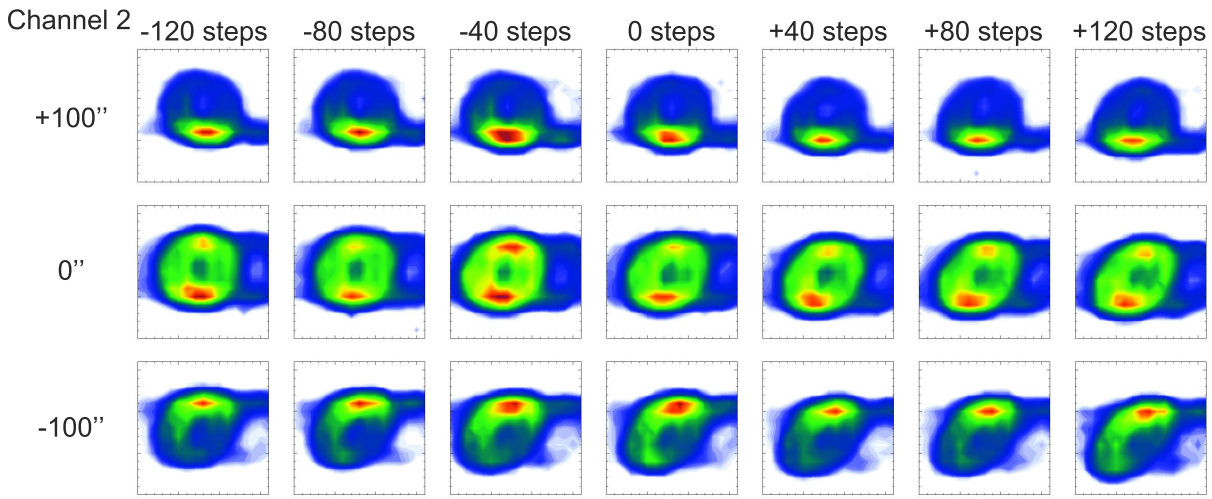

Figure 3.18: Lyman-α grating Z-tilt adjustment with new-M3s for channel 2. +X-axis is toward the top and $+\lambda$ toward the right. Spots are displayed in a 17x17 pixels box (221x221µm)

position was selected for the grating Z-tilt: -40 steps. The error induced on each channel was $\sim 6'$ (80 steps), which was still within the tolerance for the grating Z-tilt ($\pm 7.5'$). In addition, with the new-M3s, the spatial blur completely disappeared from the spots.

Finally, the position of the central pinhole spots was used to estimate the misalignment of the new-M3s compared to the old-M3s. Table 3.7 shows the image shift as measured on the cameras for both the channels. Considering the pixel size (13 µm) and the distance between the mirror and the camera (827.5 mm), the tilts of the mirrors can be estimated. Note that a image shift in the X-direction is caused by a M3 tilt around the Y-axis, and vice-versa.

Table 3.7: Position of the central pinhole spot on the cameras for the old-M3s and new-M3s, and resulting tilt of the new-M3s.

	Channel 1 X	Channel 1 Y	Channel 2 X	Channel 2 Y
Old M3s	207 pixels	496 pixels	206 pixels	175 pixels
New M3s	182 pixels	514 pixels	244 pixels	206 pixels
Difference	-25 pixels	18 pixels	38 pixels	31 pixels
New M3's tilt	$-1.4'$	$-1.0'$	$+2.1'$	$-1.7'$

3.3.3 Final spot at Lyman-α

The final position of the cameras was determined by scan the focus position, with images taken every 50 steps of the adjustment mechanism. The resulting spots are shown in Figure 3.19 for channel 1 and Figure 3.20 for channel 2. The sharpness of the deuterium Lyman-α double-peak emission was chosen as criterion for determining the best focus position: both peaks should be seen clearly while minimizing the dispersion in the spatial direction. From the spots, it clearly appears that the position at -1900 steps for channel 1 and at 2500 steps for channel 2 provided the sharpest double-peak features.

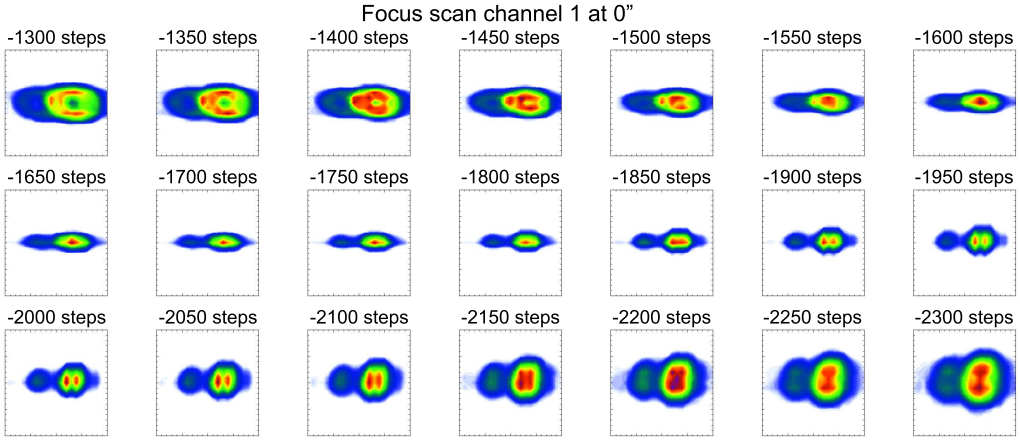

Figure 3.19: Focus scan for channel 1's CCD, showing the central pinhole spot for various incrementation of the adjustment mechanism. +X-axis is toward the top and $+\lambda$ toward the left. Spots are displayed in a 21x21 pixel box (273x273µm)

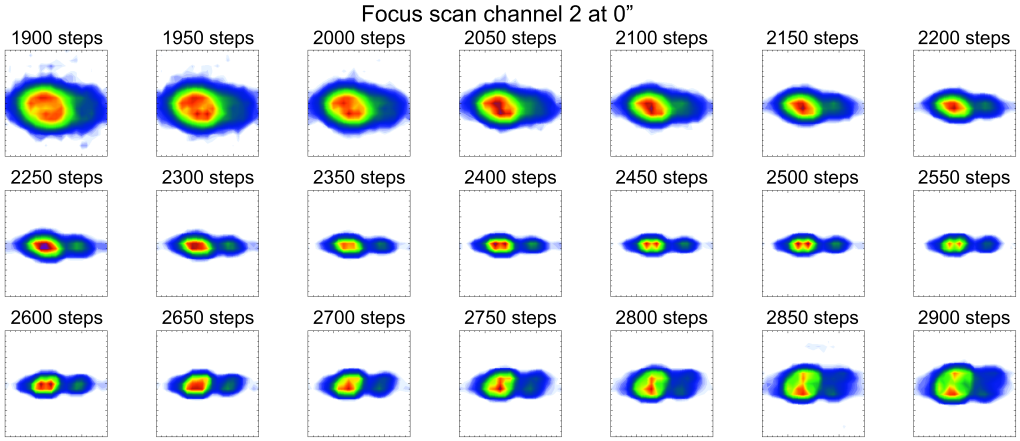

Figure 3.20: Focus scan for channel 2's CCD, showing the central pinhole spot for various incrementation of the adjustment mechanism. +X-axis is toward the top and $+\lambda$ toward the right. Spots are displayed in a 21x21 pixel box (273x273µm)

Determining the spectral and spatial resolutions at best focus by using the deuterium or hydrogen Lyman-α spots was not possible since both emission are intrinsically broad. Instead, a small emission line at $\sim$121.709nm was selected, as shown in Figure 3.21. The spots of this weak line at the best focus position are shown in Figure 3.22 for both the channels. The RMS spot radius calculation to estimate the spot size could not be used because the multiple emission in the wavelength direction affected the estimation accuracy. Therefore, spectral and spatial profiles of the spots were taken and a Gaussian function was fitted to estimate the Full-Width-Half-Maximum (FWHM , approximatively twice the RMS spot radius). Results from the fitting are shown in Table 3.8, including the corresponding spatial and spectral resolutions after multiplication with the plate scale (0.0048 nm/13 µm in wavelength and 1.11"/13 µm along the slit).

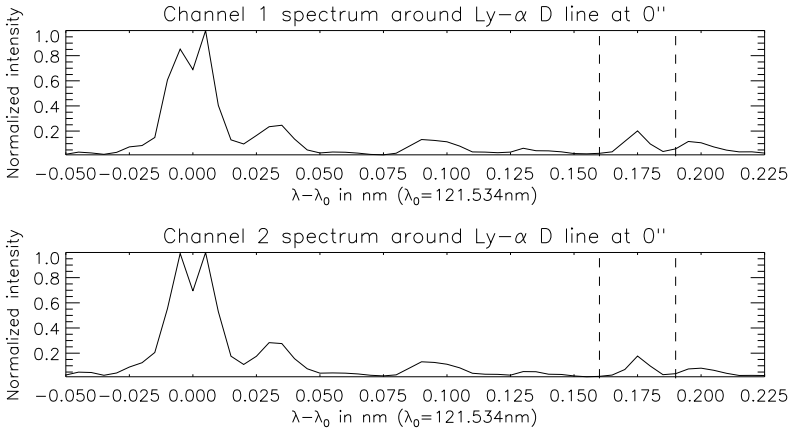

Figure 3.21: Wavelength profiles from channel 1 (top) and channel 2 (bottom). The horizontal axis shows the wavelength sampling, normalized to the deuterium Lyman-α wavelength. The two vertical dash lines shows $\pm$3 pixels around the line.

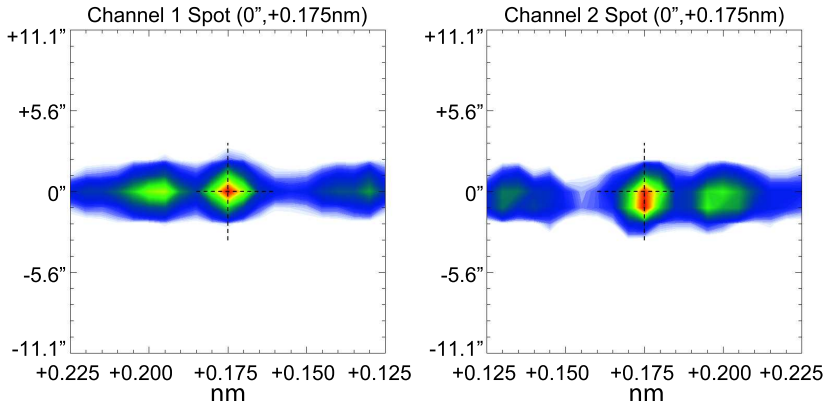

Figure 3.22: Spots for the weak line at 123.285nm, for channel 1 (left) and channel 2 (right). Boxes are 21x21 pixels (273x273µm) with spatial and spectral sampling calculated from the plate scale, and the dashed lines show the where the FWHM fitting was performed.

Table 3.8: Results for the spatial and spectral resolutions, estimated as the FWHM, for the spots at 121.709nm

	FWHM along X	Spatial FWHM	FWHM along Y	Spectral FWHM
Channel 1	22.3 µm	1.9"	24.8 µm	0.009 nm
Channel 2	22.9 µm	2.0"	22.0 µm	0.008 nm

The spatial and spectral resolutions were confirmed to be within tolerance at the center of the field of view, even with the residual misalignment of the new-M3s. The spatial and spectral resolutions were not measured at the edge of the field of view because no data were recorded for an illumination centered on the top or bottom pinhole. Nevertheless, an estimation was determined using the results from the visible-light alignment: the ratio between the RMS spot radius at the edge and at the center of the field of view was applied on the results from Table 3.8. The results when combined with the telescope performances (see Chapter 2) are shown in Table 3.9 and compared with the requirement.

Table 3.9: Resulting RMS spot radius for both channels spatial and spectral resolutions when combining the telescope and spectro-polarimeter performances at the edge of the slit. The corresponding resolution is given in bracket.

	Channel 1 Spatial	Channel 2 Spatial	Channel 1 Spectral	Channel 2 Spectral
Telescope	8.0 µm (1.9")	8.0 µm (1.9")	-	-
Spectro-polarimeter	16.1 µm (2.7")	16.8 µm (2.9")	17.9 µm (0.013nm)	16.1 µm (0.012nm)
Combined	17.7 µm (3.0")	18.4 µm (3.1")	17.9 µm (0.013nm)	16.1 µm (0.012nm)
Requirement	18.1 µm (3.1")	18.1 µm (3.1")	13.5 µm (0.010nm)	13.5 µm (0.010nm)

The optical alignment of the spectro-polarimeter was considered to be successful, although the spectral resolution achieved at the edge of the slit was slightly larger than the requirement.

3.4 Conclusion of the spectro-polarimeter optical alignment

The procedure to align the spectro-polarimeter was successfully performed. At first the off-axis mirrors tilts were adjusted in visible-light. The X-tilt and Y-tilt for the custom visible-light alignment grating was adjusted below its requirement with a theodolite. The alignment grating Z-tilt was measured using white-light to observe the dispersion direction, and adjusted to make a 90° angle with the slit direction, observed with a He-Ne monochromatic laser. The M3s tilts were then aligned by comparing the spot shape with optical simulations, to diagnose the amount of adjustment required . The resulting RMS spot radius was estimated around 8.0 µm at the center of the slit and around 11.5 µm at the edge of the slit.

The alignment grating was then replaced by the Lyman-α grating, and only its grating Z-tilt was adjusted under vacuum using a deuterium lamp to illuminate the pinhole array. Based on the spot shape observed at the center of the field of view, the grating Z-tilt could be aligned to optimize the alignment in both the channels. However, a blur in the spatial direction was also observed due to the surface figure of both the M3s, which had to be replaced. These new mirrors could not be re-aligned in visible-light. Nevertheless, the grating Z-tilt was selected to optimize the image quality on both the channels, and a focus scan was performed to adjust the focus position of the cameras. The measurements after the alignment confirmed the spatial and the spectral resolutions at the center of the field of view, and estimation also confirmed the achieved resolutions at edge of the slit.

Chapter 4

Telescope focus position adjustment to the spectro-polarimeter

4.1 Introduction and methodology

Adjusting the focus position of the telescope with respect to the slit was required to ensure the image quality on both the slit-jaw camera and the spectro-polarimeter's cameras. The focus adjustment between the telescope and the spectro-polarimeter aimed to compensate for any possible positional errors along the Z-axis due to the instrument's structure, as well as to remove the remaining defocus aberration from the optical alignment of the telescope (see Section 2). The adjustment was performed by inserting shims at the base of the screws attaching the telescope structure to the spectro-polarimeter interface plate (see Figure 4.3) with a required ±0.1mm accuracy. This ±0.1mm tolerance on the focus position was derived as half the focal depth of the telescope, calculated considering the telescope F number and RMS spot radius allocated for the defocus (see Table 2.1) compared to the width of the slit, as shown in Figure 4.1.

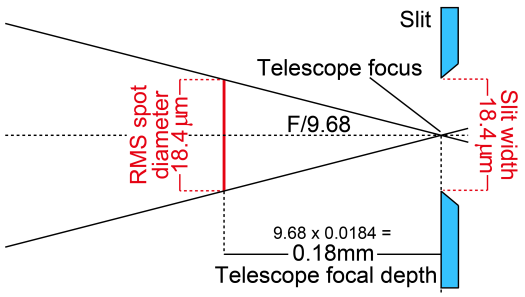

Figure 4.1: Focal depth of the telescope. To ensure the focus position to be within the focal depth, a ±0.1mm tolerance is required.

The telescope defocus was estimated by measuring the width of the slit imaged on the slit-jaw camera. Because injecting a perfectly collimater beam to the ϕ270mm aperture telescope is not trivial, a double-pass configuration was used instead: a white-light lamp (i.e. optical fibre with diverging lens at its end) was inserted by the access door of the rocket-skin to illuminate the back-side of the slit, as shown in Figure 4.2. The light transmitted by the slit passed through the

telescope, exiting by the entrance aperture as a collimated beam and was reflected back inside the telescope using a large flat mirror (ϕ600mm, RMS WFE 15nm). The reflected image of the slit was measured on the slit-jaw camera by slightly tilting the large flat mirror.

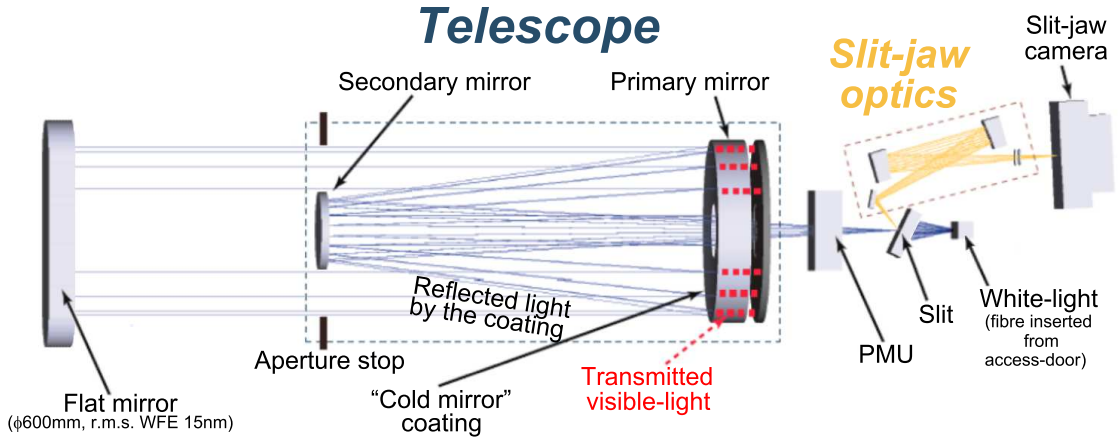

Figure 4.2: Experimental configuration for the telescope focus measurement.

Due to diffraction by the slit, some light directly propagated inside the slit-jaw optics and a direct image of the slit was observed on the slit-jaw images. Because of the "cold mirror" coating on the primary mirror, the intensity of the reflected image of the slit was much dimer than the direct image of the slit. The intensity of the light-source was increased to observe the reflected slit, which resulted in a saturated image of the direct slit. Therefore, two measurements were recorded for each shim thickness tested: one with the reflected slit and with the saturated direct slit images, and one with the unsaturated direct slit images. Figure 4.4 shows an example of these two measurements.

The slit width was estimated by measuring the full width at half maximum (FWHM) of the slit by fitting a simple Gaussian function across the slit. For a given shim thickness, each set of measurement was composed of ~100 images. For each image, the fitting was performed at every pixel along the slit, resulting in ~400 values for the FWHM. The average of the measured FWHM values was taken as the FWHM for each image, and the standard deviation was computed to estimate the measurement error. It was observed that the vibrations from the environment (e.g. ground, building itself or other instruments around the experiment) greatly affected the measured FWHM: vibrations of the flat mirror surface during the exposure time (290ms) were "blurring" the image of the reflected slit, resulting in a larger FWHM measured. Hence, the exposure with minimum FWHM value out of all the ~100 images recorded during each set of measurement was selected, as a way to minimize the effect of the vibration and to obtain consistent estimation of the FWHM. This method was valid since no physical effect can possibly decrease the reflected slit FWHM (i.e. improve the image quality). Nevertheless, even the image with minimum FWHM might still have been affected by some vibrations: this method only minimized the probability and amplitude of the effect.

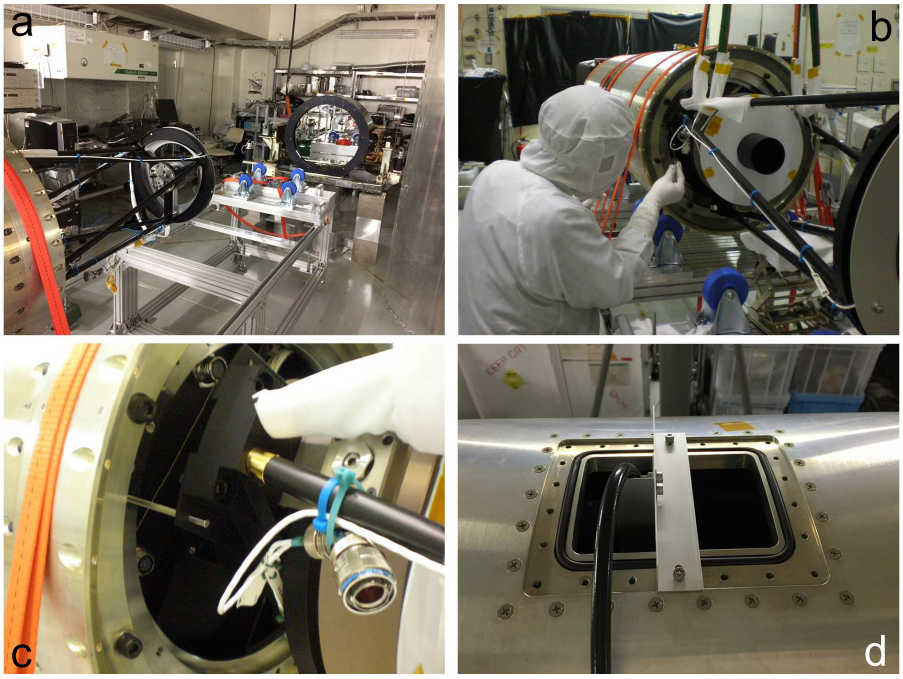

Figure 4.3: Pictures taken during the experiment: experimental configuration with the telescope located in front of the large mirror (a), telescope attached to the spectro-polarimeter and aligned with pin gauge (b), close-up to the pin gauge used and screws where the shimming was performed (c) and light-source fibre inserted through the rocket skin's top-door (d).

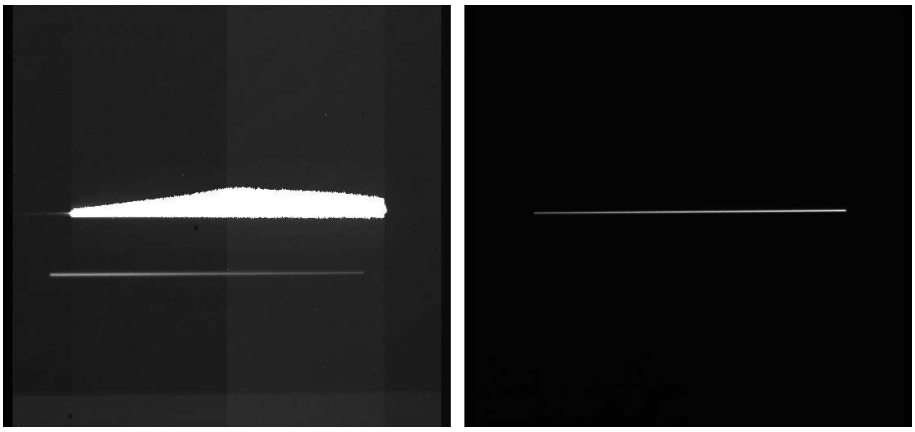

Figure 4.4: Example of slit-jaw images with the reflected slit and saturated direct slit (left) and with the direct slit unsaturated (right).

4.2 Results from the measurements

The set of measurements recorded for various shim thickness are reported in Table 4.1. As previously mentioned, the FWHM value for the reflected slit was taken from the image with minimum average FWHM across the data set, and the error was calculated as the standard deviation from all the fitted FWHM values along the slit for this given image. This estimation of the error account for the error in the fitting process along the slit, but not for the vibration effect. The same method was also performed for the direct slit, which appeared to be unaffected by vibration. This is easily understandable, as the light directly propagated from the slit to the slit-jaw camera, both of which are attached on the same structure. The results of the FWHM for the reflected slit are plotted in Figure 4.5: a clear minimum of the FWHM can be seen for a 700 µm shim thickness.

Table 4.1: Summary of the telescope focus adjustment: reflected and direct slit FWHM for various shim thickness.

Shim thickness (µm)	FWHM reflection (µm)	FWHM direct (µm)
500 (Nominal)	38.9 ± 2.5	22.8 ± 1.2
300	61.1 ± 3.1	23.7 ± 1.2
600	32.5 ± 1.2	23.1 ± 1.2
700	30.0 ± 1.0	22.9 ± 1.2
680	30.7 ± 0.9	24.1 ± 2.0
700	30.5 ± 1.0	22.9 ± 1.2
800	33.8 ± 2.9	23.2 ± 1.2
730	31.1 ± 1.2	22.4 ± 1.1

The measured FWHM for the direct slit (∼23.5 µm) can be interpreted as a combination of the slit width (i.e. 18.4 µm) and of the slit-jaw optics performance. Considering this, an estimation of the reflected slit FWHM was computed as the convolution between the direct slit FWHM and the telescope point spread function (PSF). The PSF was calculated with optical simulations using the measured wavefront error shown in Chapter 2), which included the effect of the mirror's surface figure deformation and the effect of diffraction by the entrance aperture at the light-source peak wavelength. The light-source LED spectrum was provided by the manufacturing company and is shown Figure 4.6. The light-source peak intensity was estimated around 460nm, which was selected for the PSF calculation as an approximation of the lights-source spectrum.

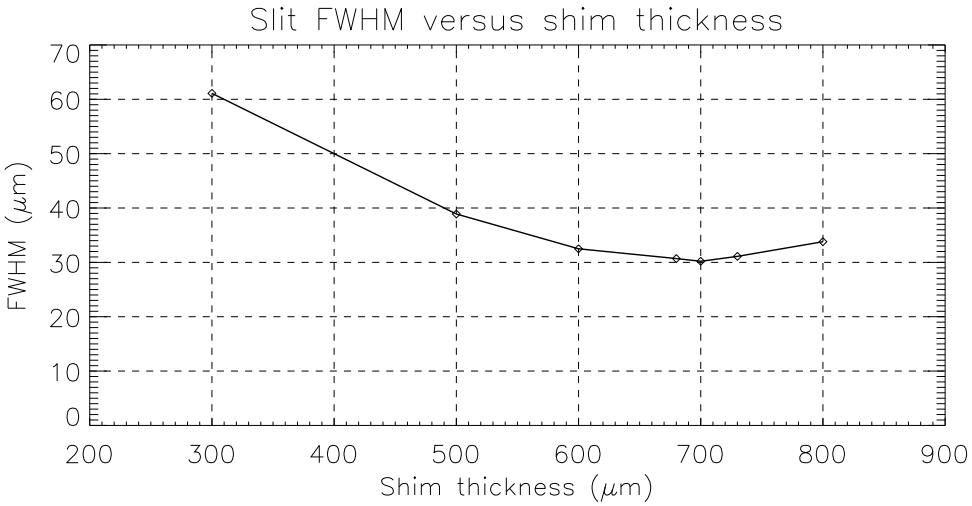

Figure 4.5: Reflected slit FWHM versus shim thickness.

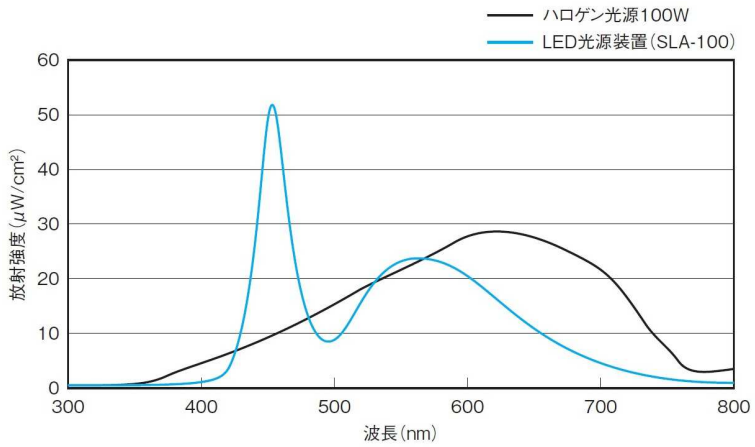

Figure 4.6: Spectrum of the LED light-source (blue) as provided by the manufacturer. X-axis shows the wavelength and Y-axis the intensity. Black curve shows the spectrum of a 100W halogen.

Figure 4.7 shows the PSF of the telescope used for the calculation, displayed in normal and logarithmic scales. Only the central part (i.e. 26 µm side box corresponding to twice the RMS spot radius derived in Chapter 2) of the PSF was used for the convolution with the direct slit (i.e. Gaussian profile with 23.5µm FWHM), as the far-wings of the PSF caused problems in the FFT calculations. This central part of the PSF contained more than 75% of the encircled energy, and was convolve twice with the direct slit to simulated the double-pass configuration. A Gaussian function was fitted across the convolved slit and the resulting FWHM was estimated at 29.9µm. This is consistent with the measured FWHM for 700 µm shims, indicating that the telescope is well focused in visible-light.

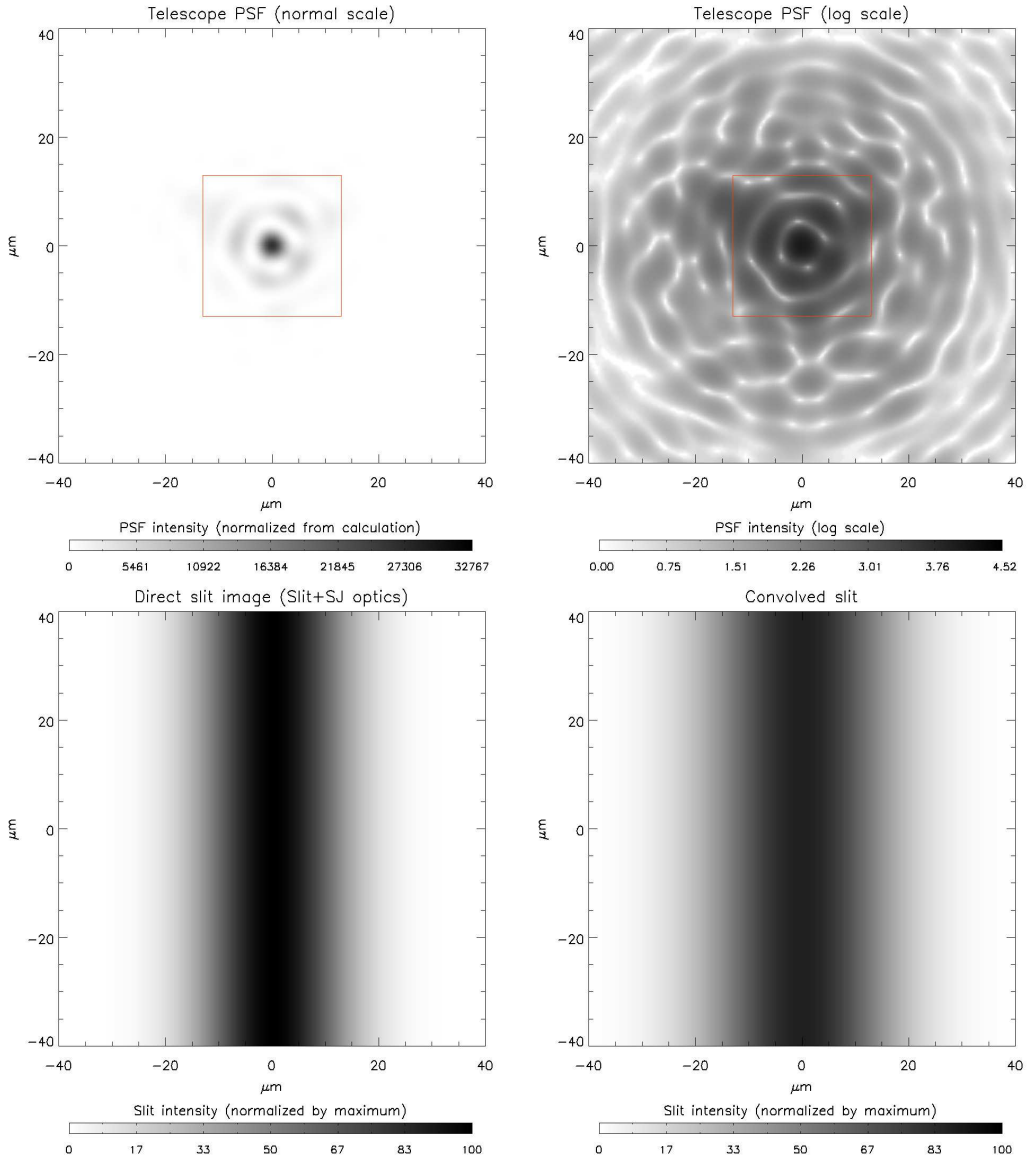

Figure 4.7: Top-left: PSF of the telescope, calculated from the optical model of the telescope including the surface figure deformation of the mirrors and the effect of diffraction, at 460nm. Top-right: PSF displayed in logarithmic scale. Red box indicates the central part of the PSF used for the convolution. Bottom-left: direct slit with 23.5μm FWHM, including the slit width (18.4μm) and the effect of the slit-jaw optics. Bottom-right: convolution of the direct slit with twice the reduced (red box) telescope PSF.

4.3 Focus position at Lyman-alpha

An additional 100 µm shim was inserted to account for the focus shift created by the MgF_2 half-waveplate's refractive index, which changes from visible to Lyman-α as shown in Figure 4.8.

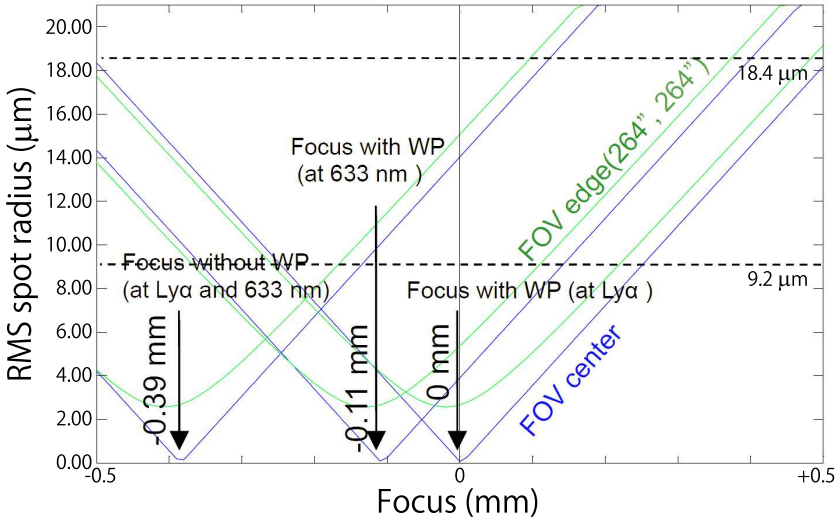

Figure 4.8: RMS spot radius versus focus position at thecenter and edge of the field of view, with and without the waveplate (WP) and at Lyman-α and He-Ne wavelengths.

In total, 800 µm shim thickness were inserted between the telescope and the spectro-polarimeter to adjust the telescope focus on the slit at Lyman-α. For reference, several measurements of the reflected slit FWHM with the 800 µm shims were recorded, as reported in Table 4.2. The reference FWHM, computed as the average of the measurements, is 32.8±1.4µm. Considering the slope from Figure 4.5, the ±100µm tolerance on the focus position is translated to approximatively 30 µm (lower-boundary, for ∼700 µm shim) and 39 µm (upper-boundary, for ∼900 µm shim) in term of the reflected slit FWHM. In conclusion, the focus position of the telescope can be ensured if the FWHM of the reflected slit is within these two boundary-values. This was checked during the pre-flight preparation (rocket integration, transportation, vibration tests) and results are presented in Chapter 7.

Table 4.2: Summary of the telescope focus adjustment: reflected and direct slit FWHM for various shim thickness.

Measurement	FWHM reflection (µm)	FWHM direct (µm)
#1	31.9 ± 0.9	23.0 ± 1.2
#2	32.4 ± 1.2	22.9 ± 1.3
#3	33.1 ± 2.1	23.4 ± 1.2
#4	33.6 ± 1.2	23.1 ± 1.3

4.4 Conclusion

The method developed to estimate the telescope focus quality by measuring the width of the reflected slit, observed by the slit-jaw camera in a double-pass configuration, was successful. The shim thickness for the best focus adjustment of the telescope to the slit was measured at 700 µm in visible-light, and an additional 100 µm shim was inserted to account for the focus shift produced by the MgF_2 half-waveplate at Lyman-α. The reflected slit FWHM for 800 µm shim thickness was measured at 32.8±1.4µm. The telescope focus was confirmed during the pre-flight preparation of the instrument by using the same measurement method and results were compared with the measured FWHM with 800 µm shim thickness. These results are presented in Chapter 7.

Chapter 5

Alignment of the PMU half-waveplate

5.1 Introduction

The Polarization Modulation Unit is responsible for ensuring the polarization modulation by rotating the MgF_2 half-waveplate with a constant speed (full rotation in 4.8s) and triggers the spectro-polarimeter camera for exposure every 300ms. The first trigger always happen after stabilization of the rotation speed and at a fixed angular position of the PMU, recorded by an encoder. The Stokes Q and U modulation presented in Section 1.3.3 requires the principal-axis of the half-waveplate to be aligned with the $+Q$ (i.e. X-axis in the mechanical coordinate system) when the first trigger for exposure occurs. Hence, to ensure a good polarization modulation and reach the accuracy needed for Hanle effect, the half-waveplate has to be carefully aligned inside the PMU. The tolerance for the polarization angle detection was defined as $\pm 0.5°$ (see Section 6.1 for more details). Hence, as the polarization angle is affected by twice the error on the half-waveplate orientation, the tolerance for the alignment of the half-waveplate principal-axis was set to $\pm 0.2°$. The principal-axis angle, hereafter called waveplate angle, was measured and adjusted experimentally, and the methodology is explained in the following. Note that the term principal-axis is used to described both the fast-axis and the slow-axis of the half-waveplate, as their are no distinctions required between both in the studied case.

5.2 Experimental setup

The waveplate angle detection and adjustment had to be performed with Lyman-α light in order to simulate the flight configuration. The UVSOR facility synchrotron beam provided a quasi-pure Lyman-α line, and has the other advantage of also being strongly linearly polarized. Nevertheless, two polarization cleaners (i.e. coated mirror at Brewster's angle) were used to ensure the linear polarization of the beam. The beam-line used during the experiment included an adjustable grating system (i.e. monochromator) upstream of the experiment chamber which allowed for a precise wavelength selection by modifying the grating's orientation.

The experiment setup, shown in Figure 5.1, was first aligned in front of the beam by selecting the zeroth order light from the diffraction grating inside the synchrotron's monochromator and looking at the white beam spot projected onto both SSD. The half-waveplate was then integrated inside the PMU, and the PMU was positioned between both polarization cleaners. For the measurements,

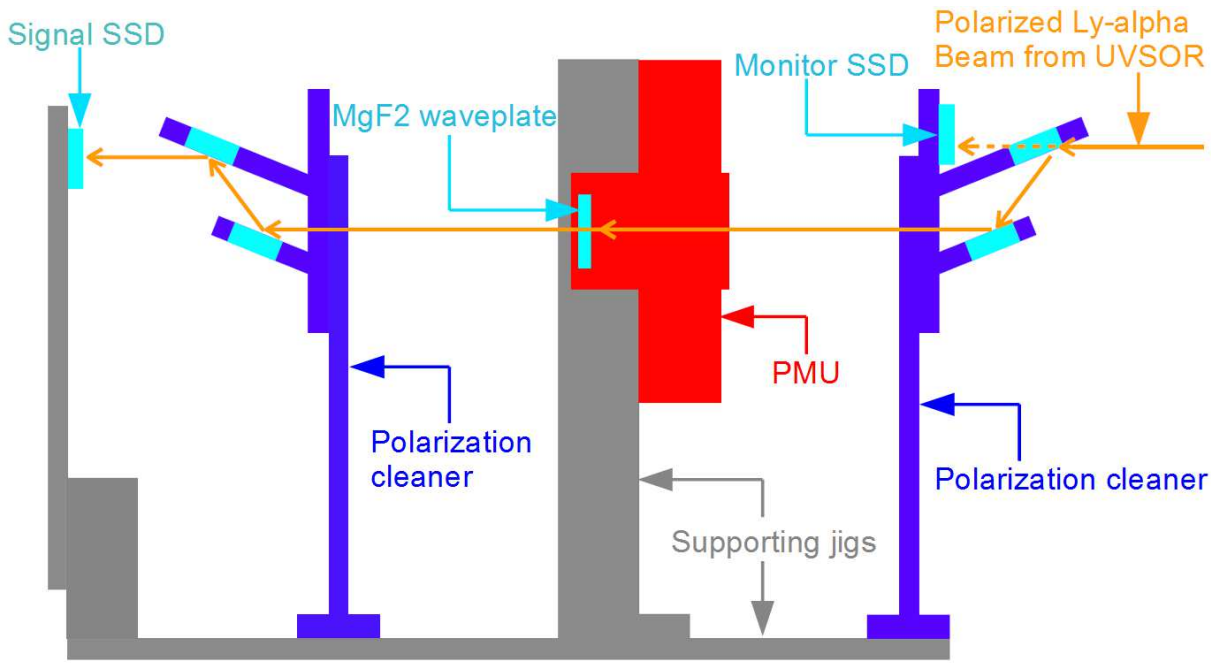

Figure 5.1: Experimental configuration with the dual polarization cleaners.

the monochromator's grating was set to the Lyman-α wavelength and a vacuum was created inside the experiment chamber.

The time duration of the measurements was chosen to be 120 seconds and SSD sampling rate to be 1000Hz. During the first 30-40 seconds, the PMU started to rotate in order to stabilize its rotation speed to 4.8s. After stabilization, the PMU used an infrared detector (i.e. encoder) to locate the reference position, which was a hole in the PMU rotation disk as shown in Figure 5.2. The PMU started to send an exposure signal every 0.3s after detecting the reference position. The modulation signal started after the first exposure signal was triggered, as shown in Figure 5.3. Note that the exposure trigger signal was 4V during the first 38s, until the PMU rotation speed was stabilized. Around fifteen modulations (i.e. waveplate rotations) were recorded on each measurement, and a fitting routine was used on the modulation signal to determine the waveplateâĂŹs initial angle.

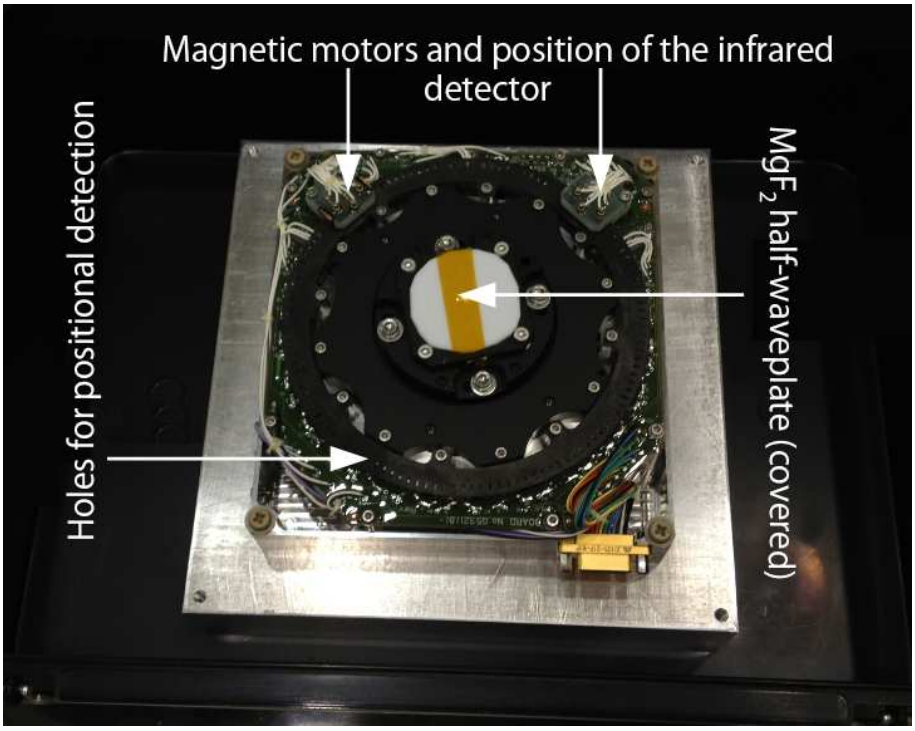

Figure 5.2: The Polarization Modulation Unit (PMU) with the infrared detector and reference holes.

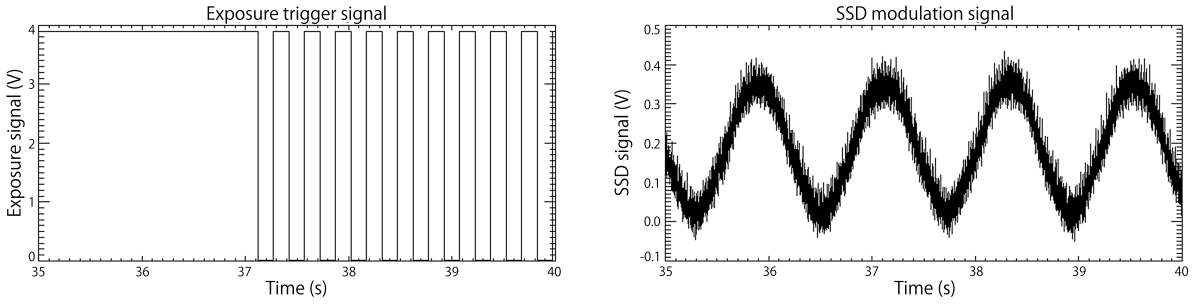

Figure 5.3: Left: Exposure trigger signal around the first trigger. Right : Modulation signal on the Signal SSD.

5.3 Infrared background issue and results

Some issues required fixing beforehand: electrical noise due to an unclean electrical ground resulted in a noisy modulation signal and the waveplate angle could not be determined accurately. Also, the infrared emission from the PMU detector was reflected by the chamber's wall back onto the SSD, corrupting the modulation signal, and both the PMU and SSDs had to be baffled with aluminium sheets (see Figure 5.4) in order to reduce the infrared background amplitude in the modulation measurements.

After fixing these issues, measurements were performed ten times with the experiment setup.

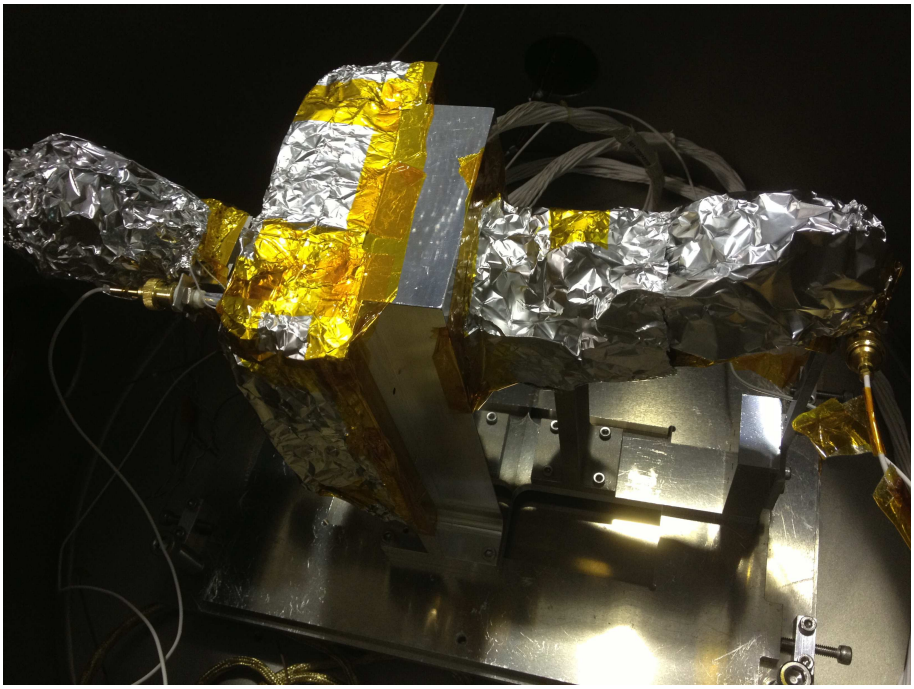

Figure 5.4: Aluminium sheets covering both PMU and SSDs to reduce infrared background.

The infrared background was also measured for both SSDs by rotating the PMU and closing the beam line to get only the infrared signal from the PMU inside the chamber. This background also presented a sort of modulation due to the PMU rotation, but with a different period as the modulation signal. As shown in Figure 5.5, the pattern for the infrared background was always the same during each measurements.

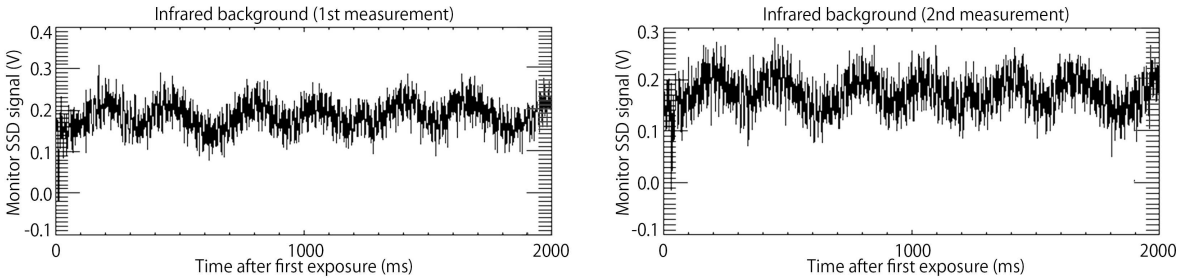

Figure 5.5: Two separate measurements of the infrared background for the monitor SSD showing similar fluctuations.

This infrared background data was averaged for both the SSDs, and respectively subtracted from each of the SSDs measurements. The signal SSD was also normalized with the monitor SSD to remove the beam fluctuation. Finally, a cosines function was fitted onto the modulation signal. Results from these measurements are summarized in Table 5.1, and the initial angle was estimated at around $+0.66°$. The sign represents the direction with respect to the principal-axis, in this case anti-clock-wise as the PMU is rotating clock-wise.

Table 5.1: Principal-axis angle of the half-waveplate from the vertical direction before adjustment.

Measurement	#1	#2	#3	#4	#5	#6	#7	#8	#9	#10
Angle (°)	0.65	0.69	0.65	0.68	0.62	0.52	0.66	0.69	0.81	0.71

The half-waveplate orientation was corrected by this angle without removing it from the PMU holder, using a specially designed jig. Ten additional measurements were performed after aligning the half-waveplate to confirm the initial position of its principal-axis at the first exposure time. Following the same infrared background subtraction and normalization of the signal SSD with the monitor SSD, the modulation measurements were fitted and the angle was determined. Results are reported in Table 5.2.

Table 5.2: Principal-axis angle of the half-waveplate from the vertical direction after adjustment. Fitting on measurement #5 didn't work, resulting in an abnormal 0.00° angle.

Measurement	#1	#2	#3	#4	#5	#6	#7	#8	#9	#10
Angle (°)	0.11	0.04	0.08	0.12	N.A.	0.02	0.10	0.07	0.03	0.17

The average angle fitted from Table 5.2 gives an initial angle of $+0.08° \pm 0.05°$ for the half-waveplate principal-axis angle with respect to the $+Q$ direction. The error was estimated as the standard deviation of the nine measurements, and the remaining angle including the error is within the required $\pm 0.2°$ tolerance required.

5.4 Conclusion on the PMU half-waveplate alignment

The half-waveplate initial angle was successfully determined experimentally and the half-waveplate adjusted inside the PMU within the 0.2° accuracy needed for the flight. The modulation data recorded during this experiment is important for the development of the instrument since it ensured the quality of the polarization modulation. This experiment also pointed out the possible contamination of the measurement by the PMU infrared detector. However, baffles inside the spectrograph should reduce this effect in the flight instrument.

Chapter 6

Pre-flight polarization calibration of the instrument

6.1 Introduction and requirements

A polarization calibration of the instrument is required to ensure the required 0.1% polarization accuracy for the Hanle effect detection in the Lyman-α line core. Polarization calibration are performed not only for ground-based (e.g. Vacuum Tower Telescope at Tenerife observatory, [44]) but also for space-borne (e.g. SpectroPolarimeter onboard Hinode spacecraft, [45]) instruments, and the methodology for the polarization calibration of spectro-polarimeter has been well established in the visible and infrared. However, as previously mentioned only few instruments were attempted to perform polarimetry in the VUV (e.g. SUMI sounding rocket, [29] and UVSP, [28]) and no instrument had ever attempted to achieved below the 0.1% polarization accuracy in this wavelength range, making CLASP a unique but also challenging instrument to calibrate.

The demodulation scheme by combining several consecutive exposures shown in Section 1.3.3 was derived using the Mueller matrix of the instrument. This formalism assumes an ideal half-waveplate and polarization analyzers and doesn't account for other source of artificial polarization (e.g. possible influence of the coating). A more realistic formalism to represent the influence of the instrument onto the measured polarization is by using the response matrix $\mathbf{X}$ ([46]), defined as $\mathbf{S'}=\mathbf{XS}$ where $\mathbf{S}$ is the incoming polarization signal expressed with its Stokes vector and $\mathbf{S'}$ is the measured one, as shown in Equation (6.1), normalized by the instrument's throughput x_{00} for simplicity. Each term of the response matrix $\mathbf{X}$ correspond to how much the measured Stokes parameters are affected by the different incoming Stokes parameters. Hereafter, the measured polarization will always be denoted by an apostrophe.

$$\begin{pmatrix} I' \\ Q' \\ U' \\ V' \end{pmatrix} = \begin{pmatrix} 1 & x_{10} & x_{20} & x_{30} \\ x_{01} & x_{11} & x_{21} & x_{31} \\ x_{02} & x_{12} & x_{22} & x_{32} \\ x_{03} & x_{13} & x_{23} & x_{33} \end{pmatrix} \begin{pmatrix} I \\ Q \\ U \\ V \end{pmatrix} \tag{6.1}$$

The optical design of the spectro-polarimeter was optimized to measure the linear polarization (i.e. Stokes Q' and U'): the PMU half-waveplate cancelled out Stokes V on every half-rotation. Hence, the bottom row of Equation (6.1) can be neglected for the response matrix, which reduces to a 4x2 matrix.

$$\begin{pmatrix} Q'/I' \\ U'/I' \end{pmatrix} \equiv \begin{pmatrix} q' \\ u' \end{pmatrix} = \frac{\begin{pmatrix} x_{01} & x_{11} & x_{21} & x_{31} \\ x_{02} & x_{12} & x_{22} & x_{32} \end{pmatrix}}{1 + x_{10}q + x_{20}u + x_{30}v} \begin{pmatrix} 1 \\ q \\ u \\ v \end{pmatrix} \tag{6.2}$$

The terms of the response matrix can be separated in four pairs : the x_{01} and x_{02} are called spurious polarization terms as they represent an offset from the true polarization signal ($I \rightarrow Q'$ and $I \rightarrow U'$ cross-talks). The x_{11} and x_{22} terms represent the scale factor in the polarization amplitude, and the x_{12} and x_{21} terms the azimuth error of the linear polarization (i.e. polarization angle or $Q \rightarrow U'$ and $U \rightarrow Q'$ cross-talks). Finally, the x_{31} and x_{32} are the $V \rightarrow Q'$ and $V \rightarrow U'$ cross-talks.

Because the solar Lyman-α intensity is expected to be much larger than the polarization signal ([19]), the x_{10}, x_{20} and x_{30} terms from Equation (6.2), which symbolize cross-talks from Q, U and V to I', could be neglected for the flight observation. However, these terms might be significant during the polarization calibration where the input polarization is almost perfectly polarized, and therefore have to be checked experimentally during the calibration.

The tolerance on each of these parameters was already determined in [38] and is recalled in Table 6.1.

Table 6.1: Tolerance for the response matrix elements. Requirements are taken from [38].

Name	Spurious polarization	Scale factor	Azimuth error
Requirement	0.017%	2%	0.5°
Matrix elements	x_{01} and x_{02}	x_{11} and x_{22}	x_{12} and x_{21}
Tolerance ($\pm$)	1.7×10^{-4}	2×10^{-2}	1×10^{-2}

The x_{31} and x_{32} terms from Equation (6.2) can be important because the Stokes V signal might affect the measured Q' and U', even though the baseline for the flight demodulation is to stack multiple rotations of the PMU half-waveplate, which should cancel out such cross-talks. Since the contribution of the Zeeman effect to the Lyman-α Stokes V signal is expected to be <1%, only the magnitude (i.e. value) of the x_{31} and x_{32} terms had to be checked experimentally. Hence the tolerance on these terms is quite different than for the other matrix elements, where the accuracy is required. A magnitude <1% is required for the V cross-talks to induce a negligible error compared to error on the spurious polarization (10^{-4} level, see Table 6.1), and was confirmed experimentally (see Section 6.4.3). Following this approximation, the response matrix of the instrument can be reduced to:

$$\begin{pmatrix} Q'/I' \\ U'/I' \end{pmatrix} \equiv \begin{pmatrix} q' \\ u' \end{pmatrix} = \begin{pmatrix} x_{01} & x_{11} & x_{21} \\ x_{02} & x_{12} & x_{22} \end{pmatrix} \begin{pmatrix} 1 \\ q \\ u \end{pmatrix} \tag{6.3}$$

The response matrix of the entire CLASP instrument includes both the telescope and the spectro-polarimeter parts. However, owing to its axisymmetric design, the polarization response of the telescope is expected to be negligible compared to the tolerance. Non-uniformity in the reflectivity of the mirror coating are the major source of spurious polarization induced by the

telescope. [38] estimated that the induced spurious polarization in Q'/I' and U'/I' created by the telescope assembly for on-axis and off-axis rays illuminating the slit at 0" and ±200" is at the 10^{-5} level. This is one order of magnitude smaller than the tolerance for the spurious polarization.

Therefore, the response matrix of the spectro-polarimeter is assimilated as the response matrix of the entire instrument, and the polarization calibration was performed only for the spectro-polarimeter.

6.2 Lyman-Alpha light-source

The matrix elements from the reduced response matrix can be determined by introducing a perfectly polarized light into the spectro-polarimeter and measuring the outputted polarization signal. For this purpose, a light-source unit able to provide a known polarization state at the required wavelength was needed.

6.2.1 Design of the light-source unit

The conceptual drawing of the custom Lyman-α light-source designed for the calibration is presented in Figure 6.1.

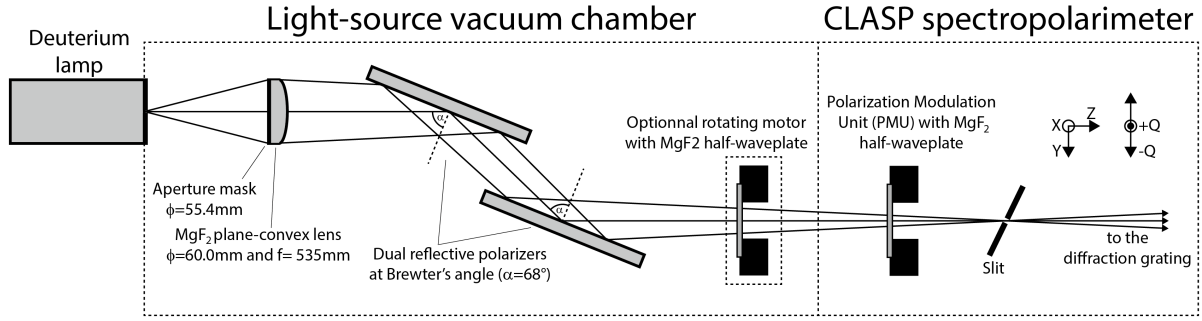

Figure 6.1: Conceptual drawing of the light-source design, as attached to CLASP spectropolarimeter. The rotating motor housing the half-waveplate or the quarter-waveplate can be removed from the light-source chamber.

This light-source is composed of a Deuterium lamp, a focusing MgF_2 lens and two polarizers. The strongest line of the lamp was the D Lyman-α line at 121.534nm, but also provided emission of the H Lyman-α at 121.567nm. The F number of the system was tuned to fit the telescope F/9.68 by placing an aperture mask with central obscuration in front of the lens ($\phi = 55.4mm$) for a resulting F/9.66. The two polarizers are flat mirrors at Brewster's angle (68°), with the same high-reflectivity coating as the two flight polarization analyzers inside of the spectro-polarimeter. The Deuterium lamp was attached to a 3-axis manipulator, not only for focusing but also for adjusting the position of the illumination on the slit. The light-source vacuum chamber was attached to the spectro-polarimeter part as shown in Figure 6.2.

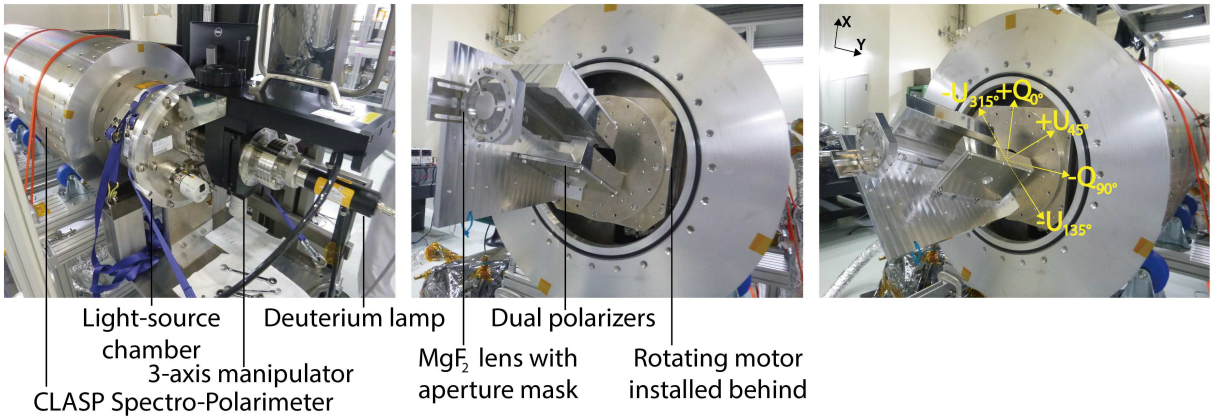

Figure 6.2: Left panel shows the Lyman-α light-source chamber with Deuterium lamp attached on CLASP spectropolarimeter. Middle panel shows the inside of the light-source chamber, with the MgF_2 lens and the two polarizers. Right panel shows the polarization input of the light-source to CLASP depending on its orientation. The subscripts refers to the orientation of the light-source. Following this notation, the light-source position in the right panel would be $+U_{45°}$, and $-Q_{90°}$ for the middle panel.

6.2.2 Optical and polarimetric performances

Figure 6.3 shows typical images taken by the slit-jaw and spectro-polarimeter cameras when the light-source illuminates the center of the slit are presented in Figure 6.3. Note that, even at best focus, the light-source spot is still large, covering more than half of the 5mm-long slit. This is due to the size of the lamp electrode (2.5mm) and to the optical aberrations of the lens. Multiple weak emission lines are seen in the spectro-polarimeter images, probably coming from residual elements in the Deuterium lamp.

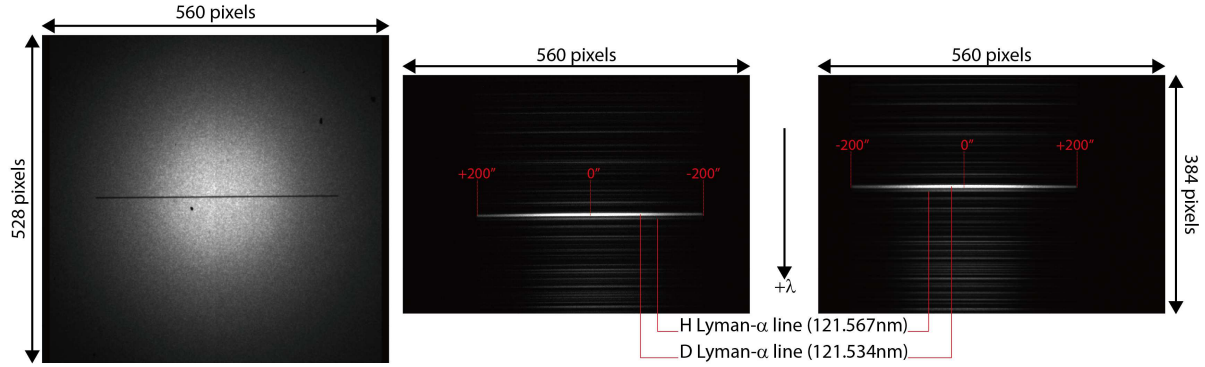

Figure 6.3: Typical images recorded by the slit-jaw (left) and spectro-polarimeter (channel 1: middle, channel 2: right) CCDs. The light-source illumination was adjusted at the center of the slit. Only a restrained portion of the spectro-polarimeter's detectors are used (560x384 pixels). Color scaling was adjusted to emphasise the intensity of the D and H Lyman-α lines.

The polarization performances of the reflection by the dual polarizers were studied with opto-polarimetric calculations, using Jones calculus to estimate the outputted polarization. The S-polarization and P-polarization reflectivity (Rs and Rp) of the SiO_2+MgF_2 coating were measured at the synchrotron facilities for the Lyman-α wavelength and at various angles of incidence (shown in Figure 6.4, and were taking into account for the calculation. Indeed, due to the MgF_2 converging lens, the rays across the pupil have different angles of incidence onto the polarizers. This effect is visually shown in Figure 6.5, where it is separated into the two extreme cases at the edge of the pupil: the meridional rays, which are contained in the plan perpendicular to the polarizer orientation and the sagital rays which are contained in the plan parallel to the polarizer orientation.

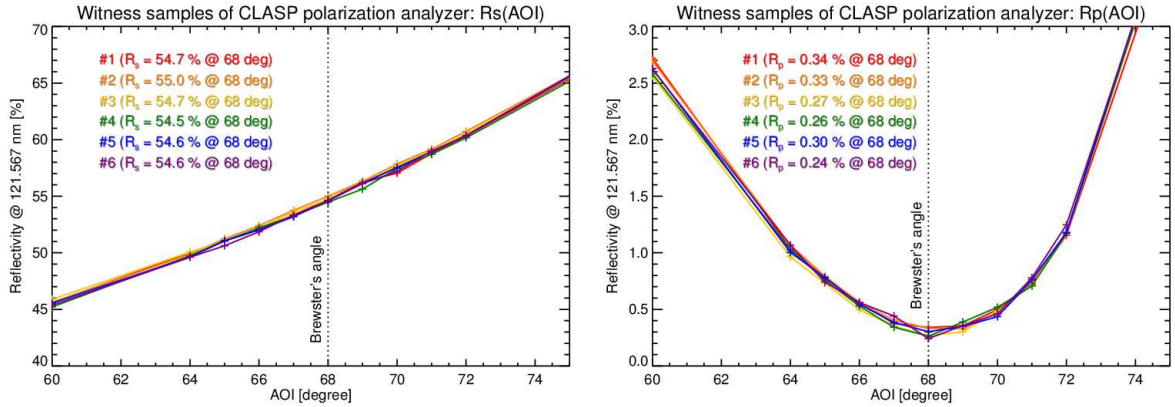

Figure 6.4: Rs (left) and Rp (right) as a function of angle of incidence (AOI) at Lyman-α wavelength for the SiO_2+MgF_2 coating, measured from six witness samples.

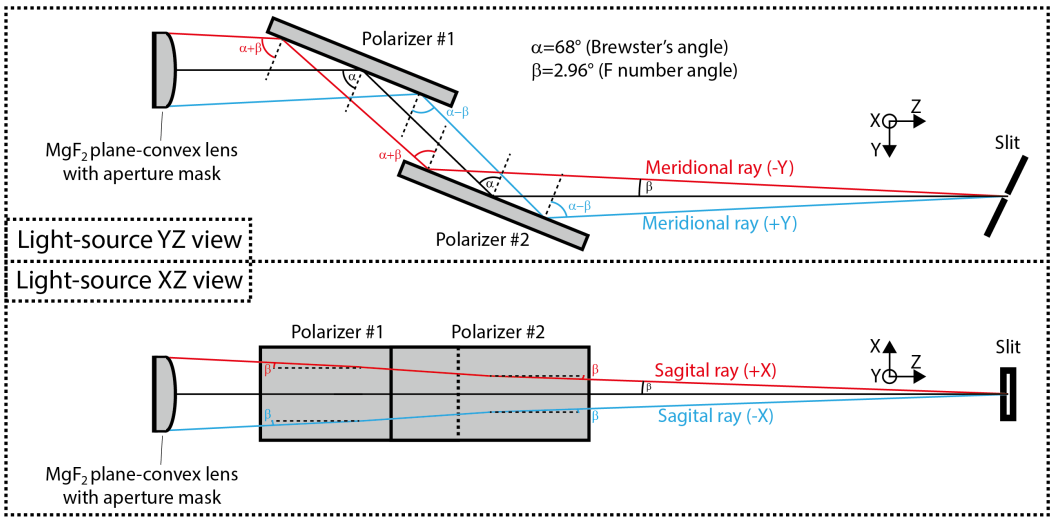

Figure 6.5: Close-up of the converging beam double-reflection by the two polarizers of the light-source. The angle α is the Brewster angle (68°) and β is F number angle (2.99°)

In the light-source configuration, the marginal rays can be defined as the meridional rays (YZ plan) and the sagital rays (XZ plan). The meridional rays are contained in the same YZ plane as the chief-ray, but have different angle of incidence on the polarizers due to the converging beam F number. Therefore, these meridional rays have a different Rs and Rp compared to the chief-ray and a gradient of polarization forms in the plane defined by these rays and the polarizers normal (Y direction in the Figure 6.5). On the other hand, the angle of incidence of the sagital rays is inclined with respect to polarizer's surface in a way which rotates the s-p axis, resulting in an rotated polarization direction with respect to the polarizer orientation.

The result at the pupil can be calculated, creating a map of the polarization after the reflection by the second polarizer for the ray's passing through the center of the slit, as shown in Figure 6.6. The aperture mask placed on the lens was considered in the calculation but the small spider-holder of the central obscuration was neglected. Note that the polarization gradient in the Y direction is very small due to the double reflection by the polarizers.

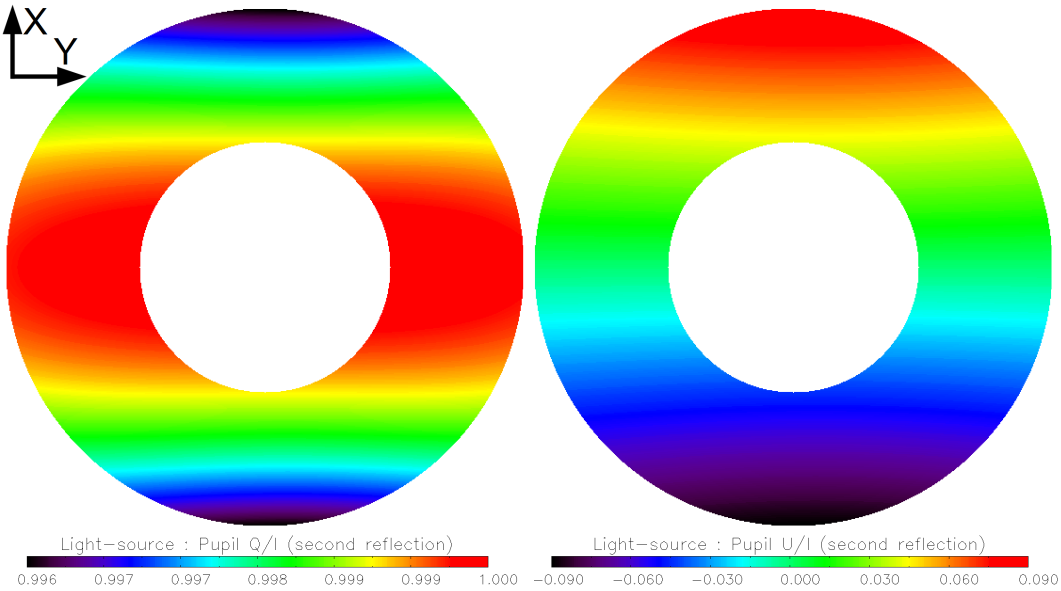

Figure 6.6: Stokes I, Q/I and U/I across the light-source pupil after the reflection by the second polarizer.

In an ideal case with perfect optics, the spot created by the light-source is expected to be point-like, and the polarization of the spot is the averaged polarization over the pupil. In this situation, the U/I (in this configuration) created by the sagital rays is cancelled out. In reality, the light-source spot is more complicated than that since the lamp electrode is not a point-like source and optical aberration from the lens also affects the image. Fully understanding how the optics affect the distribution of polarization across the spot is hard, but the polarization at the pupil indicates that the average polarization amplitude is >99.85%. The 1.5×10^{-3} difference from the perfectly polarized state could affect the estimation of the scale factor terms and were taken into account in the final error estimation. On the other hand, the polarization angle is mostly cancelled out as the spot averages the polarization across the pupil, but a residual gradient along the spot might still remained.

In addition, although the polarization might be quite uniform across the center of the spot, the inclination angle of the light rays is affected by the light-source optics: rays illuminating the top/bottom of the spot should have a different inclination angle compared to rays illuminating the center of the spot.

6.2.3 Alignment of the light-source optics

The previous calculations of the polarization at the pupil are valid only if both polarizers are exactly parallel with each other, which was controlled using theodolite measurements as shown in Figure 6.7. The reference was set using a small mirror bond onto the light-source interface plate. The angle θ and χ from Figure 6.7 around the X-axis and the Y-axis were measured as:

$$\begin{aligned} \theta'_X &= 68°00'29'' \quad \chi'_X = 67°59'52'' \\ \theta'_Y &= 00°11'19'' \quad \chi'_Y = 00°12'48'' \end{aligned} \tag{6.4}$$

The relative tilt between both polarizers was very small: only $37''$ around X axis. Tilt difference around the Y-axis was measured at $1'29''$, but the Y-axis of the polarizers was tilted from the Y axis of the LS reference mirror in this measurement. Additional measurements were performed to estimate the tilt of the polarizers around their Y-axis, hereafter Y$'$, since such tilt could induce azimuthal error in the calibration. An alignment cube (i.e. small cube with precise 90° angle and reflecting faces) was positioned on the light-source base plate at the base of each polarizers and the theodolite was used to measure the angle between each polarizers with respect to the base-plate, giving an information about the tilt around the Y-axis of the polarizers: $\theta_{Y'} = +1'22''$ and $\chi_{Y'} = +1'13''$. The measured tilt of the polarizers was introduced in the opto-polarimetric calculation, and the resulting influence on the polarization input was confirmed to be negligible.

An auto-collimator was used to measure the alignment of the light-source's polarizers to the interface plate. The auto-collimator was positioned on the left side of the light-source in Figure 6.7 and created a collimated beam in the $+Z$ direction, used to illuminate a flat mirror placed on the interface plate. Part of the collimated beam was illuminating the flat mirror after going through the two polarizers, whereas the remaining part of the collimated beam was going strait to the flat mirror. Images of both the emitted and reflected beams were imaged onto the auto-collimator display and the angle between the polarizer and the flat mirror could be deduced from the distance between the two reflected spots. The alignment of both polarizers to the interface plate was measured at $-1'1''$ around X axis and $+4'10''$ around Y-axis. Such X-tilt and Y-tilt of the polarizer's alignment represent a slight change the chief-ray's angle onto the slit and their effect on the polarization input of the light-source is negligible.

Finally, the mechanical accuracy of the pins used to align the light-source to CLASP spectro-polarimeter includes an additional $\pm\sim 2'$ error on the Z-tilt of the polarizers when attached to the spectro-polarimeter. Such possible misalignment of the light-source can only create a polarization change of $\sin \pm 2' = \pm 5 \times 10^{-4}$ in the input.

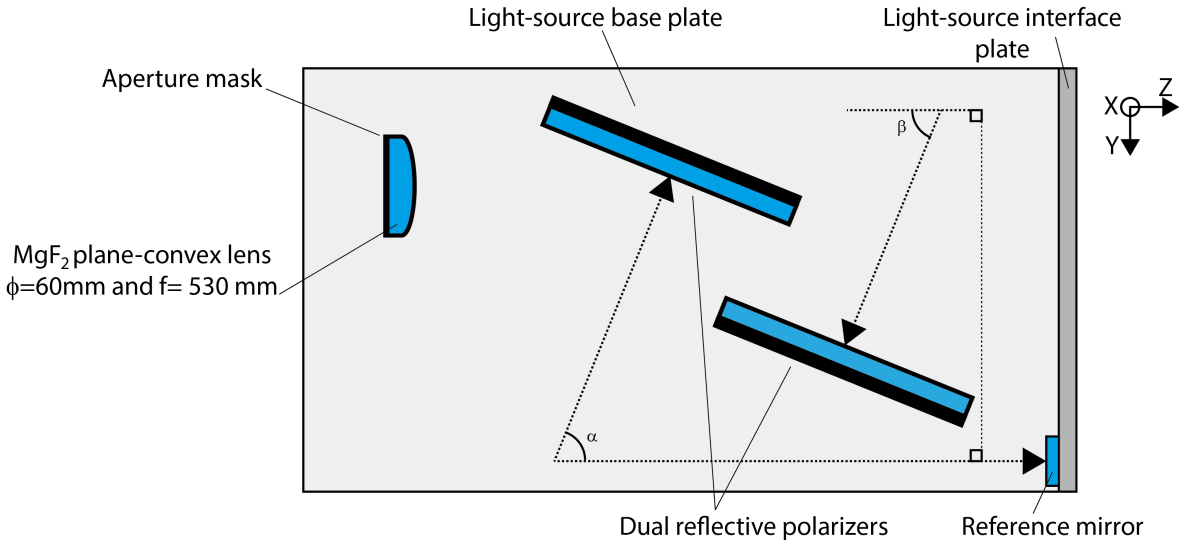

Figure 6.7: Angle measurement with theodolites (dotted lines with arrows) on the light-source polarizers with respect to the light-source interface plate.

6.2.4 Change of the polarization input

Two different methods were possible to change the orientation of the linear polarization input:

- Direct method: The polarization input can be changed by rotating the light-source (i.e. Deuterium lamp and polarizers) with respect to the spectro-polarimeter. The orientation of the light-source was controlled by mechanical pins, with a previously derived $\sim 2'$ rotational error around the Z axis. Because this method requires no optical element after the polarizers, no additional uncertainty on the polarization input is introduced. But it has the inconvenience to break the vacuum condition and alignment whenever the polarization input is changed. Rotating the light-source is also useful for confirmation of a possible polarization gradient of the light-source over the illumination (see Section 6.3.4). The right panel in Figure 6.8 shows examples of various configuration with a rotated light-source. The subscript for $-U_{135°}$ and $-U_{315°}$ inputs refers to the orientation of the light-source, one being rotated by 180° with respect to the other but both having the same $-U$ polarization state input to the spectro-polarimeter.

- Waveplate method : A half-waveplate, hereafter called LS half-waveplate, is installed in the light-source and positioned after the two polarizers. The orientation of the waveplate's principal axis and its retardance δ (182°±3°) were confirmed at the synchrotron facility beforehand. The polarization input can be changed by rotating the waveplate under vacuum with a motor. This half-waveplate is an additional optical element which could cause uncertainty in the input polarization signal, but had the advantage of performing all required polarization states without changing the light-source chamber configuration.

Because both methods have pros and cons, both were performed for the polarization calibration.

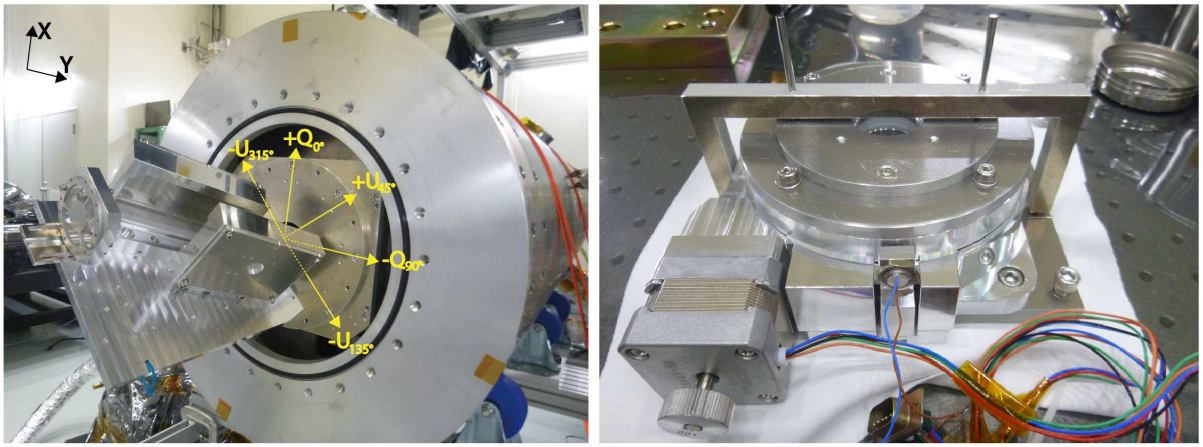

Figure 6.8: Left panel shows the different polarization states input to the spectro-polarimeter when changing the orientation of the light-source. Right panel shows the rotating motor with half-waveplate installed, used to change the polarization states without changing the orientation of the light-source. The alignment jigs with pin gauges used to set the half-waveplate fast-axis angle to the initial known position is also shown.

6.3 Preliminary investigation on the calibration measurements

6.3.1 Definition of the notation

The polarization states are defined by their Stokes parameters, in the coordinate system introduced in Figure 1.11 from Section 1.3.3. Assuming a perfect polarized light from the light-source, the $+Q$, $+U$, $-Q$ and $-U$ inputs are given as $(I, Q, U, V)^\top = (1, 1, 0, 0)^\top$, $(1, 0, 1, 0)^\top$, $(1, -1, 0, 0)^\top$ and $(1, 0, -1, 0)^\top$ in the Stokes formulas. The light-source orientation is indicated with a subscript with the angle of the light-source polarizer axis, e.g. $+Q_{0°}$ input, as shown previously in Figure 6.8. An additional notation is introduced to identify the retrieved Q'/I' and U'/I' depending on the polarization input:

- For a $\pm Q$ input, the measured $Q'/I'$is called “major term" as its value should be close to ± 1, and the measured U'/I' is called “minor term", as its should be close to zero.
- Oppositely, for a $\pm U$ input, the measured Q'/I' is the “minor term" and the measured U'/I' is the “major term".

Although this notation might seem obscure at this point, it will come handy when discussing the measurements.

6.3.2 Measurement sequence

The measurement sequence performed with each method were different:

- The measurements performed with direct method for various orientation of the light-source were recorded for one hour each. This correspond to approximatively 12000 exposures, or 3000 modulations, or 750 complete PMU rotations. Measurements were performed for the light-source in $+Q_{0°}$, $+U_{45°}$, $-Q_{90°}$ and $-U_{135°}$ positions. Additional measurements at $+Q_{180°}$ and $-Q_{270°}$ were also recorded for comparison.
- The measurements with the waveplate method were recorded for fifteen minutes for each orientation of the LS half-waveplate, which correspond to slightly more than 180 complete PMU rotations. A full rotation of the LS half-waveplate was performed for a given orientation of the light-source, resulting in 16 LS half-waveplate orientations. Hence, a measurement with the LS half-waveplate for a fixed orientation of the light-source was composed of 16 measurements of fifteen minutes acquisition each, with four times ($+Q$,$+U$,$-Q$,$-U$) inputs. Measurement were performed for the light-source in $+Q_{0°}$, $+U_{45°}$, $-Q_{90°}$ and $-U_{315°}$ positions, and also in $-Q_{270°}$ position for comparison to the measurement in $-Q_{90°}$ position.

The detailed results and analysis on these measurements will be presented in Section 6.4.

6.3.3 Non-uniformity of the PMU half-waveplate

For every set of four exposures, the polarization signals Q'/I' and U'/I' were retrieved using the demodulation scheme previously introduced in Equation (1.4) from Section 1.3.3. Note that this demodulation scheme is shown for the four first exposures of a given PMU rotation: (D_1, D_2, D_3, D_4), but also applies to the remaining exposures (D_5, D_6, D_7, D_8), (D_9, D_{10}, D_{11}, D_{12}) and (D_{13}, D_{14}, D_{15}, D_{16}). However, the measured polarization signal showed periodic fluctuations every PMU rotation at the 10^{-2} level in both Q'/I' and U'/I', as shown in Figure 6.9. These fluctuations might be due to local non-uniformity of the PMU half-waveplate retardance and/or transmissivity and/or rotation speed. To avoid errors from each modulation, the demodulation was carried out for a complete PMU rotation instead of for each individual modulation.

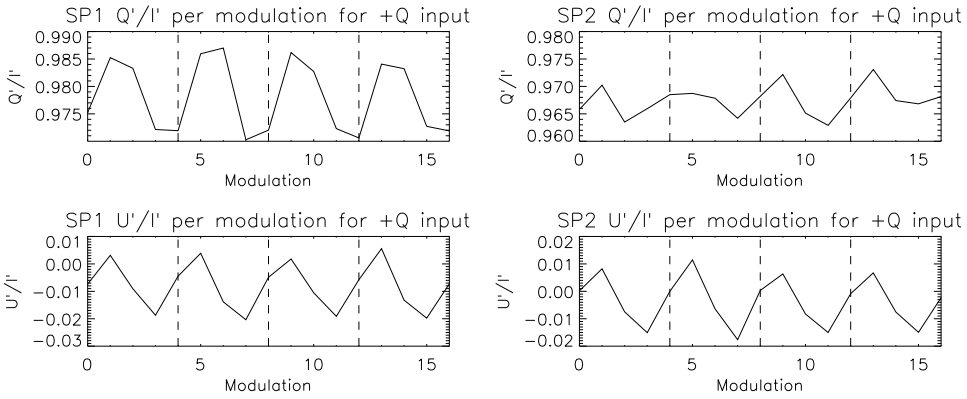

Figure 6.9: Example of Q'/I' and U'/I' demodulated for each modulation, for a $+Q$ input. Vertical dash line marks each full rotation of the PMU (i.e. four modulations).

6.3.4 Polarization gradient along the slit

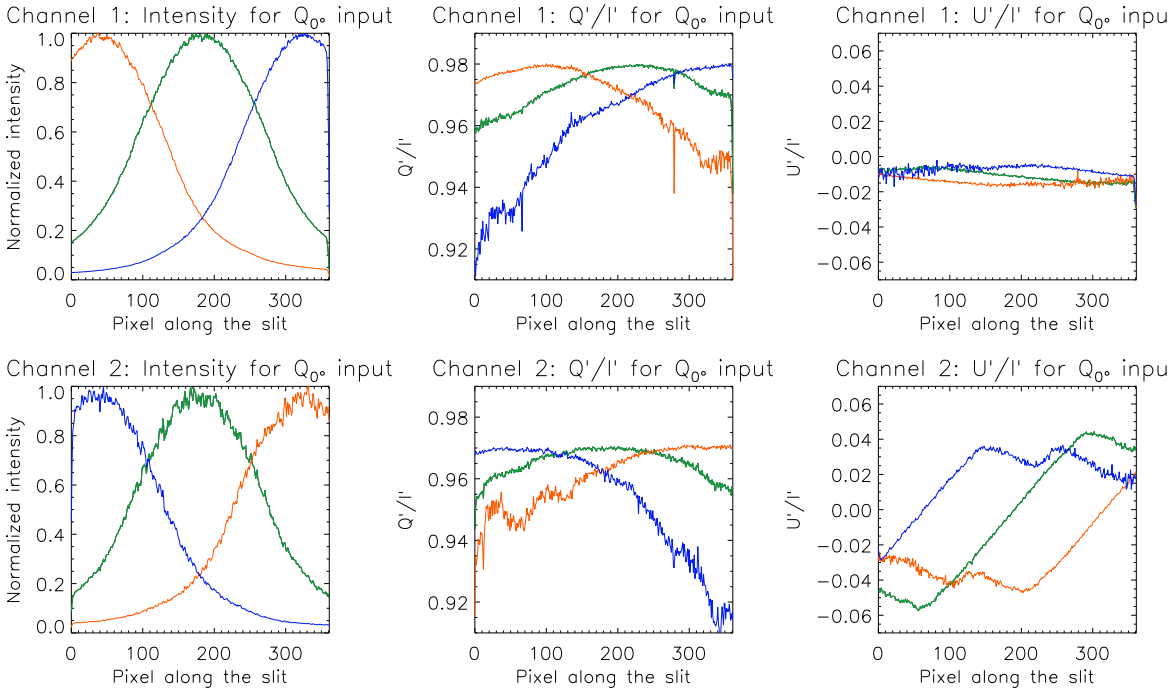

Figure 6.10: Example of Intensity (left), Q'/I' (middle) and U'/I' (right) along the slit derived after demodulation for channel 1 (top row) and channel 2 (bottom row). In this example, the input from the light-source position and half-waveplate was $+Q_{0°}$. Three measurements are presented with different positions of the illumination along the slit: in red at the bottom (-200"), in green at the center (0") and in red at the top ($+200$") of the slit. A gradient of polarization in both Q'/I' and U'/I' can clearly be seen, and is following the intensity distribution.

Figure 6.10 reveals a polarization gradient along the slit. These trends were consistently observed for the four orientations of the light-source performed during the waveplate method measurements at the center of the slit.

The quantitative shape of this gradient of polarization can be reproduced by considering that the rays forming the light-source spot onto the slit have a different average angle of incidence depending on their location along the slit, due to the light-source optics. These angles of incident are then transferred to the spectro-polarimeter's polarization analyzers and create a gradient of polarization. This effect is similar to the discussion in Section 6.2.2: since the slit is perpendicular to the orientation of the analyzer for channel 1, only a change of the angle of incidence is happening and a gradient of polarization is formed by the Rs and Rp dependency (Figure 6.4). For channel 2, the ray's angles are rotating the s-p coordinate system on the analyzer, creating a different gradient of polarization.

The observed polarization profiles along the slit were calculated (Figure 6.11) by considering a $+Q$ input beam, assuming an illumination at the center of the slit and a ray angle distribution along the slit with $\pm 2.9°$ (i.e. corresponding to the F number of the light-source), zero being the center of illumination.

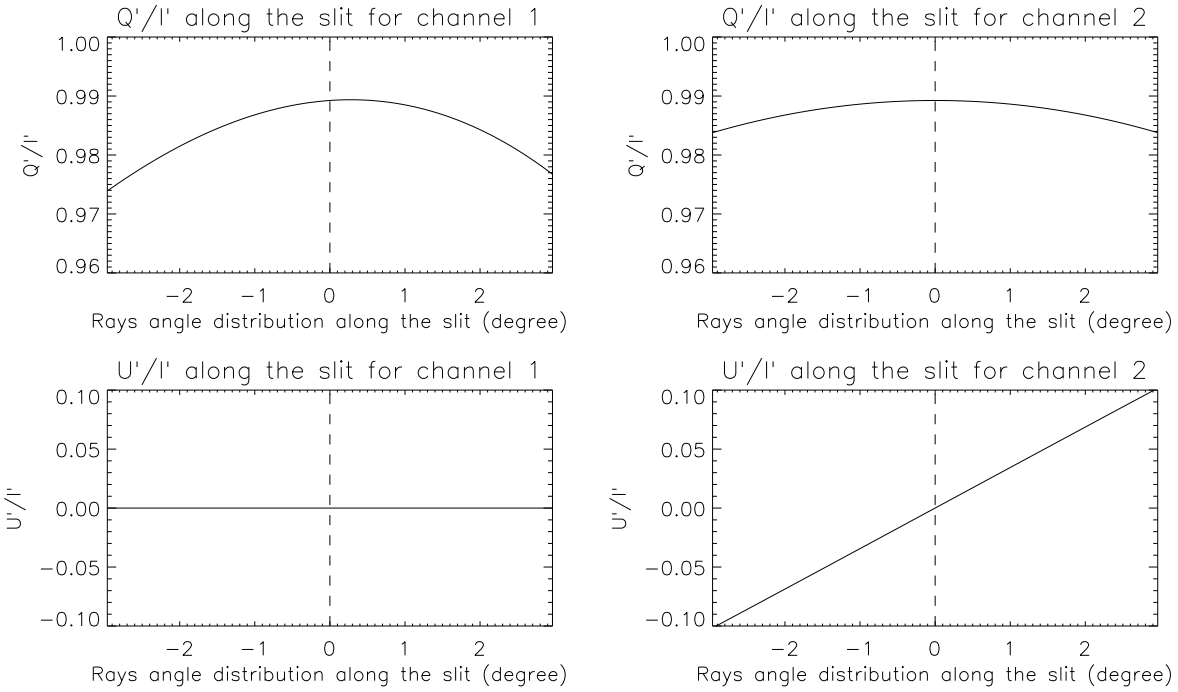

Figure 6.11: Polarization profiles observed along the slit for both channel, for a perfect $+Q$ input beam (along the slit). Dashed line shows the position of the on-axis ray (i.e. center of the illumination).

The shape of the "major term" gradient for both the channels can be reproduced by these calculations, with the "major term" maximum in channel 1 being shifted from the position of the maximum intensity (i.e. here the center of the slit). The gradient in the "minor term" of channel 2 can also be reproduced with similar order of amplitude (∼10%) considering this distribution of ray angle along the slit. The calculation couldn't reproduce the small "minor term" gradient observed in channel 1, which can be a residual "minor term" gradient created by the light-source along the polarizer axis (see Section 6.2.2), as its sign was observed to change depending on the LS orientation. The polarization in the tails of the spot's illumination could not be properly reproduced, indicating that another effect might operate, possibly a vignetting of the pupil by the grating clear-aperture for these off-axis rays.

Although the assumption of a ray angle distribution along the spot created by the lens F number is a simplification of reality, where the extended source of the Deuterium lamp and spherical aberration of the lens also play a role, this simple model quantitatively indicates that the observed polarization gradient is an artifact of the light-source rays onto the spectro-polarimeter analysers.

A tilt of all the rays including the chief-ray is introduced when moving the light-source spot to the edge of the slit. The amplitude of this tilt is ±0.27°, considering the focal length of the light-source MgF_2 lens (f=248.5mm, located at 535mm from the slit) and the slit length (l=5mm). The effect of this tilt of the rays on the light-source polarization is small, as the dual reflection by the polarizers reduces the polarization error introduced by the off-axis incidence. But this tilt does have an effect on the polarization analyzer inside the spectro-polarimeter. Channel 1 is not

affected due to its orientation, since the tilt of the rays is contained in the plan perpendicular to the analyzer orientation (meridional rays) which results only in a negligible change of the "major term". On the other hand, the tilt of the ray's angle is in the plan parallel to the analyzer for Channel 2, and creates a non-zero "minor term" at the illumination center due to the rotating the s-p coordinate. This effect was calculated as a $\pm\sim0.5°$ shift of the polarization angle at the center of illumination, directly translated to a $\pm\sim1\%$ shift in channel 2 "minor term" when moving the light-source at the edge of the field of view. This was observed in Figure 6.10, and indicates that the gradient of the azimuth error terms in channel 2 from Figure 6.20 is an artifact of the configuration used during the calibration, and is not expected to occur when the telescope feeds the spectro-polarimeter in the flight configuration, as the off-axis angle of the telescope are much smaller ($\pm$200" compared to $\pm0.27°$).

6.3.5 Polarization measurement accuracy

The measurement accuracy is mainly limited by photon noise, and should be as low as the tolerance on the spurious polarization. To improve the photon noise, spectral summing is performed in the dispersion direction at first, but only $\pm$ 4 pixels around the deuterium Lyman-α line core. There are two other ways: the summation of the intensity from several PMU rotations (i.e. temporal summation) and the summation of the intensity of several pixels along the slit (i.e. spatial summation). The appropriate number of PMU rotations and pixels to be summed spatially for reaching the 10^{-4} accuracy was estimated from a measurement taken with a $+Q$ input and composed of 180 PMU rotations, as shown in Figure 6.12. The polarization signals were retrieved for different combinations of temporal summation and spatial summation (around the intensity maximum to limit the effect of the polarization gradient), and the measurement accuracy was estimated by taking the standard deviation of the retrieved polarization signals. This method is reliable when a small number of PMU rotation is stacked, as the number of polarization values derived is large. However, the number of demodulated Q'/I' and U'/I' values is small when the large number of PMU rotations is stacked, and the standard deviation may not be reliable. As a comparison, the theoretical accuracy was calculated from the error derived for a single pixel and five PMU rotations stacking. Assuming only photon noise, this error was divided by the square root of the number of pixel summed and by the square root of the number of PMU rotations stacked. Figure 6.12 reveals that stacking more than 50 PMU rotations and spatially averaging 31 pixels bring the measurement uncertainty at the 10^{-4} level but strangely only for the "major term" (here Q'/I'), whereas the accuracy for the "minor term" (here U'/I') seems limited at 10^{-3} regardless of the intensity summing.

The limited accuracy on the "minor term" can be explained by a small change of the exposure time. Figure 6.13 shows the evolution of both the "major term" and the "minor term" during the same measurement, derived for each PMU rotation. No global trend on the "major term" appears whereas the "minor term" shows a decreasing trend. These trends indicate that the angle of the demodulated linear polarization drifts by $\sim0.15°$ over 15 minutes. Note that the effect of such rotation is clearly seen in the "minor term" since the slope of the modulation function (see Figure 1.12 from Section 1.3.3) is steeper at 0°.

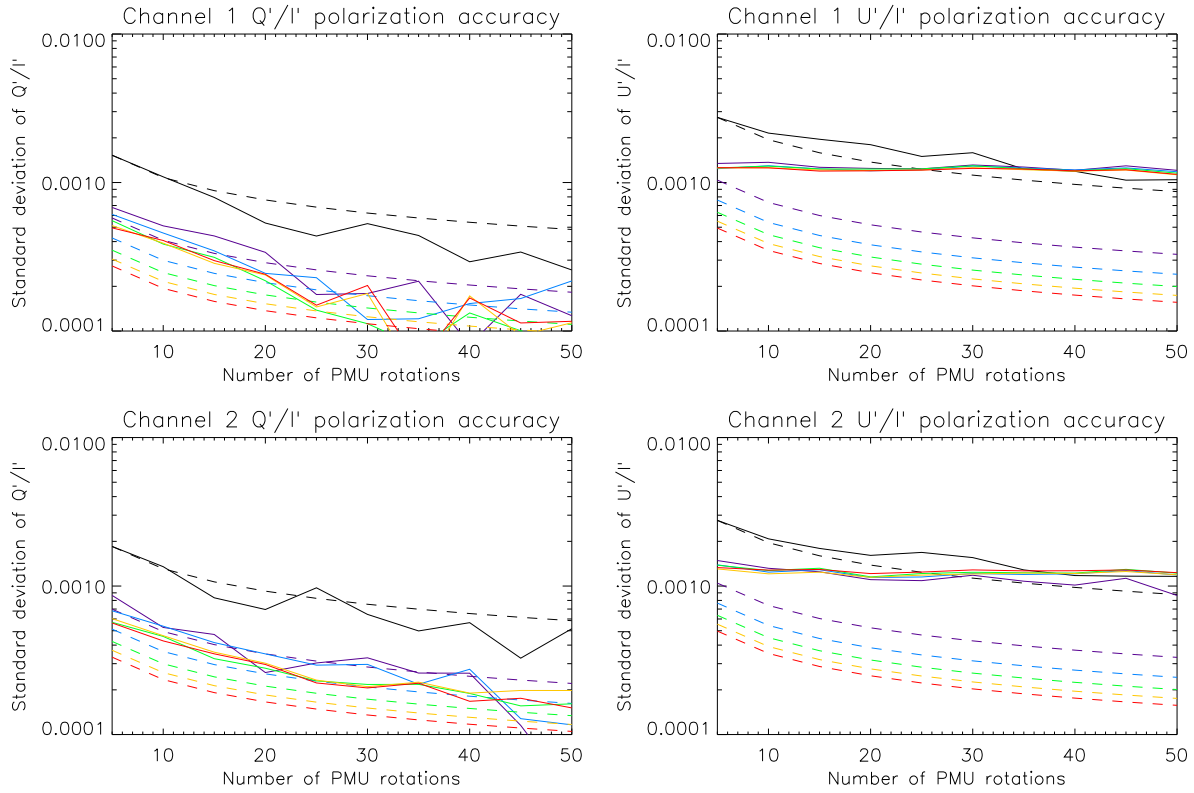

Figure 6.12: Evolution of the polarization accuracy on the Q'/I' and U'/I' measurements for different number of PMU rotation stacking and pixel summation in the spatial direction. Solid lines shows the measurements, whereas dashed lines shows the theoretical estimation of the accuracy, assuming only photon noise. Color are used for different number of pixel summed around the location of the intensity maximum: 1 pixel (black), 7 pixels (purple),13 pixels (blue), 19 pixels (green), 25 pixels (orange) and 31 pixels (red). Q'/I' was "major term" and U'/I' "minor term" as input for this measurements was $+Q_{0°}$.

The bottom panels of Figure 6.13 show the difference between the measured average exposure time and the nominal average exposure time per PMU rotation (300 ms) for both the channels, and it is found that the average exposure time decreases over time during the 15 minutes of the measurement, by up to 11.2 µs for the last PMU rotation (i.e. 16 ×0.7 µs exposure time difference per exposure). If this change of the exposure time is caused by the synchronization error between PMU trigger and camera exposures, the trend seen in the minor term (i.e. rotation of demodulated linear polarization signal) can be explained. Such synchronization error causes a misalignment between the direction of the principal axis of the PMU half-waveplate during the exposure and the PMU mechanical axis, which accumulate over time. The rate of the "de-synchronization" for the 15 minutes period can be estimated as half of the maximum shift of the average exposure time difference, 5.6 µs. The drift of the polarization angle after 15 minutes becomes ∼0.15° (2 x 5.6 µs x ∼180 PMU rotation x 360° / 4.8 s), which is consistent with the rotation of the demodulated linear polarization by 0.15°.

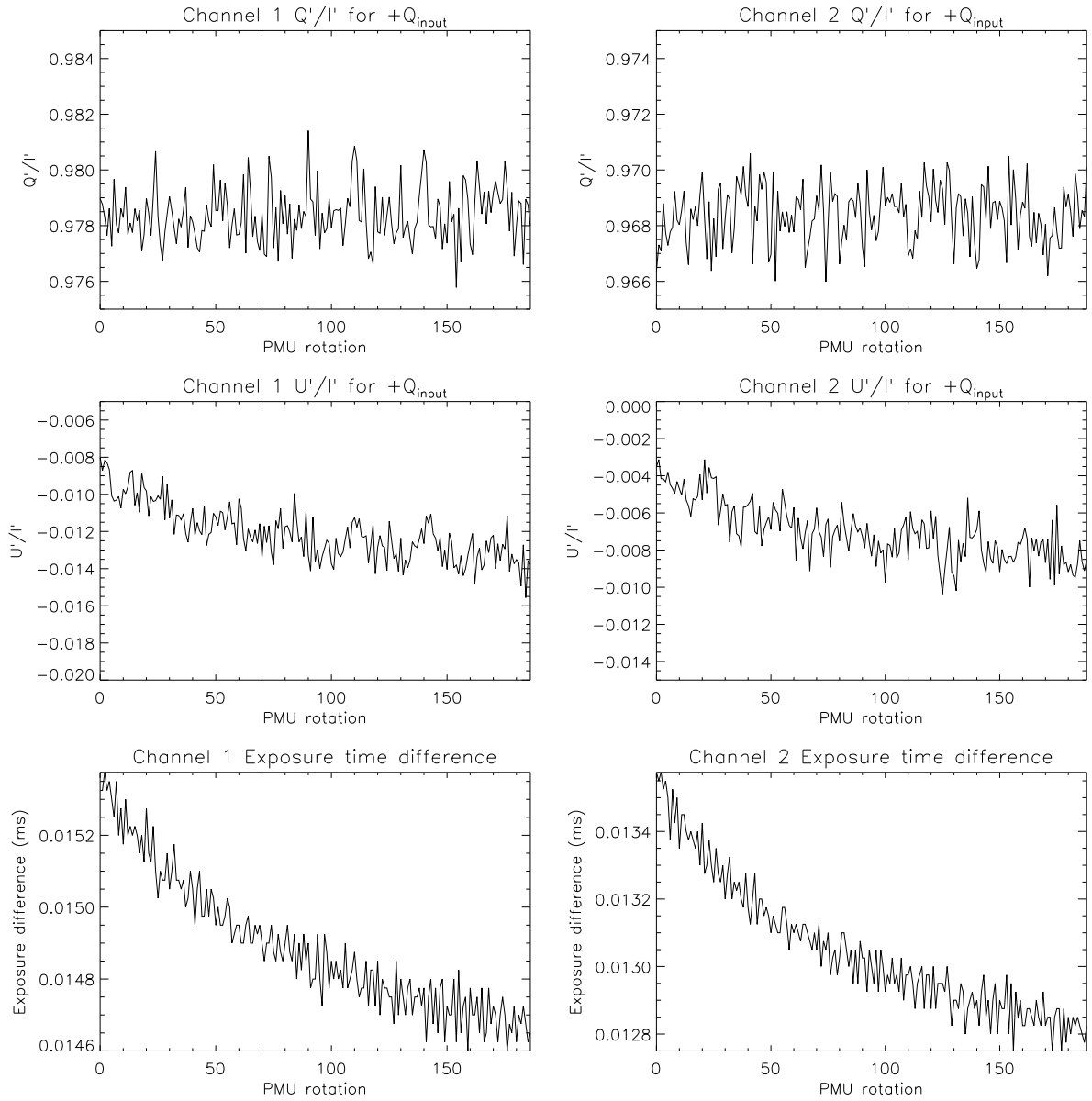

Figure 6.13: Q'/I' (left) and U'/I' (middle) retrieved for each PMU rotation. Right shows the mean exposure difference for each PMU rotation, during a 15 minutes measurements. In this example, input was $+Q$.

To wrap-it-up, Figure 6.12 suggested that the 10^{-4} accuracy of the "major term" can be safely reached by stacking 180 PMU rotations and spatially averaging over ± 15 pixels around the intensity maximum. However, it appeared that the accuracy on the "minor term" cannot be reduced below 10^{-3}.

6.3.6 Cross-talks from Q and U to I'

The contamination from Q and U to I' can be important in the polarization calibration case where almost ∼100% of the light-source intensity is polarized. For example, in case of a $+Q$ input, the measured x_{01} term should be multiplied by a factor $(1 + x_{10})$.

Determining x_{10} and x_{20} values can be done by checking the intensity changes between two measurements with opposite polarization, $+Q$ and $-Q$ for x_{10}, or $+U$ and $-U$ for x_{20}. Indeed, from Equation (6.1), one can directly obtain:

$$I' = I + x_{10}Q + x_{20}U \tag{6.5}$$

The light-source intensity, i.e. input Stokes I, is unknown. However, the assumption of a perfectly polarized light gives $Q = +I$ for a $+Q$ input, and $Q = -I$ for $-Q$ input. Hence, the following system of equations can be written for these two inputs:

$$\begin{aligned} I'_{+Q} &= I(1 + x_{10}) \\ I'_{-Q} &= I(1 - x_{10}) \end{aligned} \tag{6.6}$$

With $I'_{\pm Q}$ being the measured intensity for a $\pm Q$ input. After trivial algebra, x_{10} can be obtained as:

$$x_{10} = \left(\frac{R-1}{R+1}\right), \text{ where } R = \frac{I'_{+Q}}{I'_{-Q}} \tag{6.7}$$

The same equation is also valid for x_{20} and $\pm U$ inputs.

The amplitude of the cross-talks to I' were confirmed by using the waveplate method measurement with light-source in $+Q_{0°}$ input and the resulting x_{10} and x_{20} parameters were estimated to be of the order of 10^{-2} for both the channels, whereas x_{30} was neglected as the amount of circular polarization produced by the light-source is negligible. These cross-talks from Q and U to I' induce a 1% error on each matrix elements which, depending on the value of the matrix element, can be critical when compared to their respective tolerance. This error was taken into account for the final error estimation of the spurious polarization, scale factor and azimuth error terms.

6.3.7 Error due to the PMU rotation non-uniformity

The rotation speed of the PMU is expected to be constant. However, systematic fluctuation were recorded by the PMU driver, which produce systematic error on the half-waveplate angle at each exposure, as shown in Figure 6.14. This angle error on each exposure can be taken into account when integrating the Mueller equation from the initial angle of the half-waveplate (i.e. including the corresponding angle error) β_i to the final angle β_f (see Appendix A), and results in different scaling factors on the modulated Q and U of each exposure. The demodulated polarization signal was calculated for the mean angle error using a given PMU rotation (i.e. 16 images) taken with the light-source with $+Q_{0°}$ input. Similar calculations were also conducted for a PMU rotation with a $+U_{45°}$ input. The results were slightly different than from the simple demodulation scheme presented in Equation (1.4) but this error is already included in the elements of the response matrix. However, possible uncertainty of the angle error on each exposure (i.e. error bar in Figure 6.14) can produce an additional error on the estimated polarization signal. This $\sigma_{modulation}$ error might be important and had to be quantified.

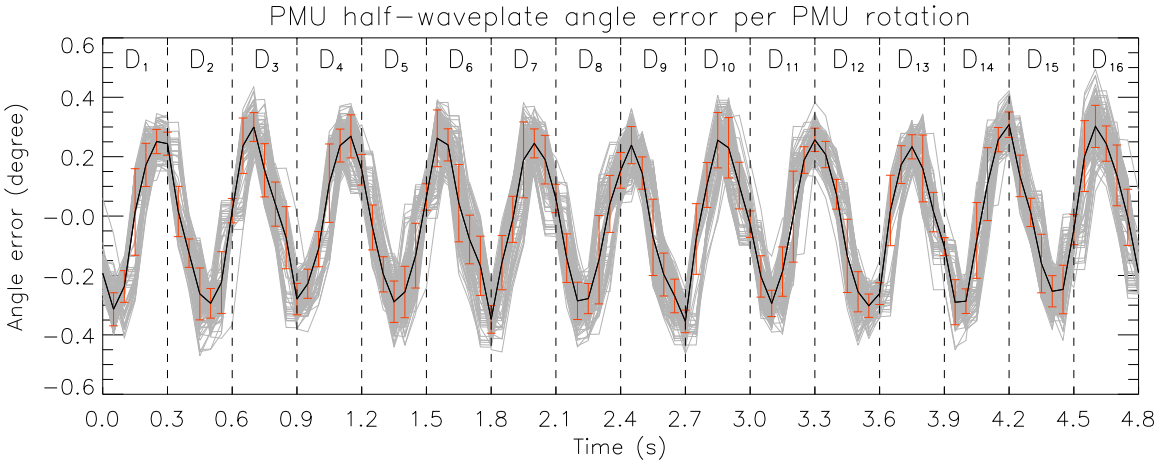

Figure 6.14: Average angle error on the PMU half-waveplate due to the non-uniform rotation speed, per full PMU rotation. Data from the PMU driver were recorded for 180 PMU rotation shows by the grey curves, and the error bar shows the standard deviation of the angle error at each point.

The $\sigma_{modulation}$ was estimated using a Monte-Carlo (MC) method: the polarization signal was demodulated by varying the angle error on each exposure for multiple trials. The angle error on each exposure was taken from the PMU driver data: assuming random fluctuation of the angle error is not correct because the consecutive angle errors are correlated (i.e. within the time-scale of the PMU feed-back loop). Hence, the angle error of 16 consecutive exposures was selected randomly along the 160 PMU rotation considered from the PMU driver data, effectively increasing the number of possibilities from 160 (i.e. PMU rotation only starting at D_1) to more than 2700 while keeping the correlation between the different angle error. The polarization signal was demodulated for each of these 2700 possibilities (i.e. N=2700).

The final $\sigma_{modulation}$ was calculated as the standard deviation out of the N polarization signal obtained with the MC method. The results per PMU rotation are dependent on the measured q' and u', and are shown in Figure 6.15. The $\sigma_{modulation}$ decreases as the square-root of the number of PMU rotation stacked when demodulating, as the angular error of the PMU tends toward the mean angle error. In case of the polarization calibration, although the $\sigma_{modulation}$ for a full polarized is close to 1.5%, 180 PMU rotation were summed for each measurement, decreasing the $\sigma_{modulation}$ to around 0.1%. In addition, since the response matrix elements were derived from 16 measurements taken at each of the four different light-source orientations in the wavelpalte method, the residual effect of the $\sigma_{modulation}$ is already included in the error from the fitting (see Table 6.3). However, in case of the direct method, the error on the polarization amplitude might be larger, explaining the 0.1% dependence of the input polarization amplitude on the light-source orientation (see Section 6.4.1). This error is expected to be of limited importance during the flight, where the input polarization is weakly polarized (<5%), although it might have to be considered when using a limited number of PMU rotations.

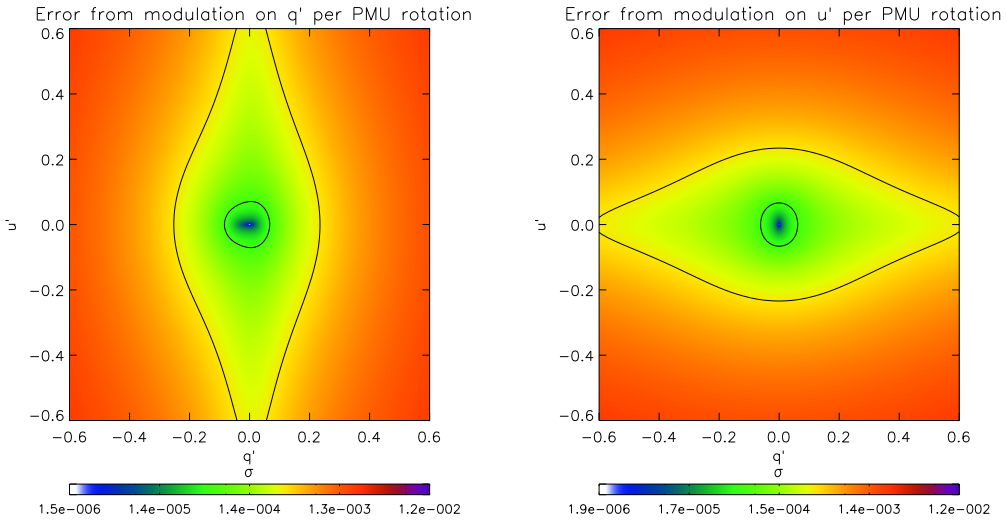

Figure 6.15: Estimated $\sigma_{modulation}$ per PMU full rotation, as a function of the measured Q/I and U/I. The two contour lines shows where the $\sigma_{modulation}$ is 0.1% (outer) and 0.01% (inner).

6.4 Experimental results of the polarization calibration

6.4.1 Measurement with direct method

Measurements were performed with the light-source in $+Q_{0°}$, $+U_{45°}$, $-Q_{90°}$ and $-U_{135°}$ inputs. In addition, two others measurements were performed at $+Q_{180°}$ and $-Q_{270°}$ for comparison with measurements at $+Q_{0°}$ and $-Q_{90°}$, as a way to exclude influence of the light-source orientation on the measurements. Each measurement was performed with illumination at the center of the slit and composed of ∼720 PMU rotations. The polarization signal was demodulated after the temporal, spatial and spectral summation as discussed in Section 6.3.5 (Figure 6.16).

Figure 6.16 clearly shows that the accuracy on the “major term" is better than on the “minor term", as previously indicated by Figure 6.12. By considering a perfect input from the light-source, the matrix elements can be analytically calculated from Equation (6.1) as:

$$\begin{aligned} x_{01} &= \frac{q'_{+Q} + q'_{-Q}}{2} \quad x_{11} = \frac{q'_{+Q} - q'_{-Q}}{2} \quad x_{21} = \frac{q'_{+U} - q'_{-U}}{2} \\ x_{02} &= \frac{u'_{+U} + u'_{-U}}{2} \quad x_{12} = \frac{u'_{+Q} - u'_{-Q}}{2} \quad x_{22} = \frac{u'_{+U} - u'_{-U}}{2} \end{aligned} \tag{6.8}$$

The notation used should be read as q'_{+Q} being the measured Q'/I' for a $+Q$ input to the spectro-polarimeter. The perfect input is an assumption, but the estimation of the light-source performances are ensuring its validity and deviation from a perfect input would only affect the scale terms (i.e. diattenuation of the light-source's polarizers) and the azimuth terms (i.e. tilt of the light-source's polarizers). Note that the spurious polarization terms could also be derived from an other expression, using the “minor term". However, this was intentionally put aside since the “minor term" showed a larger uncertainty.

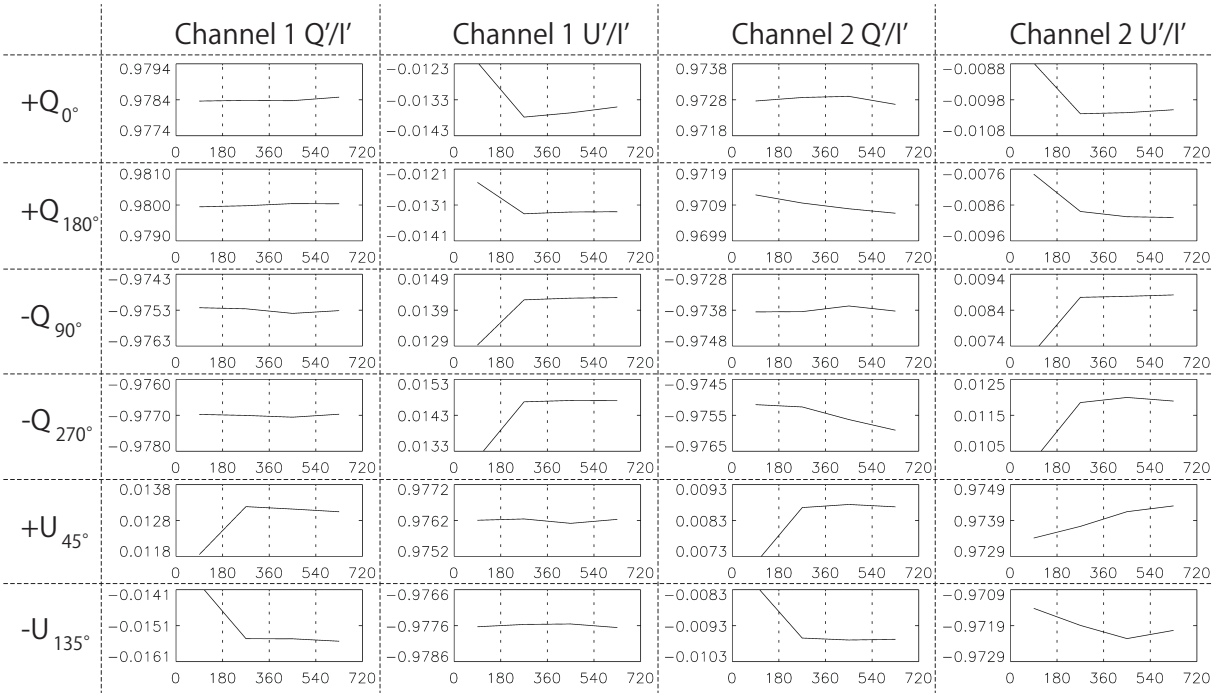

Figure 6.16: Summary of the demodulated Q'/I' and U'/I' from the measurements without the LS half-waveplate, derived every 180 PMU rotations. Vertical dashed line shows every 180 PMU rotations. First point of each plot is derived for the first 180 PMU rotations stacked, second points for the 180 PMU rotation between the 180em and 360em PMU rotations, etc. The spot was located at the center of the slit.

The combination of opposite polarization inputs shown in Equation (6.8) can be performed straightforwardly using the measurements with $+U_{45°}$ and $-U_{135°}$ inputs for x_{02}, x_{21} and x_{22}. However, multiple combinations are possible using the $+Q_{0°}$, $+Q_{180°}$, $-Q_{90°}$ and $-Q_{270°}$ inputs for x_{01}, x_{11} and x_{12}. The results of the possible four combinations are reported in Table 6.2 after averaging the polarization signal over the 720 PMU rotations.

As a result, an inconsistency larger than the tolerance (8×10^{-4}, calculated as the maximum deviation from the average) in the spurious polarization term x_{01} can be observed in Table 6.2. This is unexpected since the measurements at $+Q_{0°}$ and $-Q_{90°}$ are thought to be equivalent to the measurements at $+Q_{180°}$ and $-Q_{270°}$, respectively. On the other hand, the scale factor and azimuth error terms x_{11} and x_{12} errors are $\sim 10^{-3}$ for the different orientation of the light-source, which is acceptable compared to the tolerance. Note that errors for x_{02}, x_{22} and x_{21} cannot be discussed since only one pair of measurements was performed. A change in the “major terms" amplitude depending on the light-source orientation could create an artificial error on the spurious polarization, since those terms are derived from two “major terms" taken with different light-source orientations. However, as previously discussed, a simple tilt of the light-source around the propagation axis of the light between two measurements should not induce a significant difference in the “major terms". Therefore, it was not possible to conclude on the nature of the spurious polarization error observed from only the direct method measurements.

The same measurements were also conducted at the edge of the slit, by adjusting the position

Table 6.2: Matrix element derived from the possible combinations of the measurements without the LS half-waveplate.

Slit center (0")	Ch1 x_{01}	Ch1 x_{11}	Ch1 x_{12}	Ch2 x_{01}	Ch2 x_{11}	Ch2 x_{12}
$+Q_{0°}/-Q_{90°}$	0.00155	0.97683	-0.01358	-0.00050	0.97329	-0.00907
$+Q_{0°}/-Q_{270°}$	0.00070	0.97768	-0.01382	-0.00133	0.97413	-0.01067
$+Q_{180°}/-Q_{90°}$	0.00237	0.97765	-0.01348	-0.00142	0.97237	-0.00846
$+Q_{180°}/-Q_{270°}$	0.00152	0.97851	-0.01371	-0.00226	0.97321	-0.01005
Mean	0.00153	0.97767	-0.01365	-0.00138	0.97325	-0.00956
Error (±)	0.00084	0.00084	0.00017	0.00088	0.00088	0.00111
Tolerance (±)	0.00017	0.02000	0.01000	0.00017	0.02000	0.01000
	Ch1 x_{02}	Ch1 x_{22}	Ch1 x_{21}	Ch2 x_{02}	Ch2 x_{22}	Ch2 x_{21}
$+U_{45°}/-U_{135°}$	-0.00069	0.97689	0.01397	0.00102	0.97291	0.00879

of the light-source with the 3-axis manipulator and a similarly large error on the x_{01} spurious polarization term was observed as the expected $\pm 10^{-2}$ change in channel 2's azimuth error terms (see Section 6.3.4).

In conclusion, the accuracy on the scale factor and azimuth error terms was measured to be within the required tolerance with the direct method. However, the accuracy on the spurious polarization derived for different orientations of the light-source was around 10^{-3} and was not acceptable for the instrument requirement.

6.4.2 Measurement with the waveplate method

6.4.2.1 Measurement flow and results

Figure 6.17 summarized the measurements performed with the waveplate method, taken for four orientations of the light-source, each with complete rotation of the LS half-waveplate. The Q'/I' and U'/I' signals were obtained from the measurements after demodulation and are shown in Figure 6.18 as a function of the LS half-waveplate angle.

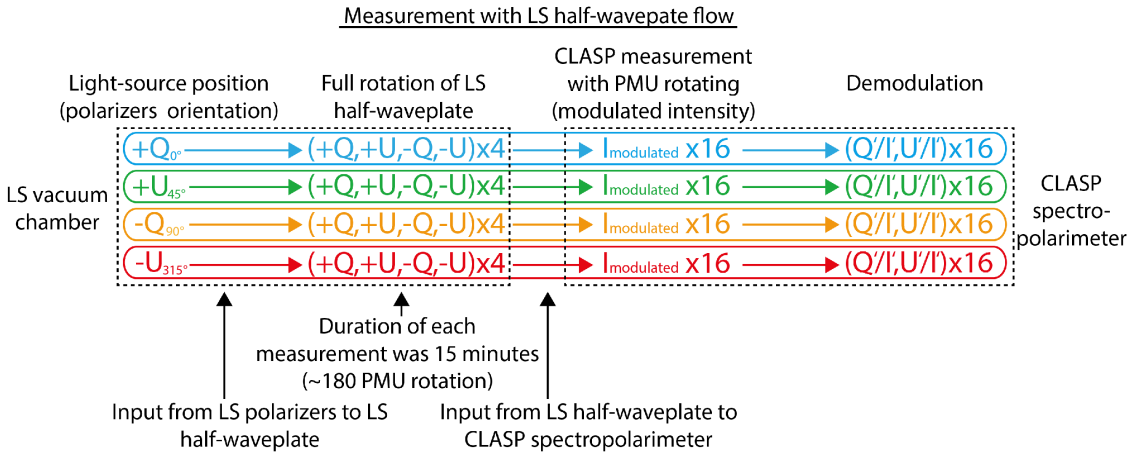

Figure 6.17: Flow chart summarizing the measurements performed with the LS half-waveplate.

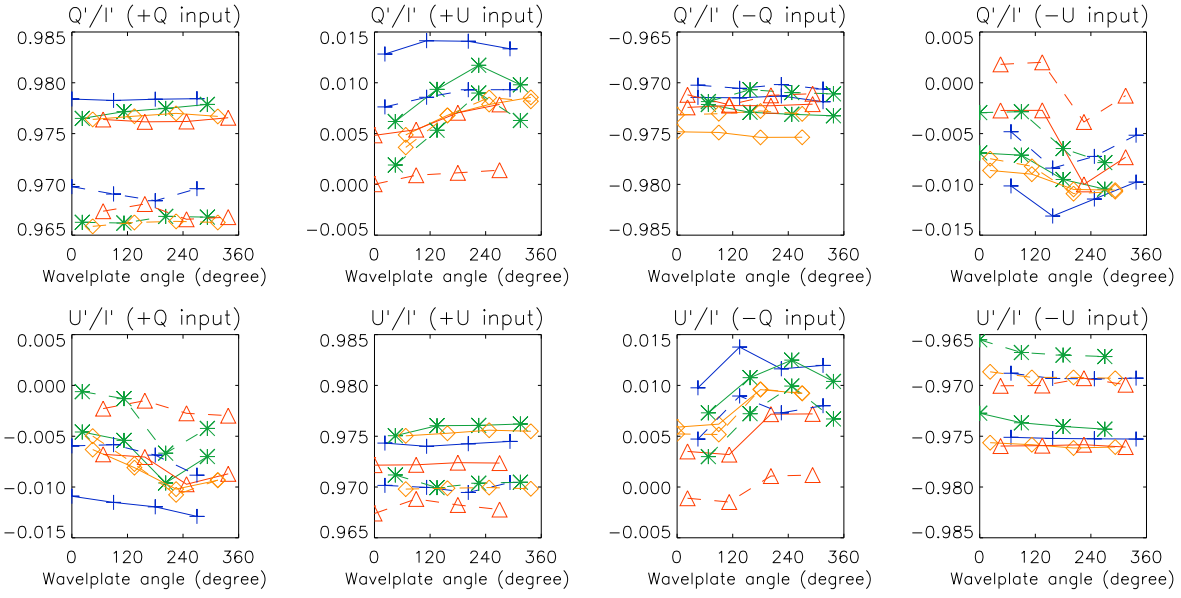

Figure 6.18: Summary of the measurement with the LS half-waveplate, as a function of the LS half-waveplate position. Solid line is for channel 1 and dashed line is for channel 2. Blue color shows the measurement for the LS in $+Q_{0^\circ}$ position, green for the LS in $+U_{45^\circ}$ position, orange for the LS in $-Q_{90^\circ}$ position and red for LS in $-U_{315^\circ}$ position.

6.4.2.2 Methodology to estimate the matrix elements

A least square fitting was used to estimate the response matrix by taking into account all the measurements. However, as seen previously, the accuracy on the "minor terms" is limited to 10^{-3} and this could affect the 10^{-4} accuracy needed on the spurious polarization. But on the other hand, these measurements cannot be ignored because they are important for determining the azimuth error terms x_{21} and x_{12}.

The solution was to use a two-steps least square fitting method. In this method, the input polarization from the light-source was a fixed parameter assumed to be perfect, but the effect of the LS half-waveplate also had to be taken into account as it affected the input polarization before entering the spectro-polarimeter. It was possible to estimate the LS half-waveplate retardance from the measurements recorded with various light-source configurations and the estimated value of 184.4°±0.4° was consistent with the previous result (182°±3°) measured prior to the polarization calibration at a synchrotron facility. This method is detailed in Section 6.4.2.3).

In the first fitting, the equations were combined to remove the spurious polarization terms, as shown in Equation (6.9). The two top equations are for the first row of the response matrix, and the two bottom equations for the second row. The subscript annotation indicates the polarization state input into the spectro-polarimeter, which were input as fixed parameters after considering the LS half-waveplate retardance. The fitting used both the "minor" and the "major" terms from the measurements to determine the scale factor and azimuth error terms.

$$\begin{aligned} q'_{+Q} - q'_{-Q} &= x_{11}(q_{+Q} - q_{-Q}) + x_{21}(u_{+Q} - u_{-Q}) \\ q'_{+U} - q'_{-U} &= x_{11}(q_{+U} - q_{-U}) + x_{21}(u_{+U} - u_{-U}) \\ \\ u'_{+Q} - u'_{-Q} &= x_{12}(q_{+Q} - q_{-Q}) + x_{22}(u_{+Q} - u_{-Q}) \\ u'_{+U} - u'_{-U} &= x_{12}(q_{+U} - q_{-U}) + x_{22}(u_{+U} - u_{-U}) \end{aligned} \tag{6.9}$$

The second fitting used only the measured "major term" to obtain the spurious polarization terms from Equation (6.10), which is derived directly from Equation (6.3). The scale factor and azimuth error terms derived from the first fitting were used as fixed parameters in the second fitting, leaving only the spurious polarization as a free parameter.

$$\begin{aligned} q'_{+Q} &= x_{01} + x_{11}q_{+Q} + x_{21}u_{+Q} \\ q'_{-Q} &= x_{01} + x_{11}q_{-Q} + x_{21}u_{-Q} \\ \\ u'_{+U} &= x_{02} + x_{12}q_{+U} + x_{22}u_{+U} \\ u'_{-U} &= x_{02} + x_{12}q_{-U} + x_{22}u_{-U} \end{aligned} \tag{6.10}$$

6.4.2.3 Estimation of the LS half-waveplate retardance

As mentioned in the previous section, the input polarization to the spectro-polarimeter is a fixed parameter for both fittings. To estimate it, the perfect input from the light-source is a good assumption. However, the effect of the LS half-waveplate also has to be taken into account, as it affected the input polarization before entering the spectro-polarimeter and can create artificial spurious polarization.

Indeed, a deviation from the perfect retardance of the LS half-waveplate (δ=180°) could affect the estimation of the spurious polarization terms depending on the position of the light-source and on the LS half-waveplate orientation. This can be understood as the spurious polarization terms are derived from the (q'_{+Q},q'_{-Q}) pair of measurements for the x_{01} term and from the (u'_{+U},u'_{-U}) pairs of measurements for the x_{02} term. In a configuration with the light-source at $+Q_{0°}$, the LS half-waveplate would affect the inputs in different ways depending of the position of its principal-axis: $+Q$ input would not be affected by the LS half-waveplate because the principal-axis is aligned with the polarization direction, i.e. full transmission. On the other hand, q'_{-Q} would be multiplied by $\cos\delta$ due to the angle between the LS half-waveplate principal-axis and the polarization direction of the light-source (±45°). Finally, the angle between the half-waveplate's principal-axis and the polarization direction is the same for both u'_{+U} and u'_{-U} positions (±22.5° both) and therefore the factor affecting both of them is the same: $(1-\cos\delta)/2$. Hence, the x_{02} terms would not be affected by the LS half-waveplate retardance, as the same factor affecting both measurement would cancel out. However, x_{01} would be affected, as the retardance of the waveplate affects differently the q'_{+Q} and q'_{-Q} measurements.

The LS half-waveplate retardance was determined from the measurements recorded with the waveplate method in $+Q_{0°}$ and $+U_{45°}$ configurations, by applying the two-steps fitting method for various value of the LS half-waveplate retardance. Changing the retardance imply changing the input polarization state (fixed parameter of each fitting), and therefore having different effect on the resulting spurious polarization terms depending on the light-source orientation, as previously explained. Results can be seen in Figure 6.19, where for the $+Q_{0°}$ position, the x_{02} term appears to be almost insensitive to the LS half-waveplate retardance, only varying at the 10^{-5} level. On the other hand, the x_{01} terms have a much higher dependency with the retardance. As expected, this effect is opposite when the light-source is in the $+U_{45°}$ position, with x_{01} being insensitive and x_{02} being affected by the retardance. With these measurements, it is possible to estimate the LS half-waveplate retardance by reading the retardance when the matrix elements is dependant for the value of this matrix elements when it is unaffected. For example in Figure 6.19, x_{01} term for channel 1 is unaffected by the LS halfwaveplate retardance when the light-source is in $+U_{45°}$ position, with average value around 2.19×10^{-3}. The retardance of the LS half-waveplate can be obtained by reporting this value in the x_{01} measurement with light-source in $+Q_{0°}$ position, giving δ around 184.1°. Similarly, the measurements at $+U_{45°}$ gives around δ=184.8°, leading to the LS half-waveplate retardance estimated at 184.4°±0.4°.

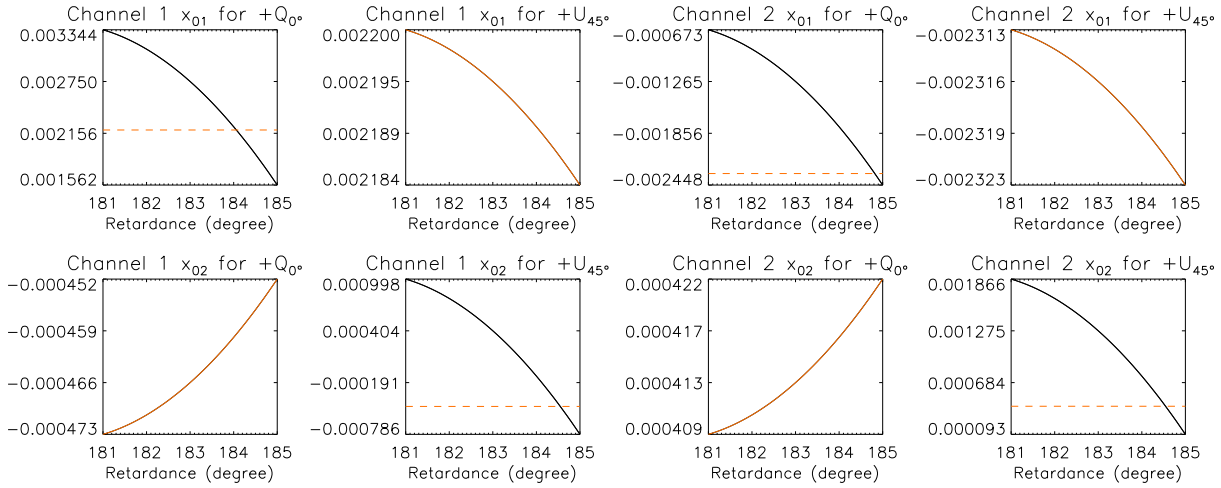

Figure 6.19: Resulting spurious polarization terms after fitting when the input polarization varied by changing the retardance of the LS half-waveplate. Light-source positions were $+Q_{0^\circ}$ and $+U_{45^\circ}$. Red solid lines indicated when the matrix elements are determined independently of the half-waveplate retardance, with dashed line indicating their value on the corresponding matrix elements dependant on the half-waveplate retardance.

6.4.2.4 Matrix elements

Results for the four positions of the light-source were obtained using the two-steps fitting method and are shown in Table 6.3. The error was estimated as the maximum deviation from the average value. The azimuth terms have a larger variation than the other terms, probably because these terms are more sensitive to the misalignment of the input polarization (e.g. position of the half-waveplate's principal-axis) between two measurements due to the positional accuracy of the LS rotating motor. Nevertheless, the variation of all matrix elements were well within their respective tolerances, except for the spurious polarization term for Stokes Q in channel 2, x_{01}, which was slightly larger.

Table 6.3: Response matrix elements at the center of the slit derived with the two independent least square fitting method for four positions of the light-source. Top table is for channel 1 and bottom table is for channel 2. Error was derived as the maximum difference from the average value.

Channel 1	x_{01}	x_{11}	x_{21}	x_{02}	x_{12}	x_{22}
Light-source $+Q_{0^\circ}$ input	0.00198	0.97639	0.01238	-0.00046	-0.01182	0.97618
Light-source $+U_{45^\circ}$ input	0.00219	0.97649	0.00890	-0.00037	-0.00846	0.97620
Light-source $-Q_{90^\circ}$ input	0.00223	0.97735	0.00836	-0.00030	-0.00812	0.97708
Light-source $-U_{315^\circ}$ input	0.00204	0.97573	0.00599	-0.00040	-0.00667	0.97555
Mean	0.00211	0.97649	0.00891	-0.00038	-0.00877	0.97625
Error ($\pm$)	0.00013	0.00086	0.00347	0.00008	0.00305	0.00082
Tolerance ($\pm$)	0.00017	0.02000	0.01000	0.00017	0.01000	0.02000

Channel 2	x_{01}	x_{11}	x_{21}	x_{02}	x_{12}	x_{22}
Light-source $+Q_{0^\circ}$ input	-0.00203	0.97123	0.00757	0.00042	-0.00707	0.97103
Light-source $+U_{45^\circ}$ input	-0.00232	0.97027	0.00534	0.00051	-0.00496	0.96998
Light-source $-Q_{90^\circ}$ input	-0.00198	0.97103	0.00807	0.00037	-0.00777	0.97091
Light-source $-U_{315^\circ}$ input	-0.00211	0.97073	0.00059	0.00055	-0.00115	0.97037
Mean	-0.00211	0.97081	0.00539	0.00046	-0.00524	0.97057
Error ($\pm$)	0.00021	0.00055	0.00480	0.00009	0.00409	0.00059
Tolerance ($\pm$)	0.00017	0.02000	0.01000	0.00017	0.01000	0.02000

The response matrix was also derived at the edges of the slit from two measurements in the light-source configurations $+Q_{0^\circ}$ and $+U_{45^\circ}$. Average matrix elements as a function of slit position (bottom, center and top) are shown in Figure 6.20. Measurements at the edge of the slit were essentially consistent with those at the center of the slit, within their respective tolerance. The azimuth error terms for Channel 2 show a consistent gradient significantly larger than the previously derived measurement error ($\pm 10^{-2}$ compared to $\pm 10^{-3}$), even though this gradient is still within the $\pm 10^{-2}$ tolerance. This was expected to be artificially created by the light-source optics (see Section 6.3.4).

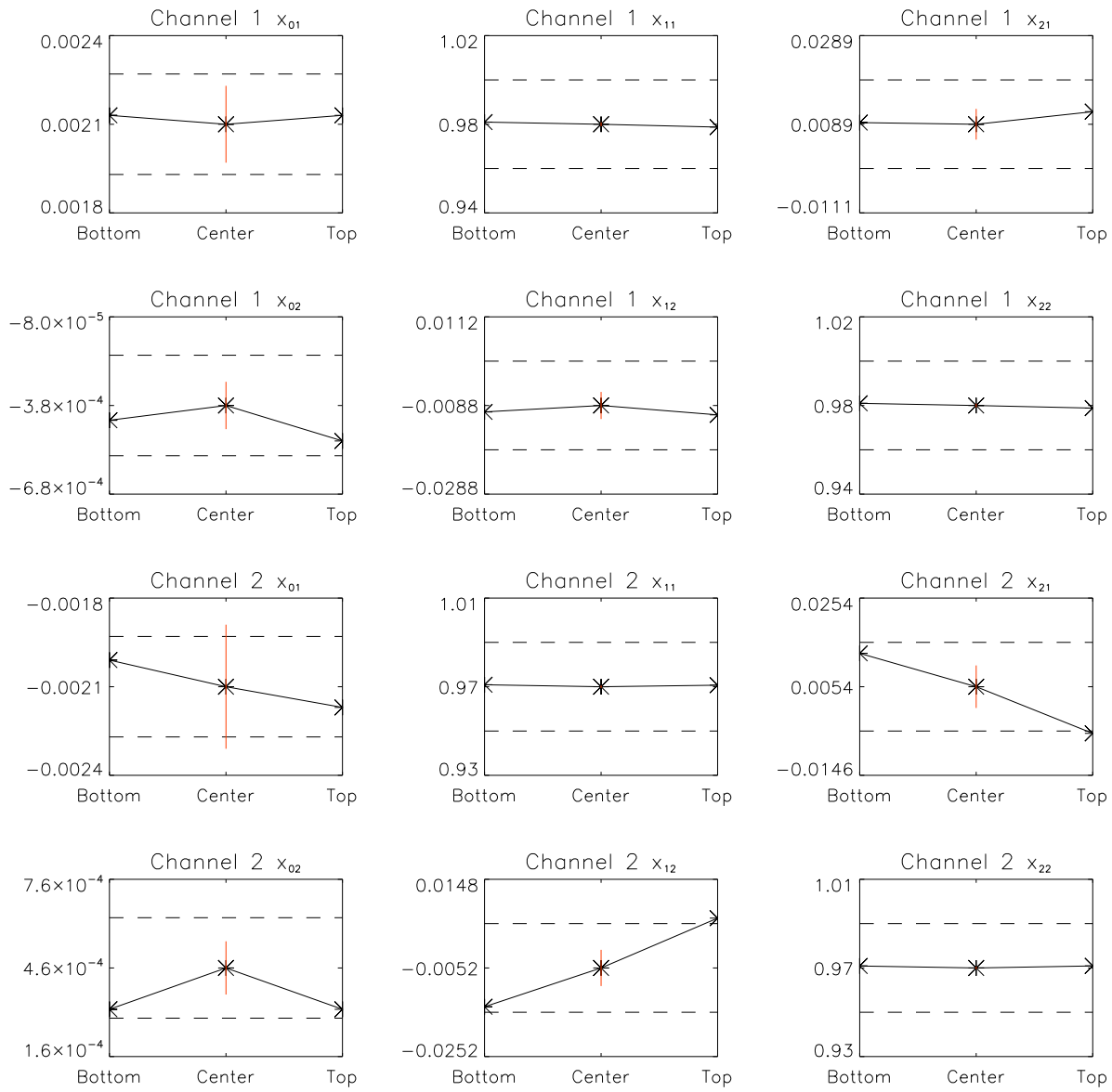

Figure 6.20: Matrix elements along the slit for channel 1 (top two rows) and channel 2 (bottom two rows). Horizontal dash lines shows the respective tolerance of each matrix elements, centred on the measurement at the center of the slit. Vertical line shows the error, derived only for the measurement at the center of the slit.

6.4.2.5 Effect of the light-source orientation

The effect of the light-source orientation onto the spurious polarization was checked by taking an additional measurement with the light-source in $-Q_{270°}$ and comparing it to the measurement taken with light-source at $-Q_{90°}$. For this measurement, only half-rotation of the LS half-waveplate was performed. Figure 6.21 shows the result of the measurement at $-Q_{270°}$, compared with the corresponding measurement at $-Q_{90°}$. The matrix elements derived for the measurement at $-Q_{270°}$ are shown in Table 6.4, as well as those for light-source at $-Q_{90°}$ position, recomputed for only the corresponding half-rotation.

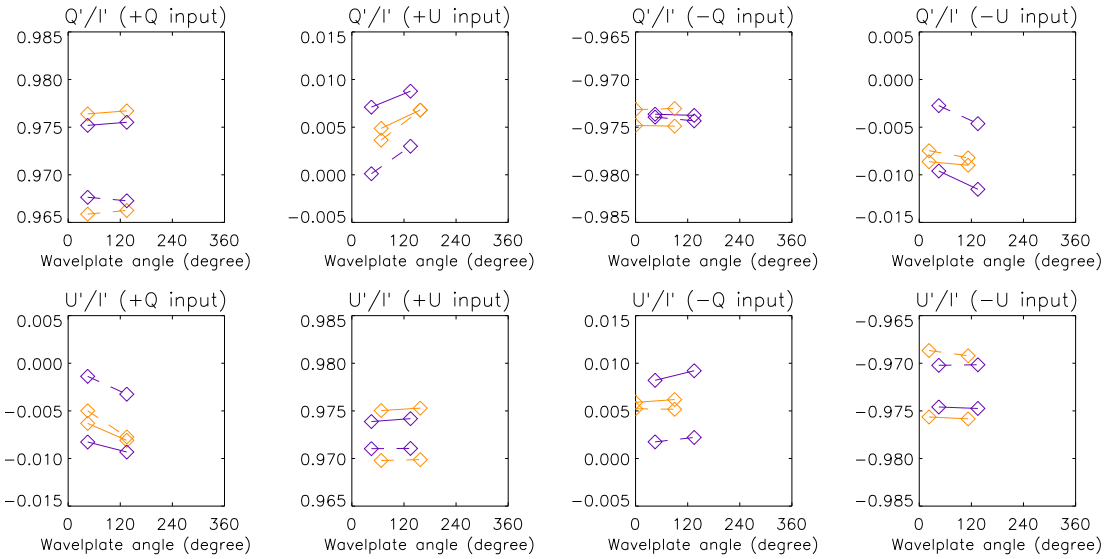

Figure 6.21: Comparison of Q'/I' and U'/I' for the measurements with light-source in $-Q_{90°}$ position (orange) and $-Q_{270°}$ (purple), for channel 1 (solid line) and channel 2 (dashed line), at the center of the slit.

Table 6.4: Response matrix elements at the center of the slit derived for the measurements taken with light-source at $-Q_{90°}$ and $-Q_{270°}$.

	x_{01}	x_{11}	x_{21}	x_{02}	x_{12}	x_{22}
Channel 1 LS $-Q_{90°}$ input	0.00228	0.97716	0.00733	-0.00030	-0.00663	0.97689
Channel 1 LS $-Q_{270°}$ input	0.00226	0.97596	0.00926	-0.00033	-0.00876	0.97579
Channel 2 LS $-Q_{90°}$ input	-0.00209	0.97101	0.00654	0.00044	-0.00579	0.97082
Channel 2 LS $-Q_{270°}$ input	-0.00191	0.97223	0.00262	0.00042	-0.00215	0.97205

Table 6.4 confirms that the position of the light-source does not influence the spurious polarization significantly. On the other hand, scale factor terms are affected at the 10^{-3} level by the orientation of the light-source. Azimuth error terms are also changed by 2×10^{-3}, which is within its tolerance and the previously derived accuracy. In conclusion, these measurements with waveplate method confirmed that the large error on the spurious polarization measured with the direct method were created artificially by a change of the "major terms" depending on the light-source orientation.

6.4.3 Measurement with the LS quarter-waveplate

Cross-talks from Stokes V were checked by replacing the LS half-waveplate by a quarter-waveplate. The light-source was installed in a $+Q_{0^\circ}$ configuration, and the quarter-waveplate's principal-axis was oriented at $+45^\circ$ and -45° from the light-source polarization direction in order to input Stokes $+V$ and $-V$, respectively. The measured Q'/I' and U'/I' showed a periodicity every half-rotation of the PMU half-waveplate, with amplitude around 5×10^{-3}. These fluctuations were due to the PMU half-waveplate properties (i.e. residual modulation of Stokes V every half-rotation if δ is not exactly 180°). Averaging for a complete PMU rotation cancels this residual modulation, and combining both measurements at $+V$ and $-V$ removes the influence of the spurious polarization, only leaving the cross-talks $V\rightarrow Q'$ in Q'/I' and $V\rightarrow U'$ in U'/I'. The matrix elements x_{31} and x_{32} were derived at the center and edges of the slit by applying with the same spatial and temporal integrations as for the LS half-waveplate measurements, and are shown in Figure 6.22. Stokes V cross-talks were measured below 10^{-2}, which meet the required tolerance. Note that the absolute sign of the x_{31} and x_{32} terms is unknown because the difference between the fast-axis and slow-axis of the quarter-waveplate was not made experimentally beforehand.

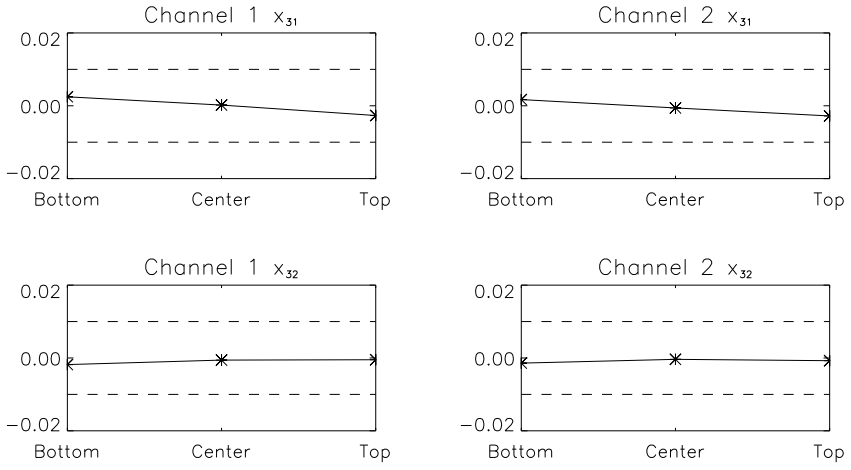

Figure 6.22: x_{31} and x_{32} matrix elements along the slit for channel 1 and channel 2. Horizontal dash lines shows the respective tolerance of each matrix elements, centered on the measurement at the center of the slit.

6.4.4 Final response matrix

The final response matrix at the center of the slit for both the channels was created by combining results from both measurement methods. The spurious polarization terms were taken from the measurements with the waveplate method, as they could be determined within the tolerance only from this method. The scale factor and azimuth error terms were taken from the direct method results, to avoid additional error due to the LS half-waveplate. The number of digit was rounded to the same order as the measured error.

$$\begin{aligned} X_{Channel1} &= \begin{pmatrix} x_{01} & x_{11} & x_{21} \\ x_{02} & x_{12} & x_{22} \end{pmatrix} = \begin{pmatrix} 0.0021 & 0.978 & 0.014 \\ -0.0004 & -0.014 & 0.977 \end{pmatrix} \\ X_{Channel2} &= \begin{pmatrix} x_{01} & x_{11} & x_{21} \\ x_{02} & x_{12} & x_{22} \end{pmatrix} = \begin{pmatrix} -0.0021 & 0.973 & 0.009 \\ 0.0005 & -0.010 & 0.973 \end{pmatrix} \end{aligned} \tag{6.11}$$

A summary of the achieved accuracy at the center of the slit compared to the tolerance is given in Table 6.5. In this estimation, the measurement errors derived from the waveplate method were taking into account. This is a safe overestimation of the error on the scale factor and azimuth error terms from the direct method, as this measurement error also includes the effect of the LS half-waveplate. For each term, the error due to the cross-talks from Q and U to I' was calculated as 1% of the corresponding matrix elements value, as discussed in Section 6.3.6. The uncertainty on the polarization input due to the light-source orientation were estimated from the measurement performed with two opposite orientation of the light-source (see Section 6.4.2.5), for the scale factor and azimuth error. Finally, the possible error on the light-source degree of polarization (i.e. deviation from a perfectly polarized state, based on the pupil calculation) were also considered for the scale factor. The total error was computed as the root sum square (RSS) of all the components.

6.4.5 Discussion on the measured response matrix

In an ideal case with a perfect response matrix, the spurious polarization terms and azimuth error terms should be zero, i.e. no cross-talks between Stokes parameters, and the scale factor terms should be unity, meaning a perfect transmission of the polarization amplitude. However, the response matrix elements shown in Equation (6.11) are different from a theoretically perfect response matrix.

6.4.5.1 Scale factor terms

The scale factor terms can be partially explained with the same explanation as shown in Section 6.3.6: a non-zero Rp at the Brewster's angle would decrease the amplitude of the polarization signal. The estimation doesn't fully account the observed scale factor terms (only $\sim$0.98), but additional possibilities such as diattenuation at the mirror's coatings or non-180° retardance of the PMU half-waveplate are also included in the measured scale factors.

6.4.5.2 Azimuth terms

The azimuth error terms were measured around 1.3×10^{-2} for channel and slightly smaller for channel 2, with opposite signs for x_{21} and x_{12}. Although the uncertainty is close to 5×10^{-3} and is probably due to misalignment of the LS half-waveplate and/or polarizers, the values of both x_{21} and

Table 6.5: Achieved accuracy on each matrix elements at the center of the slit.

Channel 1	x_{01}	x_{02}	x_{11}	x_{22}	x_{12}	x_{21}
Measurement	1.3×10^{-4}	8.0×10^{-5}	8.6×10^{-4}	8.2×10^{-4}	3.1×10^{-3}	3.5×10^{-3}
Light-source orientation	–	–	$\sim10^{-3}$	$\sim10^{-3}$	$\sim2\times10^{-3}$	$\sim2\times10^{-3}$
Light-source input	–	–	1.5×10^{-3}	1.5×10^{-3}	–	–
x_{10}/x_{20} error	2.1×10^{-5}	3.8×10^{-6}	9.8×10^{-3}	9.8×10^{-3}	1.4×10^{-4}	1.4×10^{-4}
Total (RSS)	1.3×10^{-4}	8.9×10^{-5}	1.0×10^{-2}	1.0×10^{-2}	3.7×10^{-3}	4.0×10^{-3}
Tolerance	1.7×10^{-4}	1.7×10^{-4}	2.0×10^{-2}	2.0×10^{-2}	1.0×10^{-2}	1.0×10^{-2}

Channel 2	x_{01}	x_{02}	x_{11}	x_{22}	x_{12}	x_{21}
Measurement	2.1×10^{-4}	9.0×10^{-5}	5.5×10^{-4}	5.9×10^{-4}	4.1×10^{-3}	4.8×10^{-3}
Light-source orientation	–	–	$\sim10^{-3}$	$\sim10^{-3}$	$\sim2\times10^{-3}$	$\sim2\times10^{-3}$
Light-source input	–	–	1.5×10^{-3}	1.5×10^{-3}	–	–
x_{10}/x_{20} error	2.1×10^{-5}	3.8×10^{-6}	9.7×10^{-3}	9.7×10^{-3}	1.0×10^{-4}	1.0×10^{-4}
Total (RSS)	2.1×10^{-4}	9.8×10^{-5}	9.9×10^{-3}	9.9×10^{-3}	4.6×10^{-3}	5.2×10^{-3}
Tolerance	1.7×10^{-4}	1.7×10^{-4}	2.0×10^{-2}	2.0×10^{-2}	1.0×10^{-2}	1.0×10^{-2}

x_{12} is similar for each measurement with opposite signs, which might indicate that some residual azimuthal error is present in the system. This can be explained considering a misalignment of the fast-axis for the PMU half-waveplate with respect to the $+Q$ direction. Indeed, the orientation of the PMU half-waveplate's principal-axis was adjusted experimentally to be parallel with the Stokes $+Q$ direction, which is the position where the first exposure always starts. However, the residual angle error on the fast-axis was measured a $+0.08°$ after adjustment. This residual was smaller than the tolerance ($\pm0.2°$) for the PMU half-waveplate alignment but could still produce systematic azimuthal error in the measurements.

A misalignment of the PMU half-waveplate's principal-axis with respect to the $+Q$ direction can be represented as a small angle shift Δ in the Mueller equation of the instrument (see Equation (A.4) and Equation (A.5) from Appendix A). Considering the retardance of the PMU half-waveplate δ as 180°, the Stokes Q, U and I can be obtained from the Mueller equations as:

$$\begin{aligned} Q' &= \Big[Q\cos 4\Delta + U\sin 4\Delta\Big] \\ U' &= \Big[-Q\sin 4\Delta + U\cos 4\Delta\Big] \end{aligned} \tag{6.12}$$

Equation (6.12) shows that the measured Stokes I is not affected by a misalignment of the PMU half-waveplate. However, a cross-talks between Stokes Q and U is introduced. Taking $\Delta = +0.08 \pm 0.05°$, and considering a perfect polarized input of the light-source to the spectro-polarimeter, the measured Q'/I' would be proportional to $\cos 4\Delta \sim 1$ and U'/I' to $-\sin 4\Delta \sim$

-0.006 which is comparable to the measured U'/I' for a $+Q$ input. In addition, the sign of "minor term" term for the different possible input ($+Q$, $+U$, $-Q$ and $-U$) nicely match the observations.

6.4.5.3 Spurious polarization terms

Explaining the measured spurious polarization is not obvious. The polarization calibration revealed that a larger spurious polarization level, with $\sim 2\times\ 10^{-3}$ and $\sim 5\times 10^{-4}$ for x_{01} and x_{02}, respectively, are produced in the spectro-polarimeter. This magnitude is larger than the spurious polarization from design, expected to be null. Opposite signs were observed in both channels, which can be explained by the demodulation scheme if spurious polarization is affecting the intensity recorded by the exposures in the same way for both the channels: the resulting sign of the spurious polarization would be opposite since the demodulation scheme has opposite signs between channel 1 and channel 2. The intensity on each exposure might be affected by possible non-uniformity (retardance, thickness, transmittance and/or dust) of the PMU half-waveplate. In order to confirm such possibility, the response matrix was evaluated not for the full rotation of the PMU half-waveplate, but for every quarters independently, by using the data set taken by the waveplate method in $+Q_{0^\circ}$ configuration (Table 6.6). This shows that the spurious polarization terms are highly dependent on which quarter of the PMU half-waveplate is used. Both scale factors and azimuth errors are also affected. These changes indicate non-uniformity of the PMU half-waveplate, which might have a net effect on the spurious polarization when averaging for a full rotation.

6.5 Conclusion on the pre-flight polarization calibration

An end-to-end polarization calibration of CLASP spectro-polarimeter was performed to derive the response matrix. This investigation revealed many important features for polarization calibration in VUV which are summarized here in the hope of providing a guideline for future spectro-polarimetric mission in the VUV.

Having a complete understanding of the light-source used for the calibration is important: even with its fairly simple design, the light-source used for the calibration had a complicated polarization input, with dependency on the illumination position along the slit due to the chief-ray tilt and with an unknown dependency on the light-source orientation. Using a rotating motor to set the orientation of a half-waveplate is a suitable solution since the light-source orientation can be kept unchanged. However, the retardance of such half-waveplate is a crucial parameter for reducing the errors in the spurious polarization. Precise measurement of the retardance before the calibration is preferable but it is also possible to determine the retardance in the calibration by taking at various orientation of the light-source. A careful estimation of the errors in the demodulated Q'/I' and U'/I' measurements is also important, since they directly affect the accuracy on the response matrix elements.

In conclusion, the polarization calibration for the CLASP spectro-polarimeter was successfully conducted. The response matrix of the instrument was determined within the required accuracy (except for one spurious polarization term with an error marginally larger than the tolerance), with an accuracy on the spurious polarization accuracy close to the 10^{-4} level. Reaching such unprecedented precision should ensure CLASP to obtain polarization measurements below the 0.1% accuracy for the first time in VUV range. CLASP was successfully launch on September 3^{rd} 2015, and the response matrix was compared to the results of the in-flight polarization calibration.

Table 6.6: Response matrix elements for the measurement at the center of the slit with $+Q_{0^\circ}$ input of the light-source and LS half-waveplate.

Channel 1	x_{01}	x_{02}	x_{11}	x_{22}	x_{12}	x_{21}
Modulation 1	-0.00151	0.97334	0.05466	-0.00210	-0.00941	0.98000
Modulation 2	0.00344	0.98130	-0.00048	-0.00076	0.00053	0.97409
Modulation 3	0.00525	0.98130	0.00202	0.00143	-0.01592	0.97277
Modulation 4	0.00080	0.97942	0.02017	-0.00044	-0.02262	0.97784
Mean	0.00200	0.97884	0.01909	-0.00047	-0.01186	0.97784
Error (±)	0.00351	0.00550	0.03557	0.00190	0.01239	0.00383

Channel 2	x_{01}	x_{02}	x_{11}	x_{22}	x_{12}	x_{21}
Modulation 1	0.00129	0.96795	0.00062	0.00202	-0.00427	0.97502
Modulation 2	-0.00317	0.97620	-0.00537	0.00067	-0.00497	0.96907
Modulation 3	-0.00523	0.97424	0.01503	-0.00115	-0.01068	0.96749
Modulation 4	-0.00105	0.96655	0.01989	0.00010	-0.01821	0.97255
Mean	-0.00204	0.97124	0.00754	0.00041	-0.00953	0.97103
Error (±)	0.00333	0.00497	0.01291	0.00161	0.00868	0.00399

Chapter 7

Optical checks of the instrument

7.1 Purpose of the optical checks

Optical checks were conducted at several key-points of the flight preparation, as a way to ensure the optical alignment and performances of the instrument. After the optical preparation and calibration of the instrument at the National Astronomical Observatory of Japan (NAOJ, Mitaka, Japan), vibration tests on the scientific payload attached to a dummy avionic section were conducted at the Institute for Space and Aeronautic Science (ISAS, Sagamihara, Japan). The instrument was then shipped to the Marshall Space Flight Center (MSFC, Huntsville, USA) for the integration of the electronics with the flight avionic section. Upon completion, the instrument was finally shipped to the White Sand Missile Range (WSMR, New Mexico, USA) for the final rocket preparation, where an additional vibration test was performed before flight. The optical checks consisted of two parts: a measurement of the telescope focus position and a measurement of the image quality for the spectro-polarimeter, both of which were conducted several times in-between the previously cited vibration tests and transportations.

7.2 Checking the telescope focus

The telescope focus check measurements followed the same method as described in Section 4.1, where an optical fibre was introduced from the top access-door of the rocket-skin, to illuminate the back-side of the slit with white-light. The image of the slit was recorded on the slit-jaw camera after reflection by a flat mirror located in front of the telescope aperture, and the width of the slit was measured to estimate the telescope focus position. Table 7.1 summarizes the various measurements performed for this optical check.

Because some measurements were conducted outside Japan, the large flat mirror (ϕ600mm) could not be transported and a smaller mirror (ϕ150mm) was used instead. As the full aperture of this mirror couldn't cover the entire entrance aperture of the telescope, its position in front of the entrance aperture was kept the same throughout the different optical check measurements. The configuration with the small mirror is shown in Figure 7.1. Since the vibration environment at MSFC and WSMR was unknown, the duration of the reflected slit measurement was extended to 15 minutes acquisition, to further decrease the influence of the vibration on the measured FWHM. Results of the measurements are summarized in Table 7.2. The telescope focus position was confirmed to be within the $\pm$100µm tolerance after the vibration tests and shipments, as the

Table 7.1: Summary of the optical checks performed for the telescope focus.

Optical checks	Note
#1	Pre-vibration test at ISAS
#2	Post-vibration test at ISAS
#3	After delivery at MSFC
#4	After delivery at WSMR
#5	Post-vibration test at WSMR

reflected slit FWHM was measured between 30 µm and 39 µm (see Section 4.3). In addition, the final measurement was similar to the FWHM for the nominal 800 µm shim (FWHM 32.8±1.4µm). Finally, the direct slit measurement showed no significant changes, implying that the performances of the slit-jaw optics were not significantly affected either.

Table 7.2: FWHM of the reflected slit and of the direct slit for the different optical check measurements.

Optical checks	FWHM reflection (µm)	FWHM direct (µm)
#1	34.3 ± 1.8	23.5 ± 1.1
#2	32.1 ± 1.4	23.2 ± 1.1
#3	33.9 ± 2.6	23.6 ± 1.1
#4	33.9 ± 1.7	22.8 ± 1.1
#5	32.8 ± 1.7	23.5 ± 1.3

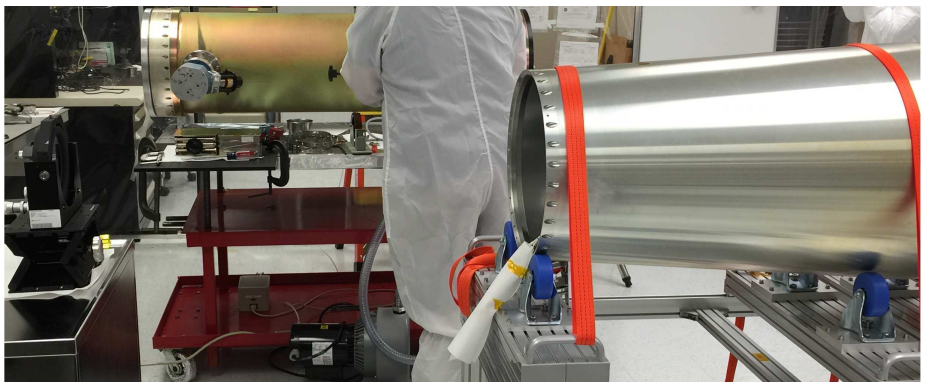

Figure 7.1: Experimental configuration with the small mirror (on the left) located in front of the telescope aperture (on the right) for the telescope focus check, at MSFC.

7.3 Checking the spectro-polarimeter image quality

7.3.1 Methodology

The second optical check aimed to confirm the image quality of the spectro-polarimeter. A Lyman-α collimator was attached to the telescope part of the rocket skin, as shown in Figure 7.2. A deuterium lamp (similar as in Section 6) was used to provide Lyman-α light, with the strongest intensity in the deuterium Lyman-α line at 121.534nm, a weaker emission in the hydrogen Lyman-α at 121.567nm, and numerous weak emission lines from other elements.

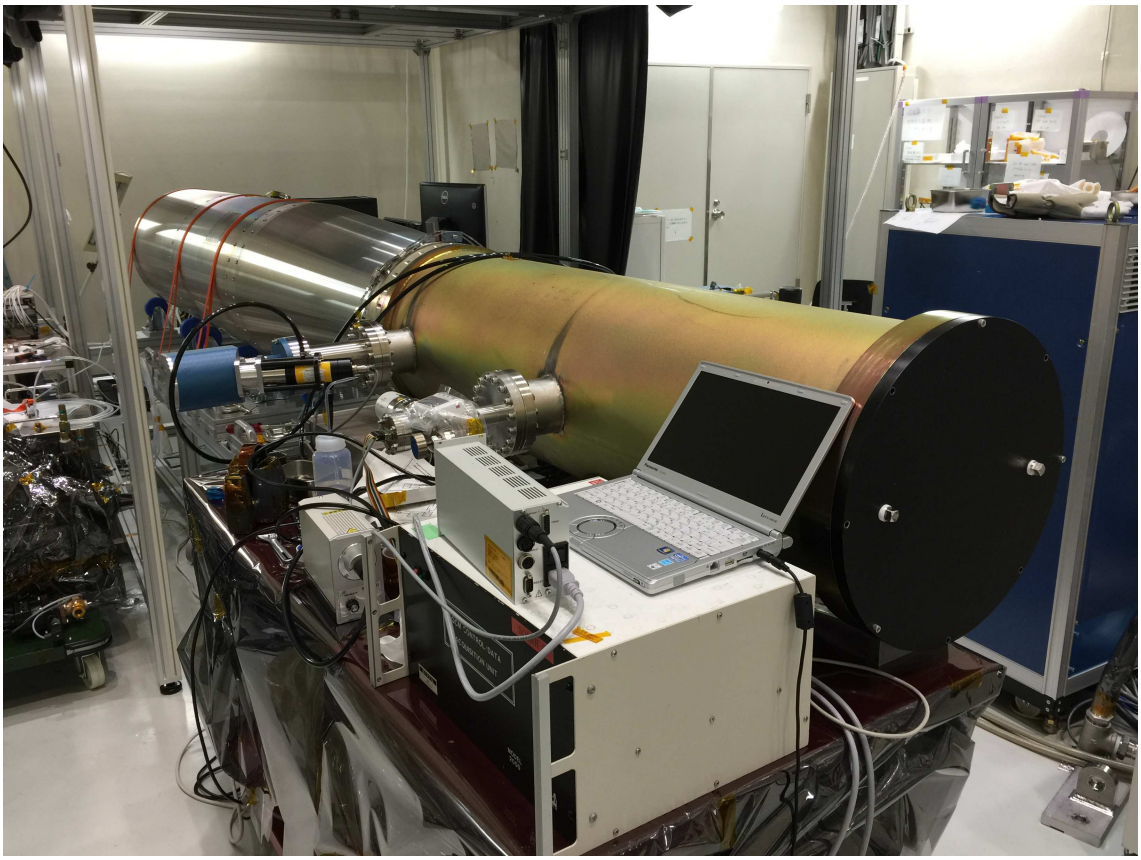

Figure 7.2: Configuration for the spectro-polarimeter optical check, with the Lyman-α collimator attached to the instrument.

The configuration provided a collimated Lyman-α beam illuminating the slit after passing through the telescope, and the optical performance of the spectro-polarimeter could be measured by estimating the width of the slit image for a given spectral line. However, both the deuterium Lyman-α line and the hydrogen Lyman-α line are intrinsically broad and therefore not suitable for estimating the performances. For this purpose, two sharper and weaker emission lines, hereafter referred to S1 and S2, were selected on each side of the Lyman-α wavelength, as shown in Figure 7.3.

The measurements for checking the spectro-polarimeter image quality were carried as reported in Table 7.3. The collimator had two possible configurations: focused and defocused, depending on how the spot created by the deuterium lamp was focused onto the slit. This was controlled

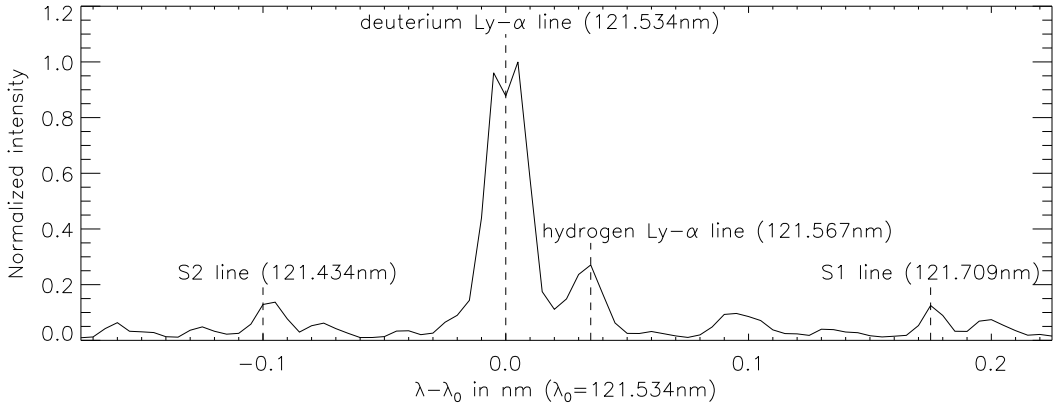

Figure 7.3: Profile along the wavelength direction, with the deuterium Lyman-α, the hydrogen Lyman-α and the two S1 and S2 lines.

by adjusting the position of the pinhole located after the deuterium lamp using shims. Both measurement modes were used, and although the illumination pattern on the slit changed between the focused and the defocused configurations, no significant differences on the measured slit width were observed. During these measurements, the width of the slit image for the S1, S2 and deuterium Lyman-α lines were estimated with a Gaussian fitting. The FWHM was estimated independently for ten pixels along the slit direction, at three positions along the slit: 0" (i.e. center of the slit) and ±100". The FWHM for the three positions along the slit was calculated as the averaged value out of their ten respective fitted values, and the standard deviation was used to estimate the fitting error.

Table 7.3: Summary of the optical checks performed on the instrument.

Optical checks number	Collimator mode	Note
#1	Defocus	Pre-vibration test at ISAS
#2	Defocus	Post-vibration test at ISAS
#3	Defocus	After delivery at MSFC
#4	Focus	After delivery at MSFC
#5	Defocus	Launch practice #1 at MSFC
#6	Defocus	Launch practice #2 at MSFC
#7	Focus	After channel 2 CCD replacement at MSFC
#8	Focus	Pre-vibration test at WSMR
#9	Focus	Post-vibration test at WSMR

7.3.2 Results

The results for the spectro-polarimeter optical checks are shown in Figure 7.4 for channel 1 and in Figure 7.5 for channel 2. The measured FWHMs for the different optical check measurements show some fluctuations with larger error bars, probably because some fittings did not properly converged. Nevertheless, the differences in FWHM from the optical alignment at NAOJ until prior to launch at WSMR is ±5µm at maximum. Compared to the ∼0.009 nm spectral resolution measured after the spectro-polarimeter alignment on the S1 line (FWHM 24.3 µm for channel 1 and 22.7 µm for channel 2, see Section 3.3.3), an increase of ∼5µm in FWHM corresponds to a ∼0.011 nm spatial resolution. This spectral resolution was slightly larger than the 0.010 nm requirement, but was accepted for the flight.

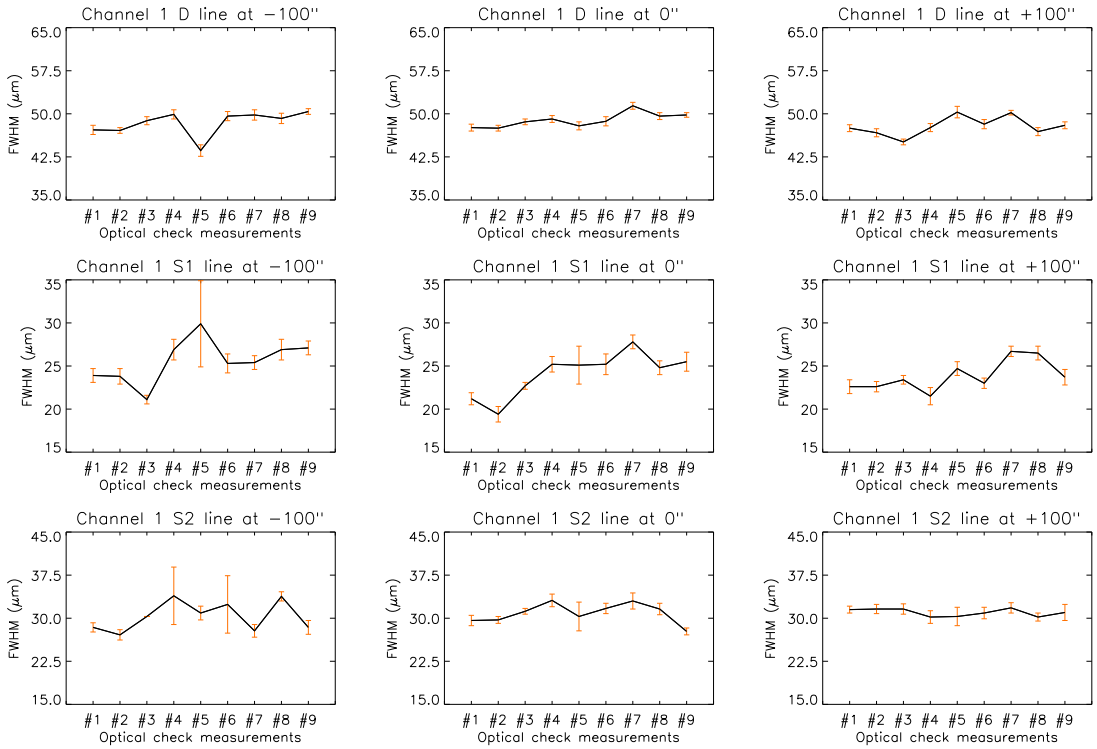

Figure 7.4: Measured FWHM of the deuterium Lyman-α (top), S1 (middle) and S2 (bottom) lines at −100" (left), 0" (middle) and +100" (right) for channel 1, for the various optical check measurements performed prior to launch. Error bars are calculated as the standard deviation of the ten fitting at each position along the slit.

The position of the slit image on the cameras was also checked during the measurements, and results are reported in Figure 7.6. A shift of the image position was noticed during the various optical check measurements. The measurement showed similar amplitude of the position shift, with opposite sign in both the channels: the different vibration tests and transportations might have affected a common optical to both the channels (e.g. the diffraction grating). Measurement #6 is an exception because channel 2's camera was replaced due to an electronic problem, and the shift in position of the image also included misalignment of the camera after re-attachment.

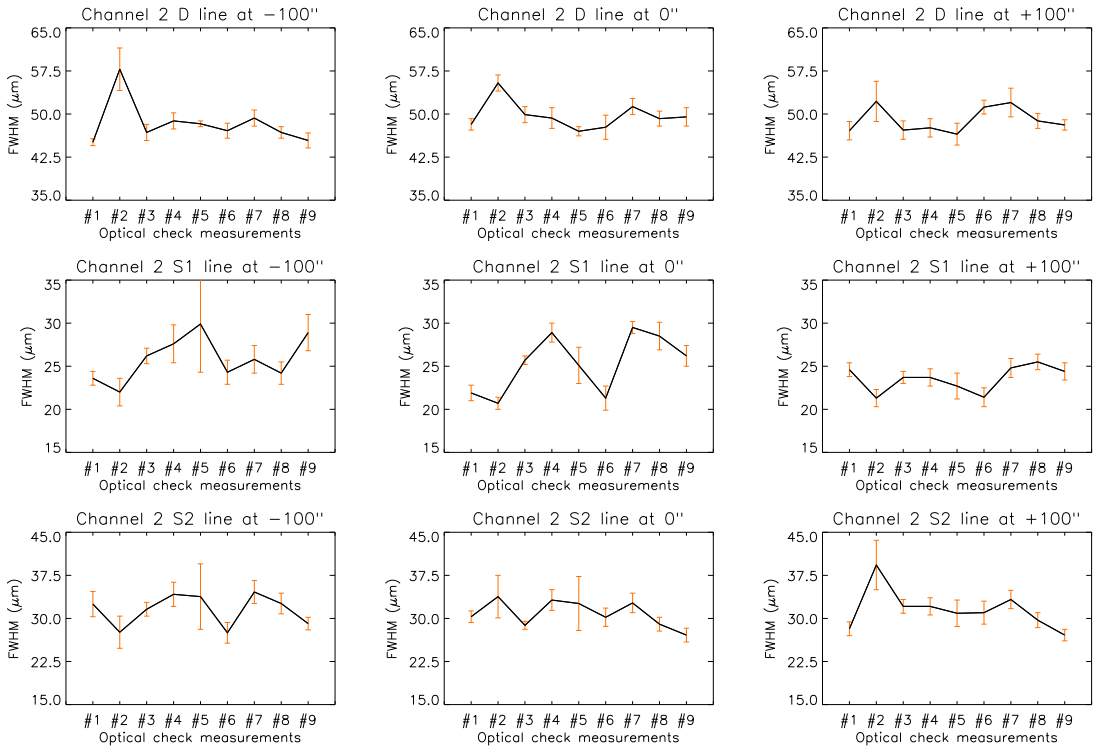

Figure 7.5: Measured FWHM of the deuterium Lyman-α (top), S1 (middle) and S2 (bottom) lines at −100” (left), 0” (middle) and +100” (right) for channel 2, for the various optical check measurements performed prior to launch. Error bars are calculated as the standard deviation of the ten fitting at each position along the slit.

The amplitude of the image position shift was larger along the Y-axis, but almost cancelled out in the overall optical check measurements. On the other hand, the shift in the X-direction was smaller but kept adding up over time. In average, the resulting image shift from the optical alignment of the spectro-polarimeter until prior to launch was around ∼20 pixels (i.e. ∼260µm) for both the channels, and the expected image shift due to the launch vibration were estimated at ∼30 pixels along the Y-axis and ∼5 pixels along the X-axis, based on the measurements taken before and after the vibration tests. These measurements ensured the position of the image to be within the CCD detector throughout the flight: the position of the image measured prior to flight was confirmed to have enough clearance in both the X-direction and the Y-direction.

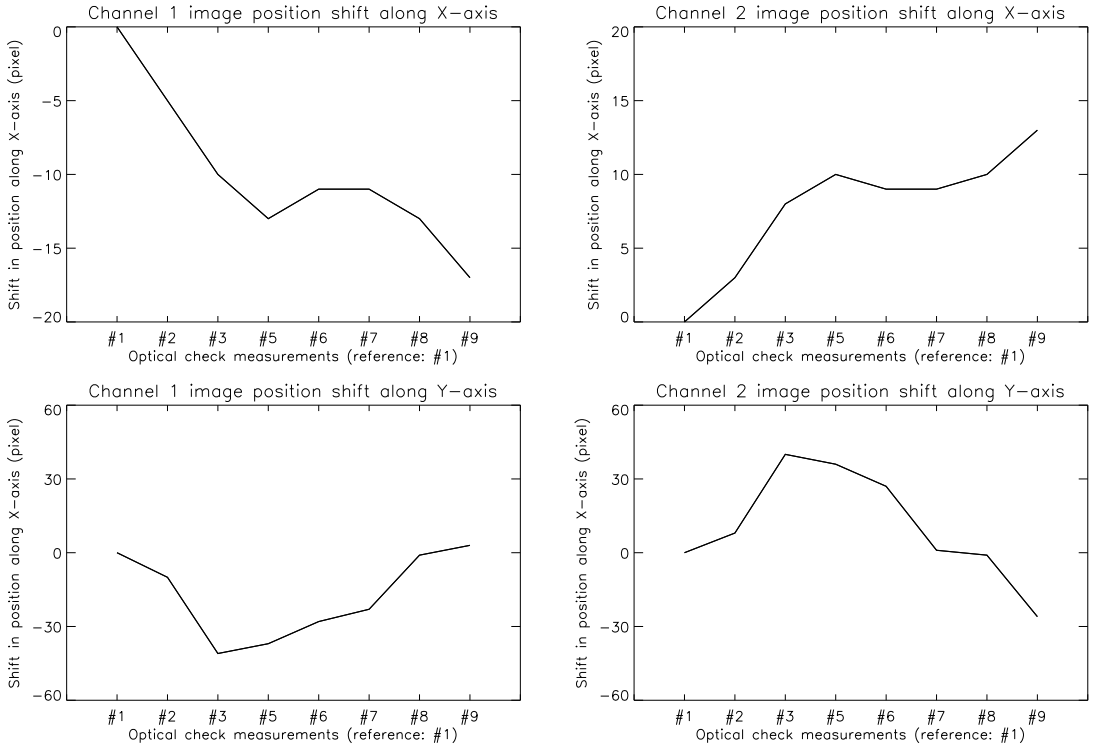

Figure 7.6: Shift of the image position with respect to the initial position (measurement #1) for channel 1 (left) and channel 2 (right), along the X-axis (top) and Y-axis (bottom).

7.4 Conclusion

Optical checks were conducted to monitor the optical performances of the instrument during the flight preparation, especially after the different vibration tests and transportations. As a result, the telescope focus was successfully confirmed to be within its ±100µm tolerance, and the spectral resolution of the spectro-polarimeter was measured to be around its 0.010 nm requirement. The position of the slit image on the cameras was also confirmed to have enough clearance to be within the CCD detector even after the expected launch vibrations. These measurements ensured the healthiness of the instrument and its performances prior to launch.

Chapter 8

Flight results

8.1 Summary of the flight observations

CLASP was launched on September 3^{rd} 2015 from White Sands Missile Range (New Mexico, USA) onboard a Black Brant IX rocket as shown in Figure 8.1. The flight duration was approximatively 15 minutes, from take-off to landing, with apoapsis ∼270km. Observations were conducted above the atmosphere: the disc center was initially observed for ∼15s after the door opened. Then, after re-pointing and stabilization of the instrument, the observations close to the limbs (i.e. main science target) were performed during ∼240s. Dark current images were also recorded during the flight, before the door opened and after the door was closed. Figure 8.2 shows an example of the typical measurements recorded during the flight with the slit-jaw and spectro-polarimeter cameras at disc center and close to the limb.

Figure 8.1: The Black Brant IX rocket carrying the CLASP instrument during lift-off.

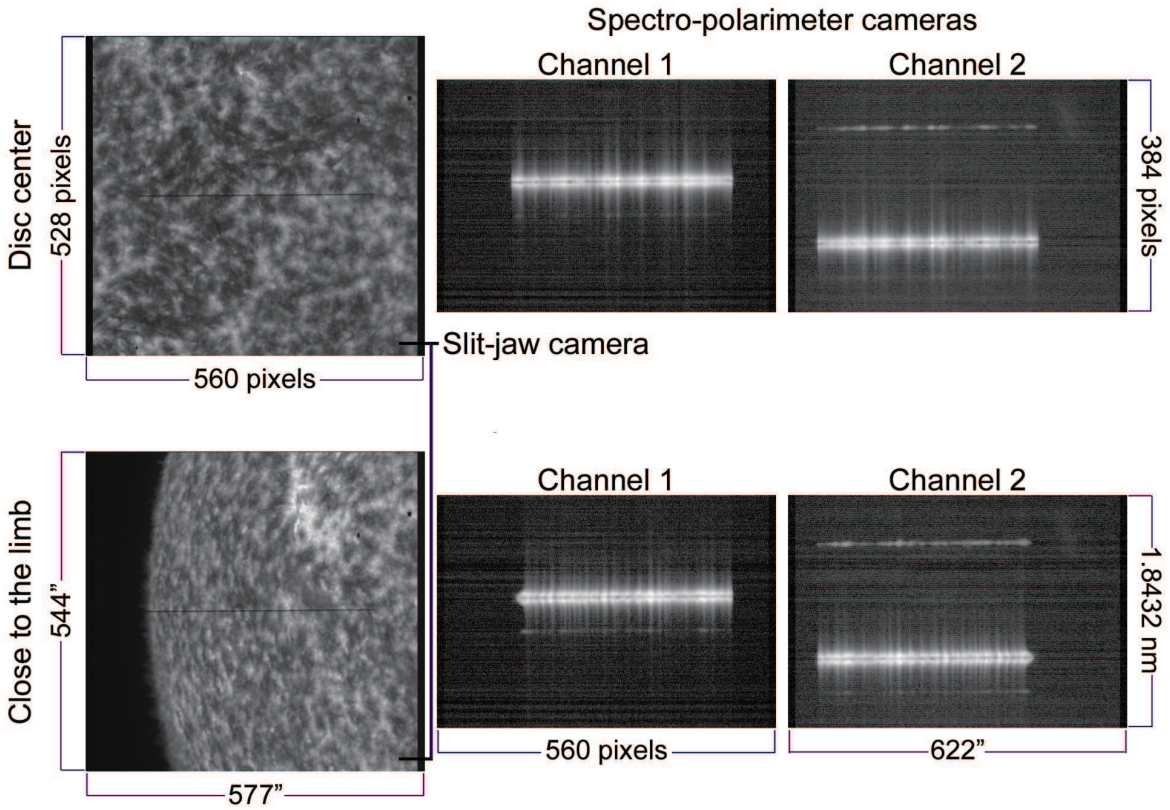

Figure 8.2: Typical images recorded during the flight with the slit-jaw camera (left), channel 1 camera (middle) and channel 2 camera (right) for the spectro-polarimeter at the disc center (top row) and close to the limb (bottom row). Intensity is shown in logarithmic scale.

The location of the instrument pointing was confirmed after the flight by co-aligning the images observed by the slit-jaw with full-disc observation from the Atmospheric Imaging Assembly (AIA onboard SDO spacecraft, [47]), using the 30.4nm band as shown in Figure 8.3. The solar coordinates were taken as (X,Y), where the X-axis is toward the solar-west and the Y-axis toward the solar-north. In the disc center observations, the center of the slit was locate at ($-16.3''$,$-12.1''$) from the actual solar disc center, whereas for the limb observations, the coordinates of the center of the slit were ($+465.6''$, $-627.1''$).

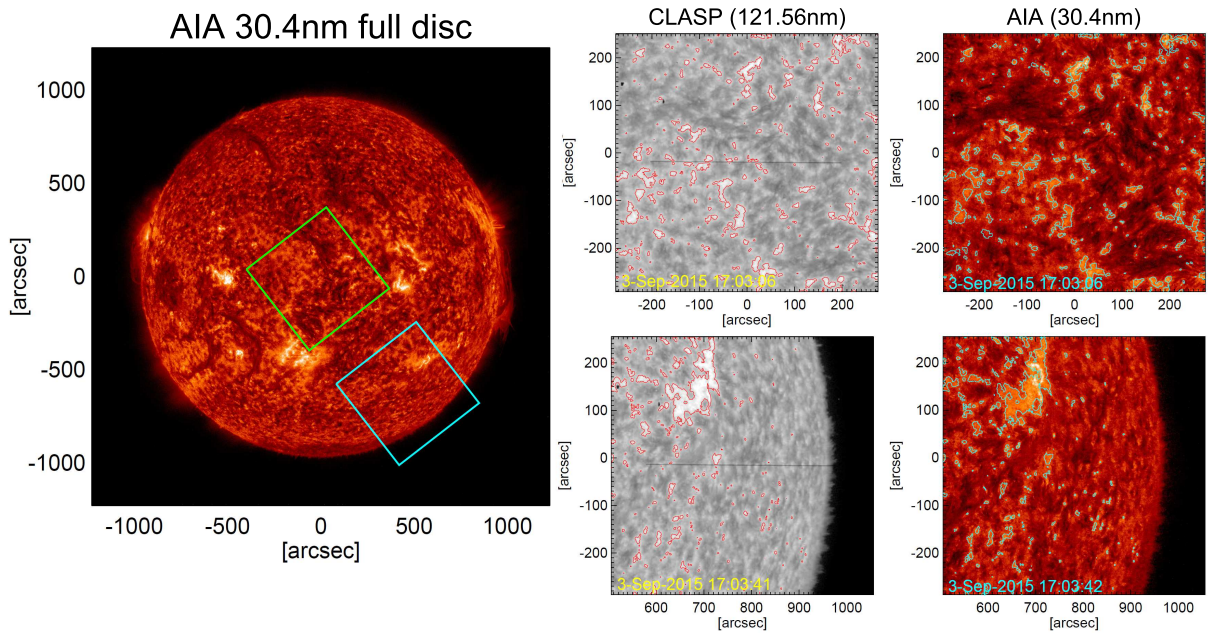

Figure 8.3: Co-alignment of CLASP observations with AIA. CLASP observations are shown in grey-color scaling, with contours co-aligned with the AIA 30.4nm images, shown in red-color scaling.

8.2 Confirmation of the achieved spatial and spectral resolutions

The spatial resolution achieved by CLASP during its flight was checked by comparing with the AIA 30.4nm co-aligned observations. For this analysis, the disc center observations were used since the entire field of view and slit was illuminated and three regions were selected along the slit, around its center and edges: ∼60”×∼60” for the slit-jaw and ∼40” along the slit for the spectro-polarimeter. The AIA data were convolved with various PSF, taken as a Gaussian function (1D for the spectro-polarimeter and 2D for the slit-jaw) and with increasing FWHM (i.e. resolution). The origin of the coordinate system used for the spatial data is the center of CLASP slit.

8.2.1 Slit-jaw spatial resolution

Figure 8.4 shows an example of the CLASP and AIA data comparison for various convolution between AIA and PSFs. Note that the intrinsic resolution of AIA is around 1.5”. Hence, the final resolution was calculated as the root sum square of the PSF FWHM and 1.5”.

The correlation between the CLASP data and the AIA data with various spatial resolution was calculated using the Spearman rank correlation coefficient on the 2D regions. This coefficient indicates the degree of correlation between two datasets by considering the rank of each value (i.e. sorted from maximum to minimum within each dataset). Hence, it is unaffected by the different amplitude of the values between the datasets. A coefficient of 1 indicate a perfect correlation, whereas 0 is no-correlation between the dataset and −1 is a perfect anti-correlation. As a results, the best correlation between both the observations is for a spatial resolution of 4.3”, 3.7” and 4.6”, respectively at the top, center and bottom of the slit. This spatial resolution is derived

from the comparison with AIA is a upper limit to the achieved spatial resolution: a closer look at fine-structures revealed that the actual spatial resolution is probably ~ 1" better than the derived numbers, as shown in Figure 8.6. However, only focusing on small structures provides inconsistent results since both wavelength are different: some features appear sharper in CLASP whereas some others are shaper in AIA, and only selecting apparently similar features in both the instruments would be biased since the observations don't provide information on the underlying physics of the line formations. On the other hand, comparing a larger area as previously performed indicates the correlation between both the instrument for the extended structure (moss and bright patches) and partially lose the resolution of the small-scale features.

Hence, the actual spatial resolution is most probably between the pre-flight expectation and the upper limit defined from the observation, which is within the range of the expected performances for the telescope and slit-jaw optics.

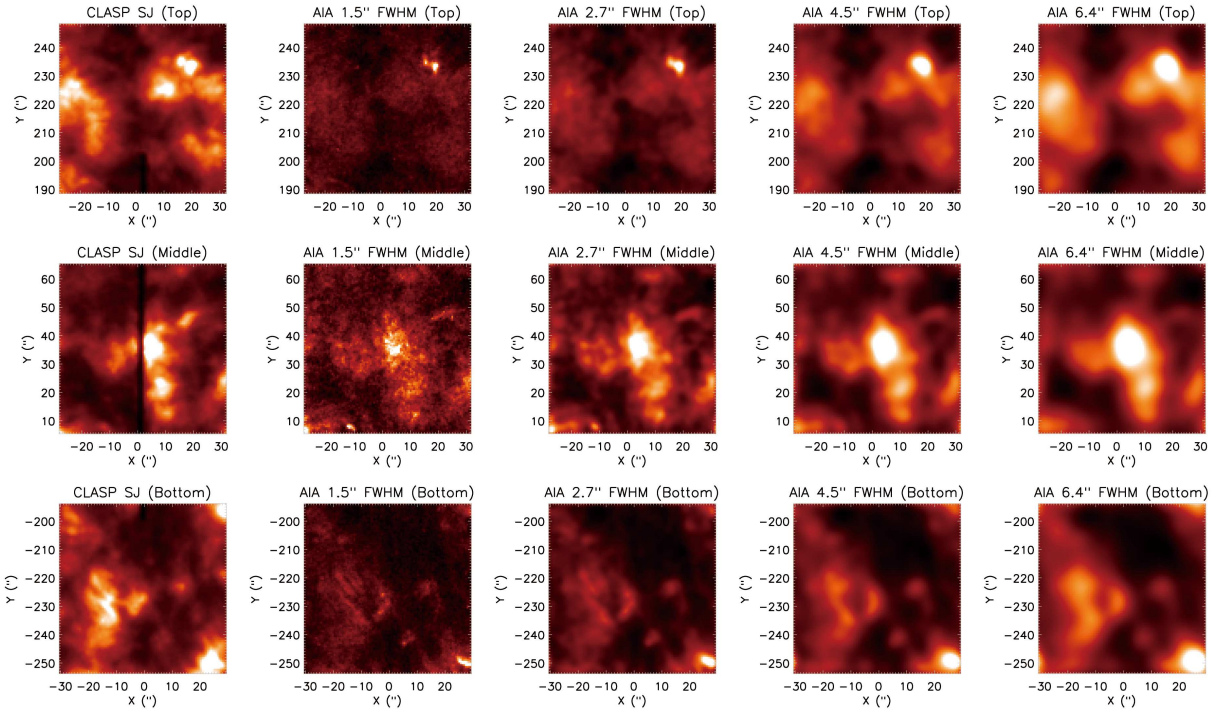

Figure 8.4: CLASP SJ observations at disc center, compared with co-aligned AIA 30.4nm convolved with various PSF FWHM.

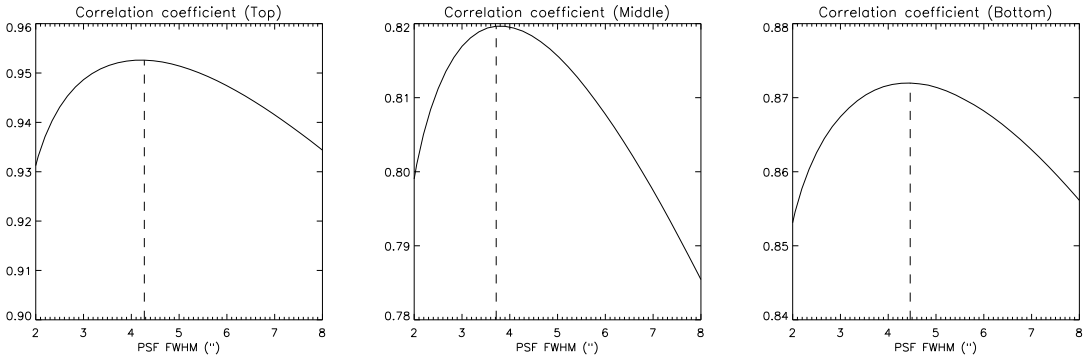

Figure 8.5: Spearman rank correlation coefficient between CLASP and AIA for various PSF FWHM. Dash line shows the position of the maximum.

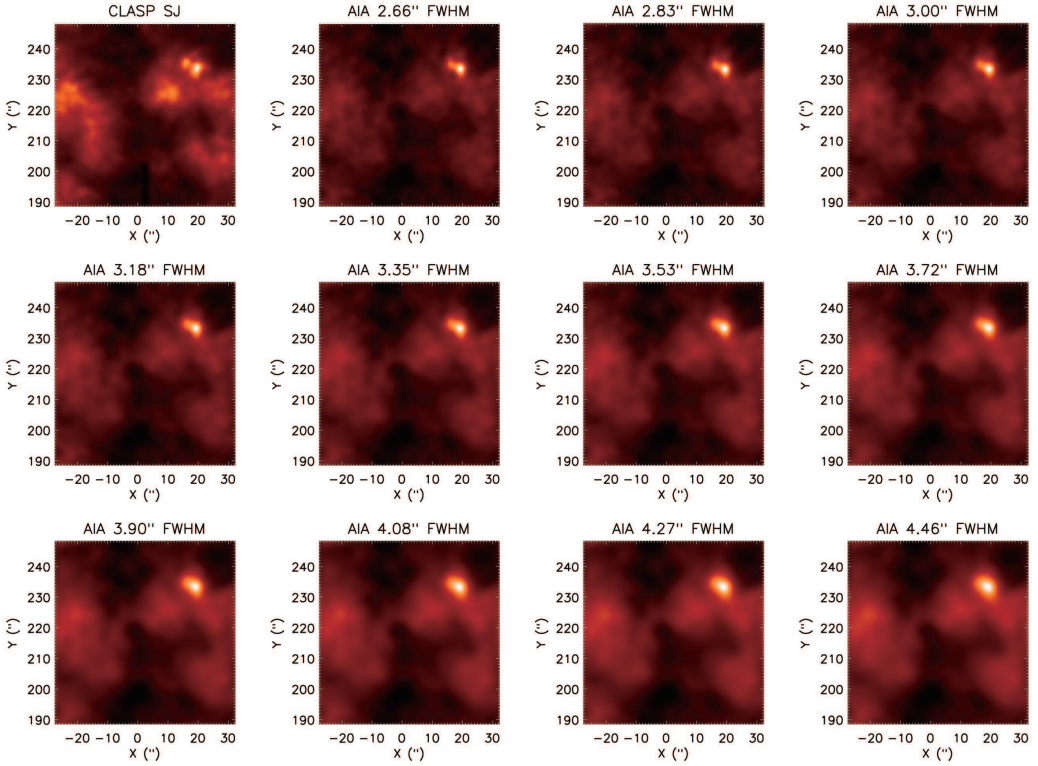

Figure 8.6: Detail comparison between CLASP SJ observations at disc center compared with co-aligned AIA 30.4nm convolved with various PSF FWHM at the top of the slit. Color scaling is different than for Figure 8.4.

8.2.2 Spectro-polarimeter spatial resolution

Similarly as for the slit-jaw, the Lyman-α intensity observed by the spectro-polarimeter was compared to the corresponding intensity from AIA 30.4nm. Figure 8.7 shows an example of these intensity profiles from channel 1 and 2, compared to the AIA profiles for various convolution with PSF. The intensity profiles were normalized by their respective maximum values.

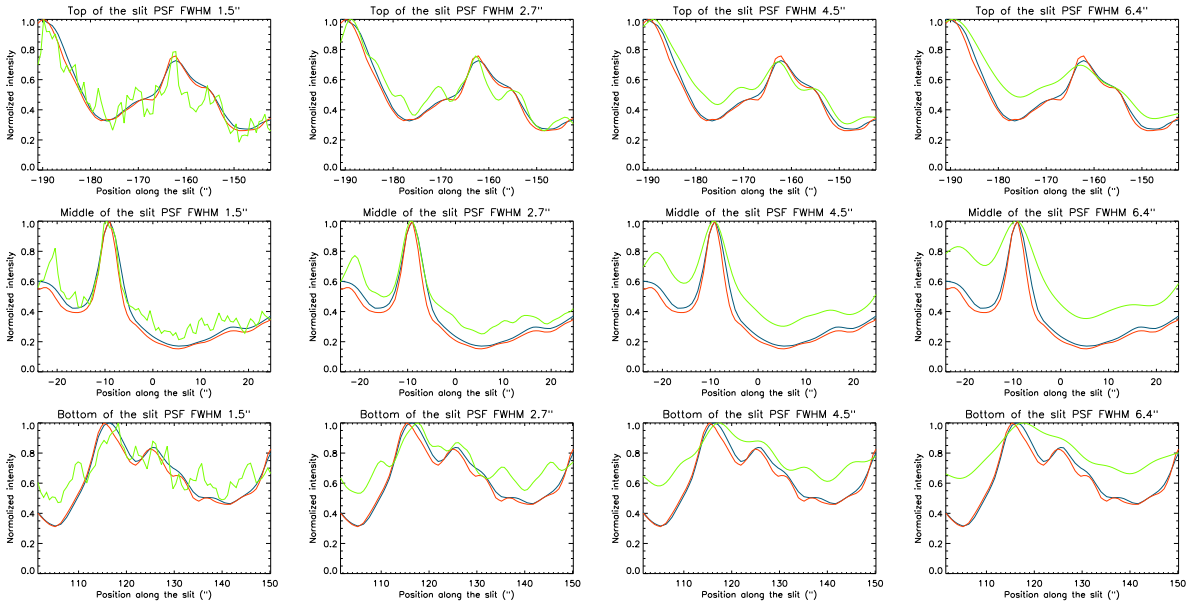

Figure 8.7: CLASP Lyman-α intensity at disc center, in blue for channel 1 and in red for channel 2, compared with the corresponding AIA 30.4nm intensity convolved with various PSF FWHM in green.

The normalized intensity profiles were compared by calculating the standard deviation of their difference: a smaller variation indicates a better correlation between the profiles. The spatial resolution for channel 1 was estimated around 4.5", 3.5" and 4.6", respectively at the top, middle and bottom of the slit. For channel 2, the achieved spatial resolution 3.9", 2.7" and 4.8" (top, middle and bottom of the slit). The better spatial resolution observed in channel 2 can be seen when carefully examining the images. Note that. similarly as for the slit-jaw, this estimation of the spatial resolution is a upper-limit of the instrument's performances. The actual spatial resolution achieved is probably ~ 1" better.

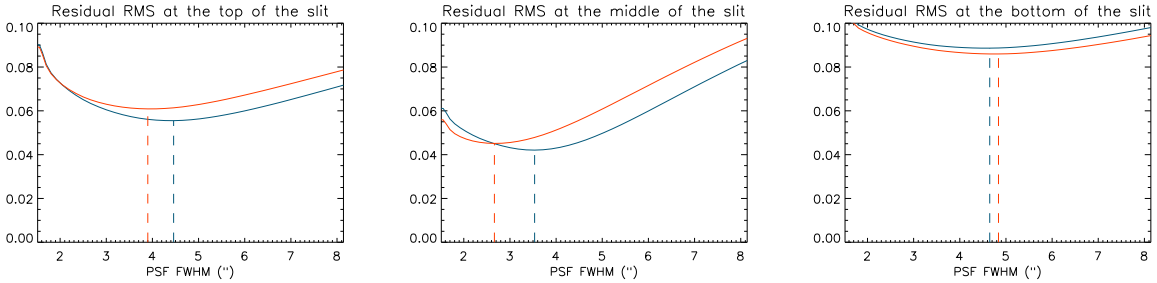

Figure 8.8: RMS residual between CLASP (channel 1 in blue, channel 2 in red) and AIA for various PSF FWHM. Vertical dash lines indicated the location of the minimum.

8.2.3 Spectro-polarimeter spectral resolution

Obtaining a confirmation for the spectral resolution was more difficult since no coordinate observations covered a similar spectral window and also because the Lyman-α profile is intrinsically broad. The solution adopted was to compare the geocorona absorption observed by CLASP with the absorption recorded by the OSO8/LPSP instrument in 1975 in a Quiet Sun region ([23]). The geocorona absorption is due to the hydrogen present in Earth's corona, absorbing the Lyman-α radiation only in the very core of the line (i.e. at exactly the Lyman-α wavelength). The OSO8 observations were carried out with a 0.002nm spectral resolution, which precisely sampled the geocorona absorption (see Figure 1.6). CLASP intensity profiles were taken at the top, middle and bottom of the slit by averaging several pixels along the slit. These profiles were selected to match the peak separation observed in the OSO8 observations. This is important since some profiles observed by CLASP shows a larger spectral separation between the Lyman-α double-peak, probably due to thermic and dynamic effects. The OSO8 profile was convolve with various PSF FWHMs: examples are shown in Figure 8.9)

The standard deviation of the difference between normalized profiles was used to quantified the correlation between the profiles for various PSF FWHM. Note that only the region between the two peaks was used for the comparison. As a result, the achieved spectral resolution was estimated at 0.010nm, 0.008nm and 0.011nm for channel 1, at the top, middle and bottom of the slit. Similarly, the spectral resolution for channel 2 was around 0.010nm, 0.009nm and 0.011nm.

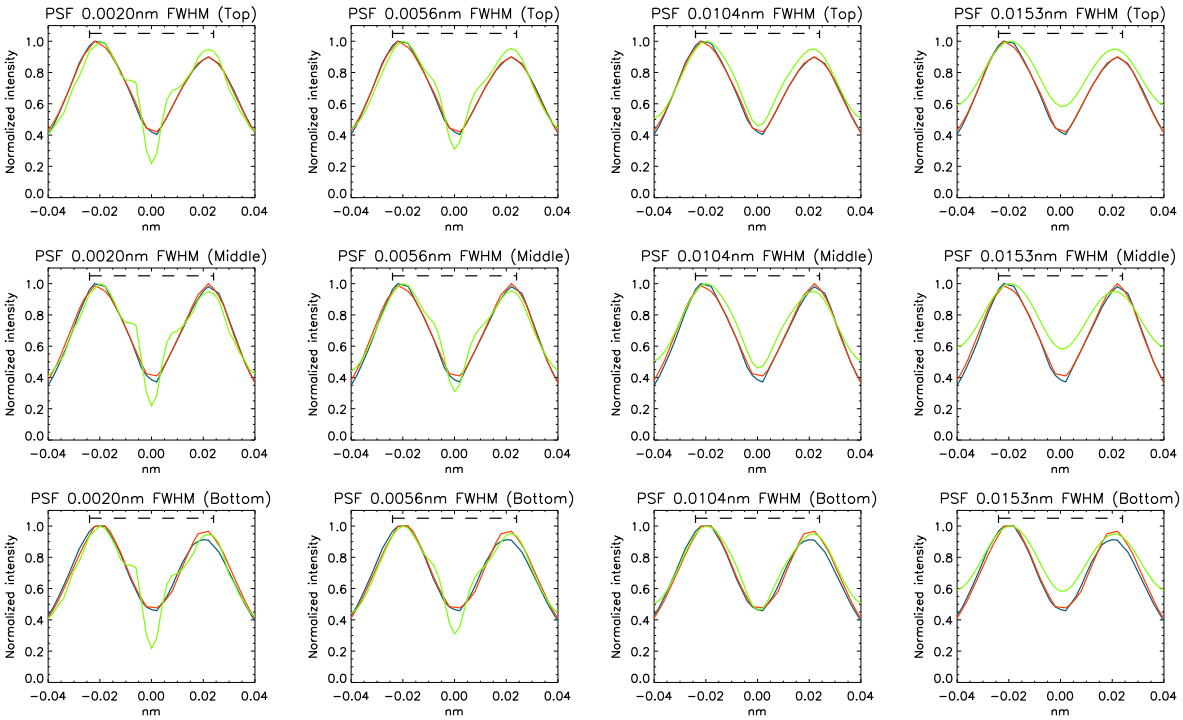

Figure 8.9: CLASP Lyman-α intensity profiles at disc center, in blue for channel 1 and in red for channel 2, compared with the OSO8 profiles, convolved with various PSF FWHM in green. Black dash lines shows the region used for the comparison.

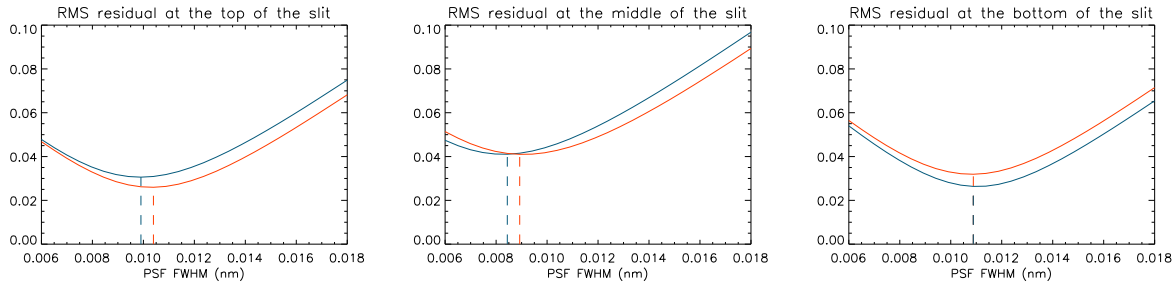

Figure 8.10: RMS residual between CLASP (channel 1 in blue, channel 2 in red) and OSO8 profiles for various PSF FWHM. Vertical dash lines indicated the location of the minimum.

8.2.4 Comparison with pre-flight expected spatial and spectral resolutions for the spectro-polarimeter

The estimated spatial and spectral resolutions achieved during the flight are essentially consistent with the expected resolutions from the telescope and spectro-polarimeter alignment (see Chapter 3), as summarized in Table 8.1. The upper-limit for the spatial resolution is slightly larger than the expectation, and a difference between both the channels can be seen: this might be due to additional small misalignments of the optics during the flight, and is still within the requirement of <10". In addition, the estimation of the achieved resolutions are also limited by the sampling size of CLASP data (i.e. 13.0 µm pixel size): the FWHM of the spot is only slightly larger than twice the pixel size.

Table 8.1: Comparison between the expected and achieved spatial and spectral resolutions for the spectro-polarimeter.

	Spatial resolution		Spectral resolution	
	Expected	Achieved	Expected	Achieved
Channel 1 at +200"	3.0"	<4.5"	0.013nm	0.010nm
Channel 1 at 0"	2.7"	<3.5"	0.009nm	0.008nm
Channel 1 at −200"	3.0"	<4.6"	0.013nm	0.011nm
Channel 2 at +200"	3.1"	<3.9"	0.013nm	0.010nm
Channel 2 at 0"	2.8"	<2.7"	0.008nm	0.009nm
Channel 2 at −200"	3.1"	<4.8"	0.013nm	0.011nm

8.3 In-flight polarization calibration

The disc center was observed to provide the data for an in-flight calibration of the polarization. Because of symmetry, the atomic-level polarization vanishes at μ=1. However, more realistic three-dimensional calculation suggested that the local anisotropy of the radiation field due to the chromosphere temperature and density of solar atmosphere's topology irregularities can also create scattering polarization locally ([27]), even at disc center. Nevertheless, cancellation of the atomic-level polarization and the Hanle effect are expected by spatially averaging the polarization signals measured at various location around the disc center. By doing so, the spurious polarization level of the instrument can be estimated from the measurement at disc center, for both the channels

Spectro-polarimetric observations were only recorded for ∼15s, with three complete PMU rotations (i.e. 48 images) having a stable pointing. After correcting for dark current, gain and orientation (i.e. tilt of the slit/dispersion direction with respect to the camera pixel grid), the Stokes parameters I', Q' and U' were demodulated from the 48 images. The demodulation scheme used for the in-flight data is shown in Equation (8.1) for channel 2 (minus sign for channel 1), which is different from the one used in Chapter 6. This demodulation scheme minimizes the possible spurious polarization on U'/I' caused by the dI/dt if the intensity of the observed source fluctuates during the modulation, which was observed to be significant in the flight case. Note that the polarization coordinate system is still defined as in Chapter 6, with $+Q$ along the slit. Figure 8.11 shows the demodulated Stokes parameters at disc center. Coherent patches of linear polarization can be seen in the Lyman-α wings, indicating that the zero scattering polarization assumption does not hold: the measured linear polarization might be produced by local anisotropy due to the three-dimensional nature of the solar atmosphere.

$$\begin{aligned} \frac{Q'}{I'} &= \frac{\pi}{2}\left(\frac{D_1 - D_2 - D_3 + D_4}{D_1 + D_2 + D_3 + D_4}\right) \\ \frac{U'}{I'} &= \frac{\pi}{2}\left(\frac{D_2 - D_3 - D_4 + D_5}{D_2 + D_3 + D_4 + D_5}\right) \end{aligned} \tag{8.1}$$

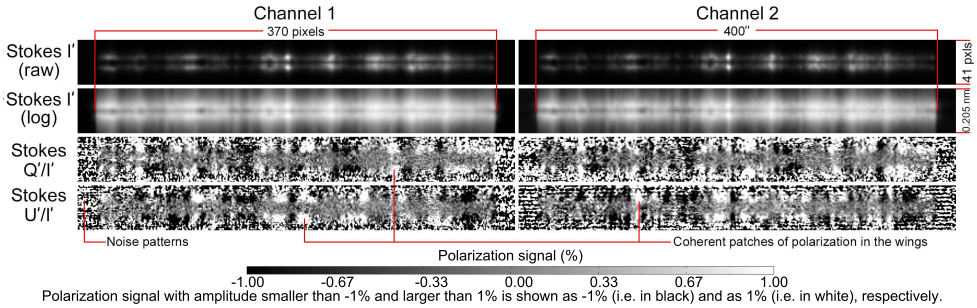

Figure 8.11: Stokes I' (raw and log), Q'/I' and U'/I' demodulated with 3 PMU rotations at disc center for both the channels.

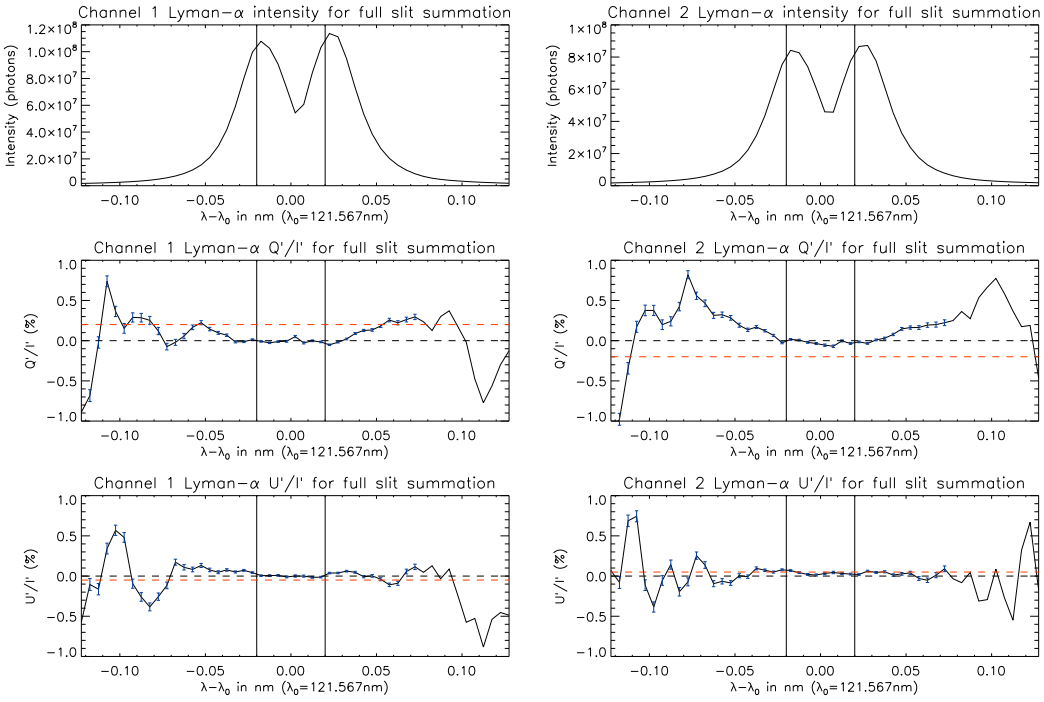

Figure 8.12: Stokes I', Q'/I' and U'/I' profiles for a full slit spatially summed, for both the channels. Horizontal black dashed line shows the location of the zero in Q'/I' and U'/I'. Horizontal red dashed line shows the expected spurious polarization offset from the pre-flight calibration. Vertical black solid line shows the line-core (i.e. $\pm 0.02nm$ around the line-center). Error bars indicate the noise (1-σ), including both the photon noise and the read-out noise, and are shown in blue on the polarization signals.

Spatial binning along the slit was required to cancel out the local anisotropy of the Sun. This summation was also needed to reduce the noise due to the low number of photons measured during the short observing time. Figure 8.12 shows the Lyman-α profile for a full slit summation (i.e. 360 pixels, except for the very edge of the slit) in both the channels. The Q'/I' and U'/I' are shown with the corresponding noise (i.e. one σ error-bars, composed of both the photon noise and the read-out noise from the cameras). The noise is smaller in the line core (i.e. 0.01%), and larger in the wings due to the low intensity (i.e. 0.05%). A clear polarization signal remains in the wings, much larger than the noises. The polarization signal for the summed line-core, hereafter defined as the band $\pm$0.02nm from the line-center (i.e. central minimum in intensity), is close to the zero polarization level (below $\pm$0.05%). This result is different from the spurious polarization offset derived from the pre-flight polarization calibration, as shown by the horizontal red dashed lines in Figure 8.12 (see Section 6.4).

This first result indicated a smaller than expected spurious polarization level of the instrument. However, although the fluctuations from solar origin might be mostly cancelled out by a full slit summation, a proper quantification of the error for the line-core is required. The standard deviation was used to estimate the solar fluctuations along the slit, and is displayed onto the histograms of the polarization signals for the integrated line-core in Figure 8.13. The error on the polarization due to the solar fluctuations σ for the full slit was around 0.20%.

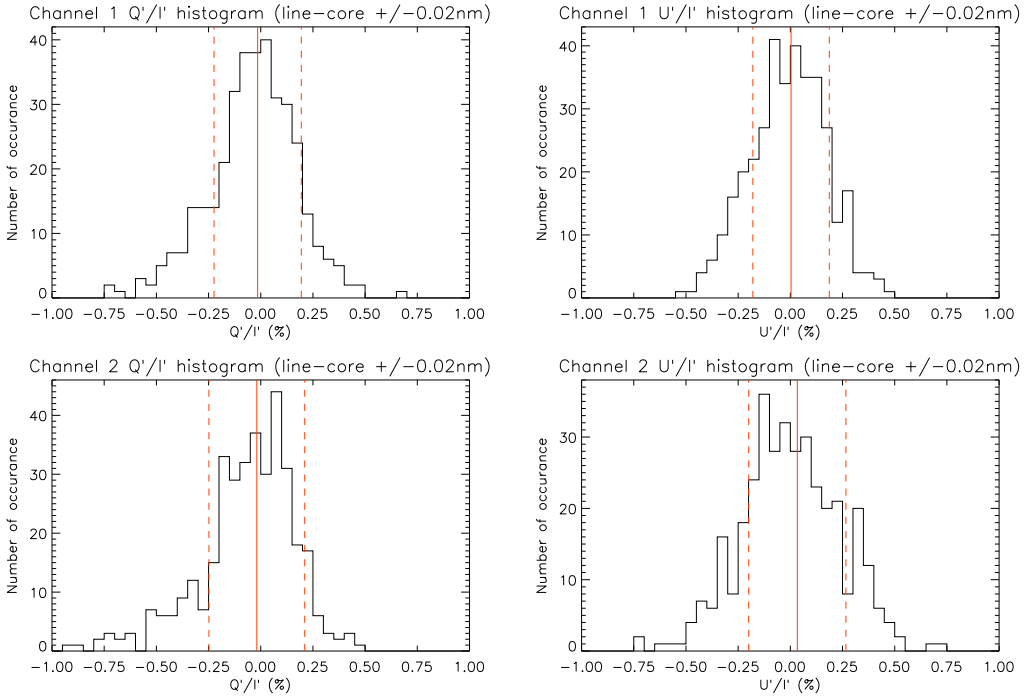

Figure 8.13: Histogram of the Q'/I' and U'/I' polarization signals along the slit for both the channels for the integrated line-core. Wavelength summing was performed at $\pm$0.02nm around the line-center. The $\pm\sigma$ from the standard deviation are shown by two vertical dashed red lines around the average value (vertical solid red).

The evolution of the solar fluctuations σ as a function of the number of pixel spatially summed was confirmed experimentally: for each number of pixel summing n_{pixel}, n_{pixel} were randomly selected, summed (for the three Stokes parameters) and removed from the slit until the remaining number of slit was smaller than n_{pixel}. The standard deviation was used to calculated the variation (σ_t) of the Q'/I' and U'/I' calculated from this pixel summing along the slit. This process was repeated $N = 100$ times, and the solar fluctuations σ for each n_{pixel} was calculated as $\left(\sum_N \sigma_t\right)/N$. Results are shown in Figure 8.14 and are consistent when compared to the theoretical prediction assuming the solar fluctuations σ decreases as the square root of the number of pixel summed (i.e. $\sqrt{n_{pixel}}$).

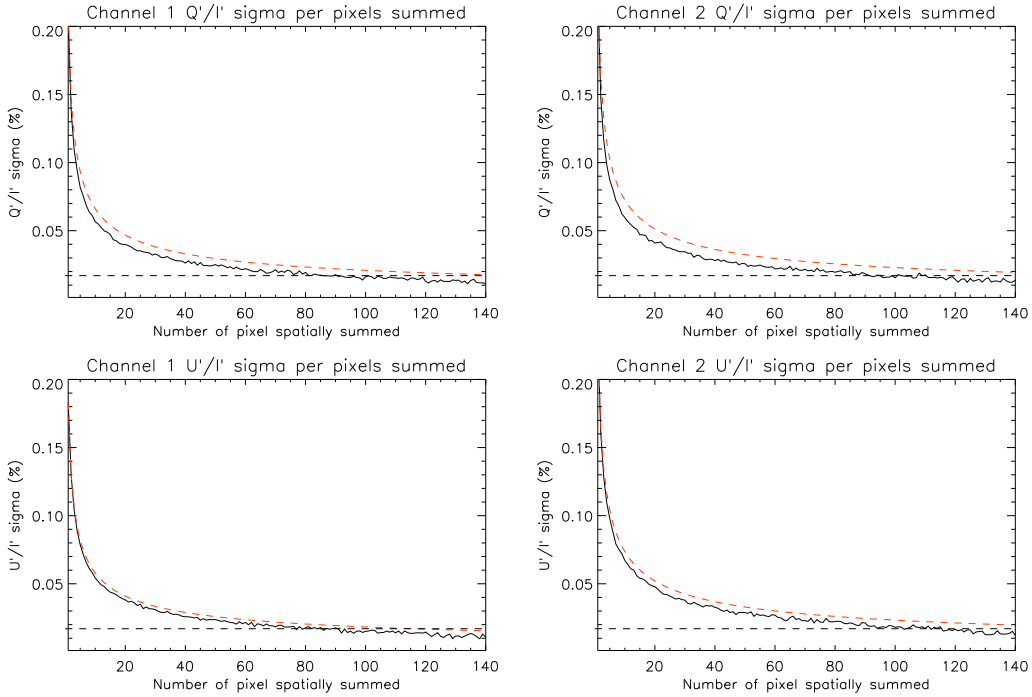

Figure 8.14: Evolution of the solar fluctuations σ as a function of the number of pixels summed spatially. The X-axis shows the number of pixels summed (n_{pixel}). Black solid line shows the σ calculated as the averaged σ_t (i.e. out of $N = 100$ values). For each n_{pixel}, the σ_t were obtained with the standard deviation of pixels randomly selected and summed along the slit. This process was repeated N times. The red dashed line shows the theoretical decrease of σ, taken as the σ for $n_{pixel} = 1$ divided by $\sqrt{n_{pixel}}$. Horizontal dashed line shows the 0.017% accuracy required on the spurious polarization.

The final spurious polarization level for the full slit summation measured during the flight at disc center are reported in Table 8.2, with error calculated as the standard deviation along the slit divided by the square root of the number of pixel summed. Note that this error also includes the photon noise and read-out noise, as it is derived from the data. Based on the tolerance from the pre-flight polarization calibration (Chapter 6, [38]), the accuracy on the spurious polarization is required to be <0.017%, which was satisfied as shown by Table 8.2.

Table 8.2: Final spurious polarization level for the flight, estimated as the full slit summation of the line-core. The 1-σ error is calculated as the standard deviation along the slit divided by the square root of the number of pixels.

	Q'/I' (%)	U'/I' (%)
Channel 1	-0.015 ± 0.012	0.003 ± 0.014
Channel 2	-0.019 ± 0.012	0.033 ± 0.014

Although the solar fluctuations could not be properly cancelled with a smaller than ∼120 pixels summing, an estimating of the spurious polarization at different location along the slit was still performed. The slit was spatially summed every 60 pixels, creating six regions along the slit. The standard deviation was used to estimate the corresponding solar fluctuations σ from each region. Figure 8.15 shows the polarization profiles along the slit, revealing variations larger than the errors. Q'/I' for both the channel, as well as U'/I' for channel 2, show a non-linear trend (i.e. local peak) which might indicate that the solar fluctuations could not be fully removed within the corresponding region of the slit. Hence, the remaining polarization signal might come from the solar structures and not from the instrument's spurious polarization. From this figure, no clear conclusion can be drawn about a possible gradient of the spurious polarization along the slit, although it seems within a ±0.1% range from the derived value in Table 8.2. No significant changes were expected along the slit from the pre-flight calibration and this was re-discussed in Section 8.4, where the explanations of the difference between in-flight and pre-flight spurious polarization level are presented.

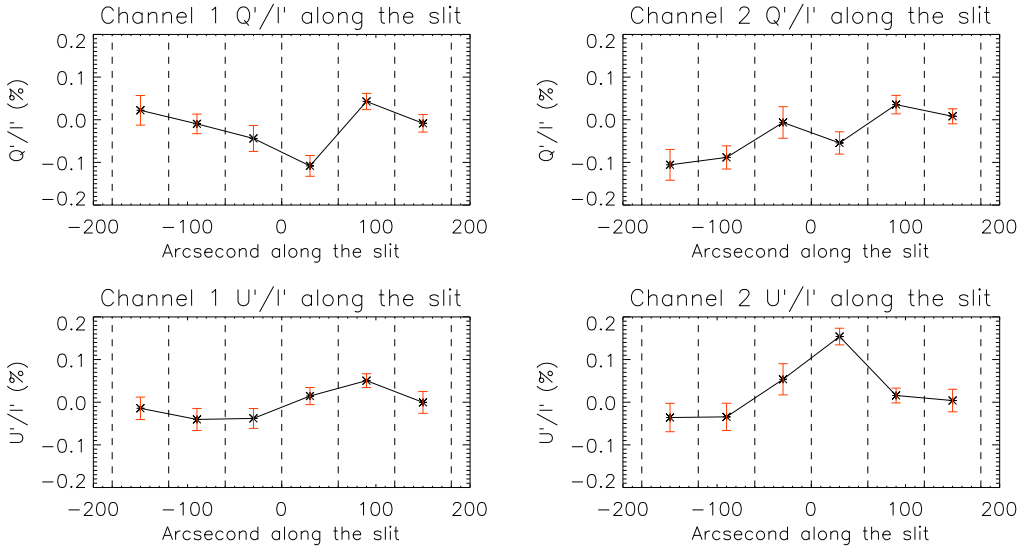

Figure 8.15: Q'/I' and U'/I' polarization signals along the slit, averaged every 60 pixels. The red error bar shows the standard deviation of these values (1-σ), calculated as the standard deviation on each 60-pixel regions.

8.4 Differences with the pre-flight calibration

Table 8.2 clearly revealed a smaller spurious polarization level compared to the one from the pre-flight calibration, where a shift by $\pm 0.2\%$ in Q'/I' and by $\mp 0.05\%$ in U'/I' were expected, for channel 1 and channel 2, respectively. After further investigation, a possible origin for this discrepancy was pinpointed to an erroneous treatment of the spurious intensity, i.e. the x_{10} and x_{20} terms in the response matrix, in opposition to the spurious polarization. These terms represent the cross-talks from Stokes Q and U to Stokes I', as recalled by Equation (8.2).

$$\begin{pmatrix} Q'/I' \\ U'/I' \end{pmatrix} \equiv \begin{pmatrix} q' \\ u' \end{pmatrix} = \frac{\begin{pmatrix} x_{01} & x_{11} & x_{21} \\ x_{02} & x_{12} & x_{22} \end{pmatrix}}{1 + x_{10}q + x_{20}u} \begin{pmatrix} 1 \\ q \\ u \end{pmatrix} \tag{8.2}$$

In the analysis of the pre-flight calibration data (see Chapter 6), these terms were considered as an additional error on the spurious polarization, scale factor and azimuth error terms and were only roughly estimated using the intensity recorded for different polarization inputs (see Section 6.3.6). These terms were neglected during the fitting of the response matrix elements, and only considered as a fixed error afterwards. However, another interpretation can be drawn when considering these terms directly multiplying the measured polarization. Equation (8.3) illustrates this idea: one can easily see that the measured polarization can be greatly affected by the incoming polarization (i.e. q or u), especially during the pre-flight calibration in which the polarization input was almost perfectly polarized. This effect also depends on the sign of the polarization input and produces a difference in the measured polarization for opposite input polarization, for example the measured q' for a $+Q$ and $-Q$ input. In the previous analysis of the pre-flight calibration data, differences of the measured polarization for opposite input polarization were observed and were interpreted as the spurious polarization, but might actually have been produced by the spurious intensity.

$$(1 + x_{10}q + x_{20}u) \begin{pmatrix} q' \\ u' \end{pmatrix} = \begin{pmatrix} x_{01} & x_{11} & x_{21} \\ x_{02} & x_{12} & x_{22} \end{pmatrix} \begin{pmatrix} 1 \\ q \\ u \end{pmatrix} \tag{8.3}$$

The spurious intensity had to be more precisely determined from the pre-flight calibration measurements. The simplest way is to get these terms from the intensity difference among the different polarization inputs. However, using this method from two different measurements was not suitable for a precise estimation of these terms since the input intensity from the light-source also fluctuates between measurements. The stability of the light-source intensity was measured to decrease by $\sim$2% over a one hour period of the light-source being on. As the measurements with opposite polarities (i.e. $\pm Q$ and $\pm U$) were recorded 30 minutes apart, a $\sim$1% error can be expected on these matrix elements. Therefore, a more suitable method was required for estimating the x_{10} and x_{20} terms using the measurements from the pre-flight calibration.

For this purpose, a new least-square fitting method was applied on the waveplate method measurements (see Section 6.4.2). The two rows of matrix element were fitted as shown in Equation (8.4). The input polarization states q and u were taken a fixed parameter during the fitting and were calculated considering a perfect input from the light-source, changed depending on the LS half-waveplate orientation with a retardance δ=184.4° (see Section 6.4.2.3).

$$q' = \frac{x_{01} + x_{11}q + x_{21}u}{1 + x_{10}q + x_{20}u} \qquad u' = \frac{x_{02} + x_{12}q + x_{22}u}{1 + x_{10}q + x_{20}u} \tag{8.4}$$

As seen during the pre-flight calibration, the accuracy on the "major terms" was better than the accuracy on the "minor terms" by one order of magnitude (see Section 6.3.5). However, applying the fitting to only the "major terms" measurements raised some issues. At first, the x_{10} and x_{20} terms are present in both the equations and therefore the fitting has to be performed on both the equations simultaneously. For a given measurement, if q' is the "major terms", u' is the "minor terms" by definition, and oppositely. Additionally, because the spurious intensity have a similar effect as the spurious polarization (i.e. offset of the polarization level), fitting by only using the "major terms" for each equation independently does not work: the fitting process cannot converge due to these two competing parameters.

Hence, both the "major terms" and the "minor terms" from each measurement have to be used in both the equations simultaneously. For this purpose, the merit function χ^2 to be minimized by the fitting was defined as shown in Equation (8.5).

$$\chi^2 = \sum_{n=1}^{16} w_n (q'_n - f_{q'}(q_n, u_n))^2 + \sum_{n=1}^{16} w'_n (u'_n - f_{u'}(q_n, u_n))^2 \tag{8.5}$$

In this equation, q'_n and u'_n correspond to the measured Q'/I' and U'/I' for the nth measurements out of the 16 measurements performed for a given orientation of the light-source (i.e. full rotation of the LS half-waveplate). $f_{q'}(q_n, u_n)$ refers to the estimated Q'/I' calculated using the left expression in Equation (8.4), for a given input (i.e. q_n and u_n, depending on the light-source position and LS half-waveplate orientation) and set of parameters x_{01}, x_{11}, x_{21}, x_{10} and x_{20}. On the other hand, $f_{u'}(q_n, u_n)$ is the estimated U'/I' calculated from the right expression in Equation (8.4), for the parameters x_{02}, x_{12}, x_{22}, the same parameters x_{10} and x_{20} and the same fixed input q_n and u_n. Finally, w_n and w'_n are weighting factors depending on whether which of q'_n or u'_n is the "major terms" in the nth measurements. Gaussian weighting (i.e. instrumental) was considered, defined as $1/\sigma^2$ with σ being the accuracy of the "major" and "minor" terms (i.e. 10^{-4} and 10^{-3}, respectively, from Section 6.3.5). This weighting system favorizes the "major terms" measurements while still including the influence of the "minor terms" measurements in the χ^2 calculation. The eight parameters (i.e. namely x_{10}, x_{20}, x_{01}, x_{11}, x_{21}, x_{02}, x_{12} and x_{22}) were obtained by minimizing the merit function using the four sets of 16 measurement taken with the light-source in $+Q_{0°}$, $+U_{45°}$, $-Q_{90°}$ and $-U_{315°}$ configurations (Section 6.2.4). The global minimum of the eight-dimensions hyperspace was found using a gradient-expansion algorithm to compute a non-linear least squares fitting of the χ^2. The fitting initial guesses were set to zero for the x_{10}, x_{20}, x_{01} and x_{02} terms, and to their values derived by the last analysis for the scale factors and azimuth error terms (see Section 6.4.4).

The fitting converged to similar parameters for the four sets of measurements at the center of the slit, as shown in Table 8.3. The results showed non-zero spurious intensity terms, and indicated a much smaller spurious polarization level than from the previous fitting method applied in Chapter 6. Additionally, the scale factor and azimuth error terms were obtained with similar amplitudes as previously derived. Note that the 0.017% on the spurious polarization terms was not reached, probably due to cross-talks between the (x_{10} & x_{20}) and the (x_{01} & x_{02}) terms, as they both a similar effect on the measured polarization and are competing parameters in the fitting. Nevertheless, this result seems to indicate a spurious polarization level smaller than 0.1%, and a non-zero x_{10} and x_{20} terms.

The larger amplitude of the x_{10} term compared to the x_{20} term can be quantitatively understood from the equations from the Mueller matrix of the instrument, as shown by Equation

(A.4) and Equation (A.5) from Appendix A. In these equations, the intensity measured on each exposure is affected by a contribution from Stokes Q if the retardance of the PMU half-waveplate is not exactly 180°. This contribution only comes from Stokes Q due to the orientation of the polarization analyzers with respect to the polarization coordinate system, has an opposite sign for each channel and is not modulated by the PMU rotation. Hence, this contribution should cancel out when demodulating the measured Q' and U', but does affect the measured I'. A simple estimation using these equations shows that the measured x_{10} term can be explained by considering a retardance δ for the PMU half-waveplate equal to 176.3°, although this value is slightly smaller than the measured retardance, including error (i.e. 178.8°±1.3°).

Table 8.3: Response matrix elements at the center of the slit, derived by minimizing the merit function shown in Equation (8.5). Top table is for channel 1 and bottom table is for channel 2. Error was derived as the maximum difference from the average value. LS refers to Light-source.

Channel 1	x_{10}	x_{20}	x_{01}	x_{02}	x_{11}	x_{22}	x_{12}	x_{21}
$+Q_{0°}$ input	-0.0022	0.0005	-0.0002	0.0000	0.9764	0.9762	-0.0118	0.0124
$+U_{45°}$ input	-0.0019	0.0008	0.0004	0.0004	0.9765	0.9762	-0.0085	0.0089
$-Q_{90°}$ input	-0.0022	-0.0001	0.0001	-0.0004	0.9773	0.9771	-0.0081	0.0084
$-U_{315°}$ input	-0.0018	0.0005	0.0003	0.0000	0.9757	0.9755	-0.0067	0.0060
Mean	-0.0020	0.0004	0.0002	0.0000	0.9765	0.9763	-0.0088	0.0089
Error (±)	0.0002	0.0005	0.0003	0.0004	0.0009	0.0008	0.0031	0.0035

Channel 2	x_{10}	x_{20}	x_{01}	x_{02}	x_{11}	x_{22}	x_{12}	x_{21}
$+Q_{0°}$ input	0.0018	-0.0002	-0.0003	0.0002	0.9712	0.9710	-0.0071	0.0076
$+U_{45°}$ input	0.0027	-0.0002	0.0003	0.0003	0.9703	0.9700	-0.0050	0.0053
$-Q_{90°}$ input	0.0022	-0.0009	0.0002	-0.0005	0.9710	0.9709	-0.0078	0.0081
$-U_{315°}$ input	0.0025	-0.0004	0.0003	0.0002	0.9707	0.9704	-0.0012	0.0006
Mean	0.0023	-0.0004	0.0001	0.0001	0.9708	0.9706	-0.0052	0.0054
Error (±)	0.0005	0.0005	0.0004	0.0005	0.0005	0.0006	0.0040	0.0048

The relevancy of the set of matrix elements shown in Table 8.3 was tested by changing the weights applied on the fitting to Poisson weights (i.e. statistical) defined as $1/\sigma$, and to removing the weights (i.e. w_n and w'_n equal to unity). The results for both the fittings provided exactly the same values for the eight matrix elements, indicating that this set of parameters is statistically relevant. As comparison, the same fittings were performed by forcing the x_{10} and x_{20} to be zero (i.e. similar to the last analysis of the pre-flight polarization calibration). The resulting matrix elements for the Gaussian weighting were consistent with the results from Chapter 6. However, results on the spurious polarization terms diverged significantly for the Poisson weights and without weighting, as shown in Figure 8.16. The scale factor and azimuth error terms were derived with similar values for all three types of weighting. This result indicates that the solution of the fitting when forcing the x_{10} and x_{20} to be zero is less stable than when using the x_{10} and x_{20} terms.

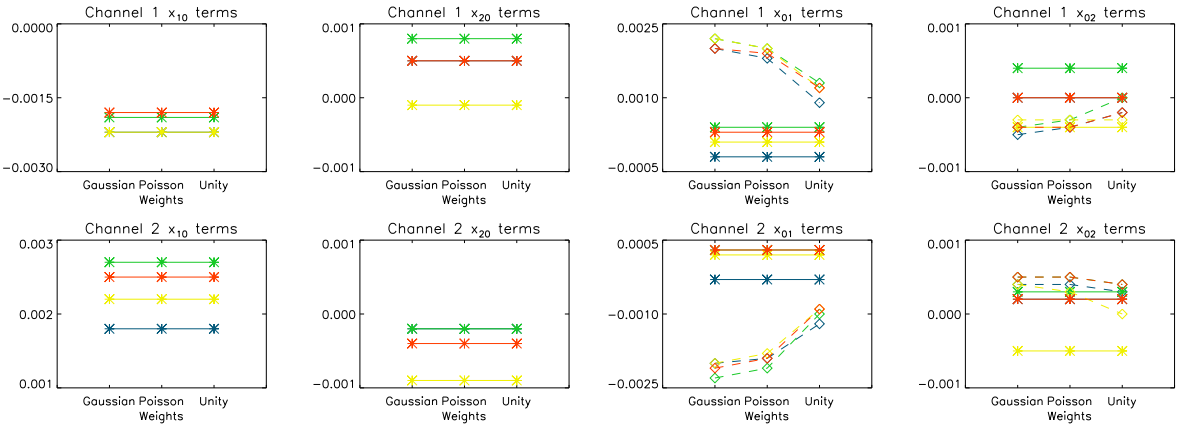

Figure 8.16: Derived x_{10}, x_{20}, x_{01} and x_{02} for three different weightings of the fitting, with (solid lines) and without the x_{10} and x_{20} terms (dashed line, i.e. set to zero) for both the channels. Color indicates the light-source orientation for each measurement: $+Q$ input (blue), $+U$ input (green), $-Q$ input (yellow) and $-U$ input (red).

After ensuring its validity, the same fitting method with Gaussian weights was applied to the waveplate method measurements recorded at the top and bottom of the slit, with light-source in $+Q_{0°}$ and $+U_{45°}$ configurations. Note that only a half-rotation of the LS half-waveplate was performed for the data set taken with the light-source in $+U_{45°}$ configuration (i.e. eight measurements). Results from both light-source orientation were average, and shown in Figure 8.17. Variations along the slit are around 0.1% for the x_{10}, x_{20}, x_{01} and x_{02} terms, which is of the same order as the measurement error determined for the eight-parameters fitting. The trends shown in Figure 8.17 indicated a gradient of the x_{01} terms in both the channels, which cannot be seen from the in-flight measurements shown in Figure 8.15.

Based on the error estimations, a possible gradient of the spurious polarization terms along the slit is smaller than $\pm 0.1\%$, from the bottom to the top of the slit. On the other hand, the scale factor and azimuth error terms were estimated with similar amplitudes as previously derived in Chapter 6, with a gradient in the azimuth error terms for channel 2 due to the light-source optics as discussed in Section 6.3.4.

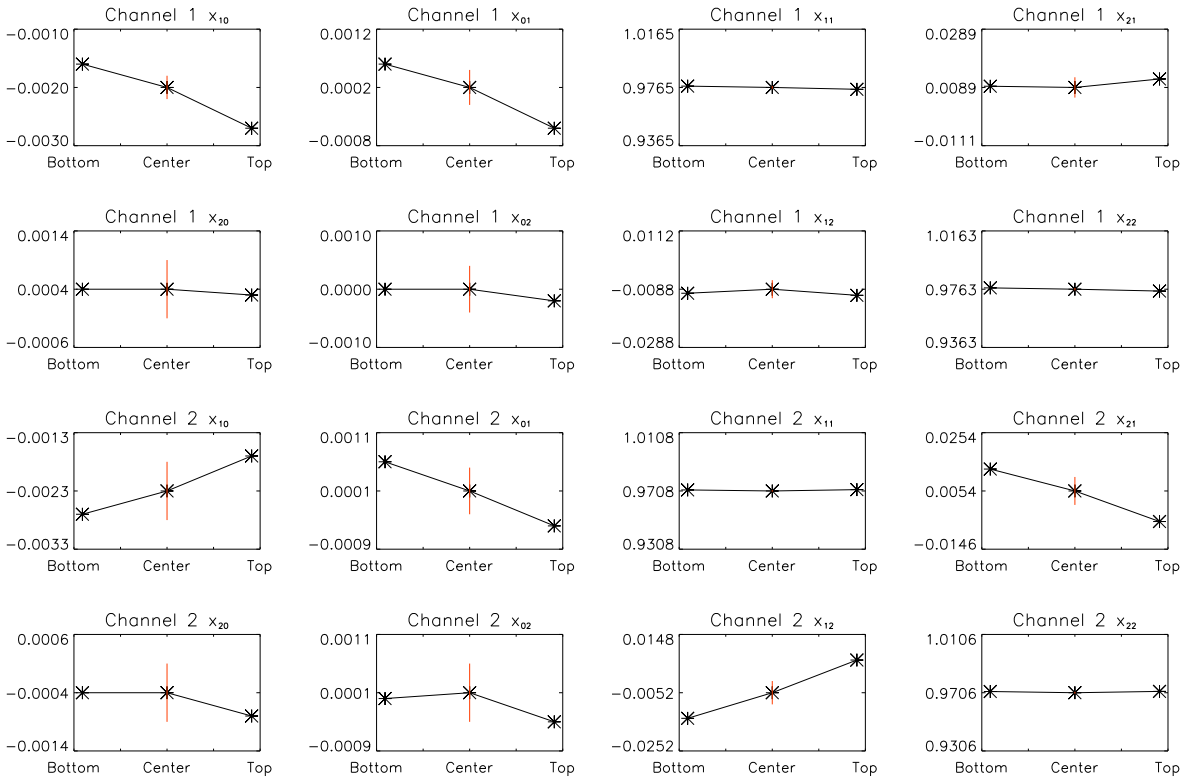

Figure 8.17: Evolution of the response matrix elements along the slit for both the channels. Vertical red line shows the error derived at the center of the slit presented in Table 8.3 ($\pm$1-σ).

In summary, a more appropriate interpretation of the spurious intensity was considered, giving a more correct response matrix for the instrument. This newly derived response matrix was confirmed to better fit the instrument than the previously derived response matrix from Chapter 6 by applying a different least-square fitting method to the pre-flight polarization calibration measurements recorded with the waveplate method. These results indicated that the spurious intensity can affect the polarization level depending on the degree of polarization input to the instrument, and also confirmed a spurious polarization level smaller than 0.1%. However, the 0.017% accuracy on the spurious polarization could not be ensure because both the “major terms" and the “minor terms" had to be used for the least-square fitting. This was due to a limitation of the polarization calibration measurements because the effect of the x_{10} and x_{20} terms was underestimated when designing the pre-flight polarization calibration experiment: only the spurious polarization, scale factor and azimuth error terms were considered to be relevant. Nevertheless, the results from the newly derived response matrix elements still provided an interpretation for the spurious polarization levels measured during the flight and ensured the 0.1% polarization accuracy of the instrument.

8.5 Correction of the polarization signal and error tranfer

The response matrix of the instrument **X** was finally determined within its required accuracy by combining the results from the new analysis of the pre-flight calibration with the spurious polarization obtained in-flight, as summarized in Equation (8.6).

$$\begin{aligned} X_1 &= \begin{pmatrix} 1 & -0.0020 & 0.0004 \\ -0.00015 & 0.9765 & 0.0089 \\ 0.00003 & -0.0088 & 0.9763 \end{pmatrix} \pm \begin{pmatrix} 0 & 0.0002 & 0.0005 \\ 0.00012 & 0.0020 & 0.0040 \\ 0.00014 & 0.0037 & 0.0020 \end{pmatrix} \\ X_2 &= \begin{pmatrix} 1 & 0.0023 & -0.0004 \\ -0.00019 & 0.9708 & 0.0054 \\ 0.00033 & -0.0052 & 0.9706 \end{pmatrix} \pm \begin{pmatrix} 0 & 0.0005 & 0.0005 \\ 0.00012 & 0.0019 & 0.0052 \\ 0.00014 & 0.0045 & 0.0019 \end{pmatrix} \end{aligned} \tag{8.6}$$

The response matrix elements can be used to correct the measured polarization signals q' and u' in order to retrieve the polarization signals observed by the instrument q and u. The equations linking these quantities were derived from $\mathbf{S'}=\mathbf{XS}$ considering $S'=(1, Q'/I', U'/I')^\top=(1, q', u')^\top$ and $S=(1, q, u)^\top$ as:

$$\begin{aligned} q &= \frac{-\left[(q'-x_{01}) - \frac{(u'-x_{02})(x_{20}q'-x_{21})}{(x_{20}u'-x_{22})}\right]}{\left[(x_{10}q'-x_{11}) - \frac{(x_{10}u'-x_{12})(x_{20}q'-x_{21})}{(x_{20}u'-x_{22})}\right]} \\ u &= \frac{-\left[(u'-x_{02}) - \frac{(q'-x_{01})(x_{10}u'-x_{12})}{(x_{10}q'-x_{11})}\right]}{\left[(x_{20}u'-x_{22}) - \frac{(x_{20}q'-x_{21})(x_{10}u'-x_{12})}{(x_{10}q'-x_{11})}\right]} \end{aligned} \tag{8.7}$$

The error on the corrected q and u was estimated taking into account the measurement error on the measured q' and u', as well as the error on each of the response matrix elements from Equation (8.6) using the error transfer formula shown in Equation (8.8) for q, and similarly for u.

$$\sigma_q = \sqrt{\sum_i \left(\frac{\partial q}{\partial x_i}\sigma_i\right)^2} \text{ where } x_i = q', u', x_{10}... \text{ and } \sigma_i = \sigma_{q'}, \sigma_{u'}, \sigma_{x_{10}}... \tag{8.8}$$

The partial derivatives of the two equations were calculated for all ten components. These partial derivatives express the importance (i.e. sort of scaling factor) of the corresponding error depending on the polarization signal measured. The partial derivatives of the corresponding Stokes parameter (e.g. $\delta q/\delta q'$ for σ_q) and spurious polarization (e.g. $\delta q/\delta x_{01}$ for σ_q) are the most dominant factors when considering a weakly polarized input (i.e. <10%), with values close to unity. Hence, the root sum square of the error on the Stokes parameters and the error on its corresponding spurious polarization matrix elements can be used as good approximation for the error transfer. However, for a larger polarization amplitude, the contributions from the partial derivative from the spurious intensity and scale factor increases. An example for the partial derivatives for the observed q as a function of the measured q' and u' is shown in Appendix D.

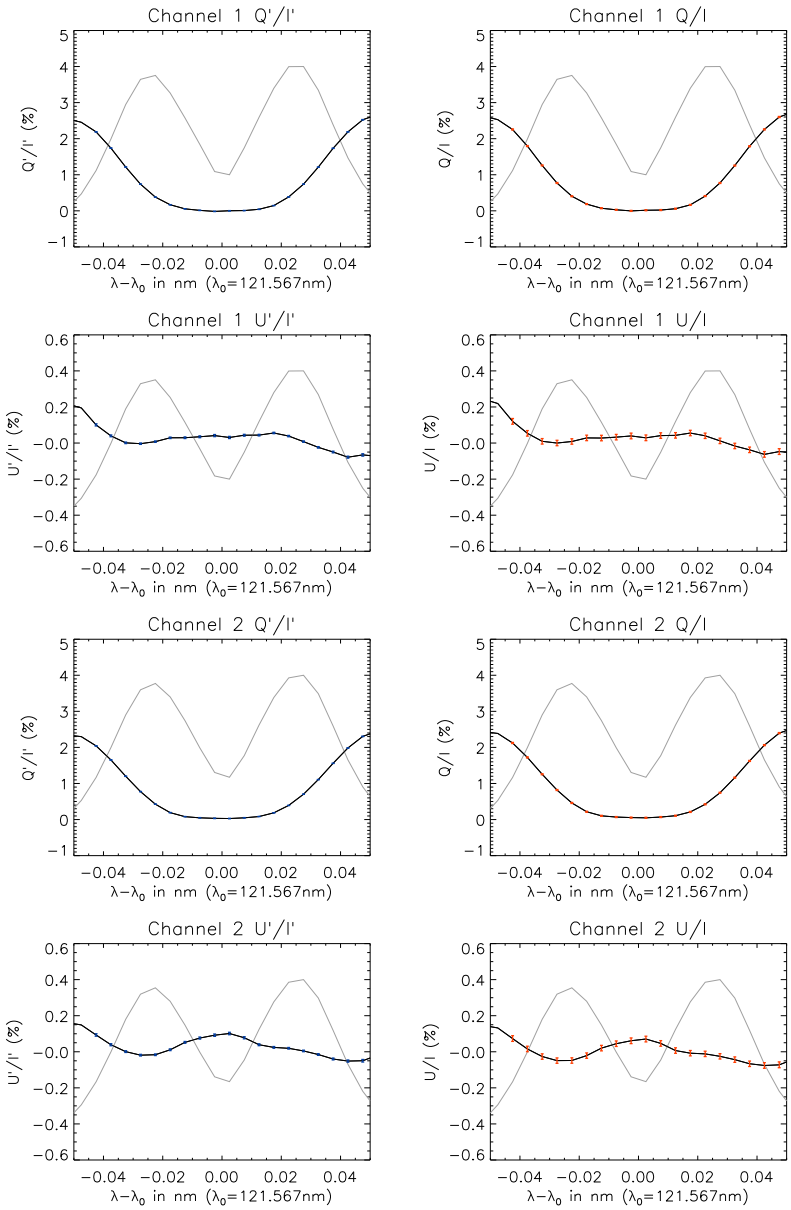

Figure 8.18: Demodulated polarization signal (left column) and corrected polarization signals (right column) as a function of wavelength for both the channels. The corresponding intensity profile is shown in the background to provide the location of the double peak and line-center. Blue error bars show the photon noise and read-out noise on the demodulated profiles. Red error bars show the combined error on the corrected profiles.

For demonstrating the achieved accuracy after correction, the polarization signals were demodulated from the limb observations by stacking 50 PMU rotations (i.e. 240s observation) and summing almost the entire slit (340 pixel) closer to the limb, from μ∼0.02 to μ∼0.53. A careful coalignment between the two channels was performed using interpolation to reach a subpixel precision. The correction was applied on polarization signals using the equations described previously. Figure 8.18 shows the demodulated and corrected profiles for both the channels. Note that the increase of the Q/I signal in the wings is positive since the $+Q$ direction is defined as along the slit and the slit was positioned perpendicularly to the limb. The effect of the correction on the demodulated polarization signal is small because the response matrix of the instrument is close to the identity matrix: changes in the line-core are ∼0.02% and mainly due to the spurious polarization offset. On the other hand, the differences in the wings are ∼0.1% due to the increase in polarization signal. Figure 8.19 shows the achieved accuracy on the corrected signal (i.e. error bars in Figure 8.18), using the error transfer method described previously to combine the photon noise, read-out noise and error on the response matrix. The achieve accuracy is mainly influenced by the photon noise, as its wavelength dependence indicates, but also by the accuracy achieved on the spurious polarization terms. Performing spectral summing could reduce the uncertainty further. Moreover, the accuracy on channel 2 is slightly worse than on channel 1 due to a difference in throughput between both the channels (i.e. different quantum efficiency of the CCDs). Note that the photon noise for Q/I and U/I is also slightly different since both polarization signals were not derived from exactly the same exposure (see demodulation scheme in Equation (8.1)) and therefore their respective intensity was slightly different.

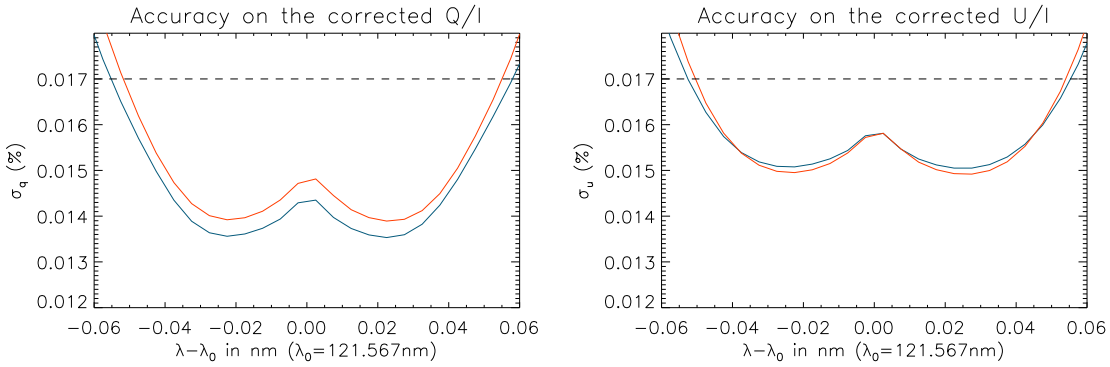

Figure 8.19: Accuracy achieved on the corrected Q/I and U/I as a function of wavelength for channel 1 (blue curve) and channel 2 (red curve). The horizontal dashed line shows the 0.017% accuracy level.

The accuracy of the correction can be estimated by comparing the polarization signals recorded in both the channels. Figure 8.20 shows a comparison between the corrected polarization signals in both the channels at the line-core. Differences remain between both the channels, and can be seen from pixel to pixel in the wavelength direction. Their amplitude can be sometimes larger than the recorded spurious polarization, both pre-flight and in-flight, and might be due to additional to spurious polarization created by $\mathrm{d}I/\mathrm{dt}$. Nevertheless, the profiles on both the channels overlap within a 2-σ accuracy. In addition, combining the polarization signals from both the channels might improve the overall polarization accuracy achieved by the instrument.

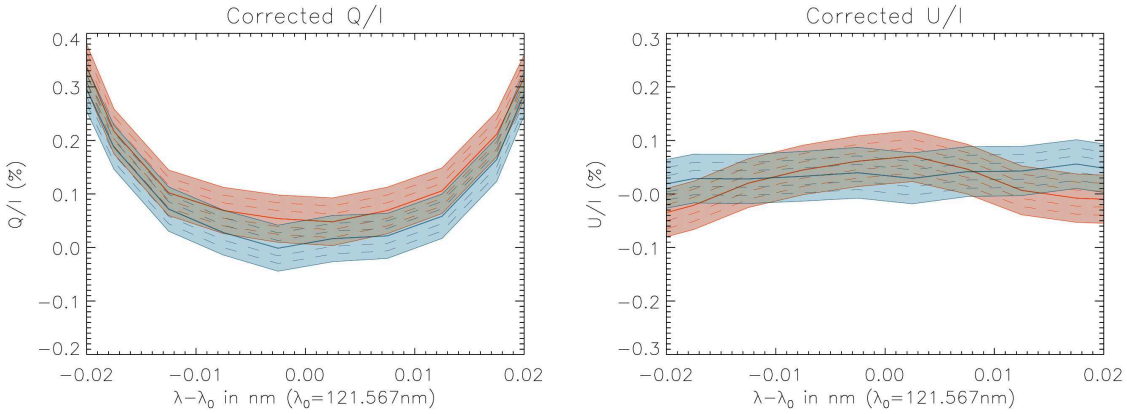

Figure 8.20: Comparison between corrected Q/I and U/I for channel 1 (blue) and channel 2 (red) at the line-core. The thick-line shows the recorded polarization signal, with dash-lines showing the 1-σ, 2-σ and 3-σ contour, with σ taken from Figure 8.19.

8.6 Conclusion

An in-flight polarization calibration of the instrument was performed using the observations conducted at the center of the solar disc. Non-zero polarization signals were observed in the line-wings during this 15s observation, indicating that local anisotropy creates scattering polarization even at disc center. A statistical approach was considered to effectively cancel out the polarization signals due to the solar structures by summing signal from pixels randomly selected along the slit. This method allowed to remove the polarization signals originated from the Sun and to estimate the spurious polarization levels of the instrument (i.e. the measured Q'/I' and U'/I' corresponding to the response matrix x_{01} and x_{02} terms, respectively), for both the channels. These terms were estimated to be below 0.05%, which was much smaller than the expected spurious polarization from the pre-flight calibration.

Investigations were conducted to understand the discrepancy between the measured spurious polarization terms during the pre-flight and in-flight calibration, and pointed out a misinterpretation of the spurious intensity terms. These terms were though to only imply an additional error on the other matrix elements (i.e. spurious polarization, scale factor and azimuth error terms) but were actually offsetting the measured polarization in a similar fashion as the spurious polarization, but depending on the degree of polarization of the incoming light. The response matrix elements were re-estimated with the x_{10} and x_{20} terms taken into account using a least-square fitting on

the pre-flight polarization calibration measurements performed with the waveplate method. This newly derived response matrix was confirmed to be a better fit for pre-flight measurements compared to the previously estimated response matrix, and indicated a spurious polarization level smaller than 0.05%. However, the 0.017% accuracy on the spurious polarization could not be reach, probably because the (x_{10} & x_{20}) and the (x_{01} & x_{02}) terms were competing parameters in the fitting. The scale factor and azimuth error terms were also confirmed with similar amplitude as previously derived. These results from the pre-flight calibration measurements matched the spurious polarization level estimated with the in-flight data. In addition, the larger x_{10} term compared to the x_{20} term could be quantitatively understood from the equations extracted from the Mueller matrix of the instrument if the PMU half-waveplate retardance differs from 180°.

The impact of the spurious intensity terms was not understood properly during, but also before, the pre-flight calibration. Therefore, the experiment was only designed to estimated the spurious polarization, scale factor and azimuth error terms, and not for accurately estimating these two terms. The lessons learned from this is that additional measurements should be performed for future similar pre-flight calibration. For example, using unpolarized light to directly measure the spurious polarization level. This could pass by the effect of the x_{10} and x_{20} terms and, combined with the measurement performed with fully polarized light, providing a clear determination between both these terms and the spurious polarization terms.

In conclusion, the spurious polarization derived from the in-flight data with a 0.017% accuracy (1-σ) was included in the final response matrix of the instrument, used to correct the flight observations performed at the limb. The other parameters (spurious intensity, scale factor and azimuth error terms) estimated from the pre-polarization calibration data were also included in the final response matrix, shown in Equation (8.6) with the number of digit corresponding to the required accuracy on each term and in the polarization coordinate system where $+Q$ is along the slit. This response matrix was tested for the correction of the polarization signals recorded during the observations at the solar limbs, using a proper error transfer method, and the resulting polarization signals between both channels overlap with a 2-σ accuracy, with σ around 0.015%. The effect of the spurious intensity was negligible during the flight since the signal was weakly polarized, and the achieved accuracy was mainly dominated by the error due to photon-noise and on the spurious polarization terms of the response matrix. This analysis ensured the 0.1% polarization accuracy of the instrument. The spatial and spectral resolutions of the instrument were also confirmed to be within the scientific requirements and expected performances from the pre-flight experiments by comparing with observations from other instruments.

Chapter 9

Conclusion

The work presented in this thesis resulted in a successful optical alignment and polarization calibration of the instrument. Innovative methods were developed to conduct the required experiments on the VUV-optimized instrument:

- The telescope was aligned with a He-Ne laser even though the narrow band filtering coating on its primary mirror only reflected around 3.5% of visible-light (Chapter 2.
- The spectro-polarimeter's off-axis mirrors were aligned in visible-light using a custom-made alignment grating to minimize the activities under vacuum, only finally aligning the flight grating Z-tilt and cameras focus position at Lyman-α (Chapter 3).
- An experiment was successfully designed and conducted to adjust the telescope focus position with respect to the slit by measuring the width of the slit after reflection in a double-pass configuration (Chapter 4).
- The alignment was controlled during the rocket-integration and vibration testing with two specific tests to measure the telescope focus position to the slit and the spectro-polarimeter spectral resolution (Chapter 7)
- An unprecedented polarization calibration at Lyman-α was performed under vacuum to estimate the spectro-polarimeter's response matrix (Chapter 6). This response matrix, composed of the spurious polarization (x_{01} and x_{02}), scale factor (x_{11} and x_{22}) and azimuth error (x_{21} and x_{12}) terms, was crucial to ensure the 0.1% polarization sensitivity of the instrument. Extensive investigations were conducted to estimate the errors on the polarization measurements and the influence of the Lyman-α light-source used for the calibration onto the resulting matrix elements. As a result, after carefully analysing the numerous measurements performed during the calibration and developing a novel method to minimize the errors from the polarization measurements, the response matrix was derived within its required tolerance.

These experiments ensured the instrument's spatial and spectral resolutions of the instrument, as well as its polarization accuracy. CLASP was successfully launched on September 3^{rd} 2015 and performed its scientific observations: at the solar disc center during ~15s and close to the limb (i.e. main science target) during ~240s. The disc center observations were used to provide an in-flight polarization calibration on the spurious polarization terms of the response matrix, as the solar polarization from scattering processes was cancelled out by spatially averaging enough pixel

along the slit at $\mu = 1$ (Chapter 8). The measured spurious polarization level was smaller than the expectation from the pre-flight calibration. Hence, the pre-flight polarization calibration measurements were re-investigated to understand the origin of the discrepancy and to provide a consistent response matrix. It appeared that the effect of the cross-talks from the observed linear polarization (i.e. Stokes Q and Stokes U) to the measured intensity (i.e. Stokes I') was misunderstood. During the pre-flight calibration, these two terms of the response matrix were neglected, as their effect was thought to only implied an additional error on the other matrix elements (i.e. the spurious polarization, scale factor and azimuth error terms), which was quantified by roughly estimating the x_{10} and x_{20} terms. However, it turned out that these two terms can significantly modify the measured intensity and therefore the measured polarization signal (i.e. Q'/I' and U'/I') in case of an highly polarized input, which was the case during the calibration:. the Lyman-α light-source provided a $\sim$100% polarized input. This effect happen to have a similar effect as the spurious polarization, offsetting the measured polarization signal for opposite polarization input (i.e. $\pm Q$ and $\pm U$). The measurements from the pre-flight calibration were recomputed, taking these two additional terms into account during the fitting, and the resulting response matrix was consistent with the spurious polarization level measured during the in-flight polarization calibration. However, the accuracy achieved on the spurious polarization with this method did not match the tight 0.017% tolerance, probably because both the $x_{10/20}$ and the $x_{01/02}$ terms were competing in the fitting. Nevertheless, this response matrix from the pre-flight measurements, combined with the spurious polarization terms derived from the in-flight calibration, successfully ensured the 0.1% polarization accuracy of the instrument. Finally, the spatial and spectral resolutions achieved during flight were confirmed to be consistent with the pre-flight expectation from the optical alignment by comparing the observations with other instruments.

The lessons learned during the preparation of the instrument are invaluable for the future experiments in the vacuum ultraviolet. This work successfully demonstrated that a polarimetric instrument in VUV is feasible, with an optical alignment almost entirely performed in visible-light. Experimental solutions were developed to pass-by the issues encounter during the preparation and achieved the requirements, which might be used as a guideline for the next VUV instrument. In addition, the optical alignment revealed an important issue on the off-axis mirrors' surface figure (i.e. periodic pattern), indicating that the requirement on the surface figure periodicity at various scales has to be controlled carefully to ensure a fine spatial and spectral resolution in VUV. Concerning the polarimetric capabilities, an unprecedented 0.1% polarization accuracy was achieved at Lyman-α, and the polarization calibration drastically improved the knowledge on the spectro-polarimeter performances, but also on the Lyman-α light-source used for the calibration. Although the initial results from the pre-flight polarization calibration provided erroneous spurious polarization terms to the response matrix, the issue was solved using the in-flight polarization calibration and confirmed by re-analyzing the pre-flight measurements. This misinterpretation revealed the importance of the x_{10} and x_{20} matrix elements, which were neglected during the pre-flight polarization calibration: the experiment configuration and measurements performed were not designed for properly determined these two terms. Nevertheless, the correct response matrix could still be estimated, although the tight accuracy on the spurious polarization could not be reached. This pointed out a flaw in the polarization calibration procedure, that could be easily resolve by adding an additional measurement to input almost unpolarized light into the spectro-polarimeter to directly measure the spurious polarization terms, by-passing the effect of the x_{10} and x_{20} terms. Such measurement could be performed by removing the two polarizers of the light-source and adjusting the Deuterium lamp position. The light-source half-waveplate could also be used for

changing the input in case the Lyman-α light was still weakly polarized. CLASP is proposed for a second flight, scheduled for 2018. The observed wavelength was changed to the magnesium II h&k lines around 280nm, implying to change the spectro-polarimeter's grating and the mirrors' coatings. Apart of those changes, the instrument preparation will be similar to the work presented in this thesis, which should therefore provide a useful guideline for CLASP2.

Appendix A

Mueller matrix of the instrument

The Mueller matrix links the incoming Stokes vector to the measured Stokes vector and can be calculated for CLASP as $M_{CLASP}(\alpha, \beta, \delta) = L(\alpha)R(\beta, \delta)$, where $L(\alpha)$ is the expression for a linear polarizer with orientation α shown in Equation (A.1) and $R(\beta, \delta)$ is the expression for a linear retarder with retardance δ and a fast-axis angle β as shown in Equation (A.2).

$$L(\alpha) = \frac{1}{2}\begin{pmatrix} 1 & \cos 2\alpha & \sin 2\alpha & 0 \\ \cos 2\alpha & \cos^2 2\alpha & cos2\alpha \sin 2\alpha & 0 \\ \sin 2\alpha & \cos 2\alpha \sin 2\alpha & \sin^2 2\alpha & 0 \\ 0 & 0 & 0 & 0 \end{pmatrix} \tag{A.1}$$

$$R(\beta, \delta) = \begin{pmatrix} 1 & 0 & 0 & 0 \\ 0 & \cos^2 2\beta + \sin^2 2\beta \cos\delta & \cos 2\beta \sin 2\beta(1 - \cos\delta) & -\sin 2\beta \sin\delta \\ 0 & \cos 2\beta \sin 2\beta(1 - \cos\delta) & \sin^2 2\beta + \cos^2 2\beta \cos\delta & \cos 2\beta \sin\delta \\ 0 & \sin 2\beta \sin\delta & -\cos 2\beta \sin\delta & \cos\delta \end{pmatrix} \tag{A.2}$$

Although the expression for the Mueller matrix $M_{CLASP}(\alpha, \beta, \delta)$ is quite complicated, only the intensity (i.e. Stokes I) can be measured by the cameras. Hence, only the first row of the matrix is important and the general expression of the intensity as a function of α, β and δ is:

$$\begin{aligned} I_{\alpha,\beta,\delta} = \frac{1}{2}\Bigg[I + \frac{1}{2}\Big(Q\cos 2\alpha + U \sin 2\alpha\Big)\Big(1 + \cos\delta\Big) + \sin\delta \sin(2\alpha - 2\beta)V \\ + \frac{1}{2}(1 - \cos\delta)\Big[(Q\cos 2\alpha - U\sin 2\alpha)\cos 4\beta \\ + (Q\sin 2\alpha + U\cos 2\alpha)\sin 4\beta\Big]\Bigg] \end{aligned} \tag{A.3}$$

The expression of the intensity is simplified since $\alpha = 90°$ for channel 1 and $\alpha = 0°$ for channel 2. The expression also has to be integrated on β, to account for the continuous motion of the PMU half-waveplate. This is shown in Equation (A.4) and Equation (A.5) with x_i the initial angle of the half-waveplate, and x_f its final angle, for any possible angular position. The factor in front of the integral is a normalization for the angular movement.

$$\begin{aligned}\int_{x_i}^{x_f} I_{\beta,\delta,Channel1} d\beta =& \frac{1}{2}\Bigg[\Bigg[I - \frac{Q}{2}(1+\cos\delta)\Bigg] \\ &- \frac{1}{(x_f - x_i)}\frac{1}{2}\sin\delta V[\cos 2x_f - \cos 2x_i] \\ &+ \frac{1}{(x_f - x_i)}\frac{1}{8}(1-\cos\delta)\Big[- Q[\sin 4x_f - \sin 4x_i] \\ &+ U[\cos 4x_f - \cos 4x_i]\Big]\Bigg]\end{aligned} \tag{A.4}$$

$$\begin{aligned}\int_{x_i}^{x_f} I_{\beta,\delta,Channel2} d\beta =& \frac{1}{2}\Bigg[\Bigg[I + \frac{Q}{2}(1+\cos\delta)\Bigg] \\ &+ \frac{1}{(x_f - x_i)}\frac{1}{2}\sin\delta V[\cos 2x_f - \cos 2x_i] \\ &+ \frac{1}{(x_f - x_i)}\frac{1}{8}(1-\cos\delta)\Big[Q[\sin 4x_f - \sin 4x_i] \\ &- U[\cos 4x_f - \cos 4x_i]\Big]\Bigg]\end{aligned} \tag{A.5}$$

Assuming a perfect half-waveplate with retardance $\delta = 180°$, the expression of the measured intensity for four consecutive exposures taken every 22.5° can be derived as:

$$\begin{aligned} I_{1,Channel1} &= \frac{1}{2}\left[I + \frac{2}{\pi}[-Q - U]\right] \quad I_{1,Channel2} = \frac{1}{2}\left[I + \frac{2}{\pi}[+Q + U]\right] \\ I_{2,Channel1} &= \frac{1}{2}\left[I + \frac{2}{\pi}[+Q - U]\right] \quad I_{2,Channel2} = \frac{1}{2}\left[I + \frac{2}{\pi}[-Q + U]\right] \\ I_{3,Channel1} &= \frac{1}{2}\left[I + \frac{2}{\pi}[+Q + U]\right] \quad I_{3,Channel2} = \frac{1}{2}\left[I + \frac{2}{\pi}[-Q - U]\right] \\ I_{4,Channel1} &= \frac{1}{2}\left[I + \frac{2}{\pi}[-Q + U]\right] \quad I_{4,Channel2} = \frac{1}{2}\left[I + \frac{2}{\pi}[+Q - U]\right] \end{aligned} \tag{A.6}$$

The measured Stokes Q'/I' and U'/I' shown in Equation (1.4) can be retrieved with a linear combination of the measured intensity from Equation (A.6). Note that Equation (1.4) is multiplied by $\pi/2$ to cancel the $2/\pi$ coming out from Equation (A.6) due to the continuous rotation of the PMU half-waveplate.

Appendix B

Zernike polynomials

The Zernike polynomials are mathematical expressions useful for modelling the wavefront error deformations. The general formula is given by Equation (B.1), where m and n are non-negative integers with $n \geq m$, ϕ is the azimuthal angle and ρ is the radial distance $0 \leq \rho \leq 1$. For simplicity, Table B.1 shows the expressions for the first eight polynomials, and are displayed in Figure B.1.

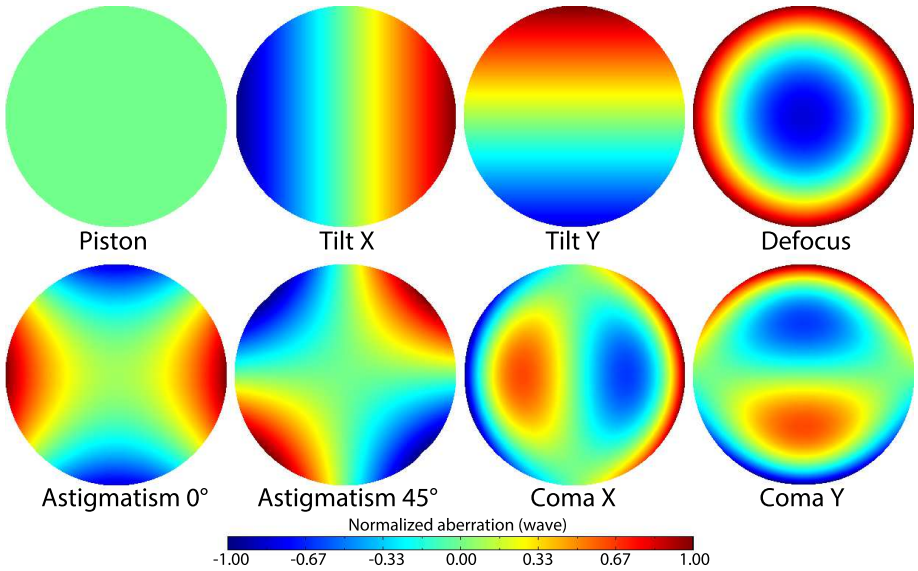

Figure B.1: Example of the eight first Zernike polynomial.

$$
\begin{aligned}
Z_n^m(\rho,\phi) &= R_n^m(\rho)\cos(m\phi) \text{ for } m \geq 0 \\
Z_n^m(\rho,\phi) &= R_n^{-m}(\rho)\sin(-m\phi) \text{ for } m < 0 \\
\text{where } R_n^m(\rho) &= \sum_{k=0}^{\frac{n-m}{2}} \frac{(-1)^k(n-k)!}{k!(\frac{n+m}{2}-k)!(\frac{n-m}{2}-k)!}\rho^{n-2k}
\end{aligned}
\tag{B.1}
$$

Table B.1: Expression of the eight first Zernike polynomials.

Radial degree n	Azimuthal degree m	Z_n^m	Aberration name
0	0	1	Piston
1	+1	$\rho\cos\theta$	Tip (X-tilt)
1	−1	$\rho\sin\theta$	Tilt (Y-tilt)
2	0	$(2\rho^2-1)$	Defocus
2	+2	$\rho^2\cos 2\theta$	Astigmatism 0°
2	−2	$\rho^2\sin 2\theta$	Astigmatism 45°
3	+1	$(3\rho^3-2\rho)\cos\theta$	Coma X
3	−1	$(3\rho^3-2\rho)\sin\theta$	Coma Y

Appendix C

Surface figure problem on the off-axis parabolic mirrors.

A periodic pattern was observed in the surface figure of both the off-axis parabolic mirrors, with ±10nm amplitude as shown in Figure C.1.

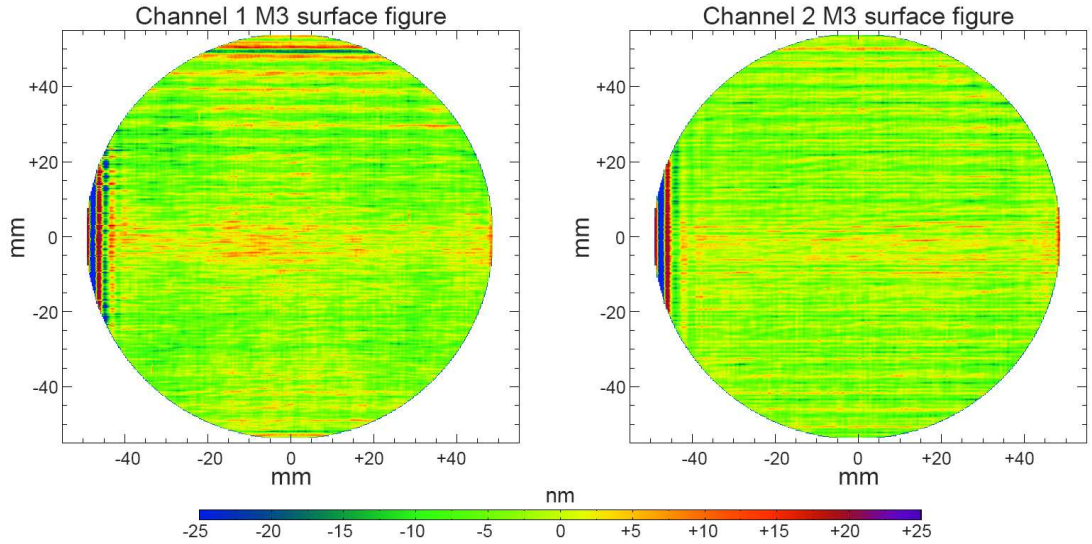

Figure C.1: Surface figure of channel 1's (left) and channel 2's (right) M3s. The scaling was limited to ±25nm, meaning some deformations greater than ±25nm are represented as ±25nm. The actual peak-to-valley for both mirrors was around ±90nm. X-axis is vertical.

This periodic pattern in the vertical direction (X-axis) created a diffraction effect, especially for the shortest wavelength. For this reason, this effect was not seen in the visible-light alignment of the spectro-polarimeter (632.8nm) but was observed at Lyman-α (121.6nm). The alignment of the Z-tilt for the Lyman-α grating was initially performed with these off-axis parabolic mirrors, and spots are shown in Figure C.2 and Figure C.3 for channel 1 and 2, respectively. The spots are shown for the various positions of the motorized rotating mechanism (i.e. grating Z-tilt adjustment), clearly showing the diffraction of the light in the spatial direction (X-axis) due to the periodic pattern of

the surface figures.

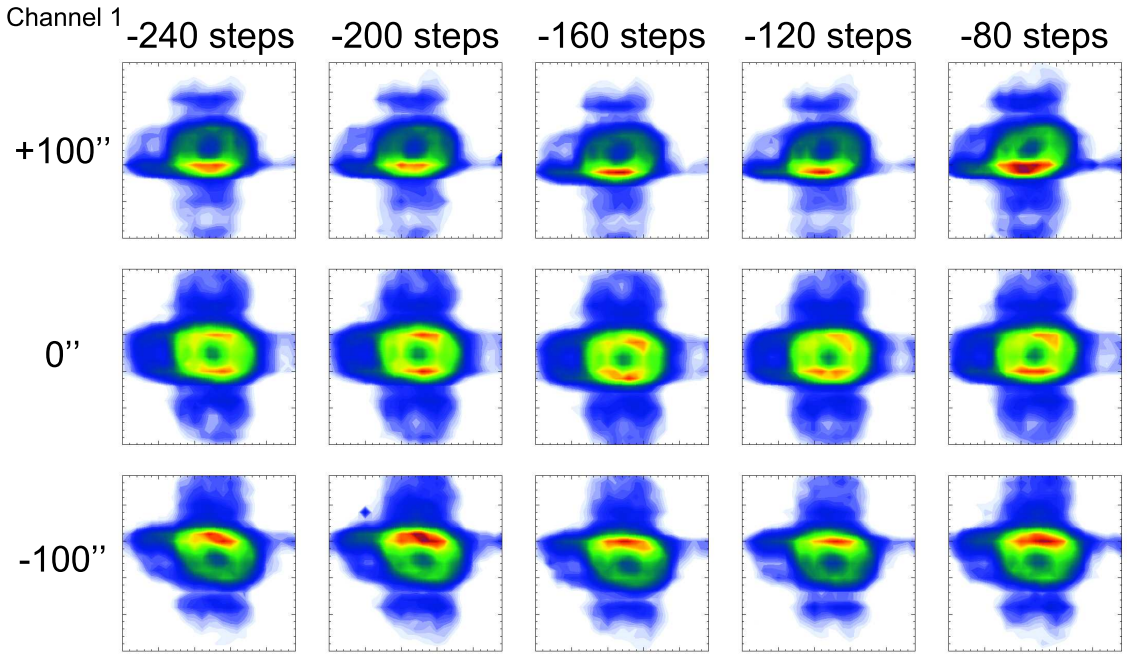

Figure C.2: Lyman-α grating Z-tilt adjustment for channel 2. +X-axis is toward the top and +λ toward the right. Spots are displayed in a 25x25 pixels box (325x325µm)

This diffraction effect in the spatial direction was a critical issue for the spectro-polarimeter spatial and spectral resolutions: new M3s were prepared to replace these mirrors. To avoid surface figure pattern with regular periodicity, the tolerance surface roughness of the new off-axis parabolic mirrors was defined for various scales: the RMS requirement was imposed and measured with five different spatial sampling x (i.e. measurement every x millimetres): x>20mm, 10<x<20mm, 2<x<10mm, 0.8<x<2mm and x<0.8mm. The surface figure of the new-M3s is shown in Figure C.4, and the spot observed at Lyman-α during the optical alignment of the spectro-polarimeter confirmed that the diffraction effect in the spatial direction was successfully removed.

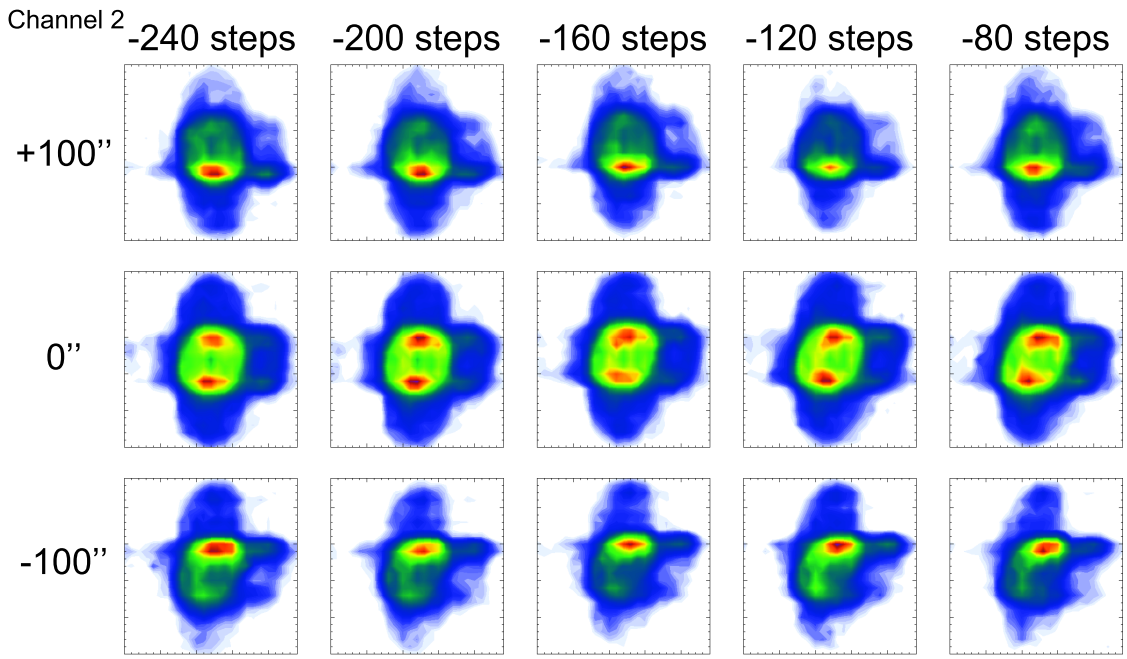

Figure C.3: Lyman-α grating Z-tilt adjustment for channel 2. +X-axis is toward the top and +λ toward the right. Spots are displayed in a 25x25 pixels box (325x325µm)

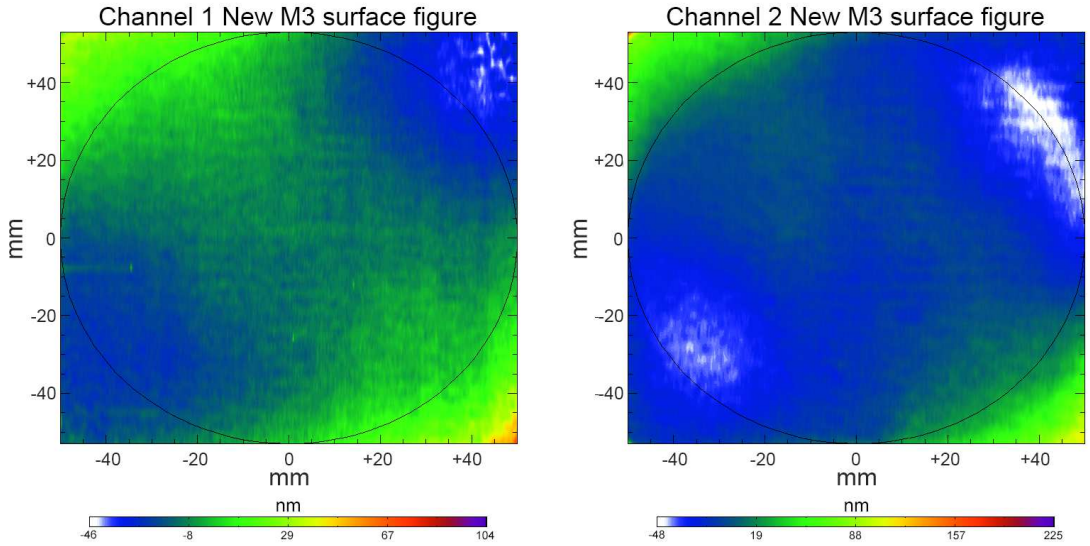

Figure C.4: Surface figure of channel 1's (left) and channel 2's (right) new-M3s. Black ellipsis shows the mirror's clear apertures.

Appendix D

Partial derivatives for the reponse matrix error transfer.

A proper error transfer method was used to combined the error from the photon noise and read-out noise on the measured polarization and the error on the response matrix elements into the final error on the corrected polarization, as discussed in Section 8.5. This method used the partial derivatives as a weighting factor accounting for the contribution of each error to the final error. The full expressions of the partial derivatives on q are shown in the following. The partial derivatives for u can be easily obtained with the permutation $q' \leftrightarrow u'$, $x_{10} \leftrightarrow x_{20}$, $x_{01} \leftrightarrow x_{02}$, $x_{11} \leftrightarrow x_{22}$ and $x_{12} \leftrightarrow x_{21}$.

$$\frac{\delta q}{\delta q'} = -\left[\frac{\left[\left(1-\frac{x_{20}(u'-x_{02})}{(x_{20}u'-x_{22})}\right)\left((x_{10}q'-x_{11})-\frac{(x_{10}u'-x_{12})(x_{20}q'-x_{21})}{(x_{20}u'-x_{22})}\right)\right]}{\left[(x_{10}q'-x_{11})-\frac{(x_{10}u'-x_{12})(x_{20}q'-x_{21})}{(x_{20}u'-x_{22})}\right]^2} - \frac{\left[\left((q'-x_{01})-\frac{(u'-x_{02})(x_{20}q'-x_{21})}{(x_{20}u'-x_{22})}\right)\left(x_{10}-\frac{x_{20}(x_{10}u'-x_{12})}{x_{20}u'-x_{22}}\right)\right]}{\left[(x_{10}q'-x_{11})-\frac{(x_{10}u'-x_{12})(x_{20}q'-x_{21})}{(x_{20}u'-x_{22})}\right]^2}\right] \tag{D.1}$$

$$\frac{\delta q}{\delta u'} = -\left[\frac{\left(-\frac{(x_{20}q'-x_{21})(x_{20}u'-x_{22})-(u'-x_{02})(x_{20}q'-x_{21})(x_{20})}{(x_{20}u'-x_{22})^2}\right)}{\left[(x_{10}q'-x_{11})-\frac{(x_{10}u'-x_{12})(x_{20}q'-x_{21})}{(x_{20}u'-x_{22})}\right]^2}\times \left((x_{10}q'-x_{11})-\frac{(x_{10}u'-x_{12})(x_{20}q'-x_{21})}{(x_{20}u'-x_{22})}\right) - \left((q'-x_{01})-\frac{(u'-x_{02})(x_{20}q'-x_{21})}{(x_{20}u'-x_{22})}\right)\times \frac{\left(-\frac{x_{10}(x_{20}q'-x_{21})(x_{20}u'-x_{22})-(x_{10}u'-x_{12})(x_{20}q'-x_{21})(x_{20})}{(x_{20}u'-x_{22})^2}\right)}{\left[(x_{10}q'-x_{11})-\frac{(x_{10}u'-x_{12})(x_{20}q'-x_{21})}{(x_{20}u'-x_{22})}\right]^2}\right] \tag{D.2}$$

$$\frac{\delta q}{\delta x_{10}} = -\left[-\frac{\left[\left((q'-x_{01})-\frac{(u'-x_{02})(x_{20}q'-x_{21})}{(x_{20}u'-x_{22})}\right)\left(q'-\frac{u'(x_{20}q'-x_{21})}{(x_{20}u'-x_{22})}\right)\right]}{\left[(x_{10}q'-x_{11})-\frac{(x_{10}u'-x_{12})(x_{20}q'-x_{21})}{(x_{20}u'-x_{22})}\right]^2}\right] \tag{D.3}$$

$$\frac{\delta q}{\delta x_{20}} = -\Bigg[\frac{\Big(-\frac{q'(u'-x_{02})(x_{20}u'-x_{22})-(u'-x_{02})(x_{20}q'-x_{21})u'}{(x_{20}u'-x_{22})^2}\Big)}{\Big[(x_{10}q'-x_{11})-\frac{(x_{10}u'-x_{12})(x_{20}q'-x_{21})}{(x_{20}u'-x_{22})}\Big]^2}\times \Big((x_{10}q'-x_{11})-\frac{(x_{10}u'-x_{12})(x_{20}q'-x_{21})}{(x_{20}u'-x_{22})}\Big) - \Big((q'-x_{01})-\frac{(u'-x_{02})(x_{20}q'-x_{21})}{(x_{20}u'-x_{22})}\Big)\times \frac{\Big(-\frac{q'(x_{10}u'-x_{12})(x_{20}u'-x_{22})-(x_{10}u'-x_{12})(x_{20}q'-x_{21})u'}{(x_{20}u'-x_{22})^2}\Big)}{\Big[(x_{10}q'-x_{11})-\frac{(x_{10}u'-x_{12})(x_{20}q'-x_{21})}{(x_{20}u'-x_{22})}\Big]^2}\Bigg] \tag{D.4}$$

$$\frac{\delta q}{\delta x_{01}} = -\Bigg[\frac{\Big[\Big(-1\Big)\Big]}{\Big[(x_{10}q'-x_{11})-\frac{(x_{10}u'-x_{12})(x_{20}q'-x_{21})}{(x_{20}u'-x_{22})}\Big]}\Bigg] \tag{D.5}$$

$$\frac{\delta q}{\delta x_{02}} = -\Bigg[\frac{\Big[\Big(-\frac{(-1)(x_{20}q'-x_{21})}{x_{20}u'-x_{22}}\Big)\Big]}{\Big[(x_{10}q'-x_{11})-\frac{(x_{10}u'-x_{12})(x_{20}q'-x_{21})}{(x_{20}u'-x_{22})}\Big]}\Bigg] \tag{D.6}$$

$$\frac{\delta q}{\delta x_{11}} = -\Bigg[\frac{-\Big[\Big((q'-x_{01})-\frac{(u'-x_{02})(x_{20}q'-x_{21})}{(x_{20}u'-x_{22})}\Big)\Big(-1\Big)\Big]}{\Big[(x_{10}q'-x_{11})-\frac{(x_{10}u'-x_{12})(x_{20}q'-x_{21})}{(x_{20}u'-x_{22})}\Big]^2}\Bigg] \tag{D.7}$$

$$\frac{\delta q}{\delta x_{22}} = -\Bigg[\frac{\Big[\Big(-\frac{-(u'-x_{02})(x_{20}q'-x_{21})(-1)}{(x_{20}u'-x_{22})^2}\Big)\Big((x_{10}q'-x_{11})-\frac{(x_{10}u'-x_{12})(x_{20}q'-x_{21})}{(x_{20}u'-x_{22})}\Big)\Big]}{\Big[(x_{10}q'-x_{11})-\frac{(x_{10}u'-x_{12})(x_{20}q'-x_{21})}{(x_{20}u'-x_{22})}\Big]^2} - \frac{\Big[\Big((q'-x_{01})-\frac{(u'-x_{02})(x_{20}q'-x_{21})}{(x_{20}u'-x_{22})}\Big)\Big(-\frac{-(x_{10}u'-x_{12})(x_{20}q'-x_{21})(-1)}{(x_{20}u'-x_{22})^2}\Big)\Big]}{\Big[(x_{10}q'-x_{11})-\frac{(x_{10}u'-x_{12})(x_{20}q'-x_{21})}{(x_{20}u'-x_{22})}\Big]^2}\Bigg] \tag{D.8}$$

$$\frac{\delta q}{\delta x_{12}} = -\Bigg[\frac{-\Big[\Big((q'-x_{01})-\frac{(u'-x_{02})(x_{20}q'-x_{21})}{(x_{20}u'-x_{22})}\Big)\Big(-\frac{(-1)(x_{20}q'-x_{21})}{(x_{20}u'-x_{22})}\Big)\Big]}{\Big[(x_{10}q'-x_{11})-\frac{(x_{10}u'-x_{12})(x_{20}q'-x_{21})}{(x_{20}u'-x_{22})}\Big]^2}\Bigg] \tag{D.9}$$

$$\frac{\delta q}{\delta x_{21}} = -\Bigg[\frac{\Big[\Big(-\frac{(-1)(u'-x_{02})}{(x_{20}u'-x_{22})}\Big)\Big((x_{10}q'-x_{11})-\frac{(x_{10}u'-x_{12})(x_{20}q'-x_{21})}{(x_{20}u'-x_{22})}\Big)\Big]}{\Big[(x_{10}q'-x_{11})-\frac{(x_{10}u'-x_{12})(x_{20}q'-x_{21})}{(x_{20}u'-x_{22})}\Big]^2} - \frac{\Big[\Big((q'-x_{01})-\frac{(u'-x_{02})(x_{20}q'-x_{21})}{(x_{20}u'-x_{22})}\Big)\Big(-\frac{(-1)(x_{10}u'-x_{12})}{(x_{20}u'-x_{22})}\Big)\Big]}{\Big[(x_{10}q'-x_{11})-\frac{(x_{10}u'-x_{12})(x_{20}q'-x_{21})}{(x_{20}u'-x_{22})}\Big]^2}\Bigg] \tag{D.10}$$

Figure D.1 shows the partial derivatives of the q function for each of the ten components, as a function of the measured q' and u'. One can see that the $\delta q/\delta q'$ and $\delta q/\delta x_{01}$ derivatives are close to unity and almost insensitive to changes in q' and u'. On the other hand, the influence of the $\delta q/\delta x_{10}$ and $\delta q/\delta x_{11}$ derivatives increases with q'. It is also interesting to notice that the $\delta q/\delta u'$ term is proportional to its corresponding azimuth error term, and the contribution of $\delta q/\delta x_{22}$ scales with u'.

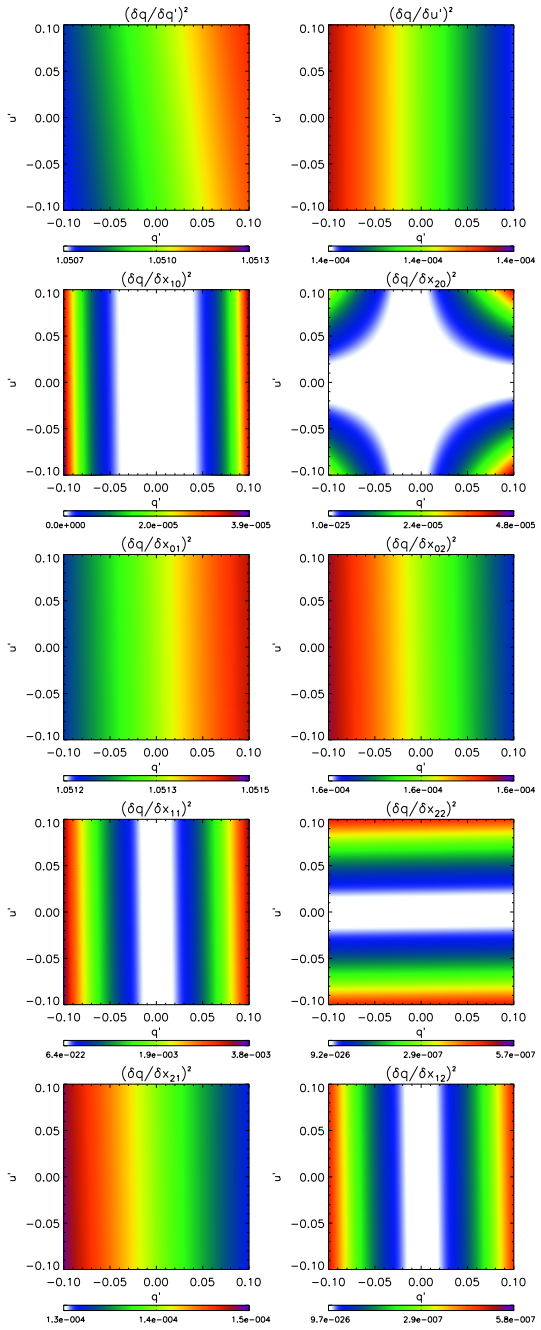

Figure D.1: Partial derivatives of the q function with respect to the ten components, as a function of q' and u'.

Bibliography

[1] Holweger, H., "Ein empirisches Modell der Sonnenatmosphare mit lokalem thermodynamischen Gleichgewicht.," *Zeitschrift fur Astrophysik* **65**, 365–417 (1967).

[2] Avrett, E., "The Solar Temperature Minimum and Chromosphere," *ASP Conference Series* **286** (2003).

[3] Young, C. A., "Spectrum observations at Burlington, Iowa, during the eclipse of 7th August 1869," *Proc. American Assoc. Adv. Sci.* **XVIII**, 78–82 (1869).

[4] Edlén, B., "Die Deutung der Emissionslinien im Spektrum der Sonnenkorona. Mit 6 Abbildungen.," *Z. Astrophys* (1942).

[5] Tousey, R., "Apollo telescope mount of skylab an overview," *Applied Optics Physics* **16**, 825–836 (1977).

[6] Vernazza, J. E., Avrett, E. H., and Loeser, R., "Structure of the solar chromosphere. Basic computations and summary of the results.," *Astrophysical Journal* **184**, 605–632 (1973).

[7] Vernazza, J., Avrett, E., and Loeser, R., "Structure of the solar chromosphere III. Models of the EUV brightness components of the quiet Sun.," *Astrophysical Journal Supplement Series* **45**, 635–725 (1981).

[8] Fontenla, J. M., Avrett, E. H., and Loeser, R., "Energy balance in the solar transition region. III. Helium emission in hydrostatric, constant-abundance models with diffusion," *The Astrophysical journal* **406**, 319–345 (1993).

[9] Gary, G. A., "Plasma beta above a solar active region rethinking the paradigm," *Solar physics* **203** (2001).

[10] Priest, E., "Magnetohydrodynamics of the Sun," *Cambridge Univserity Press* (2014).

[11] Shibata, K., "New observational facts about solar flares from Yohkoh studies Evidence of magnetic reconnection and a unified model of flares," *Advances in Space Research* **17**, 9–18 (1996).

[12] Gold, T., "The Physics of Solar Flares," *NASA Sp* **50** (1964).

[13] Parker, E., "Topological Dissipation and the Small-scale Fields in Turbulent Gases," *The Astrophysical Journal* **174** (1972).

[14] Pontieu, B. D., Erdélyi, R., and James, S., "Solar chromospheric spicules from the leakage of photospheric oscillations and flows," *Nature* **430**, 536–539 (2004).

[15] Hanle, W., "Uber magnetische Beeinflussung der Polarisation der Resonanzfluoreszenz," *Z. Phys* , 30:93 (1924).

[16] Degl'Innocenti, E. L. and Landorfi, M., "Polarization in spectral lines," *Kluwer Academic Publishers* (2004).

[17] Bueno, J. T., "A gentle introduction to the physics of spectral line polarization," *International Symposium on Solar Physics and Solar Eclipses* (2006).

[18] Ramos, A. A. and Bueno, J. T., "Advanced forward modeling and inversion of Stokes profiles resulting from the join action of the Hanle and Zeeman effects," *Astrophysical Journal* **683**, 542–565 (2008).

[19] Bueno, J. T., Štěpán, J., and Casini, R., "The Hanle Effect of the Hydrogen Lyα Line for Probing the Magnetism of the Solar Transition Region," *ApJ* **738:L11** (2011).

[20] Narukage, N. et al., "The magnetic field configuration of a solar prominence inferred from spectropolarimetic observations in the He I 10830 A triplet," *Astronomy and Astrophysics* **566** (2014).

[21] Suarez, D. O., Ramos, A. A., and Bueno, J. T., "Height vriation of the vector magnetic field in solar spicule," *The Astrophysical Journal* **803** (2015).

[22] Curdt, W., Tian, H., Teriaca, L., Schuhle, U., and Lemaire, P., "The Ly-α profile and center-to-limb variation of the quiet Sun," *A&A* **492**, L9–L12 (2008).

[23] Gouttebroz, P., Lemaire, P., Vial, J. C., and Arzner, G., "The solar hydrogen Lyman-beta and Lyman-alpha lines Disk center observations from OSO 8 compared with theoretical profiles.," *Astrophysical Journal* **225**, 665–664 (1978).

[24] Bueno, J. T., Štěpán, J., and Casini, R., "The Structure and Dynamics of the Upper Chromosphere and Lower Transition Region as Revealed by the Subarcsecond VAULT Observations," *Solar Physics* **261:53** (2010).

[25] Bueno, J. T., Štěpán, J., and Belluzzi, L., "The Hanle Effect in the Lyman-alpha Lines of H I and He II for Measuring the Magnetic Fields of the Solar Transition Region," *Astronomical Society of the Pacific* **456** (2012).

[26] Štěpán J., J., Bueno, J. T., Carlsson, M., and Leenaarts, J., "The Hanle Effect of the Lyα in a MHD model of the Solar Transition Region," *Astrophysical Journal Letters* **758:L43** (2012).

[27] Štěpán J., J., Bueno, J. T., Leenaarts, J., and Carlsson, M., "Three-dimensional radiative transfer simulations of the scattering polarization of the hydrogen lyα line in a MHD model of the chromosphere-corona transition region," *Astrophysical Journal* **758:L43** (2015).

[28] Woodgate, B. et al., "The ultraviolet spectrometer and polarimeter on the solar maximum mission," *Solar physics* **65** (1980).

[29] West, E., Kobayashi, K., Gary, A., and David, J., "The Solar Ultraviolet Magnetograph Investigation: Polarization Properties," *ASP Conference Series* **358** (2006).

[30] Henze, W., Tandberg-Hanssen, E., Hagyard, M. J., West, E. A., Woodgate, B. E., Shine, R. A., Beckers, J. M., Bruner, M., Hyder, C. L., and West, E. A., "Observations of the longitudinalmagnetic field in the transition region and photosphere of a sunspot.," *Solar Physics* **81**, 231:244 (1982).

[31] Hagyard, M. J., Teuber, D., West, E. A., Tandberg-Hanssen, E., Henze, W., Beckers, J. M., Bruner, M., Hyder, C. L., and Woodgate, B. E., "Vertical gradients of sunspot magneticfields.," *Solar Physics* **84**, 13:31 (1983).

[32] West, E., Cirtain, J., Kobayashi, K., David, J., Gary, A., and Adams, M., "MgII linear polarization measurements using the MSFC Solar Ultraviolet Magnetograph," *Proc. of SPIE* **8160** (2011).

[33] Stenflo, J. O., Dravins, D., Wihlborg, N., Bruns, A., Prokofev, V. K., Zhitnik, I. A., Biverot, H., and Stenmark, L., "Search for spectral line polarization in the solar vacuum ultraviolet," *Solar Physics* **66** (1980).

[34] Kano, R. et al., "Chromospheric Lyman-Alpha SpectroPolarimeter (CLASP)," *Proc. of SPIE* **8443** (2012).

[35] Kobayashi, K. et al., "The Chromospheric Lyman-Alpha Spectropolarimeter: CLASP," *Astron. Soc. Pacific* **233** (2012).

[36] Narukage, N. et al., "Vacuum ultraviolet spectropolarimeter design for precise polarization measurements," *Applied Optics* **54**(8) (2015).

[37] Narukage, N., Kubo, M., Ishikawa, R., Ishikawa, S., Katsukawa, Y., Kobiki, T., Giono, G., Kano, R., Bando, T., Tsuneta, S., Auchére, F., Kobayashi, K., Winebarger, A. R., McCandless, J., Chen, J., and Choi, J., "High reflectivity coatings for vacuum ultraviolet spectropolarimeter," *Applied Optics* (2015).

[38] Ishikawa, R. et al., "Strategy for Realizing High-Precision VUV Spectro-Polarimeter," *Solar Physics* **289**, 4727–4747 (2014).

[39] Ishikawa, S., Shimizy, T., Kano, R., Bando, T., Ishikawa, R., Giono, G., Tsuneta, S., Nakayama, S., and Tajima, T., "Development of the precise polarization modulator for the Chromospheric Lyman-Alpha SpectroPolarimeter (CLASP) sounding rocket experiment," *Solar physics* (2015).

[40] Bridou, F., Cuniot-Ponsard, M., Desvignes, J.-M., Gottwald, A., Kroth, U., and Richter, M., "Polarizing and non-polarizing mirrors for the hydrogen lyman-α radiation at 121.6nm," *Applied Physics A: Materials Science and Processing* **102:641** (2011).

[41] Ishikawa, R. et al., "Birefringence of magnesium fluoride in the vacuum ultraviolet and application to a half-waveplate," *Applied Optics* **52**, 8205–8211 (2013).

[42] Takeda, M., Ina, H., and Kobayashi, S., "Fourier-transform method of fringe-pattern analysis for computer-based topography and interferometry," *Optical Society of America* **72** (1982).

[43] Narukage, N. et al., "Overview of Chromospheric Lyman-Alpha SpectroPolarimeter (CLASP)," *Proc. of SPIE* **8148** (2011).

[44] C. Beck, R. S., Collados, M., Rubio, L. B., and Kentischer, T., "A polarization model for the German Vacuum Tower Telescope from in-situ and laboratory measurements," *A&A* **443**, 1047–1053 (2005).

[45] Ichimoto, K. et al., "Polarization Calibration of the Solar Optical Telescope onboard Hinode," *Solar Physics* **249**, 233–261 (2008).

[46] Elmore, D., "A polarization calibration technique for the advanced stokes polarimeter," *NCAR Technical Note NCAR/TN-355+STR* (1990).

[47] Lemen, J. et al., "The Atmospheric Imaging Assembly (AIA) on the Solar Dynamics Observatory (SDO)," *Solar physics* **275**, 17–40 (2012).